Prediction of Clear-Water Abutment Scour Depth in Compound Channel for Extreme Hydrologic Events

A Dissertation
Presented to
The Academic Faculty

by

SeungHo Hong

In Partial Fulfillment
Of the Requirements for the Degree
Doctor of Philosophy

School of Civil and Environmental Engineering
Georgia Institute of Technology
December, 2012

Prediction of Clear-Water Abutment Scour Depth in Compound Channel for Extreme Hydrologic Events

Approved by:

Dr. Terry W. Sturm, Advisor
School of Civil and Environmental Engineering
Georgia Institute of Technology

Dr. Philip J. Roberts
School of Civil and Environmental Engineering
Georgia Institute of Technology

Dr. Donald R. Webster
School of Civil and Environmental Engineering
Georgia Institute of Technology

Dr. Thorsten Stoesser
School of Civil and Environmental Engineering
Georgia Institute of Technology

Dr. James Wray
School of Earth and Atmospheric Sciences
Georgia Institute of Technology

Date Approved: December 19th, 2012

ACKNOWLEDGEMENTS

This study was accomplished under the invaluable guidance of Professor Terry W. Sturm, thesis advisor and chairman of the reading committee, who initially suggested the topic and offered excellent guidance and support and asked innumerable questions throughout the duration of the study. I also wish to express his sincere appreciation to all of those individuals who played an important role in making this thesis possible. First, I would like to express my special appreciation to Dr. Philip J. Roberts, Donald R. Webster, Thorsten Stoesser and James Wray, all at the Georgia Institute of Technology, for their assistance and their time in reviewing and commenting on this thesis. Sincere thanks are due to Andy Udell, whose assistance in the construction of the model was indispensable. Finally, special thanks go to my parents and family, who have provided me with inestimable and patient support and encouragement. In particular, I would like to thank HaeSun Byun, my wife, and three kids, Junhwa, Seohwa, and Junghwa for their support and patience, which have became a robust bridge from what I have been to what I will become.

This study would not have been possible without the financial support of the Georgia Department of Transportation.

TABLE OF CONTENTS

LIST OF TABLES

LIST OF FIGURES

LIST OF SYMBOLS

B_f, B_m	=	Floodplain and main channel width, respectively;
C_w	=	Weir discharge coefficient;
D_{50}	=	Median rock riprap diameter;
d_{50}	=	Median sediment size;
d_*	=	Dimensionless grain diameter $=((SG-1)gd_{50}^3/\nu^2)^{1/3}$;
d_{max}	=	Maximum scour depth measured from an undisturbed floodplain elevation;
H_b	=	Distance from the initial bed to bridge low chord in the floodplain;
H_E	=	Height of the embankment;
HW_r	=	Head measured above the crest in the weir;
K	=	Total turbulence kinetic energy $(=0.5(<u'^2>+<v'^2>+<w'^2>))$;
K_b	=	Total turbulence kinetic energy near the bed;
$\overline{K_b}$	=	Width-averaged total turbulence kinetic energy near the bed;
K_s, K_θ	=	Abutment shape and alignment factor, respectively;
k_f, k_m	=	Roughness height of the floodplain and main channel bed;
k_s	=	Equivalent sand grain roughness height;
k_s^+	=	Dimensionless equivalent sand grain roughness height $(=k_s u_*/\nu)$;
g	=	Gravitational acceleration;
La	=	Abutment length;
L_m	=	Transverse distance from the toe of the abutment to the maximum scour depth;

M	=	Discharge contraction ratio;
Q	=	Total discharge;
Q_f, Q_m	=	Discharge in the floodplain and main channel, respectively;
Q_{obst}	=	Obstructed floodplain discharge over a length equal to the abutment length projected onto the approach section;
Q_{ot}	=	Bridge overtopping discharge;
q_{f1}, q_{f2}	=	Floodplain discharge per unit width in the approach and bridge section, respectively;
q_{m1}, q_{m2}	=	Main channel discharge per unit width in the approach and bridge section, respectively;
r_T	=	A term for the local turbulence effects that contribute to additional scour;
R	=	Hydraulic radius;
SG	=	Specific gravity of the sediment;
t	=	Time;
T_{eq}	=	Time required to reach equilibrium scour depth;
U	=	Time-averaged point velocity;
u', v', w'	=	Fluctuating longitudinal, lateral and vertical velocity components;
$sqrt<u'^2>$, $sqrt<v'^2>$, $sqrt<w'^2>$	=	Turbulence intensity for longitudinal, lateral and vertical components;
u_*	=	Shear velocity;
u_{*c}	=	Critical value of shear velocity;
V_{f1}, V_{f2}	=	Mean floodplain flow velocity in the approach and bridge section, respectively;
V_{m1}, V_{m2}	=	Mean main channel flow velocity in the approach and bridge section, respectively;
$V_{cf1,}$ V_{cm1}	=	Critical velocity for initiation of sediment motion in the approach floodplain and main channel, respectively;

W	=	Setback distance;
W_e	=	Width of the embankment in the flow direction;
x, y, z	=	Longitudinal, lateral and vertical coordinate;
y_0	=	Flow depth for unconstricted flow;
y_1, y_2	=	Flow depth in the approach and bridge section, respectively;
y_{2max}	=	Maximum flow depth after scour;
κ	=	Van Karman constant;
σ_g	=	Geometric standard deviation of the particle size distribution;
τ_c	=	Critical shear stress for incipient sediment motion;
τ_{*c}	=	Shields parameter;
ν	=	Kinematic viscosity of the fluid;
$\gamma_s, \ \gamma$	=	Specific weight of sediment and fluid, respectively;

SUMMARY

Abutment scour around bridge foundations has been recognized as one of the significant causes of bridge failures. Even though numerous studies have been conducted on scour around bridges since the late 1950s, there is still no widely applicable abutment scour formula, or for that matter, even a distinct definition of abutment scour because of difficulties in understanding the complex flow structures and scour mechanisms around an abutment. Furthermore, almost all of the previous studies have focused on the case of free-surface flow in simpler idealized situations relative to the channel and bridge geometry even though floods of extreme magnitude can result in bridge overtopping flow in combination with submerged orifice flow. In this study, abutment scour experiments were carried out in a compound channel to investigate the characteristics of abutment scour in free-surface flow, submerged orifice flow, and overtopping flow cases. To investigate a submerged orifice flow and overtopping flow, a bridge deck model was constructed based on the bridge design and dimensions commonly used by Georgia DOT in a rural region. Three different lengths of erodible embankment/abutment protected by rock rip-rap were used on the left floodplain to simulate different flow contraction ratios while the abutment was set on the bankline in the right floodplain for all experiments. In the moveable bed experiment, detailed bed contours were measured at six intermediate time durations and at the occurrence of scour equilibrium in order to understand the complex flow physics and resulting sediment transport around an abutment over time. Three components of velocities and turbulent intensities were measured by acoustic

Doppler velocimeters (ADV) in fixed bed experiments in order to observe the initial flow conditions and the initial distribution of turbulence kinetic energy, and then, equilibrium scour depth was correlated with the measured initial flow parameters. The results showed that the contracted flow around an abutment because of lateral and/or vertical contraction and local turbulent structures at the downstream region of the bridge were the main features of the flow responsible for the maximum scour depth around an abutment. From a combination of the experimental results for scour and the detailed measurements of initial flow parameters, an abutment scour prediction method was suggested that included the effect of local turbulence and flow contraction. Finally, experimental results were compared to other leading investigators' experimental results, and the comparison showed that the erosional strength of the embankment should be included in the analysis to define the two extremes of a solid abutment and foundations vs. a riprap-protected embankment and abutment.

CHAPTER I

INTRODUCTION AND MOTIVATION

1.1 *Introduction*

Scour around bridge foundations can be generally divided into three categories. First, long term aggradation or degradation represents changes in bottom elevation and accompanying changes in width of the river over a long period of time due to geomorphic adjustments. Second, contraction scour occurs when a flow is restricted by natural causes such as narrowing of a natural channel or the existence of any obstruction like an embankment and the resulting flow constriction through the bridge opening. Third, local scour around the bridge foundation is caused by an obstruction to the flow such as a pier or abutment, and is therefore localized in the immediate vicinity of the obstruction in the main channel and floodplain of the river.

Scour at bridge foundations in river beds has attracted the attention of engineers and researchers because scouring at bridge piers and abutments mainly during flood events can lead to the failure of bridges. One thousand bridges have collapsed over the last 30 years in the United States and 60 percent of those failures are due to scour at bridge foundations, resulting in large financial losses (Shirole, 1991). For example, the total financial loss to the Georgia Department of Transportation (GDOT) was approximately $ 130 million because more than 100 bridges had to be replaced and

repaired due to flooding from tropical storm Alberto (over 500 year flood event) in Georgia in 1994 (Richardson and Davis, 2001). During the 1993 upper Mississippi River basin flooding, more than 258 million dollars in federal assistance was requested for repair and/or replacement of bridges, embankment, and roadways (Parola et al. 1997). Bridge failures can also lead to loss of life such as the I-90 bridge failure over Schoharie Cree near Albany, New York in 1987, the US 51 bridge over the Hatchie River in Tennessee in 1989, and the I-5 bridges over Arroyo Pasajero in California in 1995 (Morris and Oagan-Ortiz, 1999).

Richardson et al. (1993) quoted a 1973 study for the U.S. Federal Highway Administration (FHwA) that 25% of past bridge failures involved pier damage while 72% involved abutment damage. According to Melville (1992), 30% of bridge failures in New Zealand were due to abutment scour during the period of 1960-1984. Numerous studies on scour around bridges conducted since the late 1950s have generated formulas for scour depth estimation at bridge piers (Melville and Sutherland (1988), Melville (1997), Richardson and Davis (2001), and Ettema et al., (2011)). Although some researchers have suggested the need for more research on the subject of pier scour estimation, past studies have provided acceptable pier scour predictors for given ranges of pertinent flow parameters. However, no formula for abutment scour is widely applicable, nor has this term been distinctly defined because of difficulties in understanding the complicated flow and scouring mechanisms combined with the complex geometries of bridges and various erodible bed materials such as gravel, sand, and clay.

Aware of the lack of accurate methods to predict local scour at bridge abutment,

several studies have been completed since the beginning of the 1980s (for example, Melville (2000), Chang and Davis (1998), Sturm (2006) and Sturm et al (2011)). However, engineering experience seems to indicate that computation of abutment scour depth using current scour formulas tends to overpredict scour in comparison to field measurements. The result can be overdesigned bridge foundations that increase the cost of the bridge. In fact, achieving a balance between safety and cost is a very difficult problem which is why the FHwA has mandated the use of scour prediction formulas that have a very large factor of safety to compensate for a lack of understanding of the complex physics of the scour process. One example is in GDOT bridge design manual, "Section 14.1.7 Bridge Abutment Protection ~The department of Transportation uses two sizes of riprap to protect against abutment scour: Type 1 riprap has a D_{50} of 1.14 feet and Type 3 riprap has a D_{50} of 0.64 feet.". The GDOT manual recommends using the bigger riprap size to protect against abutment scour for all locations in GA if there is no placement problem.

According to Richardson et al. (1993), one of the possible reasons for why current methods inaccurately predict scour depth is that the existing methods for estimating abutment scour depth do not take into account the complexities associated with real-world channel geometry and boundary material. A lot of research on abutment scour has focused on the simpler and idealized situations of scour in fixed-abutments placed in straight rectangular channels even though many abutments are erodible and sited in compound channels whose geometry and hydraulic characteristics are site-specific in the real world. Another possible reason for the inaccurate prediction of scour depth is that

current FHwA guidelines assume that contraction and local scour are independent processes. However, both contraction and local scour occur in cases in which a long roadway approach section and narrow bridge opening force floodplain waters to flow through the bridge opening, causing a severe contraction in flow area. In such cases, these two types of scour do not occur independently. As a result, it is difficult to separate contraction scour and local abutment scour processes. However, current scour practice assumes that contraction and local scour processes are independent and thus are determined separately and summed for total scour depth.

Further confusing the definition of abutment scour is that during extreme hydrologic events. Recent flooding in the Atlanta metro area in Georgia, USA in September 2009, as shown in Figure 1.1, resulted in extensive damage to numerous bridges due to the overtopping which caused abutment scour and failure of the approach embankment in some instances. In the extreme hydrologic events on the order of the 500-year or larger, increased upstream velocities and depth can often result in either submerged orifice flow or embankment and bridge overtopping flow in combination with submerged orifice flow. Submergence of the upstream face of a bridge produces vertical flow contraction in addition to existing lateral flow contraction caused by the embankment on the floodplain. The result of both types of contraction is a more complex flow field in the vicinity of the abutment than the free flow case. However, most studies have focused on the case of free-surface flow in simpler idealized situations even though heavy rain associated with global warming has produced an increasing number of flooding scenarios and resulted in widespread damage and the closing of bridges in recent

years, and it is likely to do so in the future. The occurrence of floods of extreme magnitude appear to be so rare as to obviate the necessity for analysis, but in 1994 (Tropical Storm Alberto) and again in 2009, extreme floods resulting in huge financial losses occurred in Georgia (Hong and Sturm (2010)). Given that embankment overtopping can and does occur and that it may even be allowed to occur if the abutment structure itself is designed to withstand complete failure, this study is a preliminary consideration of the types of scour that are present in such instances.

Figure 1.1 September 2009 Flooding at Peachtree creek in Atlanta, GA

Numerous studies have been conducted since the late 1950s on scour around bridges. However, there is still no widely applicable abutment scour formula, or for that matter, even a distinct definition of abutment scour (Sturm et al. (2011). Furthermore, almost of the studies have focused on the case of free-surface flow in simpler idealized situations even though such extreme floods can involve complex flow patterns caused by

bridge submergence and overtopping in compound river channels. The consequences include closings, widespread damage and rebuilding costs, and loss of life. In summary, this study focused on the following tasks to meet the thesis objective for improving estimation methods for abutment scour in three different flow types (Overtopping, Submerged Orifice, and Free Surface Flows):

- Assess the suggested equations for maximum scour depth around an abutment;
- Determine the important hydraulic parameters influencing maximum scour around an abutment;
- Understand the general features of the flow field in the vicinity of an abutment;
- Investigate the effects of flow distribution, as affected by abutment length and degree of bridge submergence, on clear water scour in a compound channel for abutment lengths that terminate on the floodplain as well as encroach on the bank of the main channel;
- Investigate the effects of overtopping and submerged orifice flows on clear-water abutment scour depth;
- Develop an improved scour-depth estimation method readily useable by engineers designing bridge foundations.

CHAPTER II

LITERATURE REVIEW

2.1 *Introduction*

Failure of bridges due to scour during floods has been well documented (Parola et al. 1998, Morris and Pagan-Ortiz 1999 and Richardson and Davis 2001). In many cases, the cause of failure has been classified as abutment scour. However, there is still no clear agreement on its definition because of difficulties in understanding the complicated flow and scouring mechanisms combined with the complex geometries of bridges and various erodible bed materials such as gravel, sand and clay.

In current scour prediction methodology as recommended by the Federal Highway Administration (FHwA), abutment scour is treated as local scour near the abutment while contraction scour is considered to be scour that occurs across the entire cross-section, and the two estimates of maximum scour depth can be added to obtain an estimate of total scour at the abutment because current scour guidelines assume that contraction and local scour processes are independent and are determined separately. In contrast, laboratory studies by Sturm (1999, 2006), Ettema et al. (2006), and Ettema et al. (2008) on long abutments terminating on the floodplain of compound channels have predicted abutment scour depth as a multiplying factor times the idealized contraction scour depth as suggested by Laursen (1963). A further evaluation of existing abutment

scour formulas by Sturm et al. (2011) concludes that this framework appears to be the most useful and effective approach to prediction of abutment scour but that formula refinements from more realistic experiments and carefully controlled continuous scour monitoring of bridges are needed. They pointed out that independent scour processes cannot be assumed because the severe contraction in flow area through the bridge opening tends to cause scour processes to act concurrently, and it is difficult to separate the contraction and local scour processes.

2.2 *Sediment Transport Theory*

Scour is a process of sediment transport. When water flows over a sediment bed, a hydrodynamic force is exerted by the water on the individual sediment grains at the bed surface. For non-cohesive sediments such as sands and gravels, the weight forces of the particles themselves are the only forces that resist particle entrainment. The threshold of sediment movement occurs when applied forces due to fluid drag and lift exceed the stabilizing force due to gravity. More recent and detailed studies have shown that the duration as well as the magnitude of turbulent bursting events are instrumental in determining instantaneous entrainment of sediment grains (Diplas et al. (2008))

The Shields parameter is commonly used to identify the threshold of sediment movement based on mean flow properties and characteristics of the sediment. For flow below the threshold conditions, the riverbed is stable with no movement of sediment. For flows above the threshold conditions, the boundary sediment will be entrained in the flow with sediment movement taking place. Shields collected experimental data on initiation

of motion and bedload transport of sediment and presented the Shields diagram using a dimensionless parameter τ_{*c} to express the initiation of sediment motion as a function of the boundary Reynolds number which is affected by viscosity and sediment size. Later, the Shields diagram was modified by the many other researchers, including Rouse(1939), Yalin and Karahan(1979), and Buffington (1999). The modified Shields diagram is shown in Fig. 2.1 in terms of a dimensionless grain diameter d_* which is defined by

$$d_* = \left(\frac{(SG-1)\, g\, {d_{50}}^3}{\nu^2} \right)^{1/3} \tag{2.1}$$

in which SG = specific gravity of the sediment, g = gravitational acceleration, d_{50} = median sediment grain size, and ν = kinematic viscosity of the fluid.

The critical velocity (V_c), which is the flow velocity for initiation of motion for sediment, can be determined from Keulegan's equation:

$$V_c = 5.75 \sqrt{\tau_{*c}\,(SG-1)\, g\, d_{50}}\, \log\left(\frac{12.2\, R}{k_s}\right) \tag{2.2}$$

where τ_{*c} is Shields parameter, which is equal to $\tau_c/[(\gamma_s - \gamma)\, d_{50}]$, τ_c is critical shear stress for incipient sediment motion, γ_s is the specific weight of sediment, γ is the specific weight of fluid, d_{50} is median grain size, SG is specific gravity, g is gravitational acceleration, R is hydraulic radius, and k_s is equivalent sand-grain roughness height. For uniform bed sediments it is adequate to use 1 to 2 times d_{50} to calculate V_c for the

riverbed. For non-uniform materials, d_{50} alone may be inadequate because the different sizes of sediment have different degrees of resistance to scour and their interactions are complex. Sediment non-uniformity can be described by the geometric standard deviation σ_g, of the particle size distribution.

$$\sigma_g = \sqrt{\frac{d_{84}}{d_{16}}} \tag{2.3}$$

where d_{16} and d_{84} are the sediment sizes for which 16% and 84% of the sediment is finer by weight. Sediment material is considered uniform if σ_g < 1.5.

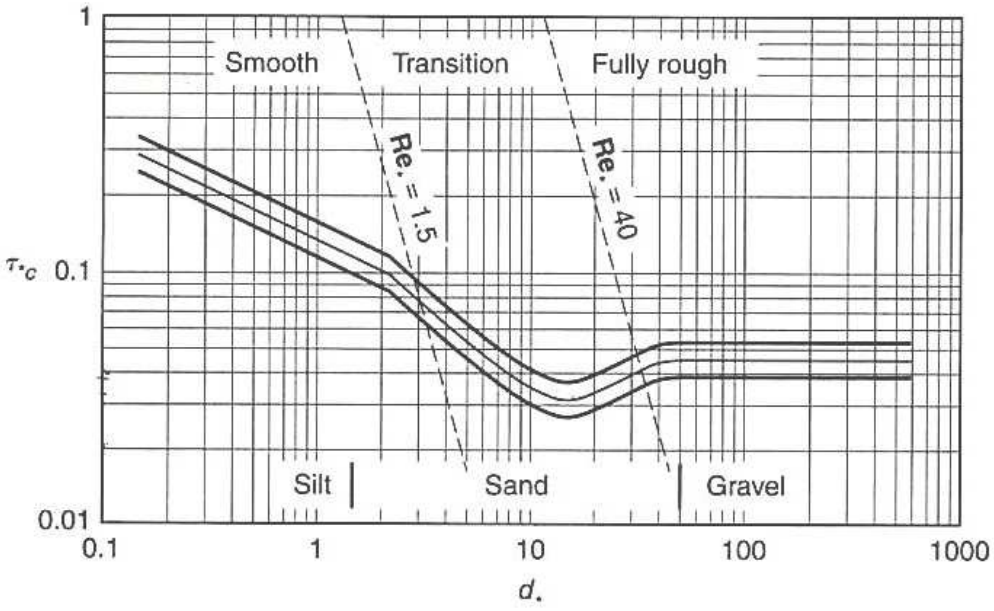

Figure 2.1 Shields diagram for direct determination of critical shear stress (Sturm 2001)

2.3 *Types of Scour at Bridge Crossings*

Scour at bridge crossings can be generally divided into three different types; general scour, contraction scour ,and local scour. Furthermore, contraction and local scour are both induced by the existence of the bridge, and can occur either as clear-water scour or live-bed scour.

General scour: Fluvial, geomorpological and hydrometeorological processes in a river result in long-term variations in the flow conditions which cause changes in geomorphic form of the river including both downcutting and deposition. These river form adjustment processes are often referred to as long-term aggradation or degradation, but gradual translation of meanders and even changes between geomorphic river types such as meandering and braided can occur. General scour occurs irrespective of the presence of a bridge structure. Lateral shifting of the channel banks due to meandering can result in bridges being outflanked by the river.

Contraction scour: The flow at a bridge usually converges as it approaches the bridge because the bridge structure causes a constriction of the flow. The encroachment from the abutments causes the flow to contract, separate from the abutments and accelerate through the bridge section. Downstream of the bridge the flow decelerates, gradually re-distributing itself throughout the river channel. The accelerated flow in the bridge section exerts a greater shear stress on the bed sediment, which results in a contraction scour throughout the contracted area.

Local scour: Local scour is caused by the direct interference of the bridge abutment or pier with the flow, setting up three-dimensional flow structures and vortex systems responsible for inducing local scouring process. Local scour only occurs if the local flow field has enough energy to transport the bed sediment and it is characterized by the formation of scour holes adjacent to the abutment or pier. Inter-related local scour processes include separation of the approach flow from the bed, downflow in front of the obstruction, formation of a horseshoe vortex that wraps around the base of a pier or abutment, a separated shear layer adjacent to the pier or abutment, and a wake region immediately downstream of the obstruction. (Lee and Sturm (2009))

Clear-water scour: Clear-water scour occurs when the sediment in the approach flow just upstream of the scour area is at rest. This happens when the shear stress exerted on the sediment by the flow is less than the critical shear stress of the sediment. Under clear-water conditions, no sediment is transported into the scour hole from upstream, and the maximum scour depth occurs when the flow can no longer remove sediment from the scour hole; that is, when the shear stress there falls to its critical value.

Live-bed scour: Live-bed scour occurs when the sediment upstream of the scour area is being transported, such that there is sediment transport by the river. This happens when the shear stress exerted on the sediment by the flow is greater than the critical shear stress of the sediment. Under live-bed conditions, the local scour hole develops rapidly and then oscillates about the equilibrium scour depth due to the propagating bed-forms. The magnitudes of the bed-forms influence the maximum scour because the troughs of the

bed-forms momentarily and locally lower the bed as they propagate through the bridge cross-section. The equilibrium scour depth is attained when the rate at which sediment is transported into the scour hole is equal to the rate at which it is removed from the scour hole.

2.4 *Characteristics of Flow Around a Bridge Abutment*

Bridge abutment scour is one type of local scour that manifests itself as a scour hole around a bridge abutment caused by sediment transport driven by flow contraction and local flow structures induced by the abutment. The flow through a bridge waterway narrowed by a bridge abutment and its embankment is similar to flow around a short contraction. When flow area at the flood stage is reduced by the bridge opening, velocity and bed shear stress will be increased in order to satisfy continuity and momentum equations. The higher velocity results in increased erosive force, so more bed material is removed from the contracted section. Furthermore, local flow structures associated with the bridge obstruction and higher velocity results in additional scour around the abutment. Due to the local flow structures, the scour depth near the upstream edge or corner of the abutment is usually deeper than that near the center of the channel. In general, the local flow structure around an abutment consists of the downflow at the upstream face of the abutment, the principal vortex (horseshoe vortex) system around the base of the abutment, the separation zone adjacent to the abutment face, and the wake vortex system at the rear of the abutment. Figure 2.2 shows flow structures around an abutment.

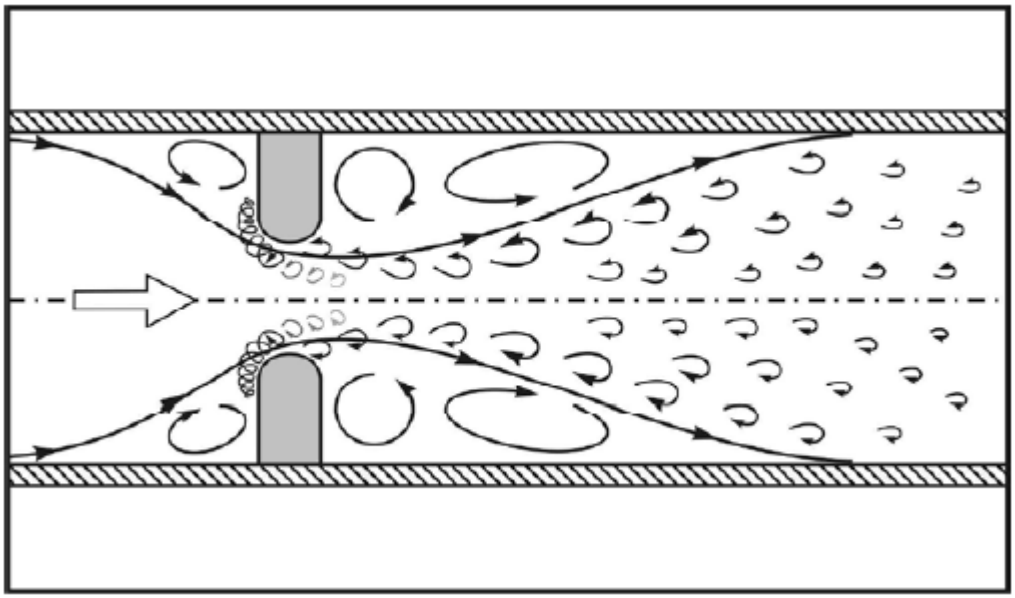

Figure 2.2 Flow structures around a short abutment (Ettema et al. 2010)

The stagnation pressure on the upstream face of the abutment decreases with the distance below the free surface as a result of the nonuniform velocity distribution in the boundary layer resulting in a weak pressure gradient along the upstream face of the abutment that drives the downward flow. The downward flow increases from the free surface to a point near the bed. The downward flow impinges on the bed like a vertical jet and erodes material from the front of the abutment. The downward flow produces a reverse bottom current near the bed that encounters the approach channel flow at some distance from the upstream face of the abutment, where a stagnation point occurs. Furthermore, due to the strong adverse pressure gradient imposed by the abutment in the streamwise approach flow direction, the boundary layer separates upstream of the bridge abutment resulting in the formation of the horseshoe vortex (principal vortex) system that

wraps around the abutment at its base. That lateral arm of the horseshoe vortex carries away the eroded bed material from the front of the abutment. The wake vortex system is formed by flow separation on the face of the abutment: its tornado-like vortices with vertical axes act like a vacuum in removing some of the bed material in the lee of the abutment. Immediately downstream of the abutment, flow is re-entrained into the constricted stream which sets up a horizontal circulation downstream of the abutment. Figure 2.3 schematically illustrates the characteristic flow features in a compound channel.

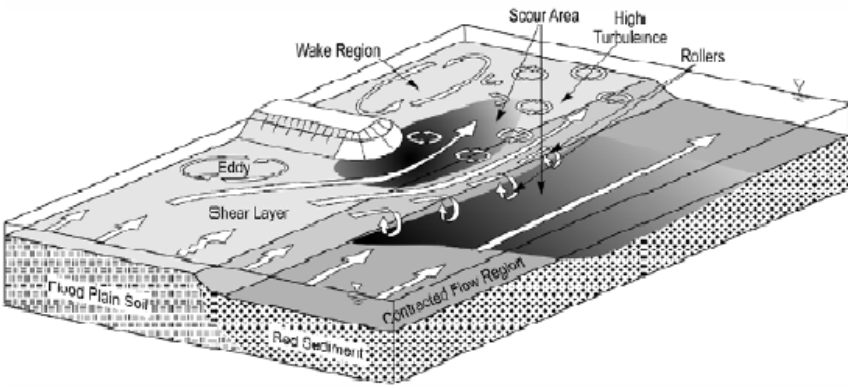

Figure 2.3 Flow structure including macro-turbulence generated by floodplain/main channel flow interaction, flow separation around abutment, and wake region on the floodplain in a compound channel. (Ettema et al. 2010)

Local flow structures around bridge foundations have been investigated in a number of experimental studies. Kwan (1988) and Kwan and Melville (1994) concluded that the flow in and around the scour hole at piers and abutments had similar features from their experimental investigations, particularly where the fixed abutment extended

only a short distance in the channel (relatively short abutment). The dominant local flow components at a short abutment were one side of the horseshoe vortex and associated downflow, which are also important local flow structures in the development of scour at bridge piers. For longer abutments, Kwan (1984) identified the strong spiral flow shown as the larger curled arrows in Figure 2.4. He also mentioned the importance of induced secondary (counter-rotating) vortices around the edge of the scour hole, shown as the smaller curled arrows in Figure 2.4. Another important feature of flows for longer abutments discussed by Melville (1997) was the existence of a quiescent region of recirculation fluid at the junction between the upstream face of the abutment and the channel wall, shown in Figure 2.4 as a weak counter-rotating eddy.

Figure 2.4 The observed flow patterns around a relatively long abutment (reproduced from Melville and Coleman, 2000)

Flow visualization by Chrisohoides et al. (2003) also successfully captured the large-scale coherent structures at the free surface upstream and downstream of an abutment with a digital camera. Figures 2.5 and 2.6 show a sequence of time-averaged digital images for the upstream and the downstream corners of an abutment, respectively. The images shown in Figure 2.5 reveal the large-scale flow at the center of the recirculation region and a smaller eddy at the junction between the abutment face and the channel side wall. The location of the stagnation point at the abutment face, marked by arrows in Figure 2.5, is also revealed. Chrisohoides et al. showed the upstream recirculating zone to be unsteady such that two or more eddies combined and split from each other on an irregular time interval. They postulated that this large-scale unsteadiness may be linked to the unsteadiness of the horseshoe vortex system. Figure 2.6 shows the large-scale eddies shed from the upstream edge of the abutment. The images clearly depict the unsteady roll up of the shear layer, the formation and shedding of eddies, and the transport of these eddies downstream.

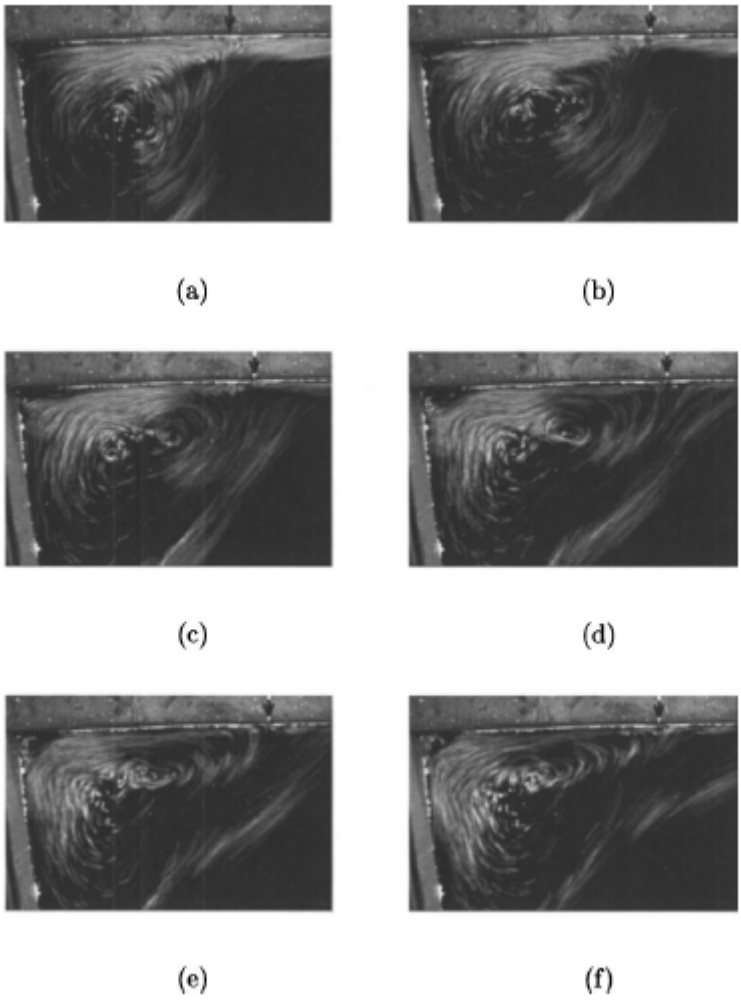

Figure 2.5 A sequence of time-averaged digital images for the upstream corner region of an abutment. (Chrisohoides et al., 2003)

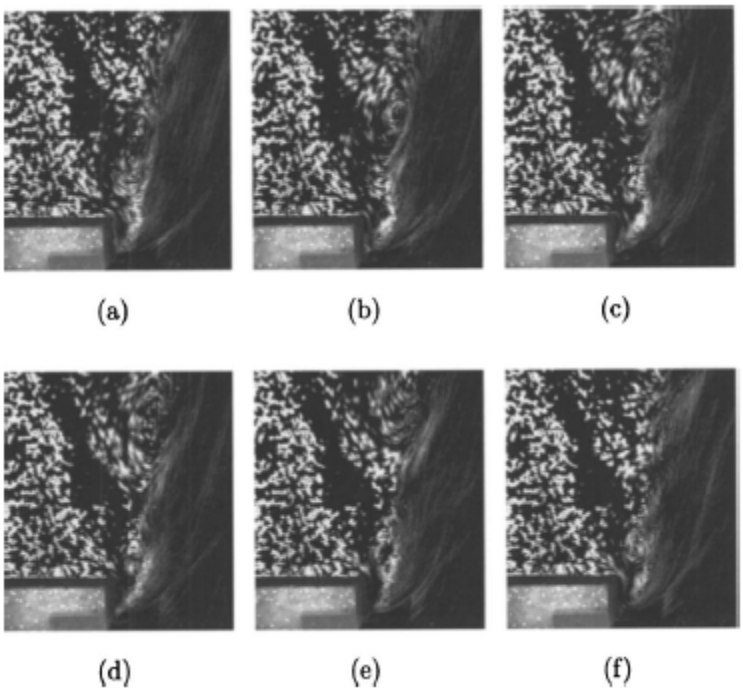

Figure 2.6 A sequence of time-averaged digital images for the downstream corner region of an abutment. (Chrisohoides et al., 2003)

Ettema et al. (2010) observed the surface flow patterns downstream of an abutment with Large Scale Particle Image Velocimetry (LSPIV). The pair of photographs in Figure 2.7 shows the LSPIV measurement of the before and after scour conditions. The large wake eddy downstream of the abutment grew and extended into the scour hole as scour progressed. The eddy's lateral extent reflects the contraction of flow passing around the abutment.

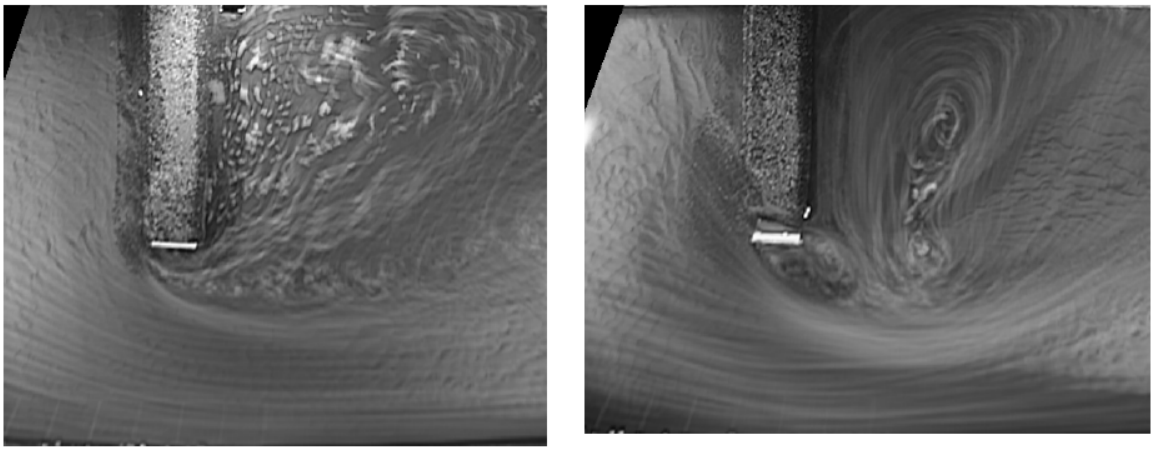

(a) (b)

Figure 2.7 Surface flow patterns determined by LSPIV; flow field before scour (a), and flow field associated with equilibrium scour (b). (Ettema et al., 2010)

Dey and Barbhuiya (2006) also experimentally investigated the three dimensional velocity and turbulence fields around a short vertical-wall abutment under clear water scour conditions using an acoustic Doppler velocimeter (ADV). Visualization of the flow field through velocity vectors upstream of the abutment showed that the flow curves down and then forms a circulatory flow with a horizontal axis at the lower portion of the abutment, which is the primary vortex. Downstream of the abutment, upward flow was comprised of irregularities owing to vortex shedding. Turbulent kinetic energy profiles showed a higher value behind and close to the abutment where the deeper scour hole occurred.

Based on the experimental results conducted by Ahmed and Rajaratnam (2000) with a short wingwall bridge abutment (ratio of the abutment length to the approach flow depth less than unity), the maximum bed shear stress around the abutment was nearly 3.63 times as high as the bed shear stress in the approach section. The area with

maximum shear stress around an abutment face corresponds to the region of initial sediment transport and a deeper scour hole as reported by Oliveto and Hager (2002) and Radice et al. (2006).

Numerical simulation has also been used to investigate the flow field around an butment. Chrisohoides et al. (2003) used URANS (unsteady Reynolds-averaged Navier-Stokes equations) with a $\kappa-\omega$ turbulence closure to investigate 3D coherent vortices induced by a vertical bridge abutment placed on the non-erodible flat bed. They successfully captured the region of recirculation flow at the upstream face of the abutment explained by Melville (1997) and showed that the flow in the vicinity of the foundation is highly three dimensional and characterized by large-scale unsteadiness. The calculated maximum shear velocity at the upstream corner of the abutment face correlated well with the experimental measurements of scour depth by Sturm (1999).

Paik and Sotiropoulos (2005) and Paik et al. (2007, 2010) simulated the flow past groyne-like structures using detached eddy simulation (DES) and successfully captured the complexity of the recirculating region at the upstream face of a groyne. Based on the findings, they concluded that the impact of recirculating flow on the scouring process may be far more direct than previously believed because the fluid in this region appears to feed the primary abutment vortex. They also demonstrated that the aspect ratio of the groyne length and the channel depth significantly affect the dynamics of coherent structures such as turbulent horseshoe vortex (THSV) around the groyne.

Ballio et al. (2009) also conducted large eddy simulation (LES) with a short trapezoidal abutment to investigate the recirculating region upstream of the abutment.

Four vortex structures were identified in the upstream region of the abutment, and they were analyzed to find their effects on shear stresses around the toe of the abutment. They concluded that the mean shear stress increases by up to one order of magnitude around the upstream corner of the abutment face, which is the region where erosion processes are known to begin from experiments with fixed abutment.

2.5 *Scour Development at Abutments in Compound Channel*

Many bridge abutments are situated in compound channels which are comprised of a main channel and a floodplain, over which flow occurs during flood conditions. The flow characteristics in a compound section have been investigated experimentally by several investigators (Rajaratnam and Ahmed 1979; Knight and Demetriou 1983; Wormleaton and Hadjipanos 1982, 1985; Myers and Brennan 1990; Myers and Lyness 1997). For small values of relative depth in a compound channel (ratio of floodplain flow depth to main channel flow depth), shallow, slower-moving flow in the floodplain adjacent to the faster-moving flow in the main channel results in a complex interaction that includes the strong transverse transfer of longitudinal momentum from the main channel to the floodplain flows. This phenomenon is more pronounced in the immediate interface region between the main channel and the floodplain, where there exists a strong transverse gradient of the longitudinal velocity. The result is that for a given stage, the total flow in the compound channel is less than what would be calculated as the sum of the flows in the main channel and the floodplain assuming no interaction. Wormleaton and

Hadjipanos (1982, 1985) applied three imaginary interfaces (vertical, diagonal, and horizontal interface) to separate the main-channel and floodplain flow and compared the accuracy of each interface method in predicting measured discharges. The result showed that even though a calculation method may give a satisfactory value for total discharge assessment in a compound channel, the distribution of flow between main channel and floodplain may be poorly modeled. In general, the floodplain discharge tends to be underestimated and this is compensated to a greater or lesser degree by overestimated main channel discharge.

When abutments are placed in the compound section geometry, the flow distribution will be different than for the abutment in a rectangular cross section. However, most laboratory models of abutment flows have been undertaken only in rectangular channels, and the results showed that abutment/embankment length was one of the primary variables affecting scour around the abutment. The approach velocity distribution in a compound channel is not subject to the idealized and uniform distribution obtained in laboratory experiments in rectangular channels as shown in Figure 2.8 (Richardson et al., 1993). Instead, the scour is a function of the redistribution of flow between the main channel and floodplain through the bridge opening. In other words, abutment length is certainly important, but the same abutment length may result in different scour depths depending on the approach flow distribution in the compound channel and its redistribution as it flows through the contracted opening (Sturm 1999). Sturm and Janjua (1994) have shown that the discharge distribution in the approach compound channel and its alteration by the bridge abutments is an important determinant

of equilibrium scour depths in clear-water abutment scour experiments. Compound channel geometries must therefore be taken into account when comparing such laboratory results to real abutments in compound channels.

Recently, Kara et al. (2012) have applied a 3D numerical model to the problem of compound channel flows because the flow and turbulence distributions are so important to the prediction of scour when a bridge abutment is placed in a compound channel. Their results show the important contribution of secondary currents and turbulent stresses to the apparent shear stress at the main channel/floodplain interface when the momentum equation is depth-averaged. Both the secondary current and turbulent stress contributions to the apparent shear stress increase as the relative depth in the floodplain decreases.

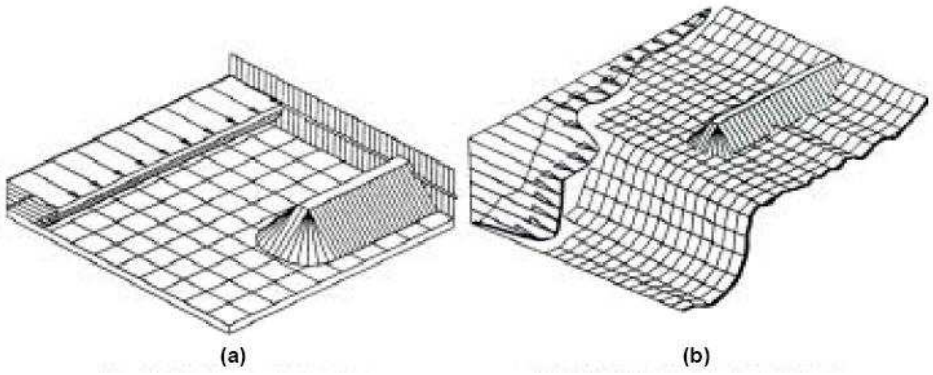

Figure 2.8 Comparison of (a) laboratory flow characteristics to (b) field flow conditions (reproduced from Richardson et al., 1993)

Whether the scour type is clear-water or live-bed usually depends on the position of the abutment relative to the river channel. If the abutment is positioned at the bank of the main channel, live-bed scour conditions are more likely to occur during flooding.

However, for abutments that are set back from the main channel and located on the river floodplain, clear-water scour conditions are more likely to occur during flooding due to the lower flow velocities that typically occur on the floodplain, and to the protection against erosion afforded by vegetation on the bed of the floodplain.

2.6 *Experimental Studies*

The experimental approach to predict scour around an abutment is the most common and significant method of analysis since the interaction between the flow and bed materials is difficult to quantify clearly as a result of the complexity of the flow field and properties of bed materials around a bridge abutment. Experimental studies can be mainly divided into two categories: (1) those that focused in explication of the three-dimensional flow field around a bridge abutment as explained in the previous section and (2) those that developed empirical correlations to predict the maximum scour depth around an abutment. The more common abutment scour depth equations can be found in the publications of Liu et al. (1961), Laursen (1962, 1963), Gill (1972), Froehlich (1989), Sturm (1993, 1996, 1998, and 2006), Richardson and Davis (1995), Chang and Davis (1998), Melville and Coleman (2000) and Ettema et al. (2008). However, there are no prior abutment scour studies for conditions when the bridge is submerged. The scour prediction methods of Froehlich (1989) and the HIRE live-bed abutment scour equation, which are recommended by FHwA, and the equations of Melville and Coleman (2000), Chang and Davis (ABSCOUR, 1998), Sturm (2006) and Ettema et al. (2008) are

summarized below. The equations that are summarized in this section apply to free flow conditions.

2.6.1 *Dimensionless Parameters*

The main difficulty in obtaining an accurate method to predict scour depth is the large number of variables affecting abutment scour. The following variables which influence the local scour around a bridge abutment are introduced:

- Parameters related to fluid properties
  - g : acceleration due to gravity
  - ρ : density of the fluid
  - ν : kinematic viscosity of fluid
- Parameters related to flow properties
  - y_1 : approach flow depth
  - V_1 : approach mean flow velocity
- Parameters related to sediment properties
  - ρ_s : density of the sediment
  - d_{50} : median sediment size
  - σ_g : geometric standard deviation of sediment size distribution
  - Cohesion of sediment

- Parameters related to time

  - t : time

- Parameters related to geometry

  - Cross-sectional shape of the approach channel

  - Length of abutment

  - Shape and alignment of abutment

  - Distance from the initial bed to the bridge low chord

In order to elucidate and identify the effect of each variable, dimensional analysis should be carried out before an experimental study. Also, the experimental data can be unified and presented in terms of dimensionless parameters through dimensional analysis.

With reference to the definition sketch in Figure 2.9, the result of dimensional analysis of the problem of local scour around an abutment founded in a compound channel can be given as (Sturm et al. (2011))

$$\frac{y_{2\max}}{y_1} = f\left(\frac{d_{50}}{y_{f1}} or \frac{V_1}{V_{c1}}, \frac{\rho V_1 L_a}{\mu}, \frac{L_a}{d_{50}}, \frac{L_a}{y_f}, \frac{W_e}{y_f}, K_s, K_\theta, \frac{H_b}{y_{f1}}, \frac{y_{m1}}{y_{f1}}, \frac{L_a}{B_f}, \frac{B_m}{B_f}, \frac{V_1}{\sqrt{g\, y_1}}, \frac{k_f}{k_m}, \frac{\sigma}{\gamma_E H_E}, \frac{V_{f1} t}{y_{f1}}\right)$$

----- (2.4)

where $y_{2\max}$ is the maximum depth of flow after scour, y_1 is the flow depth in the bridge approach section upstream of the abutment/embankment, V_1 is the approach flow velocity, V_{c1} is the approach critical velocity, ρ and μ are the density and viscosity

of the fluid, respectively, L_a is the abutment length, d_{50} is the median sediment grain size, y_{f1} and y_{m1} are the approach floodplain and main channel flow depth, respectively, W_e is the width of the embankment in the flow direction, K_s is an abutment shape factor, K_θ is a factor accounting for the abutment alignment to the flow, y_{m1} is the main-channel flow depth in the bridge approach section, H_b is distance from the initial bed to the bridge low chord in the floodplain, B_m is the main-channel width, B_f is the floodplain width, g is gravitational acceleration, k_f and k_m are roughness height of the floodplain and main channel beds, respectively, σ is bulk shear strength of the embankment fill, γ_E is bulk density of the embankment material, H_E is height of the embankment and t is time.

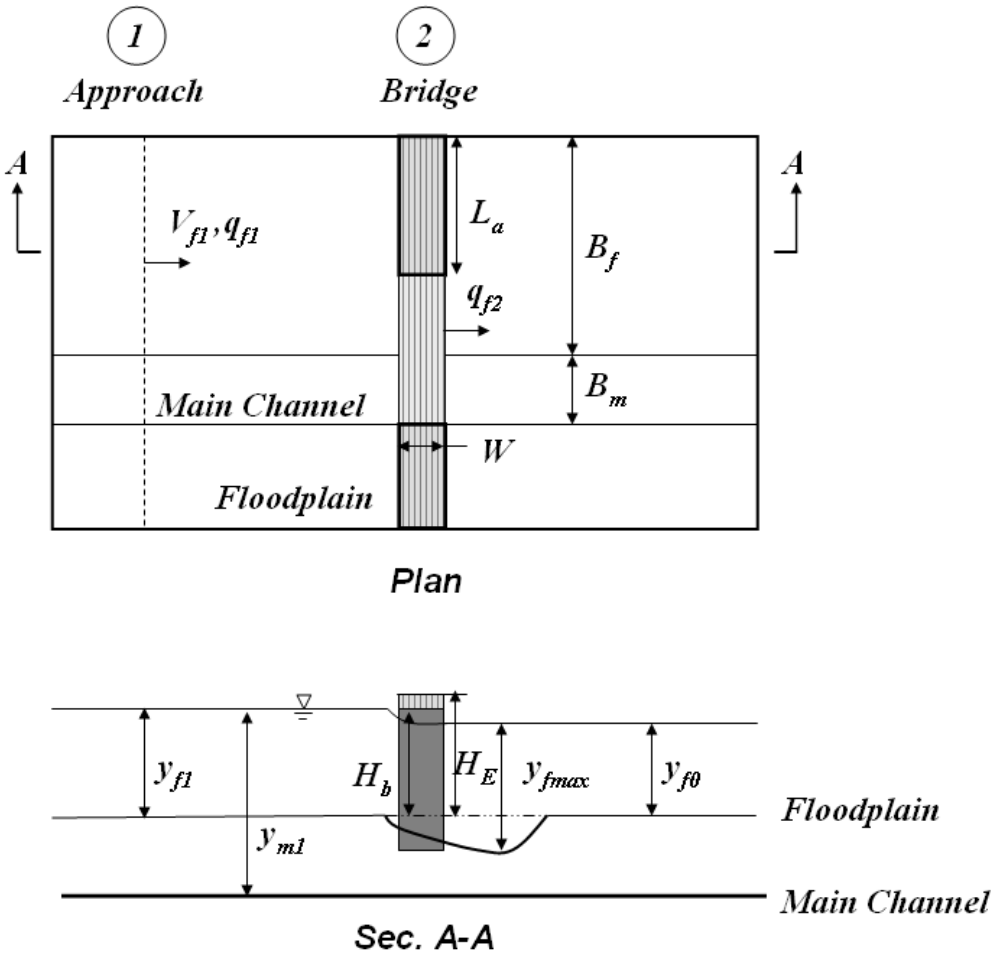

Figure 2.9 Definition Sketch

2.6.2 *Methodology for predicting scour depth*

Froehlich's Abutment Scour Equation

Froehlich's equations were derived from dimensional and regression analysis of the available laboratory data. Sources of the laboratory data are listed in Table 2.1. In total, 164 clear-water laboratory experimental results were used in the regression. Froehlich

proposed the following equation for clear-water abutment scour:

$$\frac{d_s}{y_1} = 0.78 K_s K_\theta \left(\frac{L_a}{y_1}\right)^{0.63} Fr^{1.16} \left(\frac{y_1}{d_{50}}\right)^{0.43} \sigma_g{}^{-1.87} + 1 \qquad (2.5)$$

where d_s is the scour depth, y_1 is the average depth of flow at the approach section, K_s is an abutment shape factor, K_θ is a factor accounting for the abutment alignment to the flow, L_a is the length of the active flow obstructed by the embankment and the abutment, Fr is the approach Froude number, d_{50} is median sediment grain size, σ_g is geometric standard deviation of the sediment size distribution, and "+1" is added for the factor of safety (FS). However, Froehlich's clear-water scour equation seems to greatly overestimate abutment scour depth compared to field measurements (TRB 1989). Thus, FHwA (HEC-18, 2012) suggested a modified abutment scour equation obtained from the Froehlich's regression analysis of other investigators' 170 live bed experimental results. The modified abutment scour equation is:

$$\frac{d_s}{y_1} = 2.27 K_s K_\theta \left(\frac{L_a}{y_1}\right)^{0.43} Fr^{0.61} + 1 \qquad (2.6)$$

Table 2.1 Sources of laboratory measurements (Froehlich, 1989)

Source of Measurements	Number of Measurements	
	Clear-water	Live-bed
Ahmad (1953)	11	0
Karaki (1959)	5	0
Liu and others (1961)	15	79
Garde and others (1961,1963)	25	64
Tison (1962)	3	0
Gill (1972)	60	27
Wong (1982)	6	0
Rajaratnam and Nwachukwu (1983)	6	0
Kwan (1984)	17	0
Tey (1984)	10	0
Kandasamy (1985)	6	0
Measurement Total :	164	170

Table 2.2 Shape factor (Melville and Sutherland, 1988)

Foundation Type	Shape	K_s
Abutment	Vertical wall	1.0
	Wing wall	0.75
	Spill through 0.5:1 (H:V)	0.6
	Spill through 1.0:1 (H:V)	0.5
	Spill through 1.5:1 (H:V)	0.45

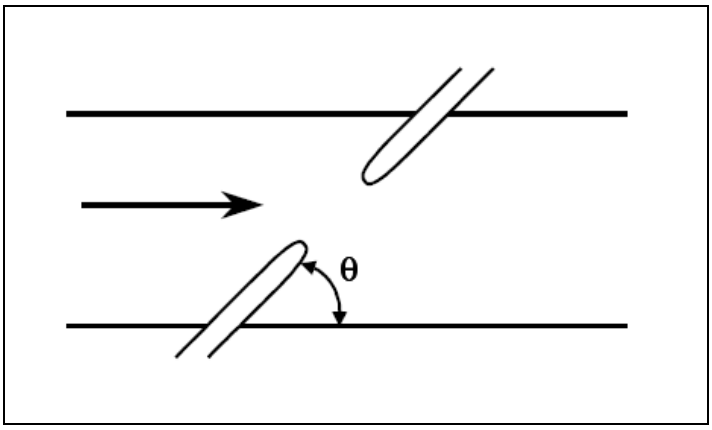

$K_\theta = (\theta / 90)^{0.13}$

Figure 2.10 Alignment factor (HEC-18, 2001)

HIRE Live-Bed Abutment Scour Equation

The HIRE equation is based on field data obtained by United States Army Corps of Engineers in the Mississippi River. This field situation closely resembles the laboratory experiment for abutment scour in that the discharge intercepted by the spur dikes is a function of the spur length. The modified equation, referred to as the HIRE equation, is applicable when the ratio of the projected length (L) to the flow depth (y_1) is greater than 25 (long abutment). The HIRE equation was derived as:

$$\frac{d_s}{y_1} = 4\ Fr^{0.33} \frac{K_s}{0.55} K_\theta \qquad (2.7)$$

where d_s is the scour depth, y_1 is the depth of flow at the abutment on the overbank or in the main channel, Fr is the Froude number based on the velocity and the depth adjacent to and upstream of the abutment, K_s is an abutment shape factor, K_θ is a

factor accounting for the abutment alignment to the flow same as for Froehlich's equation.

Melville and Coleman's Abutment Scour Equation

The abutment scour equation presented in Melville and Coleman (2000) is based on the large number of experimental results on clear-water abutment scour measured in a rectangular channel and a compound channel from Gill (1972), Wong (1982), Tey (1984), Kwan (1984, 1987), Kandasamy (1985, 1989) and Dongol (1994). The proposed design method for the maximum scour depth at a bridge abutment is:

$$d_s = K_{yL} K_I K_d K_s^* K_\theta^* K_G \qquad (2.8)$$

The maximum scour depth , d_s, depends on a product of empirical correction factors, K, which account for the various influences on scour depth. The length of the abutment and bridge approach embankment, L, relative to the depth of flow, y, has the primary influence on the scour depth and is represented by K_{yL}. The remaining scour-depth influences are K_I = flow intensity factor, K_d = sediment size factor, K_s^* and K_θ^* = abutment shape and alignment factor respectively, and K_G = channel geometry factor. The factor K_{yL} is defined by the following expressions and the abutment is classified as short, intermediate or long depending on the value of K_{yL}.

$$K_{yL} = \begin{cases} 2L; & \dfrac{L}{y} \le 1 \quad (\textit{Short abutment}) \\ 2(yL)^{0.5}; & 1 < \dfrac{L}{y} < 25 \quad (\textit{Intermediate abutment}) \\ 10\,y; & \dfrac{L}{y} \ge 25 \quad (\textit{Long abutment}) \end{cases} \tag{2.9}$$

These expressions indicate that scour depth is independent of depth of flow for short abutments and independent of abutment length for long abutments.

The flow intensity factor K_I is given by

$$K_I = \begin{cases} \dfrac{V-(V_a-V_c)}{V_c}; & \dfrac{V}{V_c} < 1 \\ 1.0; & \dfrac{V}{V_c} \ge 1 \end{cases} \tag{2.10}$$

where V_a is the mean flow velocity at the "armour peak" ($V_a = V_c$ for uniform sediments). For live-bed conditions ($V/V_c > 1$), K_I is typically less than unity, but has been set to unity to be conservative. The sediment size effect, K_d, appears only in relatively coarse size sediment ($L/d_{50} \le 25$). However, typically sediment is small relative to abutment length ($L/d_{50} > 25$), and L/d_{50} is assumed to have no effect on the scour depth. K_s (abutment shape factor) is given by 1.0 for the vertical-wall abutment, 0.75 for the wingwall abutment, and from 0.75 to 0.6 for the spill-through abutment depending on the side slope of a short abutment. For the long abutment ($L/y_1 \ge 25$), K_s

is 1.0 and K_s has a linear relationship with the value of L/y_1 for the intermediate abutment lengths ($10 < L/y_1 < 25$). The abutment alignment factor (K_θ) is varied from 0.9 to 1.1 depending on the angle between the abutment and flow direction.

K_G is given by

$$K_G = \begin{cases} 1.0\,; & Case\_A \\ \sqrt{1-\dfrac{B_f}{L}\left[1-\left(\dfrac{y_f}{y_m}\right)^{5/3}\dfrac{n_m}{n_f}\right]}\,; & Case\_B \\ 1.0\,; & Case\_C \\ \left(\dfrac{y_f}{y_m}\right)^{5/6}\left(\dfrac{n_m}{n_f}\right)^{1/2}\,; & Case\_D \end{cases} \qquad (2.11)$$

where y_m and y_f are the flow depths in the main channel and on the floodplain respectively and n_m and n_f are the Manning's roughness values in the main channel and on the floodplain. Case A to D are shown in Figure 2.7. Case A applies to the abutment sited in a rectangular channel, while Case B represents the abutment that is sited on a floodplain and extended into the main channel. Case C is an abutment set well back from the main channel such that all scour takes place on the floodplain only. Case D is the limit of Case B and C where the abutment protrudes out to the edge of the main channel. The case where the abutment is not set back sufficiently on the floodplain (in between Case C and D) is not considered in their research.

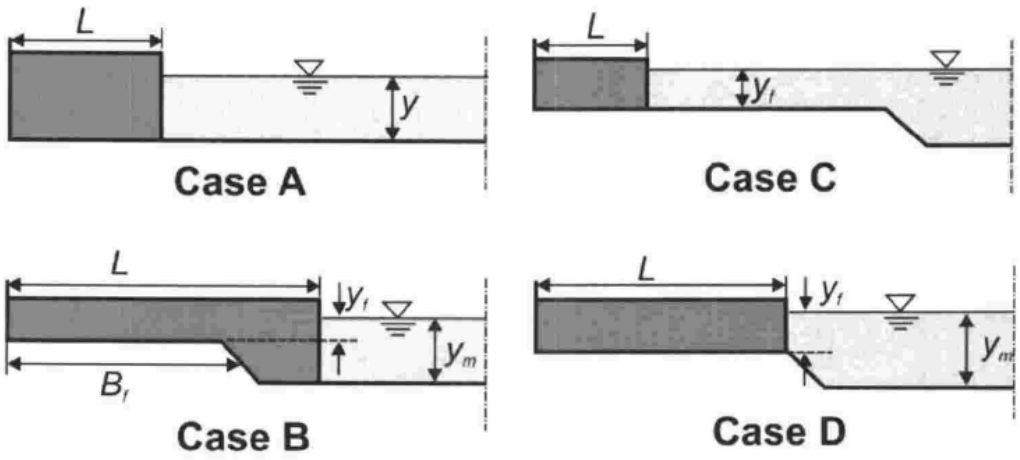

Figure 2.11 Typical cases of abutment positions in compound channels (reproduced from Melville and Coleman, 2000)

Chang and Davis's Abutment Scour Equation

Chang and Davis (1998, 1999) have applied Laursen's estimate of abutment scour at long contractions (Laursen, 1963), where local abutment scour flow depth can be assumed to be a function of contraction scour flow depth, to both clear-water and live-bed scour, and suggested the method (ABSCOUR, 2010).

$$d_s = K_t K_e \left[y_1 k_p k_f \left(k_v \frac{q_2}{q_1} \right)^{K_2} - y_0 \right] FS \qquad (2.12a)$$

$$d_s = K_t K_e \left[\left(k_p k_f k_v^{0.857} \frac{q_2}{V_c} \right) - y_0 \right] FS \qquad (2.12b)$$

where d_s is the scour depth, K_t is the modification for the abutment shape, K_e is the modification for the embankment skew y_1 is the approach flow depth, k_p is the

pressure flow coefficient, k_v and k_f are the velocity adjustment factor and spiral flow adjustment factor, respectively, q_2 is flow rate per unit width in the contracted section, q_1 is flow rate per unit width in the approach section, K_2 is sediment transport factor (0.637-0.857), y_0 is the flow depth at bridge before scour, and FS is a factor of safety. Equations 2.12a and 2.12b are for clear-water and live-bed scour, respectively. Converging flow under the bridge with the abutment near the channel bank is assumed in ABSCOUR to mix with flow in the main channel and distribute uniformly. On the other hand, if the abutment is set well back from the channel bank, it is assumed that the overbank flow and the main channel flow remain separated from each other and do not mix as the flow passes under the bridge. Thus, for the calculation of q_2, the abutment is classified by the three categories as short, intermediate and long depending on the value of the setback distance.

$$\begin{array}{ll} \text{Setback Distance} \le 5y_{c0} & \text{Short setback} \\ 5y_{c0} \le \text{Setback Distance} \le 0.75W & \text{Intermediate setback} \\ 0.75W \le \text{Setback Distance} & \text{Long setback} \end{array} \qquad (2.13)$$

where y_{co} = hydraulic depth in channel and W =floodplain width.

For the short setback abutment, the q_2 under the bridge can be computed as:

$$V_{short} = \frac{Q}{A}$$
$$then,\ q_2 = V_{short} * y_{c0} \tag{2.14}$$

where V_{short} = average velocity of flow under the bridge, Q = total flow under the bridge, A =sum of the channel and floodplain flow areas under the bridge, and y_{co} = hydraulic depth of flow on the floodplain or in the channel. For the long setback abutment, it is assumed that flow on the floodplain at the approach section remains on the floodplain as it flows under the bridge. Accordingly, the following relationship will hold true for flows on the floodplain for the approach section (1) and the bridge section (2):

$$Q_1 = Q_2$$
$$q_1 W_1 = q_2 W_2 \tag{2.15}$$
$$then,\ q_2 = q_1 * \frac{W_1}{W_2}$$

where Q_1 and Q_2 = discharge in cross-section subarea (channel or floodplain) of the approach section and bridge section, respectively, and W_1 and W_2 = width in cross-section subarea (channel or floodplain) of the approach section and bridge section, respectively. Finally, for the intermediate setback abutment, the interpolation between methods for the short setback abutment and the long setback abutment is applied to compute the velocity of flow as follows:

$$V_{short} = \frac{Q}{A} \quad \text{at a setback distance of} \quad 5y_{c0}$$

$$V_{long} = \frac{Q}{A_{sub}} \quad \text{at a setback distance of} \quad 0.75W \tag{2.16}$$

$$V_{\text{int}\,ermediate} = V_{short} - (V_{short} - V_{long}) * \frac{(setback - 5y_{c0})}{(0.75W - 5y_{c0})}$$

To account for the higher velocity and turbulence along the toe of the abutment, the velocity adjustment factor, k_v, for the nonuniform velocity distribution in the contracted section and the spiral flow adjustment factor, k_f, are suggested .

$$k_v = 0.8\left(\frac{q_1}{q_2}\right)^{1.5} + 1$$

$$k_f = 0.13 + 5.85\,Fr_1 \qquad for\ clear\ water\ scour \tag{2.17}$$

$$k_f = 0.46 + 4.16\,Fr_1 \qquad for\ live\ bed\ scour$$

The value of k_v is based on potential flow theory, and the value of k_f is determined from the abutment scour experiments in rectangular flumes. For the condition of pressure flow, the pressure coefficient, k_p (varying from 1.0 to 1.15), appears in the Equations 2.12.

Sturm's Abutment Scour Equation

Early experimental studies conducted by Garde et al. (1961) and Gill (1972) mentioned that scour around an abutment was related to the geometric contraction ratio, m, which was defined as the ratio of the width of the contracted opening to the approach channel

width (L_a/B_f in Equation 2.4). However, Sturm and Janjua (1994) argued that the geometric contraction ratio, m, which depends only on the abutment length and the approach channel width, is only appropriate for a constricted rectangular channel in which the flow rate per unit width is essentially constant across the approach and the constricted sections. In the case of a compound channel, the flow distribution across the cross section is nonuniform and dependent on the compound channel geometry and roughness. As the flow accelerates through the contracted section, it is redistributed between the main channel and the floodplain. Thus, Sturm and Janjua (1994) proposed that abutment scour depth should not depend directly on the abutment length in a compound channel, but rather on the effect of the abutment length on the flow redistribution in the contracted section for a particular compound channel geometry and roughness. They suggested the discharge contraction ratio, M, which represents the redistribution of flow between the main channel and the floodplain as the flow passes through the bridge section instead of using m

$$M = \frac{Q - Q_{obst}}{Q} \tag{2.18}$$

where Q (= $Q_{m1} + Q_{f1a} + Q_{f1b}$) is the total discharge through the bridge opening and Q_{obst} (= Q_{f1b}) is the obstructed floodplain discharge over a length equal to the abutment length projected onto the approach section as shown in Figure 2.12. They showed from their experiments that M is approximately equal to the ratio of discharge per unit width in the approach and the contracted floodplain areas, q_{f1}/q_{f2} , for an abutment that

terminates on the floodplain.

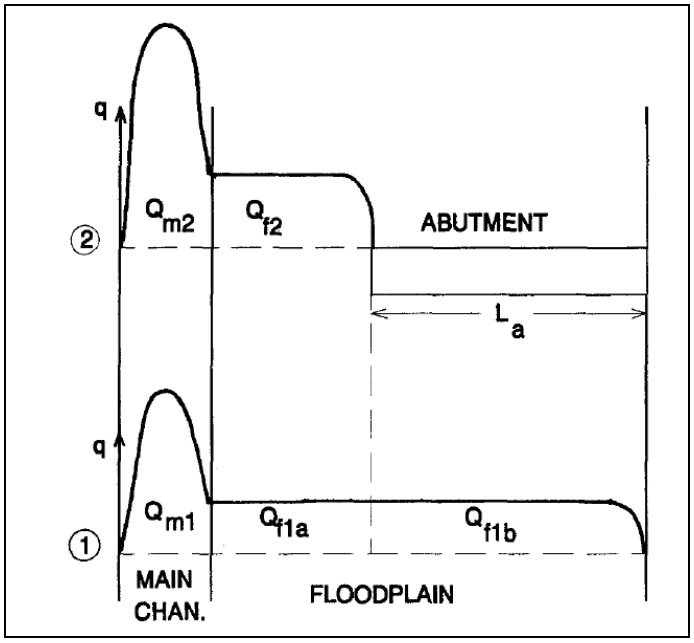

Figure 2.12 Definition sketch of discharge distribution in compound channel (reproduced from Sturm and Janjua, 1994)

In Equation 2.4, the geometric opening ratio (L_a/B_f), the remaining three floodplain geometric ratios y_{m1}/y_{f1}, B_m/B_f, and L_a/y_{f1}, and the ratio of relative roughness heights k_f/k_m can be replaced by M, discharge contraction ratio. The influence of the Reynolds number is neglected as are the variables L_a/d_{50} and W/y_{f1} based on previous experimental results. The relative roughness (d_{50}/y_{f1}) can be represented by the critical value of the Froude number $F_c = V_{cf1}/\left(g\, y_{f1}\right)^{1/2}$ for the case of fully rough turbulent flow (Pagan-Ortiz, 1991). As a result, Eq. 2.4 can be simplified to:

$$\frac{d_s}{y_{f1}} = f_2\left(K_s, K_\theta, \frac{H_b}{y_{f1}}, M, F_1, F_c, \frac{V_{cf1}\,t}{y_{f1}}\right) \tag{2.19}$$

Now if F_1 and F_c are replaced by their ratio V_{f1}/V_{cf1} while implicitly dropping the approach Froude number itself as being of secondary importance, the result of dimensional analysis of the problem of clear water abutment scour can be given as

$$\frac{d_s}{y_{f1}} = f_2\left(K_s, K_\theta, \frac{H_b}{y_{f1}}, \frac{q_{f1}}{q_{f2}}, \frac{V_{f1}}{V_{cf1}}, \frac{V_{cf1}\,t}{y_{f1}}\right) \tag{2.20}$$

Note that the geotechnical shear strength of the embankment is not considered in this formulation.

The extensive clear water abutment scour experiments done by Sturm and Sadiq (1996) and Sturm (1999, 2006) in two different compound channel geometries and two different abutment shapes (vertical wall and spill-through) with free flow produced the following equation given by

$$\frac{d_s}{y_{f0}} = 8.14\,K_s\left[\frac{q_{f1}}{M\,V_{0c}\,y_{f0}} - 0.4\right] \tag{2.21}$$

where d_s is the local clear water abutment scour, y_{fo} is the floodplain depth for unconstricted flow, K_s is abutment shape factor, q_{f1} is approach discharge per unit width in the floodplain, M is discharge contraction ratio, V_{0c} is the critical velocity in the floodplain for the unconstricted floodplain depth for setback abutments and critical

velocity in the main channel for the unconstricted depth in the main channel for bankline abutments. The floodplain depth y_{fo} was used instead of y_{f1} to account for the backwater effect. The authors suggested that q_{f1} can be determined from a one or two dimensional numerical simulation of the water surface profiles such as HEC-RAS and WSPRO. Their formulation assumed the idealized long contraction first, followed by equating the local abutment scour to some multiplier of the contraction scour as originally proposed by Laursen (1963). The shape factor K_s is equal to 1 for the vertical-wall abutment, while for the spill-through abutment, it is given by

$$K_s = 1.52\frac{\xi - 0.67}{\xi - 0.4} \qquad for \quad 0.67 \le \xi \le 1.2 \tag{2.22}$$

where $\xi = q_{f1}/(M V_{0c} y_{f0})$ and K_s =1.0 for $\xi > 1.2$ as the contraction effect becomes more important than the abutment shape.

Sturm (1999) suggested another possibility to estimate the abutment scour based on the maximum depth-averaged resultant velocity, $V_{\max}$, near the abutment face at the beginning of scour. Biglari and Sturm (1998) developed a 2D, depth-averaged $k-\varepsilon$ turbulence model to determine the flow field around a setback abutment founded on the floodplain of a compound channel. Comparison of the new scour formulation using results from the numerical simulation for $V_{\max}$ showed good agreement with experimental scour depth results. However, $V_{\max}$ could not be measured or computed reliably near the abutment face for the case of the bankline abutment because of the high degree of three-

dimensionality of the flow.

Ettema et al.'s Abutment Scour Equation

Ettema et al. (2010) presented a similar approach as Chang and Davis (1999) and Sturm (2006) for estimating the maximum abutment scour in a compound channel based on the laboratory experiments. In their experiments, the abutment was modeled as a pile-supported structure set inside an erodible, earthfill approach embankment/abutment having different lengths. They suggested the potential maximum flow depth near an abutment due to scour can be expressed in terms of an amplified contraction scour depth estimated as a function of unit discharge values for flow around an abutment. They presented envelope curves that represented maximum scour depth in ratio to the theoretical contraction scour depth as a function of the unit discharge ratio between the approach and the contracted sections for the purpose of design estimation of scour depth.

One of the most important considerations in the method proposed by Ettema et al. is the need to take into account the geotechnical failure of the embankment. Sometimes, geotechnical failure of embankment during flooding leads to flow breaching of the earthfill embankment at abutments. Once the embankment fails, flow contraction is relieved, and the scour hole does not deepen further. Therefore, Ettema et al. proposed an approach to estimate the geotechnical strength of the earthfill embankment at the bridge crossing of a waterway as a critical scour condition.

Reviewing Existing Scour Estimation Methods and Recommened Future Research

Sturm et al. (2011) reviewed existing scour estimation methods in their NCHRP (National Cooperative Highway Research Program) report under the auspices of the National Academy of Sciences, and made a series of recommendations for design estimation of abutment scour depth. They identified groups of dimensionless parameters affecting abutment scour such as flow factors, geometry factors, and other factors, and categorized existing scour estimation formulas according to the dominant parameter groups in those formulas. In order to guide their evaluation of existing abutment scour formulas, they developed five criteria to be satisfied by an ideal formula:

1. *Adequacy in addressing parameters that reflect important physical processes governing abutment scour;*
2. *Limitations of formulas in design applications with respect to ranges of controlling parameters on which they are based;*
3. *Categorization and acceptability of laboratory experiments and research methods that led to the development of the formula (e.g., experimental duration, variety of particle sizes and types of sediments, realistic geometries and scales, characterization of flow field, degree of idealization, large database)*
4. *Attempts to verify and compare formulas with other lab data and field data, if any, with which a valid comparison can be made;*
5. *Applicability and ease of use for design*

They concluded that none of the current scour formulas satisfied all of the five criteria because the process of abutment scour is difficult to model due to the complexity of the flow field, complications of fluvial geomorphology at bridge crossings, and inadequate knowledge of the erodibility of natural sediments. Therefore, they suggested further research particularly on three distinct aspects of the problem in order to determine

more accurate and applicable scour prediction methods for abutments. First, they recommended that further research should be conducted for improved understanding of the physical processes causing abutment scour by utilizing both physical and numerical models. Second, they suggested widespread use of more reliable design methods, including the integration of abutment scour countermeasures into the design. Finally, they recommended that more detailed field data collection studies should be undertaken to obtain simultaneous, real-time measurements of both the flow field and scour hole development during flood events in preference to post-flood surveys of remnant scour holes with little knowledge of the flow conditions that caused the scour.

Pressure Scour (Vertical Contraction Scour) Study

One of the main purposes of this study is to suggest a method of clear water abutment scour prediction in the submerged orifice flow condition with or without overtopping. Because pressure scour (vertical contraction scour) occurred at the bridge in the submerged orifice flow condition, the existing pressure scour studies are summarized in this section.

Arneson (1997) conducted a series of flume tests and proposed a method for the estimating pressure scour. However, a detailed review of the Arneson's datasets by Lyn (2008) concluded that the suggested method suffers from a spurious correlation. Therefore, Lyn (2008) re-examined Arneson's (1997) experimental study on pressure-flow scour and suggested the following equation given by

$$\frac{d_s}{y_1} = \min\left[0.21\left(\frac{V_a}{V_c}\right)^{2.95}, 0.6\right] \tag{2.23}$$

where d_s is the vertical contraction scour depth, y_1 is the approach flow depth, V_a is the depth-averaged velocity under the bridge, and V_c is the approach critical velocity. Because Arneson conducted his laboratory study in a rectangular flume without lateral contraction, Equation 2.23 can be considered to be valid for the case of the pressure flow without lateral contraction.

Scale Effects of Laboratory Experiments

Because reproducing prototype local scour depths in laboratory experiments is difficult, the scaling procedure has to be carefully considered when comparing laboratory data with prototype data. In addition, the need for using the appropriate non-dimensional parameters is essential when laboratory experiments are designed and conducted so that the nondimensionalized results can be compared with field data. When physical model studies have been conducted at most laboratories for high Reynolds number, all dimensionless parameters mentioned in Equation 2.4 could be maintained with the same values as the prototype except for La/d_{50}. For example, if the length ratio of model to prototype is 1:45 and it is applied to the corresponding prototype sediment size, d_{50}, the model sediment would be too cohesive or too small to be managed in the laboratory experiments. Therefore, it would be hard to accomplish the same ratio La/d_{50} between the prototype and the physical scale. However, the effect of La/d_{50} has been considered

to be negligible with respect to local scour depths when the value of La/d_{50} is greater than 25 (Melville and Coleman (2000)). In the most laboratory studies, the value of La/d_{50} is greatly larger than 25 even in the larger laboratory models.

2.6.3 *Time Development of Abutment Scour*

Figure 2.13 shows the development of local scour depth as a function of time and velocity. During its evolution, scour depth under clear-water conditions reaches equilibrium after a much longer time than it does under live-bed conditions. Live-bed scour develops more rapidly at initial stages and then begins to oscillate with time as a result of the influx of sediment upstream of a bridge and the passage of bedforms through the scour hole as shown in Figure 2.13. The equilibrium scour depth in clear-water conditions is approximately 10 percent more than the equilibrium scour depth in live-bed conditions. The equilibrium scour depth curve (shaded gray in Figure 2.13) does not start at the origin. This is because there is a minimum velocity below which local flow fields that are set up by the abutment generate insufficient turbulence and exert insufficient shear stress on the bed sediment to induce local scour. Most of the present local scour equations for predicting the depth of bridge scour have focused on the equilibrium scour depth without regard to the temporal effect, which means the equilibrium scour depth may be conservative as an estimate of prototype scour unless the time effect is taken into account. (Hager and Oliveto (2002)).

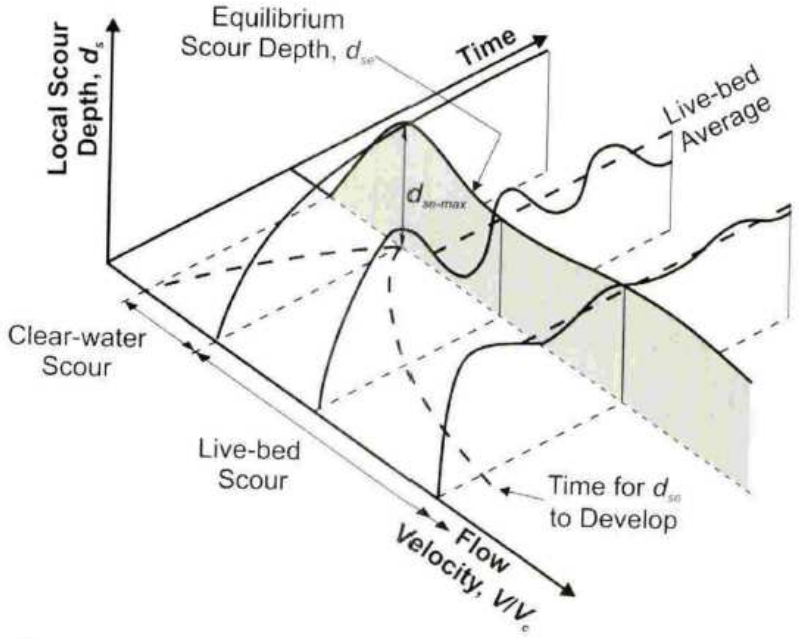

Figure 2.13 Local scour depth as a function of time and flow velocity (Melville and Coleman, 2000)

For the past 30 years, most of the research on the time development of scour has been done for situations other than abutment scour (e.g., pier scour, or hydraulic structures). Ettema (1980) described the time development of local scour around a cylindrical pier with a logarithmic formula from their experimental results. He showed that the dimensionless scour depth (d_s/b) is linearly proportional to the logarithm of $t\,d_{50}\nu/b^3$, where d_s = scour depth, b = pier diameter, d_{50} = median sediment diameter, ν =kinematic viscosity, and t = time. He found that the time development of pier scour depth consists of three segments. The first segment represents the rapid development of scour by downflow at the initial stage. The second segment consists of increasing scour depth around the pier due to the horseshoe vortex. The last segment represents the

development of equilibrium scour depth. Franzetti et al. (1982) also studied the influence of time on scour depth at cylindrical piers and suggested that dimensionless scour depth d_s/d_{se} is related to the exponential function of Ut/L, where d_s = scour depth, d_{se} = equilibrium scour depth, U = undisturbed approach velocity, t = time, and L = length scale (diameter of pier). Whitehouse (1997) proposed that dimensionless scour depth d_s/d_{se} is related to the exponential function of t/T, where d_s = scour depth, d_{se} = equilibrium scour depth, t = time, and T = time scale (T is time required to reach $d_s = 0.632\, d_{se}$). Whitehouse also gave separate equations for the calculation of T that are functions of d_{50} and L.

Recently, several researchers have adopted experimental methods to find the time development of scour around a bridge abutment. Cardoso and Bettess (1999) conducted abutment scour experiments with a rectangular abutment situated on the floodplain in a compound channel and suggested that the time history of clear water abutment scour can be described by

$$\frac{d_s}{d_{se}} = 1 - \exp\left[-1.025\left(\frac{t}{T}\right)^{0.35}\right] \qquad (2.24)$$

where d_s = scour depth, d_{se} = equilibrium scour depth, t = time, and T = time scale (T is time required to reach $d_s = 0.632\, d_{se}$). The ratio between the abutment length and the flood plain width in their experiment varied from 0.2 to 0.5. They compared the experimental results to the method suggested by Ettema (1980), Franzetti et al.(1982), and Whitehouse (1997) and concluded that the time evolution of scour around an

abutment follows a similar trend as Wihtehouse's formula with different empirical coefficients.

Hager and Oliveto (2002) summarized the laboratory data on abutment and pier scour conducted at ETH in Zurich, Switzerland. They suggested incorporating the effect of the densimetric particle Froude number as defined by Equation 2.25 on the temporal development of scour depth:

$$Fr_d = \frac{V_1}{\sqrt{g' d_{50}}} \tag{2.25}$$

where g' is reduced gravitational acceleration ($= [(\rho_s - \rho)/\rho]g$, in which ρ_s is the density of sediment). Hager and Oliveto (2007) and Kothyari et al. (2007) concluded that scour is mainly influenced by the densimetric particle Froude number and the geometrical effect, which is the width and the shape of a pier or an abutment as follows:

$$\frac{d_s}{y_1^{1/3} b^{2/3}} = 0.068\, N\, \sigma^{-0.5}\, Fr_d^{1.5} \log\left(\frac{\sqrt{g' d_{50}}}{b^{2/3} y_1^{1/3}}\, t\right) \tag{2.26}$$

where y_1 is the approach flow depth, b is the abutment width, N is the shape factor equal to 1 for the sloping abutment and 1.25 for the vertical abutment, σ is $(\sigma_{84}/\sigma_{16})^{0.5}$ = sediment nonuniformity parameter, and t is time. They assumed that the scour depth around the bridge foundation strongly depends on the difference between the total shear stress exerted by a flow and the critical shear stress for sediment transport

inception. The experiment was conducted in a rectangular flume to verify their assumption with several different lengths of abutments (the ratio of the abutment length to the channel width varied from 0.05 to 0.2). Their equation was verified using the existing literature data from Kohli (1998), Yanmaz and Altinbilek (1991), and Cunha (1975). However, Hager and Oliveto (2007) and Kothyari et al. (2007) specified that their model was applicable only to clear-water conditions with no contraction effect for median-sized bed sediment ($d_{50} \geq 0.8$ mm). The model did not account for the skewness of the approach flow velocity and the unsteadiness of the flood events.

Dey and Barbhuiya (2005) presented a semi-empirical model to compute the time variation of scour depth at a short abutment (abutment length/flow depth << 1) and verified their semi-empirical model with experimental results conducted in a rectangular channel with three different shapes of abutment, which were vertical wall, 45^o wing wall and semicircular. They applied a non-dimensional time parameter originally developed for pier scour by Yanmaz and Altinbilek (1991) and Dey (1999), $(t\, d_{50}\, [(SG-1)\, g\, d_{50}]^{0.5} / l^2$, in which t is time, SG is specific gravity, and l is the length scale (pier diameter or abutment length). Their semi-empirical model related the non-dimensional scour depth, d_{st}/l, in which d_{st} is the scour depth at a particular time t, and l is the transverse length of the abutment to the nondimensional time parameter. Their results showed good agreement with the experimental results. For an equilibrium scour hole, the characteristic parameters affecting the non-dimensional equilibrium scour depth were the excess abutment Froude number, the ratio of flow depth to abutment length, and the ratio of abutment length to sediment diameter ratio as follows:

$$\frac{d_s}{l} = 7.281 Fe^{0.314} \left(\frac{h}{l}\right)^{0.128} \left(\frac{l}{d_{50}}\right)^{-0.167} \quad \textit{for a vertical wall}$$

$$\frac{d_s}{l} = 8.319 Fe^{0.312} \left(\frac{h}{l}\right)^{0.101} \left(\frac{l}{d_{50}}\right)^{-0.231} \quad \textit{for a } 45^o \textit{ wing wall} \qquad (2.27)$$

$$\frac{d_s}{l} = 8.689 Fe^{0.192} \left(\frac{h}{l}\right)^{0.103} \left(\frac{l}{d_{50}}\right)^{-0.296} \quad \textit{for a semicircular wall}$$

where d_s is the equilibrium scour depth, l is the length of an abutment, h is the approach flow depth, d_{50} is the sediment size, and Fe is the excess abutment Froude number $(U_e/((SG-1)g\,l)^{0.5})$, where U_e is excess approach flow velocity $(U-\xi U_c)$ and the values of ξ are 0.5, 0.55, and 0.6 for the vertical wall, the 45^o wing wall, and the semicircular wall abutment, respectively.

Yanmaz and Kose (2007) also conducted experiments to investigate the time dependent characteristics of scour hole development around vertical wall abutments, and proposed an euquation for prediction of temporal development of scour around short abutments in a uniform bed material as given by

$$\frac{d_s}{l} = 0.25 Fr_d^{0.85} \left(\frac{l}{h}\right)^{0.15} (\log T_s)^{0.6} \qquad (2.28)$$

where d_s is scour depth, l is the length of an abutment, Fr_d is densimetric particle Froude number as defined by Equation 2.25, h is approach flow depth, and T_s is the non-dimensional time parameter $(t\,d_{50}\left[(SG-1)g\,d_{50}\right]^{0.5}/l^2)$ as defined in the previous paragraph.

Most of the research on time development of abutment scour given in the paragraphs above has been done for a short abutment ($L/B<0.1$, in which L is length of abutment and B is width of channel). However, when a bridge abutment occupies a significant part of the channel width, scour depth around the abutment will be affected by the flow constriction and the time development of abutment scour will be different from that for a short abutment. To investigate the effect of flow constriction on the time development of abutment scour, Ballio et al. (2009, 2010) conducted experiments with different abutment lengths. They varied the channel width obstruction ratio from 0.1 to 0.5 and found the dimensionless scour depth, $d_s/\sqrt{lh}$, in which l is the abutment length perpendicular to the incoming flow and h is the water depth, was linearly proportional to the logarithm of $tU/\sqrt{lh}$, in which t is the time and U is the approach flow velocity. It was found that the effect of the obstruction ratio on the overall time development of local abutment scour depth may not be large; however, they pointed out that a significant effect was observed during the initial phase of the scour process.

Many scour equations from laboratory data have been developed for equilibrium conditions. However, actual floods may not last nearly as long as the equilibrium time, so the design would be uneconomical. It is better to describe the effect of time and incorporate it into proposed scour calculation methods. However, because scour can accumulate over many flooding events, the effect of time must be considered carefully.

2.7 *Interaction Between Local Scour and Contraction Scour*

Because scour has contributed to the collapse of a large number of bridges in the United States, many researchers have tried to find a general method of predicting scour to prevent the failure of bridge foundations. However, current total scour prediction equations usually result in an over-estimation of total scour depth for several reasons. First, current prediction formulas have been derived from idealized and simplified experimental or numerical conditions. For example, the majority of work on contraction scour prediction has focused primarily on discharge and sediment transport continuity as suggested by Straub (1934) who assumed that sediment is transported in a long rectangular contraction and that the sediment is in equilibrium transport. However, contractions in actual field situations are more likely to have shapes that could be classified as short or abrupt contractions. In addition, flow and sediment transport conditions change continuously during flood passage. In terms of the local scour component of total scour, local scour prediction equations have been derived from experimental data based on simplified experimental conditions that differ from real field situations.

Another reason why scour prediction equations tend to over estimate scour depth is that current formulas assume that local and contraction scour processes are independent. In general, contraction scour is a result of the acceleration of flow resulting from a contraction in the flow area, while local scour is caused by the pile-up of water upstream of an obstruction that forces the downward acceleration of flow and the removal of sediment from the base of the obstruction. The contraction in the flow area tends to cause

scour processes to act concurrently; thus, the two components, local scour and contraction scour, are interactive and time dependent.

Several researchers have compared scour depths calculated from current prediction methods to scour depths measured in the field to explain the discrepancy between predicted and measured scour depths. Holnbeck et al. (1993) examined contraction scour and abutment scour occurring at U.S. 87 over Razor Creek in Montana and compared the measured results to scour predictions. Observed total scour was 2.23 m at the right abutment, 0.85 m at the left abutment, and 0.94 m at the pile bents. However, calculated scour depths were larger than the observed results. They used the output from the computer model WSPRO and then the Laursen lived-bed equation to compute contraction scour, the Froehlich live-bed equation to compute abutment scour, and the Colorado State University equation to compute pier scour. They compared the observed total scour to the calculated total scour at three locations as shown in Table 2.3. These results indicated that the equations for scour overpredicted total scour. The observed total scour depth was about 25% of the total computed scour depth at the left abutment and 48% at the right abutment. For the pier scour, the observed result was about 55% smaller than the calculated result.

Table 2.3 Comparison of computed and measured scour at U.S. 87 on Razor Creek, Montana, 1991 (Holnbeck et al. 1993)

Location	Computed scour (m)			Observed total Scour (m)
	Contraction	Local	Total	
Left abutment	0.70	2.50	3.20	0.85
Right abutment	0.70	3.66	4.36	2.23
Pile bents	0.70	1.43	2.13	0.94

Niezgoda and Johnson (1999) applied the ABSCOUR program to several Pennsylvania bridges to determine its capabilities. The results were more reasonable than using the HEC-18 formulas of Laursen to calculate scour depth at small, severely contracted bridges as shown in Table 2.4. The overprediction of HEC-18 could be attributed to the independent assumption for each of the scour components (local scour and contraction scour) to calculate total scour depth.

Table 2.4 Comparison of computed and measured scour depth (Niezgoda, 1999)

Location Method	Piney-creek	Brush Run	Little Creek
Field scour depth (m)	2.25	1.92	3.05
HEC-18 (m)	7.62	-	-
ABSCOUR (m)	4.18	2.13	3.81

Schreider et al. (2001) conducted experiments to investigate the interaction between local scour and contraction scour. Three experimental conditions were developed as below:

- Abutment scour was avoided around both abutment by using two guide banks
- Abutment scour was avoided just for one abutment by using one guide bank
- Abutment scour was not avoided

Figure 2.14 shows the experimental results. The contraction scour depth, which was measured from the original bed elevation to the horizontal portion of the bed elevation in the equilibrium scour cross section, was larger when abutment scour was avoided by means of the guide bank. When one guide bank was withdrawn, the contraction scour depth was about 50% of the measured contraction scour depth with the guide banks at both sides. Furthermore, when both guide banks were withdrawn, the contraction scour depth was only about 25% of the measured contraction scour depth for the case of two guide banks. The results illustrate evidence of the interaction that existed between contraction and abutment scour. Thus, it would not be suitable to compute both scour types in an isolated way, and then to add these effects to find the total scour. They also argued that the abutment scour developed faster than the contraction scour as shown in Figure 2.15 because the discharge distribution across the cross section was changing with time according to the evolution of the abutment scour holes. If the discharge distribution is changing while the local scour is in progress, it would be difficult to evaluate the final contraction scour using the initial values of the hydraulic parameters. Thus, they proposed to use a discharge redistribution graph developed from their experimental

results along with dimensional analysis to calculate the contraction scour depth.

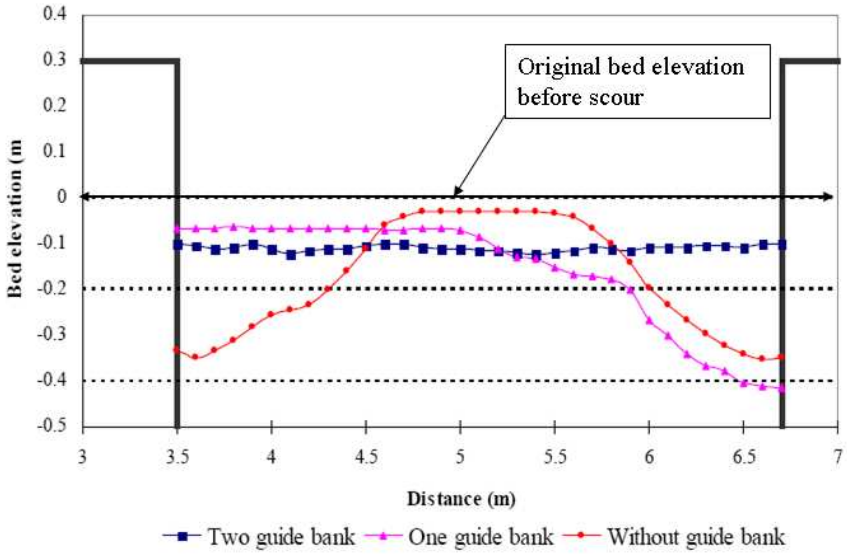

Figure 2.14 Final scoured cross section for Schreider's experiment (Schreider, 2001)

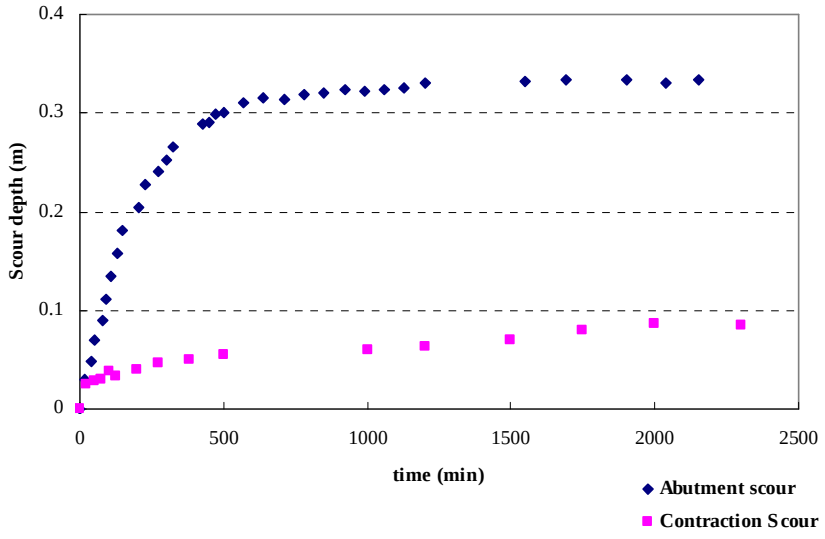

Figure 2.15 Time evolution of the contraction and abutment scour (Schreider, 2001)

Hong (2005) conducted experiments to address the interaction of bridge contraction scour and pier scour using a 1:45 scale hydraulic model of the Ocmulgee River bridge at Macon, Georgia including the river bathymetry. Two different conditions, “with the bridge piers in place” and “without the bridge piers in place”, were simulated in the laboratory to investigate the interaction. Results showed a reduction in contraction scour because of interaction with the piers as shown in Figure 2.16. The contraction scour depth measured in the laboratory model without the piers was about 25% larger than the contraction scour depth measured in the model with the piers in place. This observation may be due to the discharge redistribution across the bridge cross section as scour developed with time. Time development of the pier scour was much faster than the contraction scour as shown in Figure 2.17. This result suggests that the more rapid development of pier scour may change the discharge distribution across the bridge cross section before the contraction scour has time to fully develop. In other words, the portion of discharge that flows through the pier scour region increases significantly with respect to its initial value, and that results in less discharge in the contraction scour region because the total discharge remains constant. The discharge redistribution was evidenced by the measured specific discharge data as shown in Figure 2.18

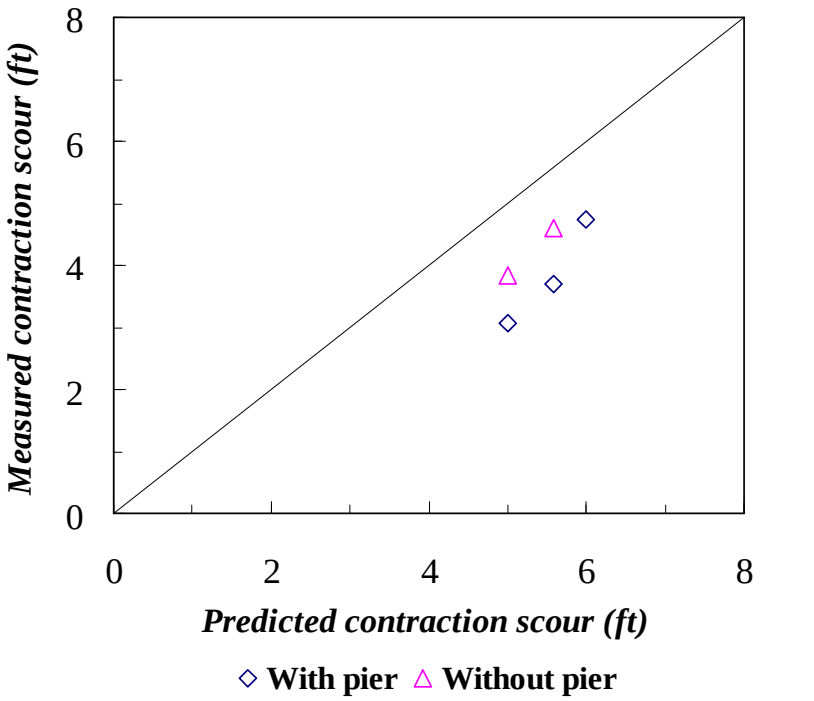

Figure 2.16 Comparison between measured laboratory contraction scour and predicted contraction scour using the Laursen live-bed formula (Hong, 2005)

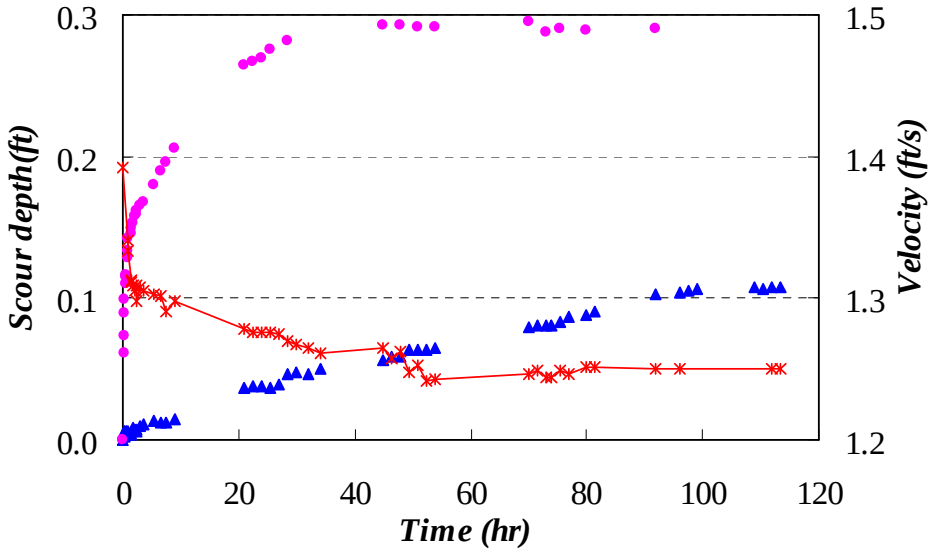

Figure 2.17 Time development with the piers in place (Hong, 2005) (Pink dot: Pier scour, Blue triangle: contraction scour, Orange line: velocity)

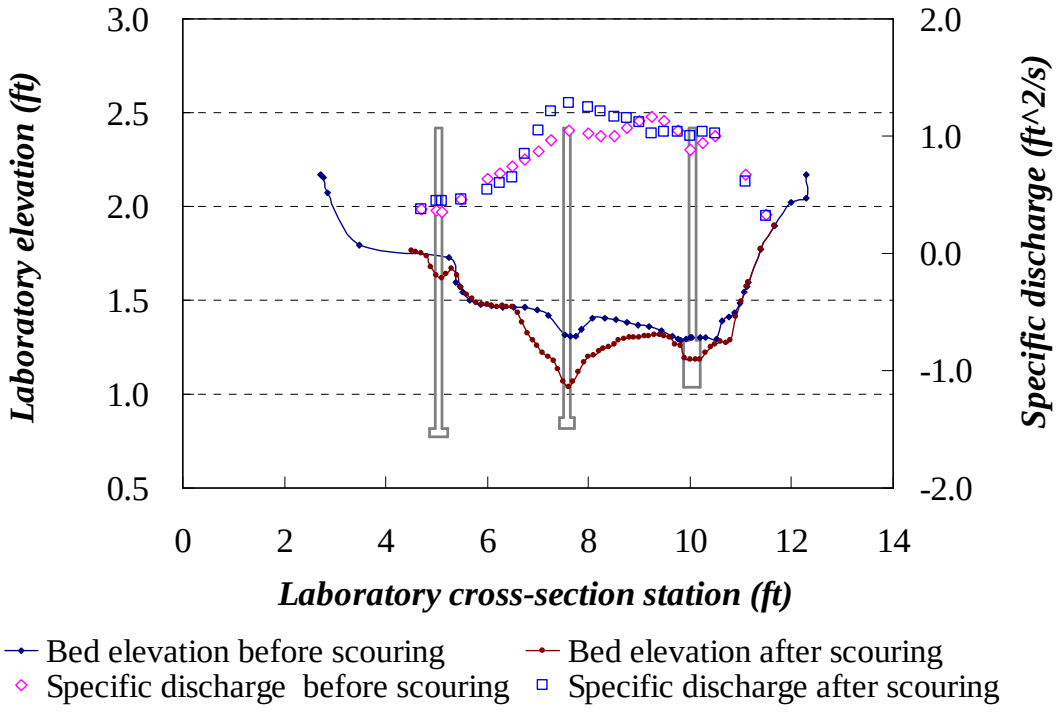

Figure 2.18 Discharge per unit width comparison before and after scour (Hong, 2005)

The contraction scour and pier scour occurred simultaneously. Thus, it is hard to separate two components from the measured total scour depth. However, Hong (2005) suggested a method to separate contraction and pier scour (Landers and Mueller, 1993). The depth of contraction scour is the difference in average streambed elevations with and without the contraction in place and is defined generally as the difference between average streambed elevations of the contracted and uncontracted sections. First, a line is passed through the average streambed elevations of the uncontracted sections upstream and downstream of the bridge to decide the reference elevation for uncontracted conditions. Second, the pier scour holes are removed from the bridge cross section by using the concurrent ambient scour surface next to the local scour holes as shown in

Figure 2.19. Then the average depth of the cross section is adjusted relative to the undisturbed longitudinal bed profile through the bridge before scour developed in the first step. The difference between the average bed elevation after scour and the adjusted bed elevation before scour is the contraction scour.

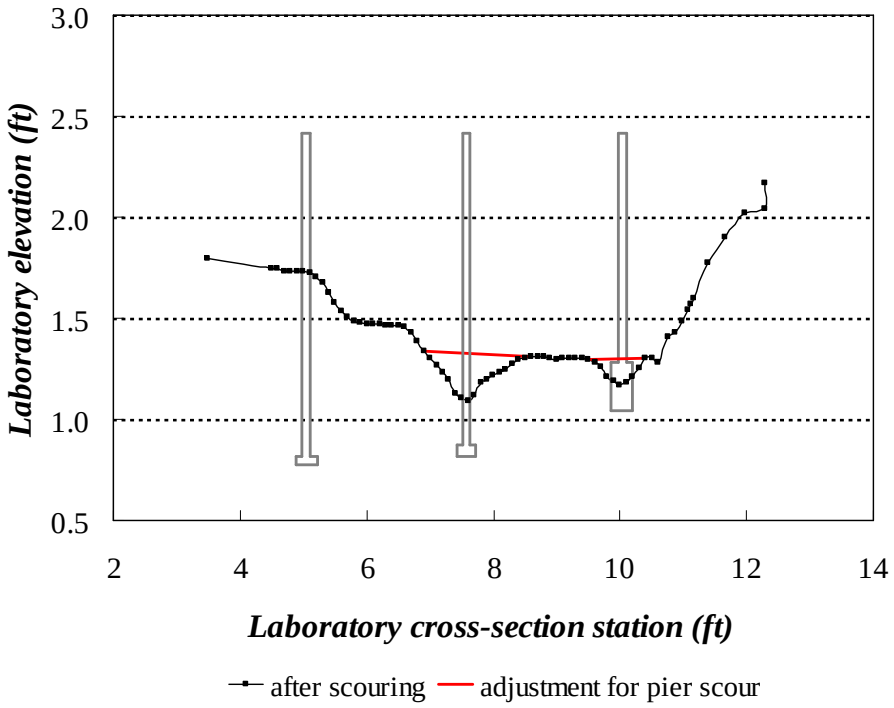

Figure 2.19 Bridge cross-section adjusted for pier scour after scouring (Hong, 2005)

In general, current methods for computing the total scour depth assume that contraction scour and local scour (pier scour and abutment scour) can be computed in an isolated way using the initial discharge and then, they can be added. However, when the abutment is located on the bank of the main channel in a compound channel, both

contraction and abutment scour occur simultaneously (Sturm, 1999). In this case, a single equation should be suggested to predict the combined abutment and contraction scour because the contraction in the flow area tends to cause scour processes to act concurrently (Sturm et al. 2011)

CHAPTER III

METHODOLOGY OF EXPERIMENTS

All experiments of local scour around bridge abutment were conducted in the School of Civil and Environmental Engineering at Georgia Institute of Technology, Atlanta, GA. Models were built inside a 14 ft wide by 80 ft long flume in the hydraulics laboratory. The maximum water flowrate is 10 ft^3/s supplied by a large constant-head thank that delivers water to the flume through 12-in. and 6-in. diameter pipes. Water supply to the flume is recirculated such that water flows into the laboratory sump at the end of the flume from which the water is continuously pumped by two centrifugal pumps into the constant-head tank which overflows back into the sump. Constant head is assured by overflow of multiple weirs in the constant-head tank that have a very large combined crest length. The flowrate into the flume is controlled by a gate valve installed in a 12-in. supply pipe.

3.1 *Experimental Equipment*

3.1.1 *Flume*

The experimental flume has a length of 80 ft, width of 14 ft, and a maximum depth of 2.5 ft: The river model and bridge were constructed inside the flume which consists of a

horizontal concrete bed with vertical steel walls bolted to the floor and water-sealed. Water flows into the head box of the flume vertically from the 12-in. supply pipe which feeds a 12-in. diameter diffuser that extends across the full width of the flume. In order to reduce the turbulence generated at the entrance of the flume, three chain fence rolls wound with a horse-hair filter are installed between the head wall of the flume and an overflow weir. Downstream of the overflow weir two baffles are installed one of which is made of offset wood slats and the other of which is a steel plate with $3/8$-in. diameter holes having a spacing of $9/16$-in.. A horse-hair filter is also inserted between the two baffles. The full flume entrance arrangement can be seen in Figure 3.1.

Figure 3.1 Entrance section of the flume

A tailgate to adjust the tailwater depth is located at the downstream end of the flume to control the flow depth as shown in Figure 3.2. An instrument carriage is set up

on longitudinal steel rails and can be moved upstream or downstream along the flume by an electric motor and a steel cable system. The point gage and a calibrated capacitance wave gage (RBR Ltd. Model WG-50) used for measurement of water surface elevations is mounted on that carriage and can be positioned accurately in three-dimensions.

Figure 3.2 Tailgate of the flume to adjust the flow depth downstream

3.1.2 *Flowmeter*

The flowrate in the 12 in. supply pipe was measured by a magnetic flow meter which has an expected uncertainty of ± 0.01 ft^3/s . (Foxboro, 2004).

3.2 *Velocity Measurements*

3.2.1 *Acoustic Doppler Velocimeter - ADV*

An Acoustic Doppler Velocimeter (ADV) was utilized to measure instantaneous point velocities and turbulence quantities with three different types of probes: 3D down-looking, 3D side-looking and 2D side-looking. When measurements were needed to be made at points close to the free surface and at shallow water depths, the 2D and the 3D side-looking ADV were used. The ADVs were mounted on a manufactured point gage located on the steel rail of the instrument carriage to measure the elevation of the ADV sampling volume. The distance between the bed and sampling volume($0.005 \ \text{in}^3$), which is 2.0 in. for the 16 MHz MicroADV, was measured by the 3D down-looking ADV (SonTek, 2001) and referenced to a point gauge measurement of bed elevation.

The operation principle of the ADV is based on the Doppler frequency shift of emitted acoustic signals after reflection by small sound-scattering particles which are assumed to be moving at the same velocity as the fluid. Scattering particles can be air bubbles or sediments, for example (Lane et al., 1998). The velocity of the scattering particles is inversely related to the shift in the wavelength of sound if the speed of sound is known exactly.

The water depth and bed elevations before and after scouring were measured by a point gage and the 3D down-looking ADV. The ADV can generally detect a boundary within 25 cm for the 16 MHz ADV, which means that the ADV can measure the distance from the center of the sampling volume to a solid boundary with ± 1 mm uncertainty as

shown in Figure 3.3. However, sometimes the ADV is not able to detect precisely bed elevations along a steep slope so that measurements with a point gage are needed. The elevation of a reference point can be determined by a point gage and compared to the elevation measured by the ADV before measuring all bed elevations

.

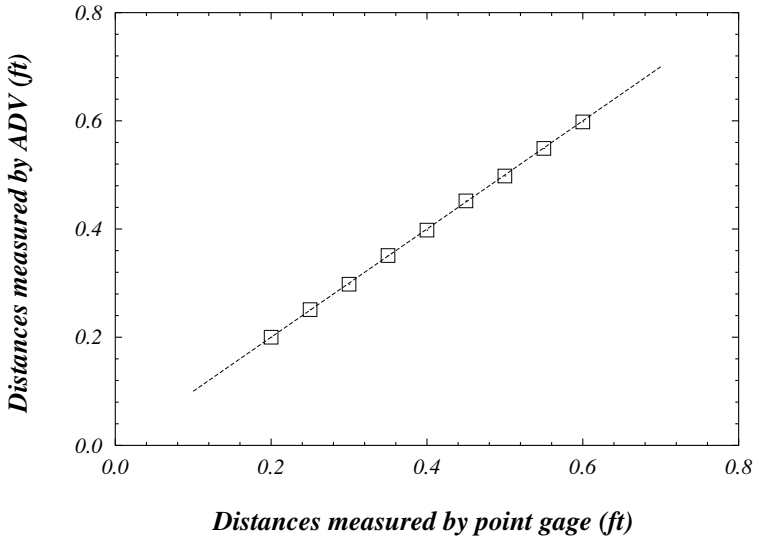

Figure 3.3 Comparison of distances from boundary measured by MicroADV and the point gage

Accuracy of the ADV measurements of velocity and turbulence quantities was evaluated by Voulgaris and Trowbridge (1998) in flume experiments. Their analysis showed that the ADV sensor can accurately measure both mean velocity and Reynolds stress. However, the existence of Doppler noise from the ADV always can occur when measuring the velocity, especially when the flow velocity exceeds the pre-set velocity range or when there is contamination from the previous acoustic pulses reflected from boundaries of complex geometries. Noise also occurs when a high level of turbulence

exists at the measuring location. Hence, the examination and filtering of the signal is needed before analyzing the mean point velocity and turbulent quantities. The first filtering protocol for reducing noise is to filter the time series data according to a minimum value of a correlation coefficient. The correlation coefficient is a measure of the relative consistency of the behavior of the scatterers in the sampling volume during the sampling period. (Wahl ,2000). The ADV collects data at a higher sampling rate than the sample reporting period, and the correlation parameter indicates the consistency of the multiple measurements that take place within each sampling period. In this study, the minimum value of the correlation coefficient was required to be 70 percent for acceptance of data from each sampling period based on the recommendation of the ADV manufacturer for measurement of turbulence properties. The phase-space despiking algorithm of Goring and Nikora (2002) was also employed to remove any spikes in the time record caused by aliasing of the Doppler signal which sometimes occurs near a boundary. The percentage of remaining number of data after filtering process was maintained to be larger than 50% for quality control. In addition to the required minimum correlation coefficient value and phase-space despiking algorithm, it is recommended by the manufacturer that the signal to noise ratio, SNR, should be greater than 15 for accurate measurements. Kaolin clay particles were used as seeding materials to improve the signal strength and correlation values. Typical correlation values in these experiments were greater than 90% and the SNR>15.

Garcia et al. (2007) pointed out “the optimum sampling time for given turbulence parameters is case dependent and no universal rule should be used in this regard.” and

also pointed out “The Acoustic Doppler Velocimeter should be operated at the maximum sampling frequency. However, the higher sampling frequency will produce a higher doppler noise of signal.” In this experiment, the required duration of the time record at each velocity measuring point was a minimum of 2 min and perhaps as much as 5 min and the sampling frequency was selected to be 25 Hz based on previous experiments at Georgia Tech (Lee, et al. (2004), Ge et al. (2005), and Hong, S. (2005)).

3.3 *Physical River Modeling*

3.3.1 *Model Construction*

In a previous study at Georgia Tech (Hong and Sturm, 2010), laboratory experiments were conducted using a 1: 60 scale hydraulic model of the Towaliga River bridge at Macon, Georgia including the full river bathymetry as shown in Figure 3.4. The field data including measured discharge, bed elevation of cross sections, and gage height from the USGS were reproduced by Froude number similarity. Figure 3.5 shows the approach cross section shape and rating curve measured in the field. The previous experimental results showed that the hydraulic model can reproduce field scour data (Hong and Sturm, 2009) and also that abutment scour can be regarded as a locally amplified contraction scour.

Figure 3.4 Laboratory model of Towaliga river bridge

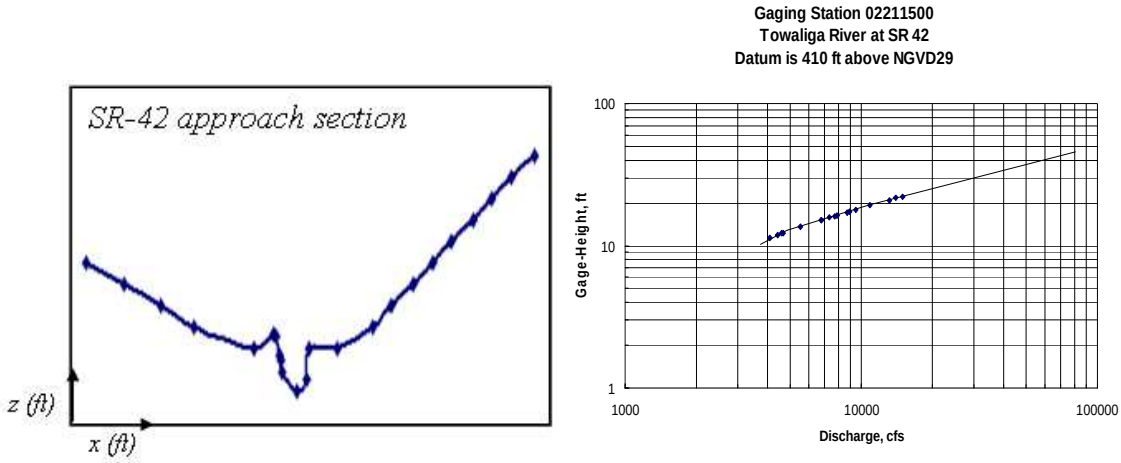

Figure 3.5 Measured approach cross-section and discharge rating curve for Towaliga river bridge

The cross section shape and river geometry used in the previous experiments were slightly modified and simplified for the experiments conducted in this thesis study to find more general features of the flow field. The shape of floodplain was horizontal on both

sides of the main channel cross-section while preserving the original parabolic shape of the main channel. Also, the channel was constructed to have a straight alignment rather than meandering. Figure 3.6 shows the experimental layout in the flume. The approach channel upstream of the bridge was 35 ft long followed by a working mobile bed section with a length of approximately 17 ft in which the bridge model was placed. The templates for the river model cross sections in the approach channel were cut from plywood sheets placed vertically at regular intervals with elevations scaled from detailed field measurements of river bathymetry and then modified for this study. The spaces between the templates were filled with bed sediment and carefully leveled to the elevations established by the templates. The approach channel bed was then fixed with polyurethane. In the mobile bed section, thin aluminum templates were used to reproduce the moveable bed bathymetry and then removed for the scour tests. The fixed bed approach section was filled with 3.3 mm gravel and the 17 ft moveable bed working section was filled with sand with d_{50} = 1.1 mm and σ_g = 1.3. In the 5 ft long sediment trap section downstream of the bridge, a surface layer of 3.3 mm gravel was fixed by spraying polyurethane; this section trapped the sediment transported out of the working section. To ensure a fully developed boundary layer at the bridge approach section consistent with the moveable bed sediment size, the fixed-bed approach channel consisted of a surface layer of fixed 1.1 mm sand having a depth of one in. and shaped to the plywood templates for a total approach flow length of 20 ft.

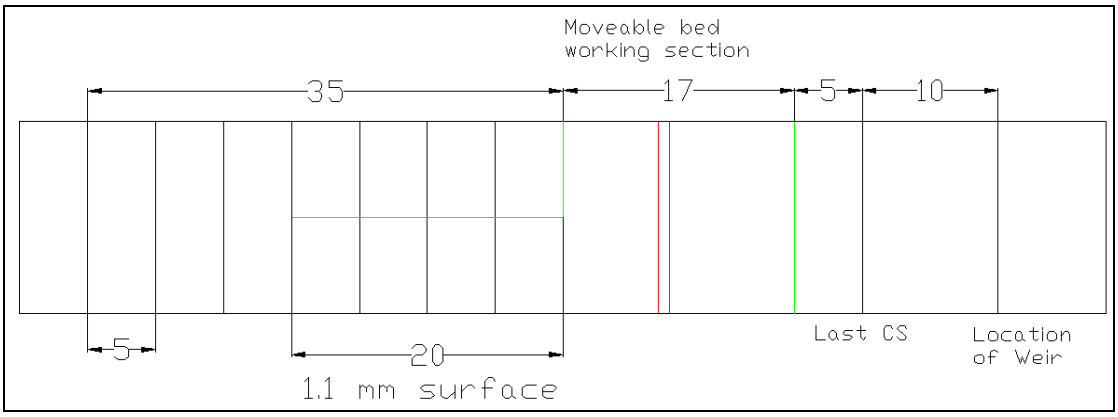

Figure 3.6 Plan view of flume for model construction (unit is ft in the figure)

The model of the embankment was constructed as an erodible fill with rock riprap protection in order to reproduce the influence of erosion of the endroll on the abutment scour in the region of the toe of the embankment (Ettema et al. 2008). First, the erodible embankment was formed by using several buckets of saturated sand (same size as bed materials) which were carefully compacted by hand using a trowel to set a 2:1 side slope. Ten buckets of saturated sand were used for the smallest length of embankment and 15 buckets for the next length of embankment. Next, the 2:1 embankment and abutment was completely covered by hand with a single layer of riprap before putting the removable model roadway and bridge deck in place. The size of the riprap (d_{50} = 9.0 mm) was determined by the method recommended in HEC-23 and included an apron of the recommended width (25 ft in prototype value, thus 0.56 ft in model corresponding to the length scale). This approach was successful in maintaining the general integrity of the embankment during overtopping as was observed in the prototype. A wide range of embankment lengths and flow contraction ratios were used on the left floodplain while the abutment was maintained at the bankline of the right floodplain for all experiments.

This arrangement allowed the simultaneous study of both bankline and setback abutments. Based on the above modifications, abutment and embankment lengths and river bathymetry to be modeled in the laboratory were constructed as shown in Figure 3.7. The ratio of the abutment length to the floodplain width, L_a/B_f (L_a is the abutment length and B_f is the floodplain width), varied from 0.53 to 1.0.

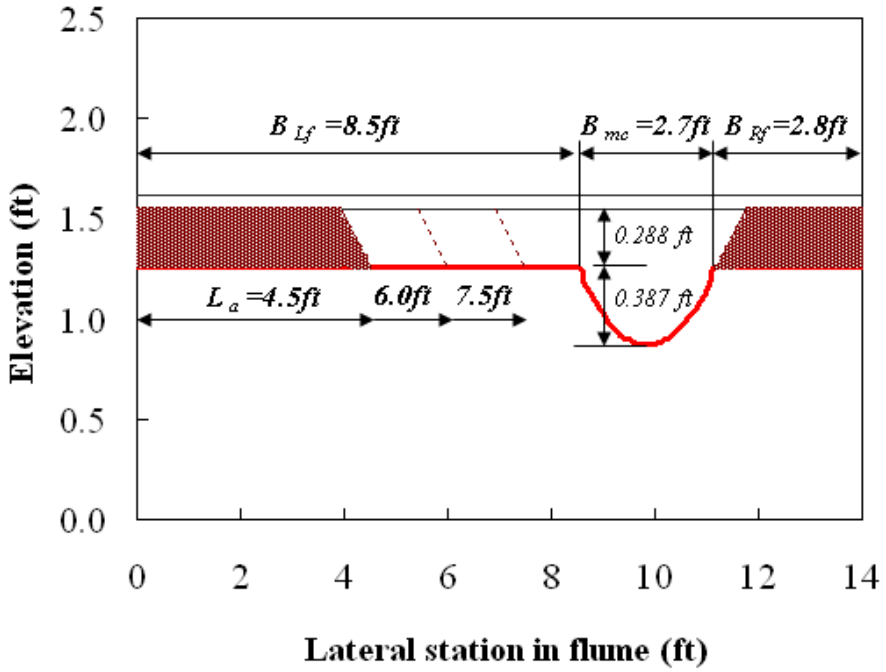

Figure 3.7 Cross-section geometry and abutments

One of the main purposes of this study is to suggest a method of clear water abutment scour prediction for extreme hydrologic conditions. In those extreme conditions, overtopping or submerged orifice flow is likely to occur at the bridge. To simulate those extreme cases, the following prototype considerations and dimensions were used for the model bridge deck.

(a) Road width of 40 ft, in accordance with standard two-lane roads;

(b) Bridge barrier 2 ft high with 1.5 ft top without sidewalks on non-bicycle routes;

(c) Slab depth of 1.5 ft including the pavement;

(d) Girders 1.4 ft wide and 1.5 ft deep with 9 ft spacing.

These design dimensions are commonly used by Georgia DOT for rural region bridges. The 1:45 length scale bridge deck was constructed as shown in Figure 3.8. A solid bridge deck model was supported and leveled with respect to an upper support beam as shown in Figure 3.9.

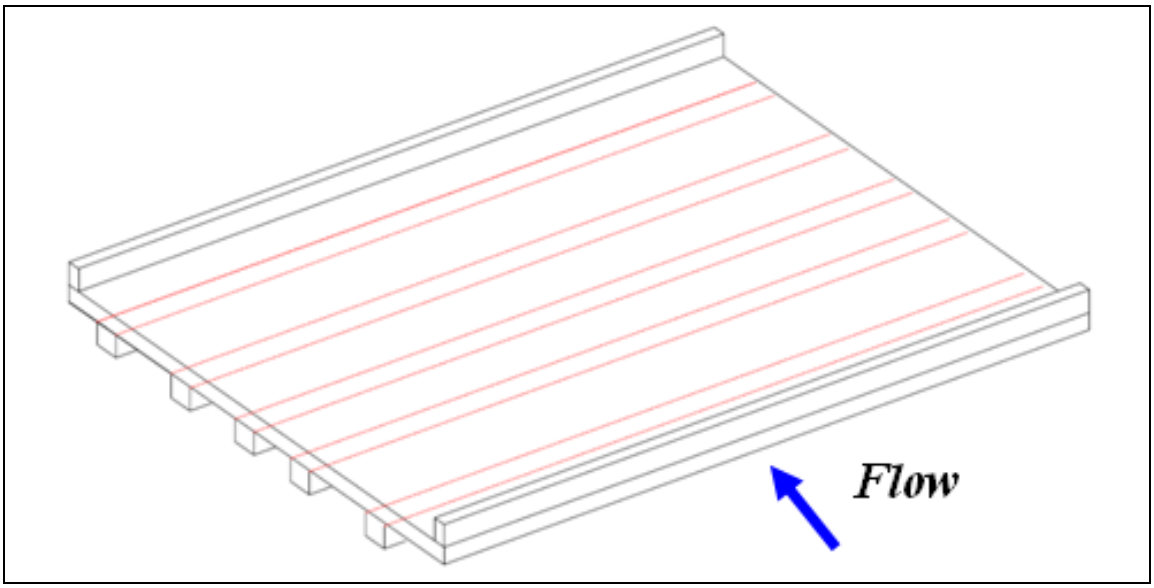

Figure 3.8 Model bridge deck

Figure 3.9 Bridge section looking downstream from right floodplain (L_a = 6ft)

3.3.2 *Bed Materials*

The result of sieve analyses for the sediment is shown in Figure 3.10. The properties for the sediment are listed in Table 3.1. The size distribution is characterized by the sieve diameter for which 50% is finer by weight, d_{50}, and the geometric standard deviation of the distribution, $\sigma_g = (d_{84}/d_{16})^{0.5}$. All bed materials for this study can be considered to be uniform in size since the standard deviation of the particle size distribution of the sediment is less than a limit of about 1.5 for uniform size sediments.

The dimensionless particle diameter, d_*, and Shields parameter, τ_{*c} in Table 3.1

were defined previously by Equation 2.1 and Figure 2.1. The critical value of shear velocity for initiation of motion of each sediment, u_{*c}, is given by

$$u_{*c} = \sqrt{\tau_{*c} (SG - 1) g d_{50}} \tag{3.1}$$

where u_{*c} is the critical value of shear velocity, τ_{*c} is Shields parameter, which is equal to $\tau_c/[(\gamma_s - \gamma) d_{50}]$, τ_c is the critical shear stress for incipient sediment motion, γ_s is the specific weight of sediment, γ is the specific weight of fluid, d_{50} is median grain size, SG is the specific gravity, and g is gravitational acceleration.

The riprap size distribution is also included in Figure 3.10. There are numerous equations for sizing riprap at bridge abutments. Equation 3.2 from HEC-23 is one of the most widely used riprap sizing equations.

$$\frac{D_{50}}{y_2} = \frac{K_s}{(SG - 1)} Fr_2^2 \tag{3.2}$$

where D_{50} is the median rock riprap diameter, y_2 is the flow depth in the contracted bridge section, K_s is the abutment shape factor (i.e., 1.02 and 0.69 for $Fr_2 < 0.8$ and $Fr_2 > 0.8$, respectively), SG is the specific gravity of the rock riprap, and Fr_2 is Froude number in the contracted bridge section. The maximum Fr_2 from the preliminary HEC-RAS calculations was 0.43 and 0.33 (actual Fr_2 was 0.47 and 0.35 from the experiments) in the floodplain and main channel, respectively. Based on the

computed values of Fr_2, Equation 3.2 resulted in riprap size estimates of 7.6 mm and 8.4 mm for the setback abutment and the bankline abutment, respectively. In this study, the final conservative choice of riprap to cover the embankment was rounded river rock having a d_{50} = 9.2 mm and σ_g =1.25 as shown in Figure 3.10.

Table 3.1 Properties of sediment for this study

Sediment	d_{50}, mm	σ_g	d_*	τ_{*c}	u_{*c}, m/s
A	1.1	1.12	27.83	0.038	0.026

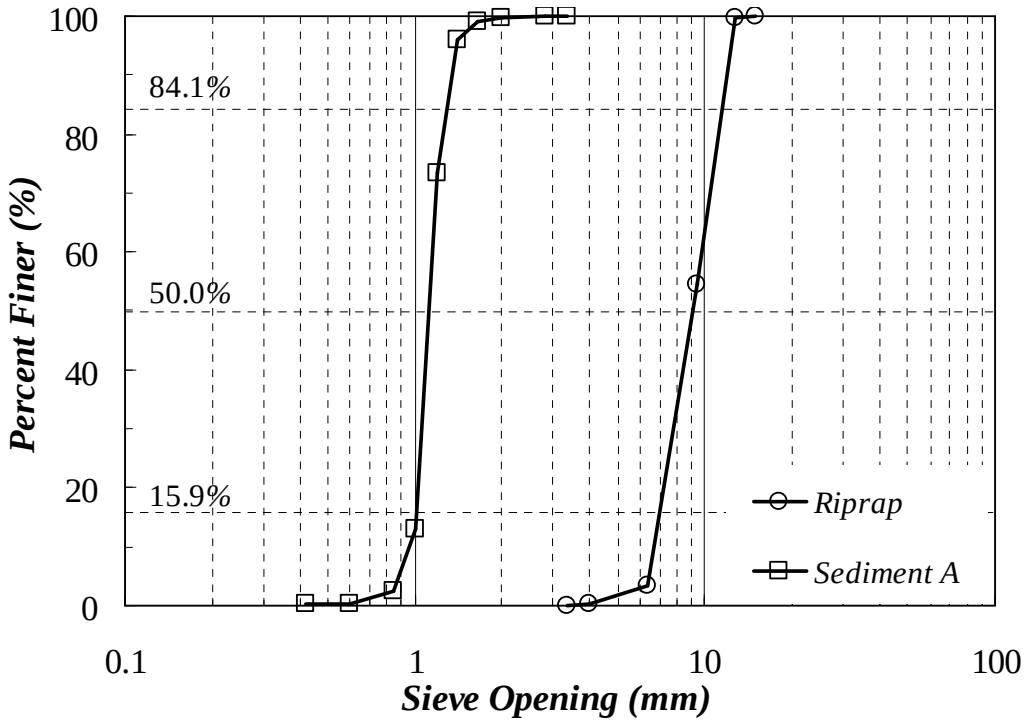

Figure 3.10 Sediment and riprap size distribution of the bed materials for this study

3.4 *Experimental Procedure*

At the beginning of each scour experiment, the flume was slowly filled with water from a downstream supply hose so that the sand was saturated without disturbing the initial bottom contours. After complete saturation, the initial bottom elevations of the entire working moveable-bed section were measured in detail throughout the test section with a spacing of 0.2 ft across each of 10 cross-sections. With the flume flooded, but at no flow, the ADV was used to measure the bed elevations before scour relative to a fixed elevation datum established on the bottom of the flume. The ADV gives the distance from the sampling volume to the bed which can be converted into elevation relative to the datum by reading the point gage. After that, the required discharge was set using the magnetic flow meter. A flow depth larger than the target value was set with the tailgate so as to prevent scour while the test discharge was set. Then the tailgate was lowered to achieve the desired depth of flow. During this time, the point gage and wave gage on the instrument carriage were used to measure the flow depth. Once the target flowrate and flow depth had been reached, the scour continued for 5 to 6 days until equilibrium was achieved. The temporal change of the entire moveable bed section was measured in sufficient detail to obtain accurate contours of scour depth and maximum scour depth at six intermediate time durations. In order to ensure that no additional scour occurred during the intermediate time measurements, the tail gate was raised and the discharge was lowered well below the required value.

At the end of the experiment, the final bed elevations were measured in the same way as the initial elevations using the ADV and the point gage. The end of the

experiment was defined when the scour depth reached the equilibrium state at which there were negligible changes in bed elevation with time. During the measurement of bed elevations with the ADV, the flume was not drained because the ADV probe needed to be completely submerged. After finishing with the bed elevation measurements with the ADV, the flume was slowly drained so as not to disturb the scour contour and the final bed elevations near an abutment were measured with a point gauge.

After completion of the moveable bed experiments, the moveable bed section was fixed by spraying it with polyurethane. In the fixed-bed experiments, the initial hydraulic conditions were obtained by measuring water-surface profiles and velocities throughout the working section. At the approach section, point velocities were measured along multiple vertical transects which were separated by 1 ft laterally in the floodplain and 0.5 ft in the main channel. Ten point velocities were taken at each vertical transect in the floodplain while measuring 15 point velocities in each vertical section in the main channel. In the bridge cross section, velocities were taken every 0.5 ft laterally in both the floodplain and the main channel. A minimum of eight measuring points in each vertical profile and as many as 15 points were measured at both C.S. 3 and C.S. 4 (Figure 4.1). In addition to detailed measurements of velocity and turbulent profiles at C.S. 3 and C.S. 4, three dimensional velocity components were also measured at cross sections located at the upstream toe and the downstream toe of the embankment (C.S. 2 and C.S. 5, respectively in Figure 4.1) and at C.S. 6 located 0.65 ft downstream of C.S. 5 at 0.5 ft lateral interval in the floodplain and the main channel. In each vertical section in the floodplain and in the main channel, three point velocities were measured at distance of 5

mm from the bed and at 20 and 40 percent of the approach flow depth at C.S. 2, C.S. 5 and C.S. 6.

3.5 *Velocity and Turbulence Measurements*

Except in the very near wall region, the mean velocity profile in a steady, open channel flow for both smooth and rough boundaries is given as (Ligrani and Moffat (1986), Krogstad and Antonia (1999) and Rahman and Webster (2005))

$$\frac{U(z)}{u_*} = \frac{1}{k}\ln\left(\frac{zu_*}{\nu}\right) + A - \Delta U^+ + \frac{2\prod}{\kappa}\omega\left(\frac{z}{\delta}\right) \tag{3.3}$$

where $U(z)$ is the time-averaged point velocity at distance z from the bed, u_* is the shear velocity, κ is the von Karman constant equal to 0.41, A is a constant equal to 5.0, ΔU^+ is the roughness function or shift in the mean velocity due to the bed roughness height, $\prod$ is the Coles wake parameter, and ω is the wake function. In the vicinity of the bed roughness, the viscous length scale of Equation 3.3 can be replaced with the equivalent roughness height, k_s, and close to the surface, the wake correction can be neglected in Equation 3.3. The resultant velocity profile becomes

$$\frac{U(z)}{u_*} = \frac{1}{k}\ln\left(\frac{z}{k_s}\right) + C \tag{3.4}$$

where k_s is the equivalent Nikuradse grain roughness., and the value of C varies with k_s^+ ($=k_s u_*/\nu$). Above an upper critical value of k_s^+(>70) (Schlichting, 1979), the value of C is equals 8.5 and the flow is fully rough. Below a lower critical value of k_s^+(<5) (Schlichting, 1979), the flow obeys the smooth-wall law of the wall and the value of C becomes

$$C = \frac{1}{k}\ln\left(k_s^+\right) + A \tag{3.5}$$

In the transitionally rough regime ($5< k_s^+ <70$), Ligrani and Moffat (1986) provided the following expression for C.

$$C = \frac{1}{k}\ln\left(k_s^+\right) + A + \left[8.5 - A - \frac{1}{k}\ln\left(k_s^+\right)\right]\sin\left(\frac{\pi}{2}g\right) \tag{3.6}$$

where

$$g = \frac{\ln(k_s^+/5)}{\ln(70/5)}, \qquad for \quad 5 < k_s^+ < 70,$$
$$g = 1, \qquad for \quad k_s^+ > 70,$$
$$g = 0, \qquad for \quad k_s^+ < 5$$

Following the Clauser procedure given next, the optimized values for u_* were found in the approach flow section.

Several methods to determine the shear velocity, u_*, are available. In this study, the logarithmic fit to velocity data points near the bed which is called the “Clauser

method" was used. The theoretical wall level is set at a position ε measured below the top of the roughness elements such that the value of ε is between zero and k_s. However, in this study, the theoretical wall level was set at the top of the sediment particle (ε=0) because the distance to the zero velocity plane was negligibly small since the commonly used value of Einstein and El-Samni (1949) is $0.2d_{50}$ = 0.22 mm below the tops of the roughness elements. The effect of the location of the theoretical wall level was examined in terms of the relative error of the values in Table 3.2. The relative errors in shear velocities (u_*) and k_s^+ calculated by setting the zero offset between ε=0 and $\varepsilon=0.2d_{50}$ were only 1.1% and 2.0%, which is negligible considering the reliability of bed leveling for each experiment.

The measured point velocity time series were fitted by the commonly used logarithmic velocity distribution to determine the slope of the velocity distribution by using a least-squares regression analysis. Figure 3.11 shows an example plot for the case of an overtopping flow with L_a/B_f =0.53 and Q=5.8 cfs (Run 3 in Table 4.2). The measured data are a composite of six vertical profiles measured across the floodplain at the approach flow cross section. Then the shear velocity, u_*, can be calculated by the product of the slope of the velocity distribution and κ (=0.41). The equivalent roughness height, k_s, was determined from Equations 3.4 and 3.6 by trial and error. A summary of flow characteristics is presented in Table 3.2.

The measured vertical distribution of the mean velocity was found to agree well with the best-fit of Equation 3.4 (R^2=0.98) in which the time-averaged point velocity is a linear function of the logarithm of the distance from the bed, as shown in Figure 3.12. For

the data analysis, the velocity data up to 60% of the flow depth were utilized for the best-fit relationship since Nezu and Rodi (1986) measured the longitudinal velocity profiles and turbulence fluctuations in a uniform open channel over a smooth bed and suggested that the log-law was formally able to be used up to 60% of the flow depth. For the main channel approach velocity and shear velocity, the same method was used as for the floodplain, but, the point velocities measured in the center line of the main channel were used for fitting Equation 3.4.

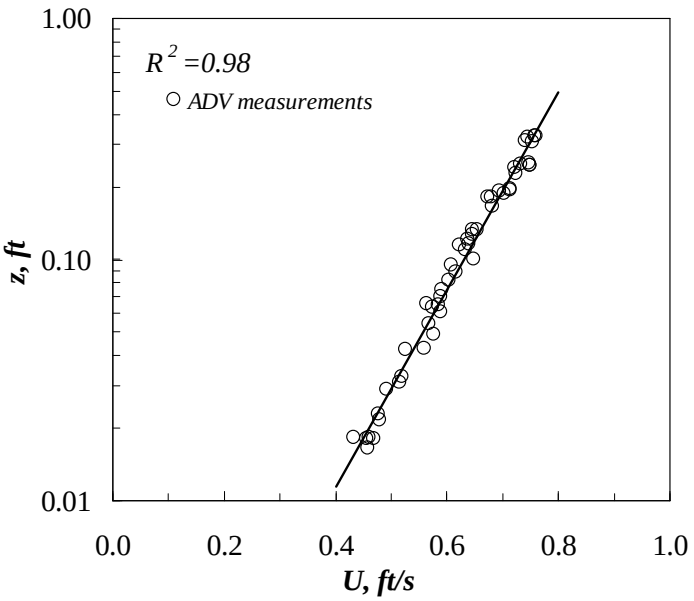

Figure 3.11 Vertical velocity distribution on approach flow floodplain for Run 3 (u_*=0.044 ft/s)

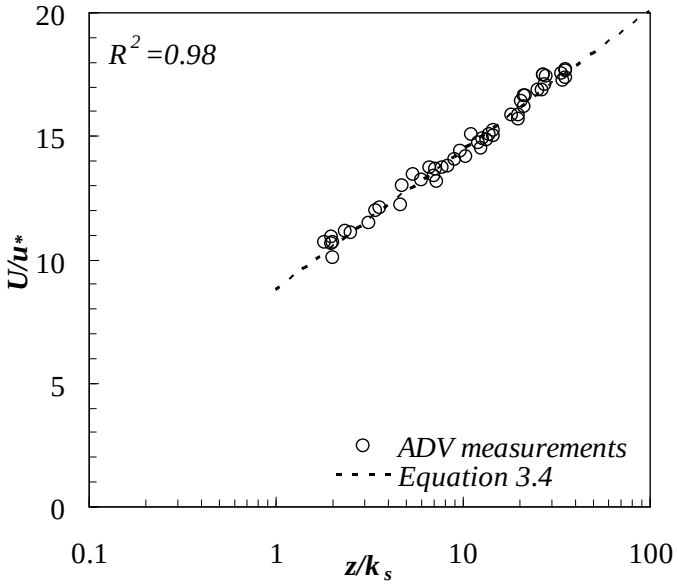

Figure 3.12 Velocity profiles on approach flow floodplain for Run 3 (u_*=0.044 ft/s, k_s=2.51* d_{50}=0.0091ft)

Table 3.2 Flow characteristics in the approach flow

Run	*Floodplain*						*Main channel*					
	L_a/B_f	u_*	$\frac{k_s}{d_{50}}$	k_s^+	$\frac{V_1}{u_*}$	C	L_a/B_f	u_*	$\frac{k_s}{d_{50}}$	k_s^+	$\frac{V_1}{u_*}$	C
		ft/s	-	-	-	-		ft/s	-	-	-	-
1	0.53	0.046	2.64	43.8	14.5	8.72	1.0	0.059	2.82	60.1	16.8	8.53
2		0.043	2.58	40.1	15.9	8.80		0.053	2.79	53.4	16.7	8.58
3		0.044	2.51	39.5	16.8	8.73		0.053	2.80	53.6	16.9	8.58
4		0.047	2.72	46.1	13.3	8.68		0.062	2.81	62.9	14.9	8.51
5		0.046	2.65	44.0	14.3	8.72		0.055	2.76	54.8	15.2	8.57
6		0.045	2.63	42.7	15.0	8.74		0.051	2.76	50.8	15.7	8.61
7	0.71	0.045	2.65	43.0	13.2	8.74	1.0	0.059	2.83	60.3	14.8	8.53
8		0.044	2.52	40.0	14.0	8.80		0.057	2.81	57.8	15.2	8.54
9		0.046	2.65	44.0	14.9	8.72		0.052	2.81	52.7	15.9	8.59
10		0.041	2.53	37.5	13.3	8.86		0.058	2.86	59.9	14.8	8.53
11		0.040	2.53	36.5	14.2	8.89		0.049	2.75	48.7	15.2	8.64
12		0.041	2.53	37.5	14.9	8.86		0.045	2.78	45.2	15.8	8.70
13	0.88	-	-	-			1.0	0.050	2.82	50.9	16.5	8.61
14		-	-	-				0.046	2.78	46.2	16.6	8.68
15		-	-	-				0.041	2.71	40.1	17.3	8.80
16		-	-	-				0.040	2.68	38.7	16.6	8.83
17		-	-	-				0.038	2.65	36.3	17.0	8.90
18		-	-	-				0.037	2.65	35.4	16.9	8.92

In order to determine the reliability of ADV measurements of turbulence characteristics, the longitudinal and vertical turbulence intensity measured in the approach flow in the model was compared with theoretical distributions and empirical distributions suggested by several researchers.

Nezu and Rodi (1986) conducted fully-developed open channel flume experiments over a smooth bed and suggested relationships for turbulence intensity given by

$$sqrt < u'^2 > = u_* D_u \exp\left(-\lambda_u \frac{z}{H}\right)$$
$$sqrt < w'^2 > = u_* D_w \exp\left(-\lambda_w \frac{z}{H}\right) \quad (3.7)$$

where $sqrt < u'^2 >$ and $sqrt < w'^2 >$ are longitudinal and vertical turbulence intensity, respectively, and D_u, λ_u, D_w, and λ_w are empirical constants with values 2.26, 0.88, 1.23, and 0.67, respectively. u_* is shear velocity and H is water depth. A more applicable set of data in comparison to the present study is that of Kironoto and Graf (1994) who proposed a similar form of the exponential relationships presented by Nezu and Rodi (1986), but with different empirical constants. They used a rough plate and a gravel bed for the channel bottom to generate two different types of roughness instead of using smooth PVC and suggested different empirical constants with values 2.04, 0.97, 1.14 and 0.76.

Nikora and Goring (1998, 2000) performed field measurements in North Canterbury, New Zealand. The median sediment size was varied from 6.4 mm to 13.4

mm. They suggested a relationship for relative turbulence intensity and the relative turbulence intensities given by

$$\frac{sqrt < u'^2 >}{u_*} = \left(1.90 - 1.32\ln\left(\frac{z}{H}\right)\right)^{0.5}$$
$$\frac{sqrt < v'^2 >}{u_*} = \left(1.19 - 0.49\ln\left(\frac{z}{H}\right)\right)^{0.5} \quad (3.8)$$
$$\frac{sqrt < w'^2 >}{u_*} = \left(0.59 - 0.22\ln\left(\frac{z}{H}\right)\right)^{0.5}$$

$$\frac{K}{u_*^2} = 1.84 - 1.02\ln\left(\frac{z}{H}\right) \quad (3.9)$$

where K is the total turbulence kinetic energy defined as $0.5*\left(< u'^2 > + < v'^2 > + < w'^2 >\right)$.

We compared the turbulence intensities and turbulent kinetic energy measured in the approach section to the theoretical and the empirical distributions suggested from the literature described above to determine the reliability of ADV measurements of turbulence characteristics. Figures 3.13 and 3.14 show one example case of vertical distributions of relative turbulence intensities and turbulent kinetic energy (Run 3 in Table 4.2). The ADV measurements of longitudinal turbulence intensity in this study follow the Nikora and Goring (1998)'s relationship but show slight overestimation compared to the experimental relationship of Kironoto and Graf (1994). The transverse and vertical turbulence intensity measurements show good agreement with other researcher's suggested relationships as shown in Figure 3.13.

The measured turbulent kinetic energy distributions agreed well for the range 0.1-0.7z/H with Nikora and Goring (1998)'s relationship, as shown in Figure 3.14. The turbulent kinetic energy is close to a constant near the water surface, then increases toward the bed and reaches the maximum, and finally decreases again to zero at the bed. The theoretical and the empirical distributions suggested from several authors (Nezu and Rodi 1986, Kironoto and Graf 1994, and Nikora and Goring 1998) are valid in the layer $0.15 < z/H < 0.7$. However, our measurements show the turbulent kinetic energy normalized by the approach shear velocity, K/u_*^2, agreed well with Equation 3.9 until the value of z/H reaches down to 0.04 which is the closest point that the ADV can measure the turbulence quantities (5 mm from the bed). The value of relative submergence (H/d_{50}) is 120 and roughness Reynold number ($u_* \cdot d_{50}/\nu$) is 12 in our experiment. Rahman and Webster (2005) showed the maximum value of K/u_*^2 located around z/H=0.04 in their experiment with similar experimental conditions (H/d_{50} = 80 and $u_* \cdot d_{50}/\nu$ = 9). In general, the ADV data measured in this study fall within the experimental uncertainties and thus provide some confidence in additional measurements of turbulence in the flow field. Accordingly, some near-field velocity and turbulence distributions were measured to provide a better physical understanding of flow structure and scour processes.

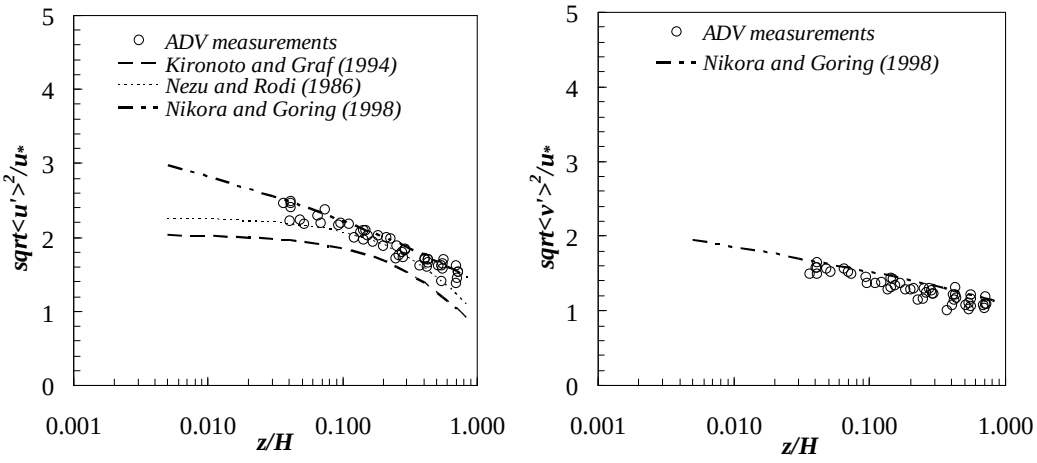

(a)

(b)

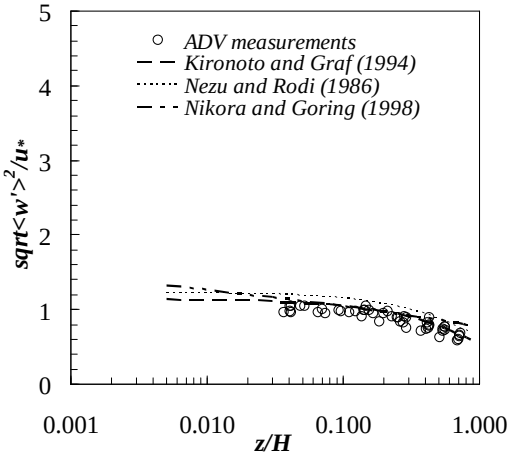

(c)

Figure 3.13 Turbulent intensities for Run 3 (u_*=0.044 ft/s, H =0.49 ft; (a) relative longitudinal turbulence intensity; (b) relative transverse turbulence intensity; (c) relative vertical turbulence intensity)

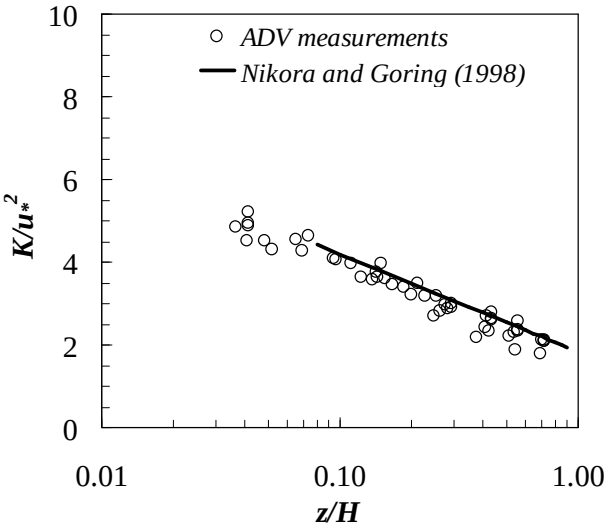

Figure 3.14 Turbulent kinetic energy for run 3 (u_*=0.044 ft/s, H=0.49 ft)

CHAPTER IV

EXPERIMENTAL RESULTS

4.1 *Introduction*

This chapter presents the experimental results collected from the laboratory studies. These results include three clear-water scour conditions: Case A - long setback abutment scour; Case B - bankline abutment scour; and Case C - short setback abutment scour. Their descriptions and classification in terms of the ratio of setback distance (W) to the approach flow depth in the floodplain, W/y_{f1}, are given below:

- Case A ($W/y_{f1} > 6$, L_a/B_f = 0.53 and 0.77 in this study): In a long setback abutment, scour occurs in the floodplain only, well removed from the main channel;
- Case B ($W/y_{f1} = 0$, $L_a/B_f = 1.0$ in this study): For a bankline abutment, maximum scour occurs in the main channel of a compound channel;
- Case C ($W/y_{f1} < 6$, L_a/B_f = 0.88 in this study): In a short setback abutment, scour occurs on the floodplain in the initial stage, but maximum scour at equilibrium occurs in the main channel because the setback distance is short.

The suggested limit of 6 is selected from the experimental results presented in the following subsection.

The first section of this chapter explains the classification of scour conditions. In

the second section, the location of velocity measurements in the approach and bridge sections is presented. Then the results for long setback and bankline abutments are presented in subsections. The subsections consisted of velocity measurements, results of time development of abutment scour depth, maximum scour depth and scour contours, water surface profiles, and velocity and turbulence flow fields. Each subsection presents figures selected as representatives of the results of Runs 1, 2, and 3. Other experimental runs are shown in the Appendix. Then, in the final section, results of the short setback abutment are presented as a separate case because of the simultaneous involvement of main channel and floodplain flow in the contracted section.

4.2 *Classification of Scour Conditions*

Several conditions of abutment scour developed in accordance with the flow field at an abutment, the physical characteristics of an abutment and the waterway in which it is located. In this study, scour conditions are classified as three cases, Case A, Case B, and Case C, in accordance with the locations of maximum scour hole. With reference to the definition sketch in Figure 4.1, the locations of the maximum scour hole are summarized in Table 4.1 in which W is the distance from the toe of the abutment to the bank of the main channel and L_m is the transverse distance from the toe of the abutment to the maximum scour hole depth.

To distinguish whether the scour hole occurs in the floodplain of the main channel, we can compare W/y_{f1} with L_m/y_{f1}. The maximum value of L_m/y_{f1} in all

experiments is 5.84 in Run 13, as shown in Table 4.1. Thus, if the value of W/y_{f1} is larger than approximately 6, the location of the maximum scour hole is expected to be within the floodplain. When the predicted value of W/y_{f1} is larger than about 6, the scour condition is classified as Case A or long setback abutment scour and the location of the maximum scour is in the floodplain. However, if the value of W/y_{f1} is smaller than approximately 6, the scour condition is classified as Case C or short setback abutment scour because the location of maximum scour is in the main channel due to the short setback distance. Finally, Case B refers to the scour condition for the bank line abutment (W/y_{f1}=0).

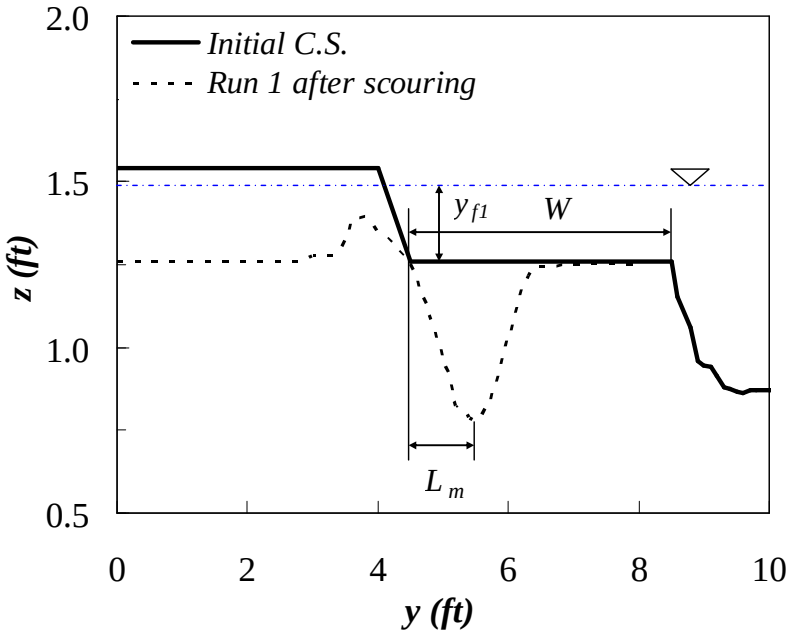

Figure 4.1 Definition sketch for classification of scour conditions

Table 4.1 Summary of locations of maximum scour hole in the floodplain (Case A = long setback, Case B = bankline, and Case C= short setback abutment)

Run	L_a/B_f	*Flow type*	y_{f1}	W	L_m	$\frac{L_m}{y_{f1}}$	$\frac{W}{y_{f1}}$	Conditions
			ft	ft	ft	-	-	
1	0.53	F	0.243	4.0	0.9	3.70	16.46	Case A
2		SO	0.347	4.0	1.3	3.75	11.53	Case A
3		OT	0.488	4.0	1.0	2.05	8.20	Case A
4		F	0.247	4.0	1.0	4.05	16.19	Case A
5		SO	0.355	4.0	1.2	3.38	11.27	Case A
6		OT	0.484	4.0	0.9	1.86	8.26	Case A
7	0.71	F	0.248	2.5	1.3	5.24	10.08	Case A
8		SO	0.337	2.5	1.7	5.04	7.42	Case A
9		OT	0.491	2.5	0.8	1.63	5.09	Case A
10		F	0.241	2.5	1	4.15	10.37	Case A
11		SO	0.343	2.5	1.4	4.08	7.29	Case A
12		OT	0.483	2.5	0.7	1.45	5.18	Case A
13	0.88	F	0.248	1.0	1.5	5.84	3.89	Case C
14		SO	0.337	1.0	1.6	4.76	2.98	Case C
15		OT	0.491	1.0	1.2	2.46	2.05	Case C
16		F	0.241	1.0	1.2	4.72	3.94	Case C
17		SO	0.343	1.0	1.5	4.44	2.96	Case C
18		OT	0.483	1.0	1.0	2.09	2.09	Case C

Note: Flow type: F=free flow; SO=submerged orifice flow; OT=overtopping flow

4.3 *Locations of Velocity Measurements*

Vertical velocity profiles, with a minimum of eight measuring points in each vertical profile and as many as fifteen points, were measured along multiple lateral transects (x in Figure 4.2) at the approach section (C.S. 1) and the bridge sections (C.S. 3 and C.S. 4). The locations chosen for measurement of the velocity profiles are shown in Figure 4.2.

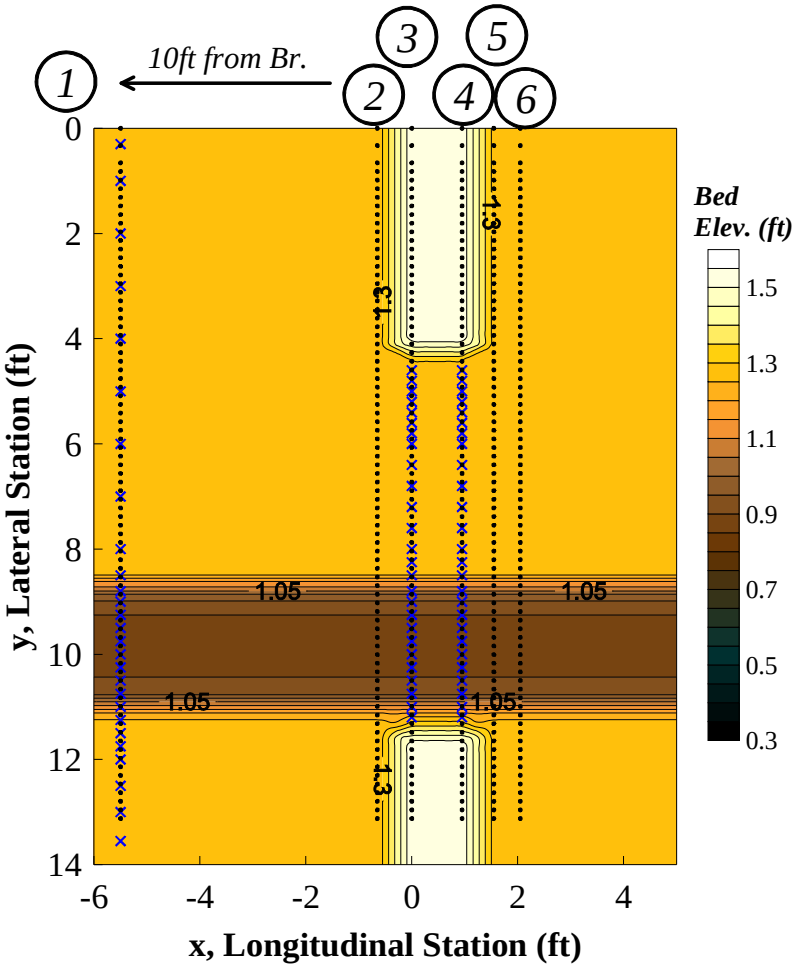

Figure 4.2 Initial contours with measurement locations

4.4 *Experiments with Long Setback and Bankline Abutments (Case A and Case B)*

The experimental conditions and results for the long setback abutment are shown in Table 4.2 in terms of total discharge, Q; the approach floodplain flow depth, y_{f1}; the floodplain flow depth measured downstream of the bridge, assumed to be the same as the unconstricted floodplain flow depth, y_{f0}; the approach floodplain mean flow velocity, V_{f1}; the discharge per unit width at the approach floodplain, q_{f1}; the discharge per unit width at the immediate upstream bridge (C.S. 3 in Figure 4.2) and downstream sections (C.S. 4 in Figure 4.2), q_{f2}; and the maximum scour depth measured from an undisturbed floodplain elevation, $d_{\max}$. Two different lengths of the abutments/embankments were simulated (L_a/B_f =0.53 and 0.71) in three different flow types (i.e., free, submerged orifice, and overtopping flow).

Table 4.3 is a summary of dimensionless parameters for the long setback abutment corresponding to the data given in Table 4.2. These parameters include the approach flow intensity, V_{f1}/V_{fc1} ; the unit discharge contraction ratio for C.S. 3 and C.S. 4, q_{f2}/q_{f1} ; the flow depth ratio of the floodplain to the main channel, y_{f1}/y_{m1} ; the ratio of the total overtopping discharge to the total discharge, Q_{ot}/Q; the ratio of the approach water depths to the downstream bridge water depth, y_{f1}/y_{f0} ; and the maximum water depth at the location of the maximum scour hole normalized by the approach water depth and the downstream water depth, $y_{\max}/y_{f1}$ and $y_{\max}/y_{f0}$

respectively. The critical velocity of the initiation of the sediment motion, V_{fc1}, was calculated from Keulegan's equation with the value of k_s presented in Table 3.2.

The ranges of dimensionless parameters in Table 4.3 are the results of experiments with two different lengths of abutment in the floodplain. Figure 4.3 shows the stage-discharge relationship for this study. In the first three runs, the flow intensity parameter, V_{f1}/V_{fc1}, had a similar value so that the effect of different flow types in clear-water scour could be examined as shown in Figure 4.3. The same conditions were also applied to other experiments as shown in Table 4.3. The experiments were conducted such that the three flow types were encountered for increasing Q while increasing the tailwater such that the value of V_{f1}/V_{fc1} remained nearly constant. The range of the unit discharge contraction ratio varied from 1.2 to 2.3 in C.S. 4 depending on the abutment length and type of flow. (The value at C.S. 4 is considered to be the value to use in the scour formula suggested subsequently because it represents the maximum contraction). For the longer abutment length, q_{f2}/q_{f1} increased due to the greater lateral contraction. For the overtopping runs, q_{f2}/q_{f1} decreased because of the significant portion of discharge overflowing the bridge deck. The effect of backwater can be observed by the ratio of the approach flow depth to the downstream value of the water depth at the bridge, y_{f1}/y_{f0}. The range of y_{f1}/y_{f0} values showed that the back water effect was not significant. With regard to compound channel effects, the maximum flow depth ratio of the floodplain to the main channel was 0.5 for the free flow and the pressure flow (submerged orifice flow) cases. The approach flow values of *Fr* number and k_s^+

($= k_s u_* / \nu$) varied from 0.12 to 0.25 and from 40 to 70, respectively. The ratio of the overtopping discharge to the total discharge varied from 0.35 to 0.41.

A summary of the measured experimental data for the bankline abutment is presented in Table 4.4, and the data are given in dimensionless form in Table 4.5 with the same parameters mentioned in the previous section, but with a different subscript, m (subscript "m" illustrates the main channel variable). The value of d_{max} are measured from the floodplain in these cases as well as the previous ones, and $y_{max} = d_{max} + y_{f0}$.

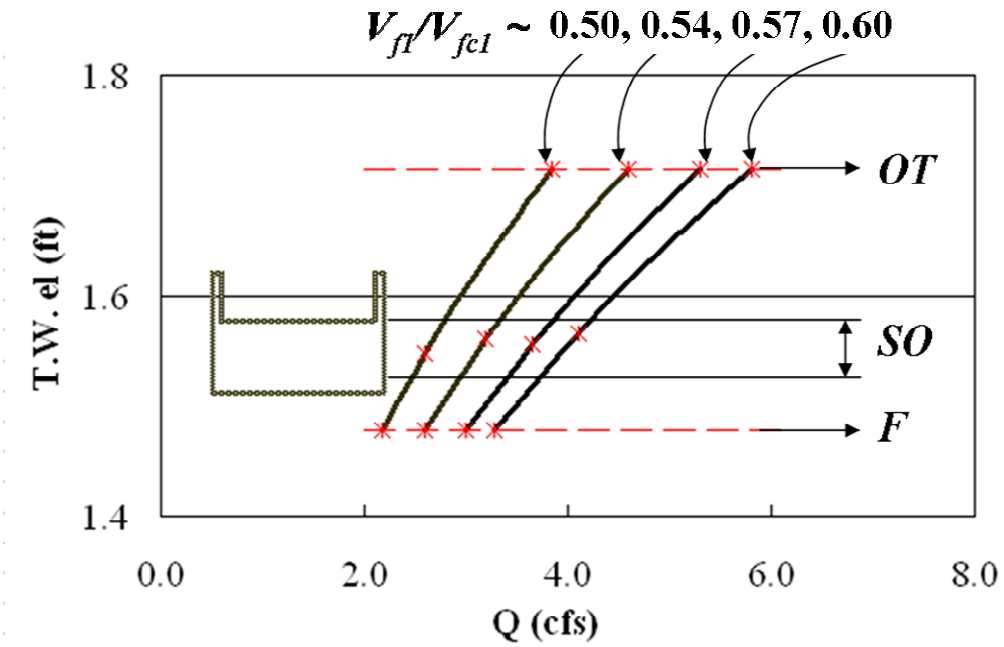

Figure 4.3 Stage-discharge relationship for this study in the floodplain

Table 4.2 Summary of measured experimental data for the long setback abutment at the beginning of scour

Run	L_a/B_f	*Flow type*	Q	y_{f1}	V_{f1}	q_{f1}	*C.S. 3* q_{f2}	*C.S.4* q_{f2}	y_{f0}	d_{max}
			cfs	ft	ft/s	ft^2/s	ft^2/s	ft^2/s	ft	ft
1	0.53	F	3.3	0.243	0.668	0.161	0.265	0.293	0.218	0.479
2		SO	4.1	0.347	0.682	0.230	0.370	0.431	0.315	0.630
3		OT	5.8	0.488	0.740	0.354	0.378	0.406	0.457	0.592
4		F	3.0	0.247	0.625	0.146	0.236	0.256	0.220	0.447
5		SO	3.9	0.355	0.656	0.225	0.334	0.401	0.325	0.591
6		OT	5.3	0.484	0.674	0.319	0.334	0.398	0.455	0.367
7	0.71	F	3.0	0.248	0.594	0.147	0.295	0.329	0.220	0.505
8		SO	3.65	0.337	0.617	0.208	0.401	0.470	0.300	0.621
9		OT	5.3	0.491	0.686	0.336	0.380	0.395	0.457	0.498
10		F	2.6	0.241	0.545	0.129	0.261	0.286	0.220	0.418
11		SO	3.2	0.343	0.569	0.182	0.353	0.404	0.308	0.540
12		OT	4.6	0.483	0.611	0.294	0.340	0.376	0.457	0.386

Note: Flow type: F=free flow; SO=submerged orifice flow; OT=overtopping flow

Table 4.3 Summary of dimensionless experimental data for the long setback abutment at the beginning of scour ($y_{max} = d_{max} + y_{f0}$)

Run	L_a/B_f	*Flow type*	$\frac{V_{f1}}{V_{fc1}}$	*C.S.3* $\frac{q_{f2}}{q_{f1}}$	*C.S.4* $\frac{q_{f2}}{q_{f1}}$	$\frac{y_{f1}}{y_{m1}}$	$\frac{Q_{ot}}{Q}$	$\frac{y_{f1}}{y_{f0}}$	$\frac{y_{max}}{y_{f1}}$	$\frac{y_{max}}{y_{f0}}$
1	0.53	F	0.61	1.646	1.818	0.38	0	1.11	2.868	3.197
2		SO	0.60	1.609	1.875	0.47	0	1.10	2.723	3.000
3		OT	0.61	1.068	1.148	0.55	0.356	1.07	2.150	2.295
4		F	0.58	1.616	1.755	0.38	0	1.12	2.700	3.032
5		SO	0.57	1.484	1.781	0.47	0	1.09	2.580	2.818
6		OT	0.56	1.047	1.250	0.55	0.364	1.06	1.698	1.807
7	0.71	F	0.54	2.007	2.236	0.39	0	1.13	2.923	3.295
8		SO	0.53	1.928	2.257	0.46	0	1.12	2.733	3.070
9		OT	0.56	1.131	1.176	0.55	0.408	1.07	1.945	2.090
10		F	0.49	2.023	2.208	0.38	0	1.10	2.647	2.900
11		SO	0.49	1.940	2.223	0.46	0	1.11	2.427	2.753
12		OT	0.50	1.156	1.278	0.55	0.392	1.06	1.745	1.845

Note: Flow type: F=free flow; SO=submerged orifice flow; OT=overtopping flow

Table 4.4 Summary of measured experimental data for the bankline abutment at the beginning of scour

Run	L_a/B_f	*Flow type*	Q	y_{m1}	V_{m1}	q_{m1}	*C.S.3* q_{m2}	*C.S.4* q_{m2}	y_{m0}	d_{max}
			cfs	ft	ft/s	ft^2/s	ft^2/s	ft^2/s	ft	ft
1	1.0	F	3.3	0.499	0.991	0.492	0.709	0.759	0.474	0.814
2		SO	4.1	0.603	0.885	0.528	0.771	0.783	0.571	0.819
3		OT	5.8	0.744	0.893	0.658	0.689	0.754	0.713	0.641
4		F	3.0	0.503	0.926	0.456	0.658	0.657	0.476	0.651
5		SO	3.9	0.611	0.834	0.502	0.701	0.711	0.581	0.687
6		OT	5.3	0.740	0.800	0.607	0.613	0.668	0.711	0.482
7	1.0	F	3.0	0.504	0.875	0.427	0.724	0.75	0.476	0.823
8		SO	3.65	0.593	0.866	0.518	0.782	0.83	0.556	0.816
9		OT	5.3	0.747	0.825	0.617	0.693	0.767	0.713	0.637
10		F	2.6	0.497	0.859	0.425	0.646	0.654	0.476	0.637
11		SO	3.2	0.599	0.747	0.448	0.689	0.738	0.564	0.776
12		OT	4.6	0.739	0.712	0.527	0.622	0.665	0.713	0.566
13	1.0	F	2.6	0.513	0.823	0.416	0.733	0.792	0.476	0.699
14		SO	3.1	0.592	0.764	0.451	0.801	0.880	0.546	0.901
15		OT	4.6	0.744	0.710	0.528	0.652	0.751	0.713	0.487
16		F	2.2	0.510	0.665	0.333	0.611	0.658	0.476	0.668
17		SO	2.6	0.594	0.644	0.377	0.674	0.717	0.546	0.747
18		OT	3.9	0.735	0.625	0.457	0.595	0.677	0.713	0.412

Note: Flow type: F=free flow; SO=submerged orifice flow; OT=overtopping flow

Table 4.5 Summary of dimensionless experimental data for the bankline abutment at the beginning of scour ($y_{max} = d_{max} + y_{f0}$)

Run	L_a/B_f	*Flow type*	$\frac{V_{m1}}{V_{mc1}}$	*C.S.3* $\frac{q_{m2}}{q_{m1}}$	*C.S.4* $\frac{q_{m2}}{q_{m1}}$	$\frac{y_{f1}}{y_{m1}}$	$\frac{y_{m1}}{y_{m0}}$	$\frac{y_{max}}{y_{m1}}$	$\frac{y_{max}}{y_{m0}}$
1	1.0	F	0.83	1.441	1.543	0.38	1.05	2.068	2.177
2		SO	0.73	1.460	1.483	0.47	1.06	1.881	1.986
3		OT	0.72	1.047	1.146	0.55	1.04	1.476	1.540
4		F	0.77	1.443	1.441	0.38	1.06	1.732	1.830
5		SO	0.68	1.396	1.416	0.47	1.05	1.656	1.742
6		OT	0.64	1.041	1.100	0.55	1.04	1.266	1.318
7	1.0	F	0.74	1.696	1.756	0.39	1.06	2.069	2.191
8		SO	0.71	1.510	1.602	0.46	1.07	1.882	2.007
9		OT	0.66	1.123	1.243	0.55	1.05	1.465	1.534
10		F	0.72	1.520	1.539	0.38	1.04	1.724	1.800
11		SO	0.61	1.538	1.647	0.46	1.06	1.810	1.922
12		OT	0.57	1.180	1.262	0.55	1.04	1.384	1.435
13	1.0	F	0.69	1.762	1.904	0.39	1.08	1.791	1.931
14		SO	0.63	1.776	1.951	0.46	1.08	2.012	2.181
15		OT	0.57	1.235	1.422	0.55	1.04	1.269	1.324
16		F	0.55	1.835	1.976	0.39	1.07	1.741	1.866
17		SO	0.52	1.788	1.902	0.46	1.09	1.746	1.9899
18		OT	0.50	1.302	1.481	0.55	1.03	1.182	1.219

Note: Flow type: F=free flow; SO=submerged orifice flow; OT=overtopping flow

4.4.1 *Velocity Measurements*

The depth-averaged velocities in the approach cross section were determined by the application of the best fit of the logarithmic velocity profile to the measured point velocities in the vertical. The depth-averaged velocity was then evaluated as the point velocity from the best-fit log relation at a relative distance above the bed of 0.4 times the depth (French, 1986). However, in the bridge section, the depth-averaged velocities were calculated by taking the integral of the point velocity measurements within each vertical velocity profile over the depth and dividing by the water depth because the velocity profile in the bridge section did not have a logarithmic relationship due to its complex three-dimensional behavior. Figure 4.4 shows the approach flow depth-averaged velocity distributions measured at a cross section 10 ft upstream of the bridge for Runs 1, 2, and 3. The velocities were higher in the main channel than the floodplain, as expected for an overbank flow, but the relative difference decreased as discharge increased and as the ratio of the floodplain to the main channel water depth increased, as observed in Tables 4.2 and 4.4 by comparing y_{f1} and y_{m1}, respectively.

Figure 4.5 shows depth-averaged velocity distributions measured at the bridge sections (i.e. C.S. 3 and C.S. 4) for Run 2. The velocities were higher in C.S. 4 than in C.S. 3 because of the lateral and vertical contraction of the streamlines through the bridge. The lateral distributions of the average velocities in the floodplain remained nearly constant for the entire width of the floodplain under the bridge except in the near field of the abutment at both C.S. 3 and C.S. 4.

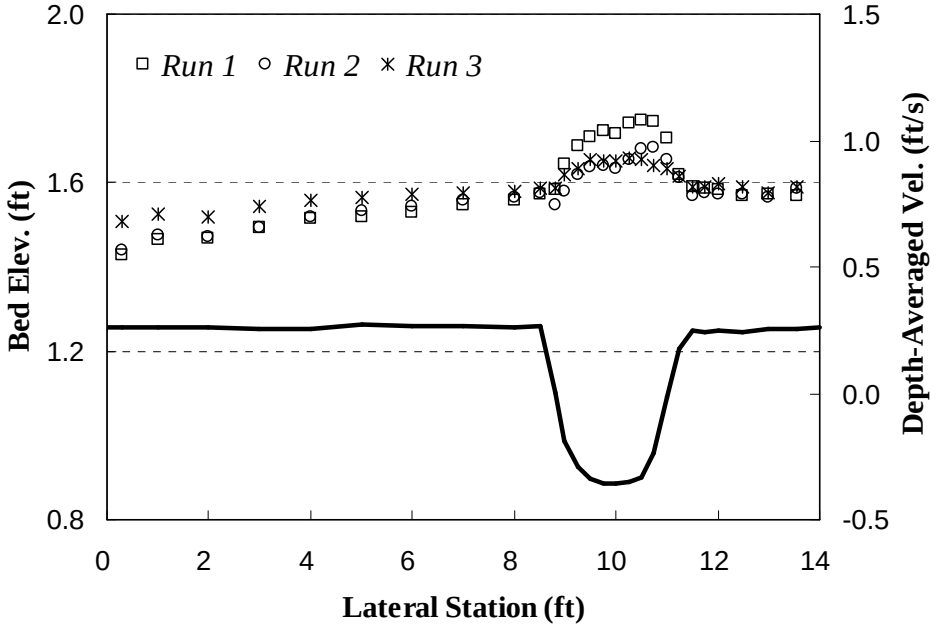

Figure 4.4 Approach flow velocity distributions for Runs 1, 2, and 3

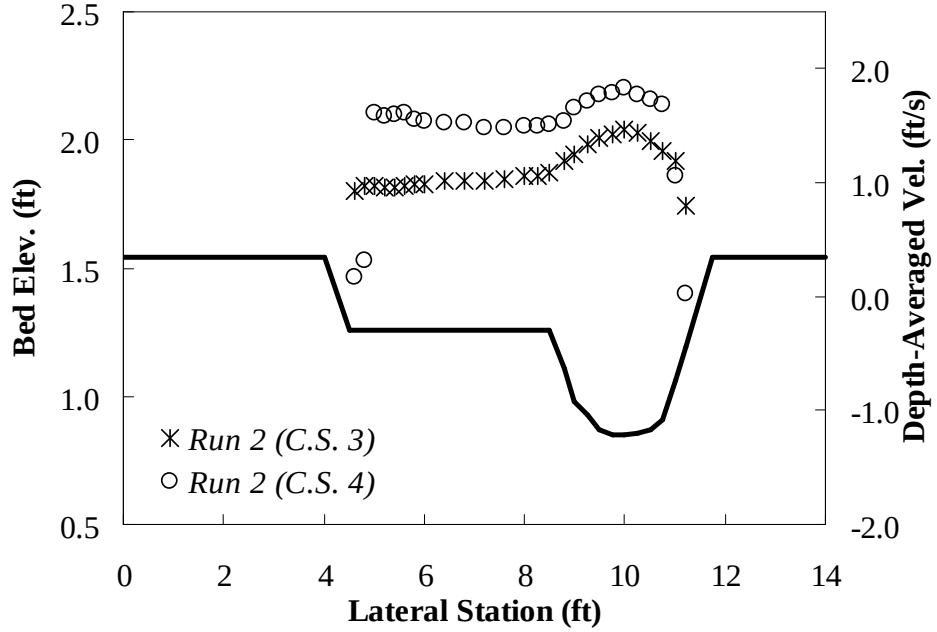

Figure 4.5 Velocity distributions at a bridge section for Run 2

4.4.2 *Time Development of Abutment Scour*

Several researchers such as Cardoso and Bettess (1999), Hager and Oliveto (2002), Dey and Barbhuiya (2005), and others measured the time development of the abutment scour depth at one fixed point (i.e., the location of the maximum scour depth) to investigate the scour depth development with time because the location of the deepest scour did not move over time in their experiments. In general, initial local scour begins at the upstream corner of an abutment. If an experiment is conducted at a solid (non-erodible) abutment, the scour depth then becomes deeper with time and reaches equilibrium (i.e., the maximum scour depth) near the upstream corner of the abutment. However, the experimental results of this study show that the region of the deepest scour moved downstream from the abutment over time because the abutment was erodible, confirming that local maximum scour over time cannot be a known value if all of the bed contours are not measured over time. The local maximum value over time was determined by measuring all of the contours with the ADV at selected time intervals throughout the experiment. Figure 4.6 illustrates one of the 18 plots for the temporal development of scour contours. Other experimental runs are shown in the Appendix.

Selected temporal variations of the abutment scour depth for each experiment are shown in Figures 4.7 and 4.8, which present temporal changes in the maximum scour depth in terms of real time on a semi-logarithmic scale for the long setback (L_a/B_f = 0.53) and bankline (L_a/B_f = 1.0) abutments, respectively. All scour depths observed in the experiments rapidly changed in the initial stage and the rate of scouring decreased with time. Finally, the scour depth reached the equilibrium state. In general, it takes more time

for the scour condition to reach equilibrium for overtopping cases than for free and submerged orifice flow cases. Detailed analysis of the temporal development will be given in Chapter 5.

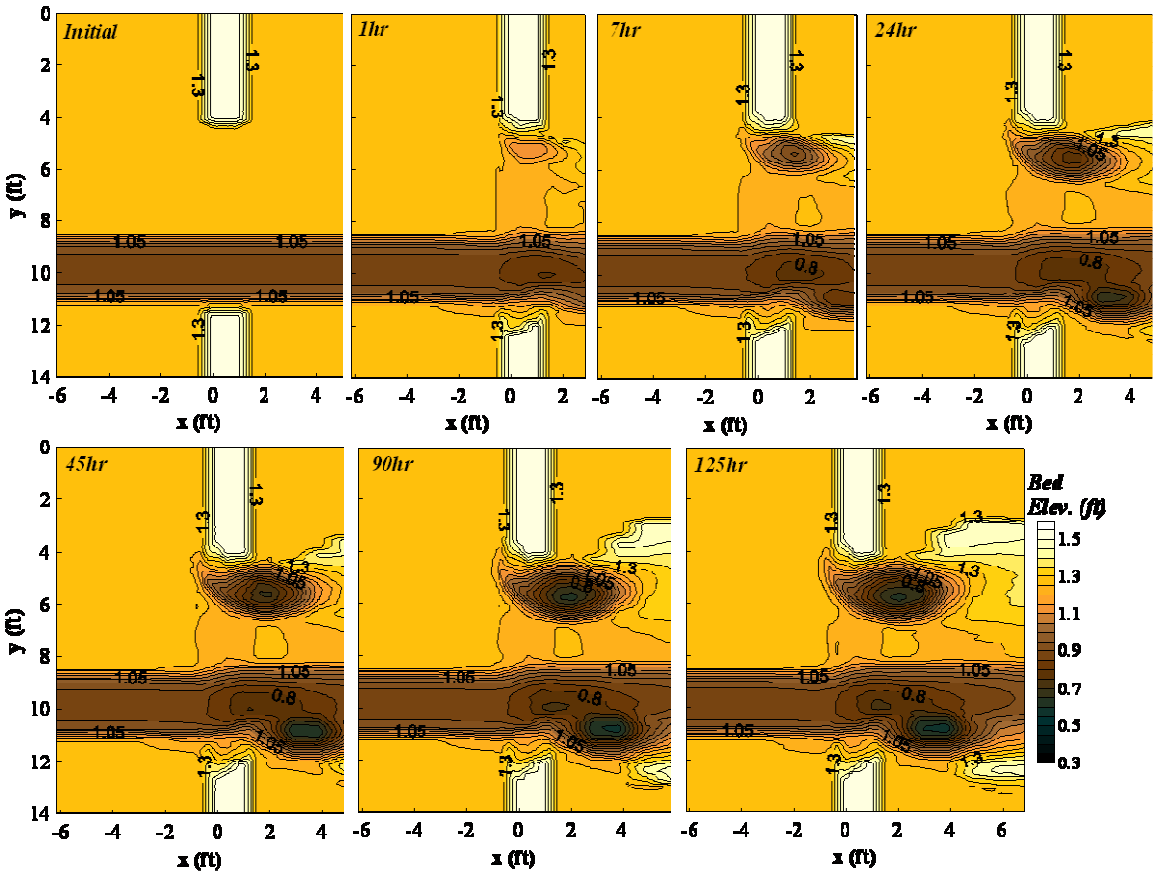

Figure 4.6 Time development of scour for Run 2 (L_a/B_f = 0.53)

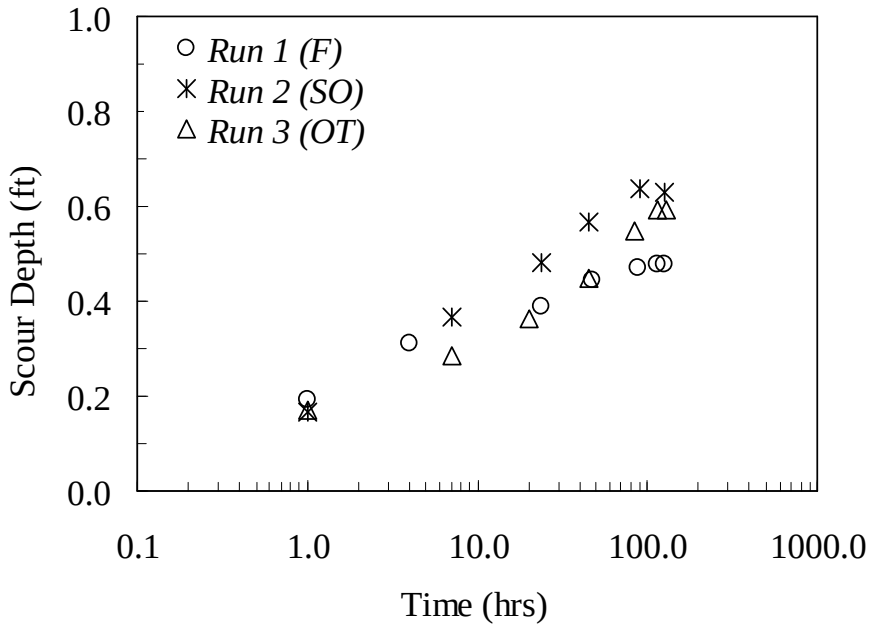

Figure 4.7 Time development of the scour depth for the long setback abutment (L_a/B_f = 0.53)

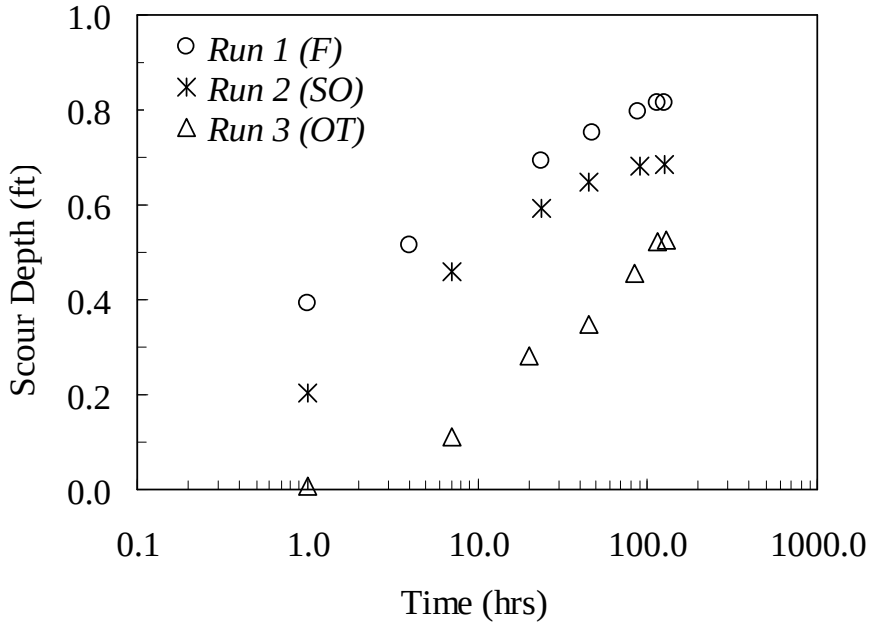

Figure 4.8 Time development of the scour depth for the bankline abutment (L_a/B_f = 1.0)

4.4.3 *Measurement of the Maximum Scour Depths and Scour Contours*

As shown in Figure 4.6, the scour hole moved downstream from the abutment over time and the region of the deepest scour hole was located near the downstream corner of the abutment face. Furthermore, as the scour process with respect to time differed depending on the flow type, the location of the deepest scour depth was case dependent. To find the location of the maximum scour depth and to measure the maximum scour depth, bed elevations after scouring were plotted for each experiment. Figure 4.9 shows the bed contours after scouring for Runs 1, 2, and 3, and the corresponding photographs at the end of scouring (equilibrium). The shape of the scour hole showed curvature around the abutment, and the resulting point of the maximum scour depth moved from the upstream corner of the abutment face to a point that was diagonally displaced in the downstream direction from the downstream toe of the abutment over time in the floodplain for free flow and submerged orifice flow. However, for overtopping flow, the scour hole was further elongated in the streamwise direction by comparison, and the resulting point of maximum scour moved in the streamwise direction to a point further downstream of the abutment over time. For the bankline abutment, the maximum scour depth occurred around the main channel bankline downstream of the bridge.

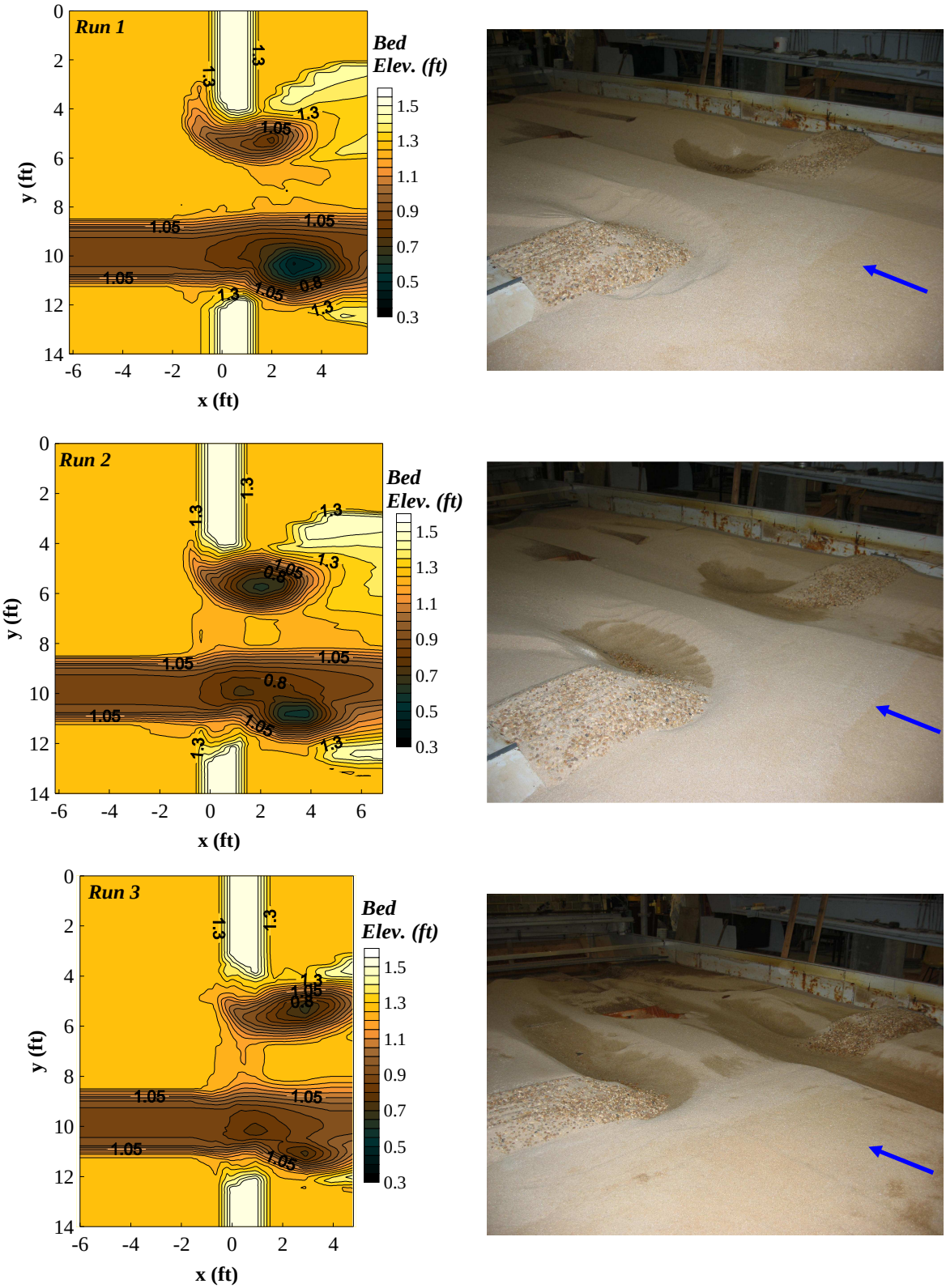

Figure 4.9 Final bed elevation contours after scouring for Runs 1, 2, and 3 (L_a/B_f = 0.53)

4.4.4 *Measurement of Water Surface Profiles*

For each experiment, water surface profiles were measured along multiple lines in the streamwise direction (five lines in the floodplain and five in the main channel) from 20 ft downstream of the bridge to 15 ft upstream of the bridge. The average water surface profile elevation was computed from these ten measurements across the channel at a given longitudinal channel station. Figure 4.10 shows the water surface profile plot for experimental Runs 1, 2, and 3. In all three cases, the effect of back water was observed, but it was not significant (i.e., $1.05 < y_{f1} / y_{f\,un-obst} < 1.15$, in which $y_{f\,un-obst}$ is the un-obstructed floodplain water depth). The acceleration of water under the bridge section was also captured by the measurements for the Run 1 water surface profile.

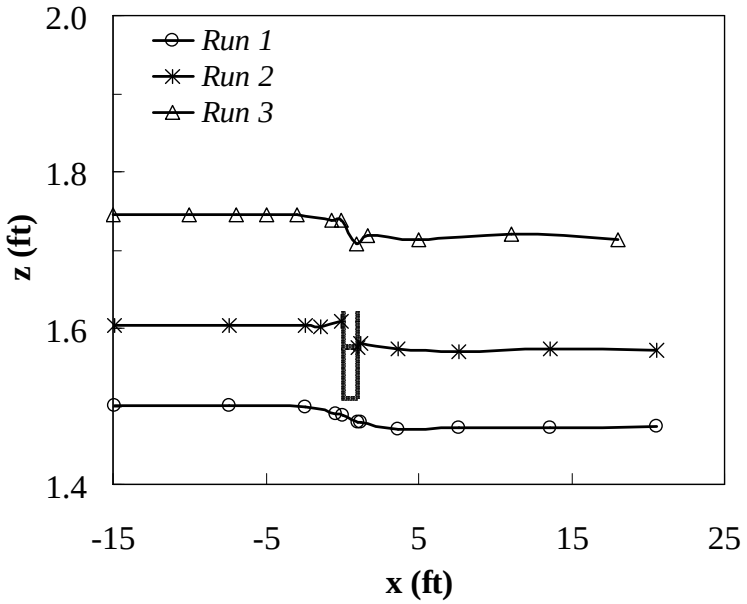

Figure 4.10 Averaged water surface profiles along the flow direction for Runs 1, 2, and 3 (L_a/B_f = 0.53)

4.4.5 *Velocity and Turbulence Flow Field Around the Abutment*

As explained in the previous section, the shape of the scour hole around an abutment is different depending on the flow types. This phenomenon, which results from a longitudinal (for the overtopping case) and diagonal (for the free and submerged orifice case) displacement of the deepest scour point relative to the abutment face, can be explained by the flow field around the abutment.

To show the complex flow physics and resulting sediment transport, velocities were measured at a height of 5 mm above the fixed bed around the bridge. The measured near-field velocity vectors superimposed on initial and final bed elevation contours are shown in Figures 4.11, 4.12, and 4.13 for Runs 1, 2, and 3, respectively. Higher velocities were measured around the abutment where deeper scour occurred as the contracted flow curved around the abutment. The long roadway approach section and the narrow bridge opening forced floodplain water to re-enter through the bridge opening, causing severe contraction in the flow area. This severe contraction in the flow area produced narrow stream lines around the abutment due to accelerated flow, which was deflected around the upstream face of the abutment and separated on the face of the abutment. It is apparent that the recirculation zone occurred behind the separation point for the setback abutment in the free flow (Run 1) and the submerged orifice flow (Run 2) cases, and the measured higher velocities are just outside of the recirculation region, as shown in Figures 4.11 and 4.12. However, for the overtopping case, the flow separation and recirculation region was located farther downstream of the abutment because the overtopping discharge (i.e., Q_{ot}/Q = 0.36 – 0.41, Q_{ot} is the overtopping discharge and Q is the total discharge)

acted like a surface jet, resulting in an elongated scour hole. Consequently, the location of the deepest scour was associated primarily with the location and the size of the recirculation zone.

In addition to velocity measurements near the bed, velocities were measured at C.S. 3 and C.S. 4, and Figures 4.14, 4.15, and 4.16 present the $v-w$ velocity plots for Runs 1, 2, and 3, respectively. The resultant velocity vectors in the floodplain and the main channel are normalized by the approach floodplain flow velocity (V_{f1}) and main channel flow velocity (V_{m1}), respectively. In the cross-sectional velocity plot at C.S. 3, higher magnitude velocity vectors are observed around the abutment resulting from lateral flow contraction. Furthermore, the submergence of the upstream face of the bridge (Runs 2 and 3) produced vertical flow contraction (i.e., the higher downward component of the velocity vectors) in addition to the existing lateral flow contraction. At C.S. 4, the magnitude of the resultant velocity vectors in the *yz* plane are smaller and the upward components of velocity are observed for Runs 2 and 3. This downward and upward flow motion through the bridge induced by the bridge deck resulted in vertical contraction scour, shown in Figure 4.9 for Runs 2 and 3. The lower bed elevation region along the upstream and downstream face of the bridge deck in the floodplain is probably the result of vertical contraction scour because of the velocity vectors being directed downward under the bridge.

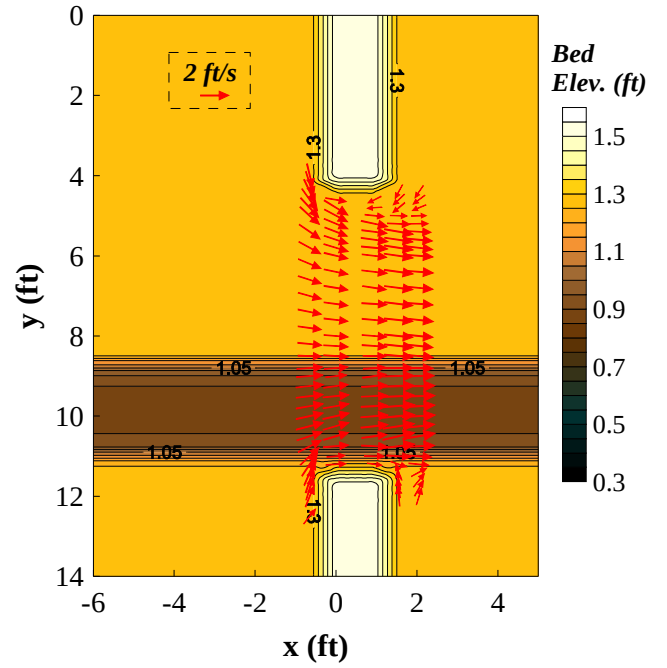

(a)

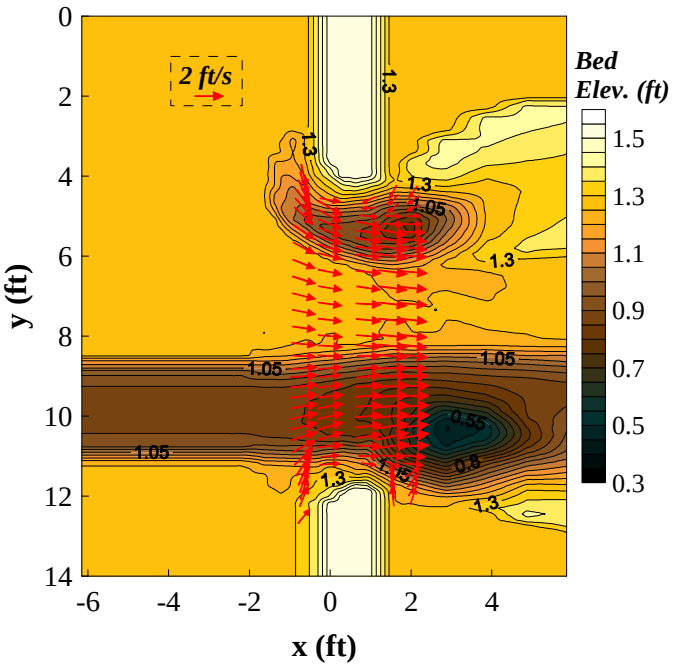

(b)

Figure 4.11 Initial velocity vectors measured at 0.5 mm above the fixed bed for Run 1 superimposed on (a) initial contours and (b) final contours (L_a/B_f =0.53, flow type = F)

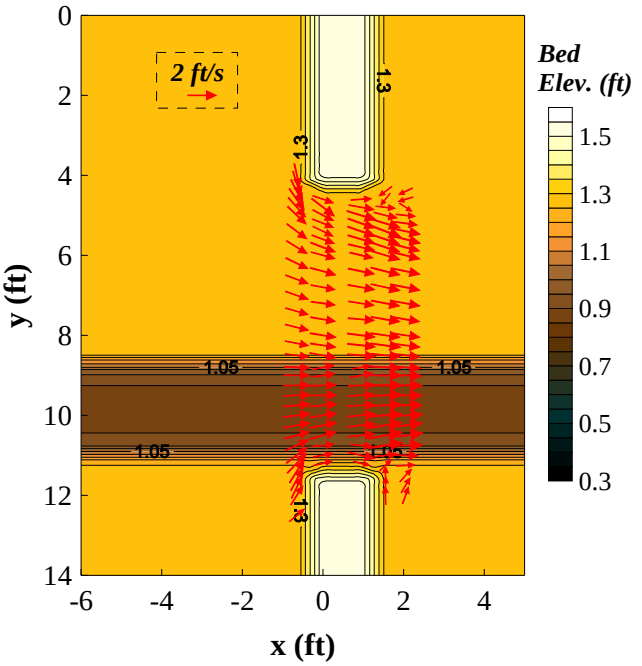

(a)

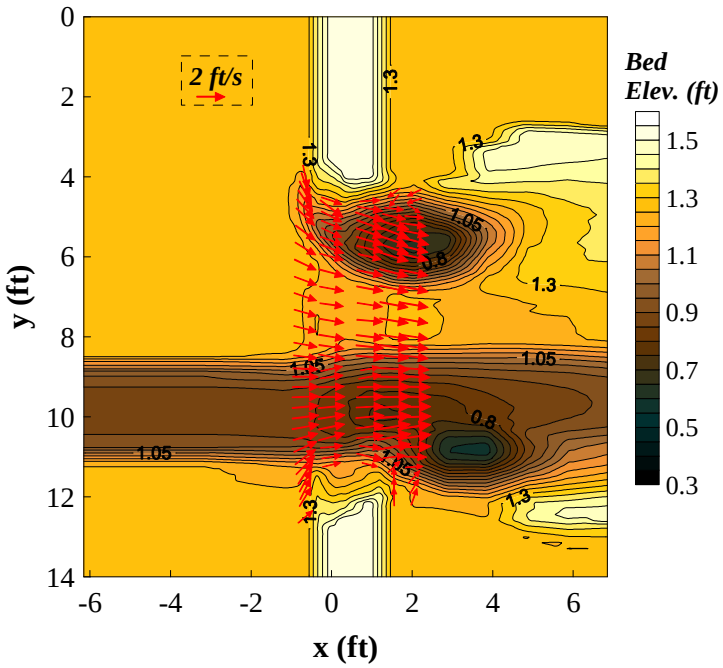

(b)

Figure 4.12 Initial velocity vectors measured at 0.5 mm above the fixed bed for Run 2 superimposed on (a) initial contours and (b) final contours (L_a/B_f =0.53, flow type = SO)

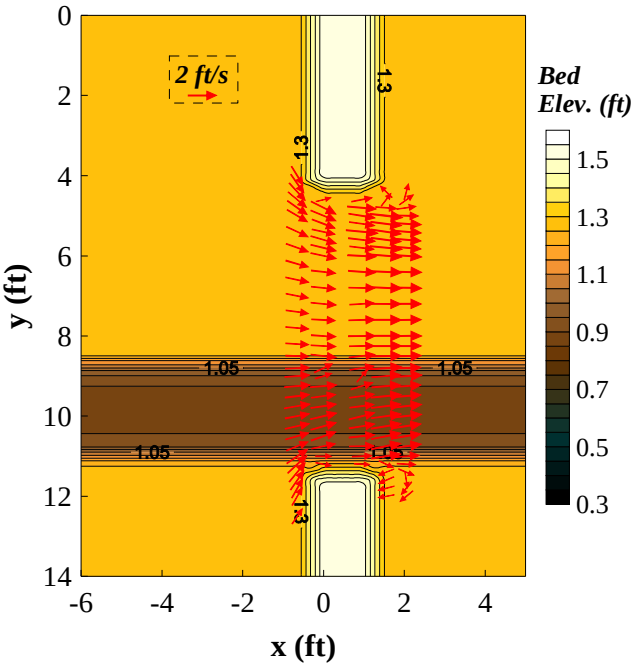

(a)

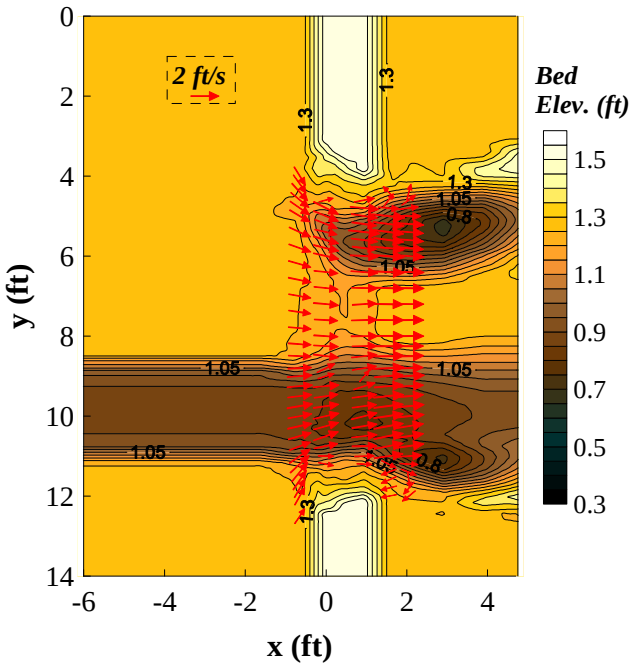

(b)

Figure 4.13 Initial velocity vectors measured at 0.5 mm above the fixed bed for Run 3 superimposed on (a) initial contours and (b) final contours (L_a/B_f =0.53, flow type = OT)

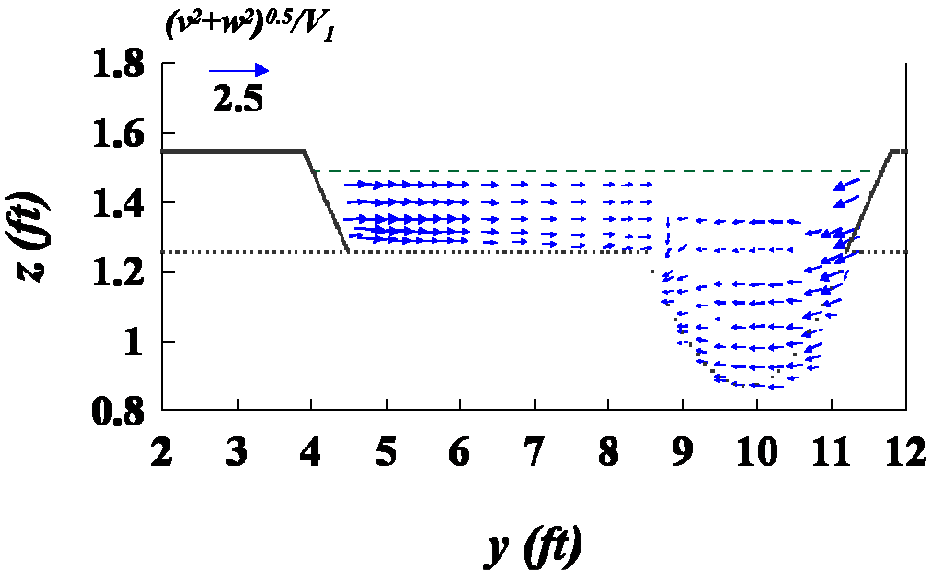

(a)

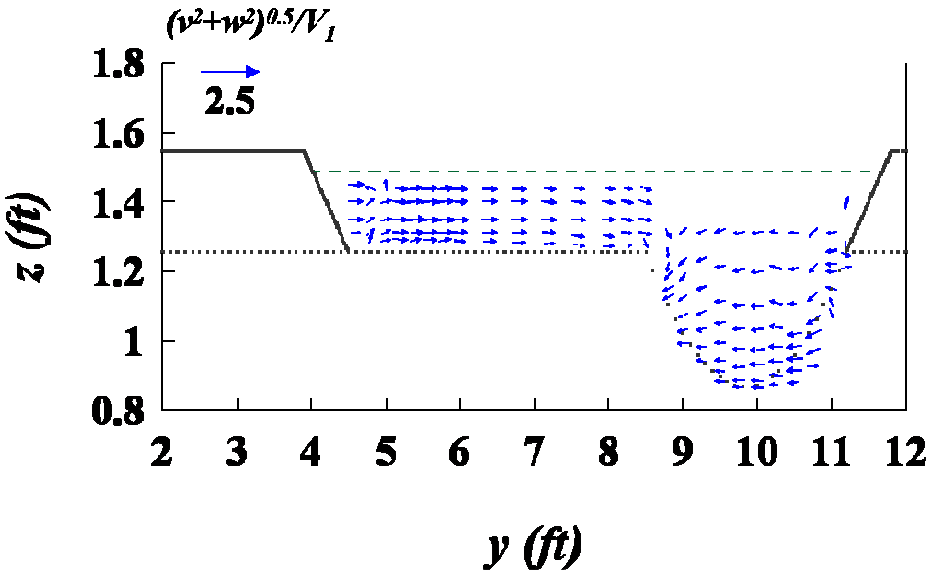

(b)

Figure 4.14 Cross-sectional velocity vectors measured at (a) C.S. 3 and (b) C.S. 4 for Run 1 normalized by approach flow velocity (L_a/B_f =0.53, flow type = F)

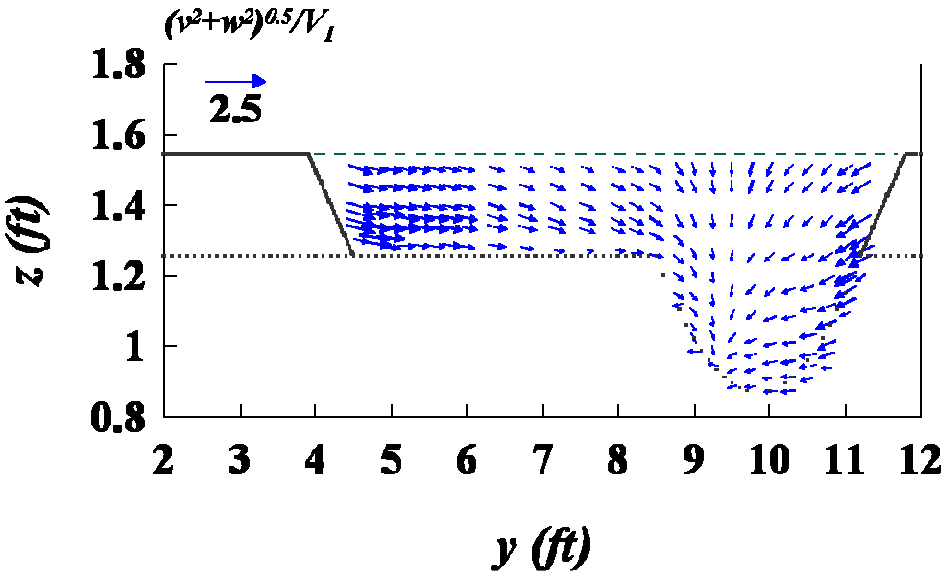

(a)

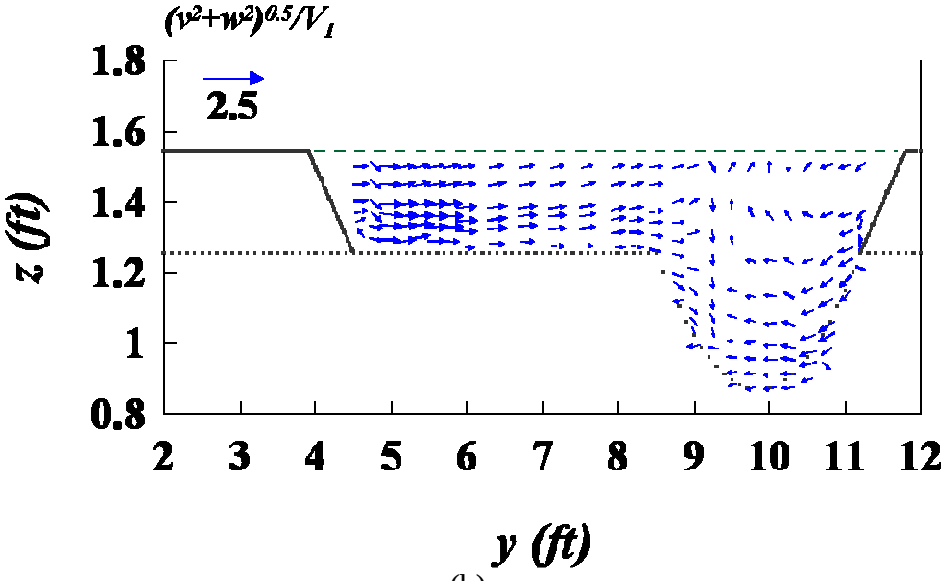

(b)

Figure 4.15 Cross-sectional velocity vectors measured at (a) C.S. 3 and (b) C.S. 4 for Run 2 normalized by approach flow velocity (L_a/B_f =0.53, flow type = SO)

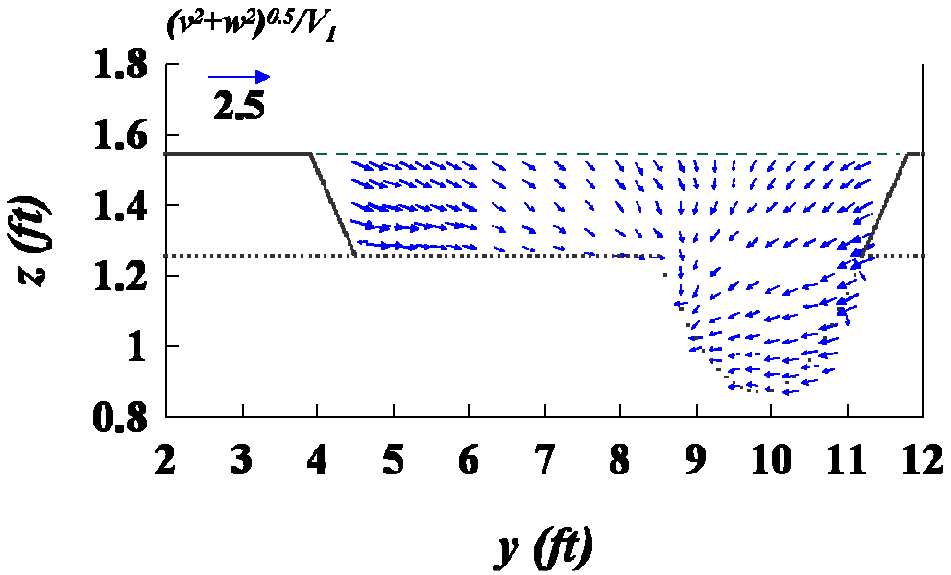

(a)

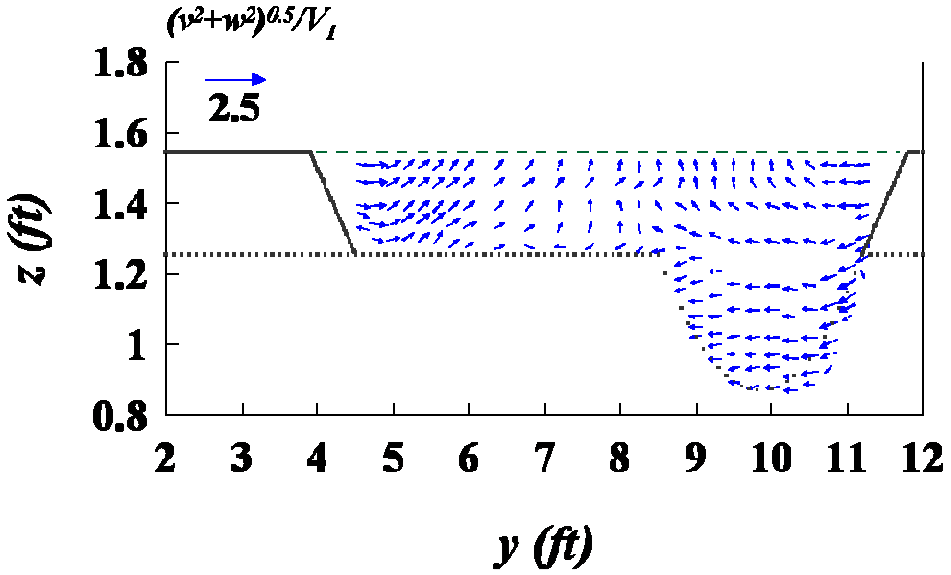

(b)

Figure 4.16 Cross-sectional velocity vectors measured at (a) C.S. 3 and (b) C.S. 4 for Run 3 normalized by approach flow velocity (L_a/B_f =0.53, flow type = OT)

As summarized in the previous chapter, local turbulence properties around the abutment in addition to flow contraction can be important factors in the local abutment scour process. To quantify the effect of local turbulence on abutment scour, three-

dimensional turbulence intensity and turbulent kinetic energy were measured with ADVs for the fixed bed. The measurements were conducted at five cross-sections, the locations of which are shown in Figure 4.2(from C.S. 2 to C.S. 6). In each cross-section, the turbulence intensity was measured along multiple vertical profiles, separated by 0.2 ft laterally in the floodplain and 0.25 ft laterally in the main channel, measuring turbulence intensities at three points (i.e., 5 mm above the bed and 20 and 40 percent of the approach flow depth from the bed).

Figure 4.18 shows vertical turbulent kinetic energy (i.e., TKE (K), $K = 0.5(<u'^2>+<v'^2>+<w'^2>)$ in which $sqrt<u'^2>, sqrt<v'^2>, and\ sqrt<w'^2>$ are longitudinal, transverse, and vertical turbulence intensities, respectively) profiles non-dimensionalized by the approach shear velocity, u_{*1}^2 for Run 1. The letter shown at the top of each subfigure corresponds to the location (i.e., the measurement point) in Figure 4.17.

As shown in Figure 4.18, at a given cross-section (from C.S. 3 to C.S. 6), the magnitude of the TKE increases in the downstream direction. In addition, in each vertical profile, the higher value of TKE was observed at the near-bed measurement. Because the value of the maximum TKE can be an important variable that accounts for the local turbulence effect associated with the vortex structure and the separated shear zone on the maximum scour around an abutment, the spatial distributions of the maximum TKE at a given cross section normalized by the approach flow shear velocity are given in Figures 4.19, 4.20, and 4.21 for Runs 1, 2, and 3, respectively, which represent flow types of F, SO, and OT. The TKE distributions are shown in each figure at five cross sections (CS2-

CS6). The values of the maximum TKE (K_b) were selected at the near-bed measurement from each vertical profile based on those presented in Figure 4.18. The K_b measured in the floodplain was normalized by the shear velocity in the approach flow floodplain section, and the K_b in the main channel was normalized by that of the approach flow main channel section.

For the long setback abutment (L_a/B_f = 0.53), in the free flow and the submerged orifice flow cases, the peak K_b/u_*^2 values in each lateral profile (see the upper right panels of Figures 4.19 and 4.20) moved towards the main channel for profiles measured farther downstream in the floodplain. However, in the overtopping case, peak K_b/u_*^2 values in each lateral profile moved away from the main channel (see the upper right panel of Figure 4.21) for profiles measured farther downstream. In contrast, for the bankline abutment, the peak K_b/u_*^2 values in each lateral profile remained at the main channel bank for profiles measured farther downstream from the abutment corner independently of the flow types (see the lower right panels of Figures 4.19, 4.20, and 4.21); interestingly, the position of the peak K_b/u_*^2 values followed the boundary of a recirculation zone that corresponded to the strong shear layer that may have been be responsible for the scour around the abutment.

When the scour hole initially formed around the abutment, riprap stones started to slide into the scour hole. The relocated riprap then covered and partially protected some portions of the scour region, causing the region of deepest scour to move farther downstream. Detailed explanations of the relocated riprap will be given in Chapter 5.

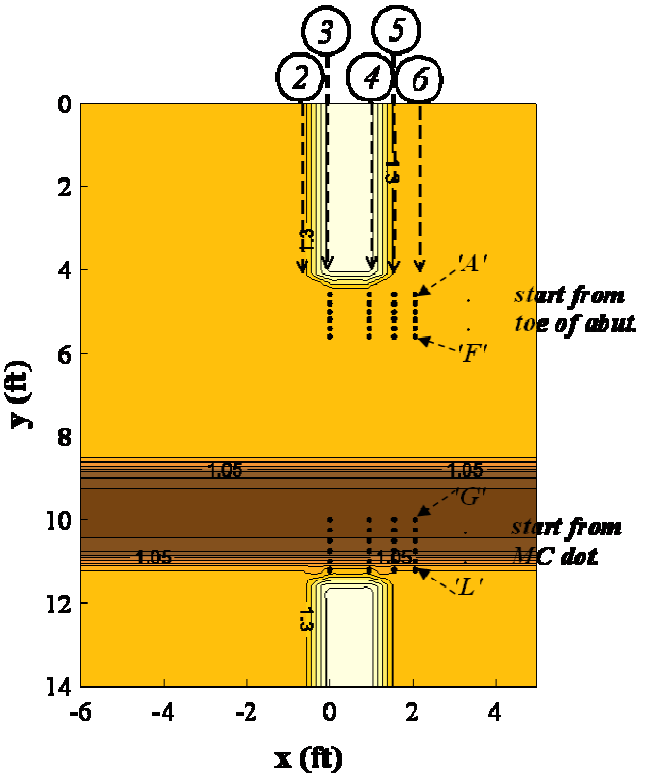

Figure 4.17 Locations of the turbulence measurement for Figure 4.18

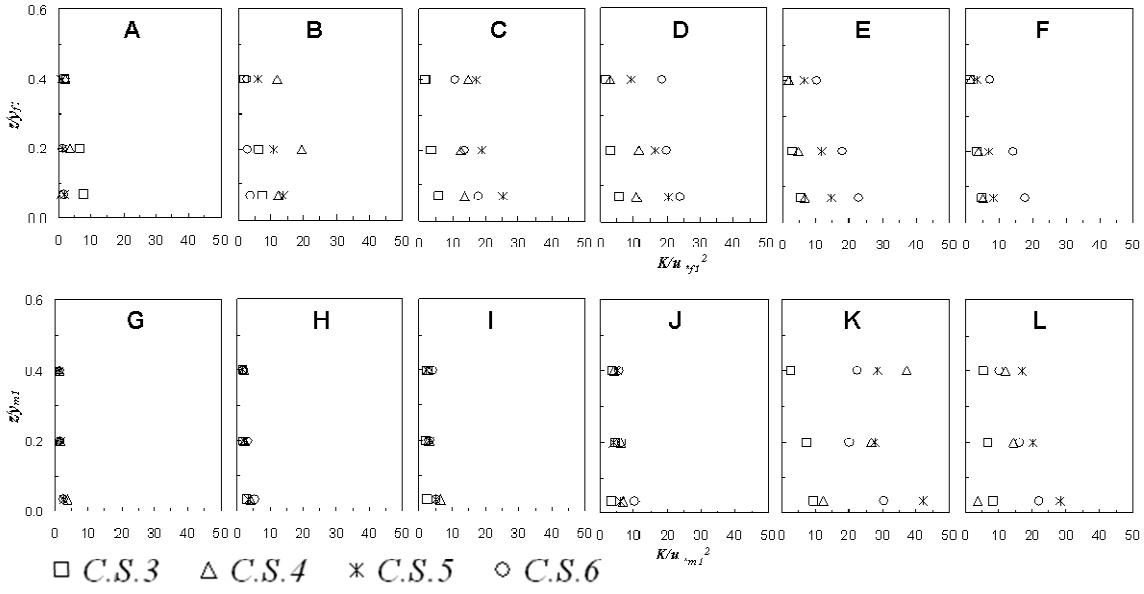

Figure 4.18 Example of turbulent kinetic energy profiles for Run 1

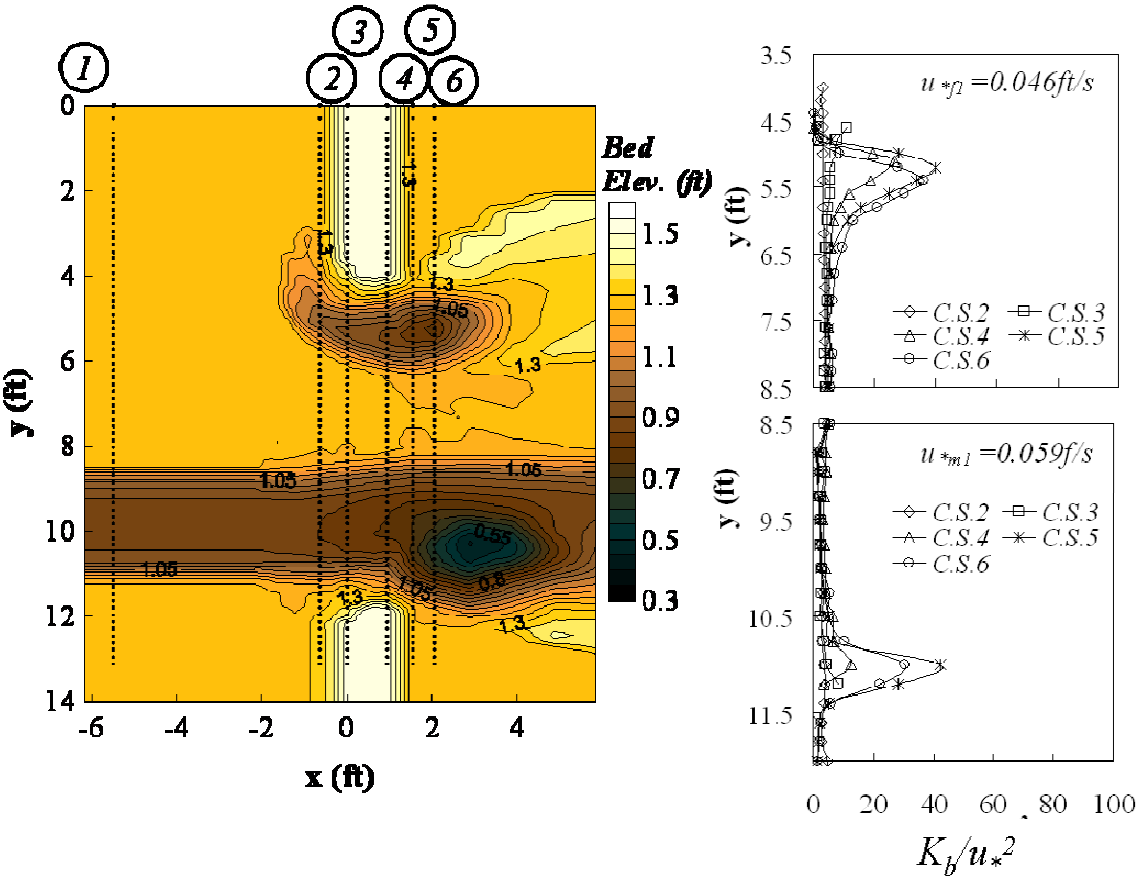

Figure 4.19 Final bed elevation picture and bed elevation contours in equilibrium condition and initial lateral turbulence kinetic energy profiles at the bed for Run 1 (L_a/B_f = 0.53, flow type = F)

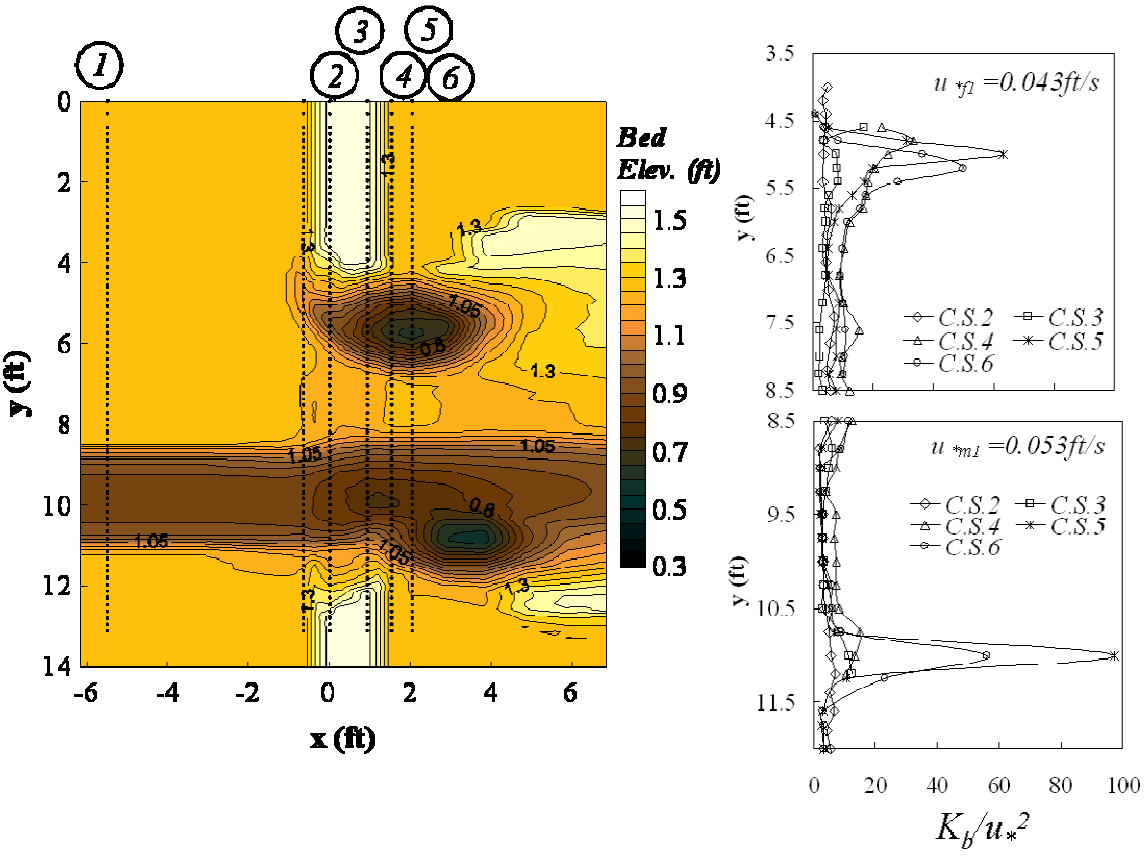

Figure 4.20 Final bed elevation picture and bed elevation contours in equilibrium condition and initial lateral turbulence kinetic energy profiles at the bed for Run 2 (L_a/B_f = 0.53, flow type = SO)

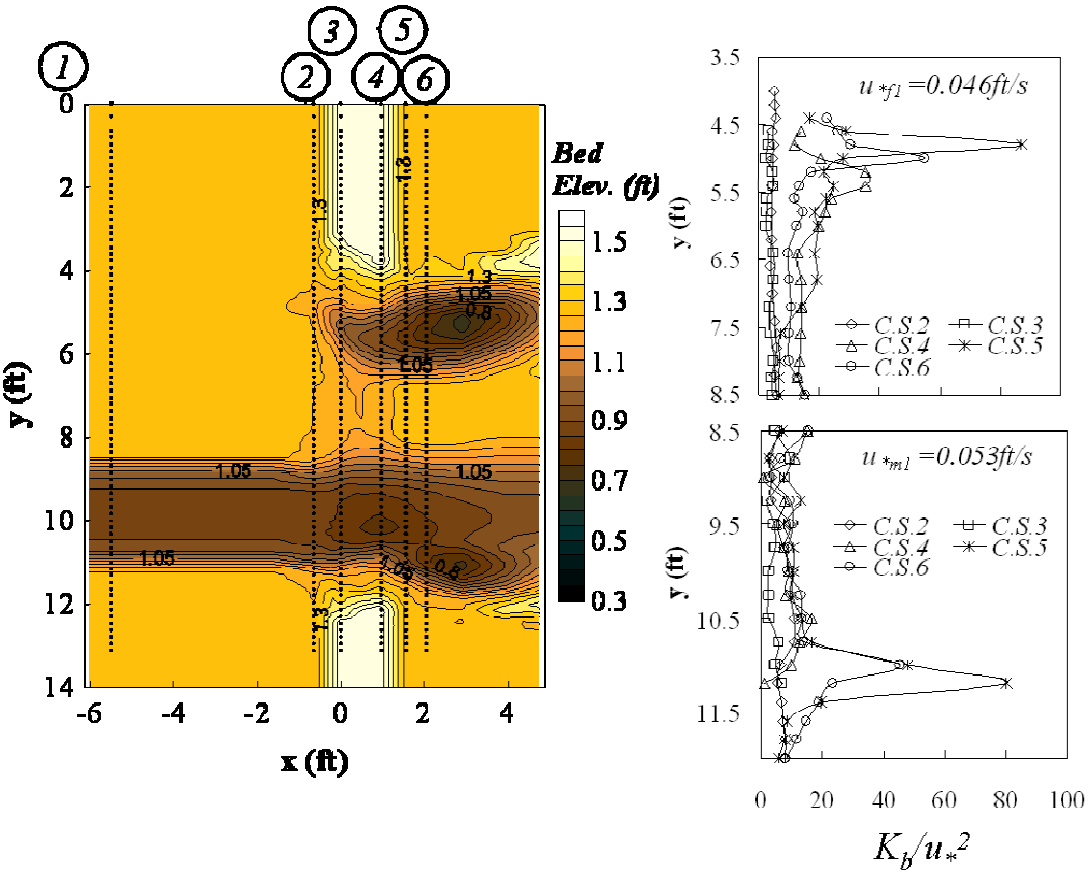

Figure 4.21 Final bed elevation picture and bed elevation contours in the equilibrium condition and initial lateral turbulence kinetic energy profiles at the bed for Run 3 (L_a/B_f = 0.53, flow type = OT)

4.5 *Experiments with Short Setback Abutments (Case C)*

The experimental conditions and results for the short setback abutment are shown in Table 4.6 in terms of approach floodplain variables as well as main channel variables, and the data are provided in dimensionless form in Table 4.7 with the same parameters mentioned in the previous section. Velocities are measured at the same cross-sections and with the same procedures as for the long setback abutments cases, as explained in the previous subsections.

Table 4.6 Summary of measured experimental data for the short setback abutment at the beginning of scour

Run	L_a/B_f	*Flow type*	Q	y_{f1}	V_{f1}	q_{f1}	*C.S.3* q_{f2}	*C.S.4* q_{f2}	y_{f0}	d_{max}
			cfs	Ft	ft/s	ft^2/s	ft^2/s	ft^2/s	ft	ft
13	0.88	F	2.6	0.257	0.481	0.120	0.348	0.357	0.220	0.719
14		SO	3.1	0.336	0.500	0.165	0.413	0.487	0.290	0.960
15		OT	4.6	0.488	0.572	0.278	0.359	0.392	0.457	0.629
16		F	2.2	0.254	0.418	0.103	0.297	0.302	0.220	0.564
17		SO	2.6	0.338	0.431	0.141	0.362	0.386	0.290	0.747
18		OT	3.9	0.479	0.514	0.242	0.324	0.355	0.457	0.458
Run	L_a/B_f	*Flow type*	Q	y_{m1}	V_{m1}	q_{m1}	q_{m2}	q_{m2}	y_{m0}	d_{max}
13	0.88	F	2.6	0.513	0.823	0.416	0.733	0.792	0.476	0.719
14		SO	3.1	0.592	0.764	0.451	0.801	0.880	0.546	0.960
15		OT	4.6	0.744	0.710	0.528	0.652	0.751	0.713	0.629
16		F	2.2	0.510	0.665	0.333	0.611	0.658	0.476	0.564
17		SO	2.6	0.594	0.644	0.377	0.674	0.717	0.546	0.747
18		OT	3.9	0.735	0.625	0.457	0.595	0.677	0.713	0.458

Note: Flow type: F=free flow; SO=submerged orifice flow; OT=overtopping flow

Table 4.7 Summary of dimensionless experimental data for the short setback abutment at the beginning of scour ($y_{max} = d_{max} + y_{f0}$)

Run	L_a/B_f	*Flow type*	$\frac{V_{f1}}{V_{fc1}}$	*C.S.3* $\frac{q_{f2}}{q_{f1}}$	*C.S.4* $\frac{q_{f2}}{q_{f1}}$	$\frac{y_{f1}}{y_{m1}}$	$\frac{Q_{ot}}{Q}$	$\frac{y_{f1}}{y_{f0}}$	$\frac{y_{max}}{y_{f1}}$	$\frac{y_{max}}{y_{f0}}$
13	0.88	F	0.44	2.900	2.975	0.39	0	1.17	3.654	4.268
14		SO	0.43	2.503	2.952	0.46	0	1.16	3.720	4.310
15		OT	0.47	1.291	1.410	0.55	0.461	1.07	2.225	2.376
16		F	0.38	2.883	2.932	0.39	0	1.15	3.087	3.564
17		SO	0.37	2.567	2.738	0.46	0	1.17	3.068	3.576
18		OT	0.42	1.339	1.467	0.55	0.430	1.05	1.910	2.002

Run	L_a/B_f	*Flow type*	$\frac{V_{m1}}{V_{mc1}}$	$\frac{q_{m2}}{q_{m1}}$	$\frac{q_{m2}}{q_{m1}}$	$\frac{y_{f1}}{y_{m1}}$	$\frac{Q_{ot}}{Q}$	$\frac{y_{m1}}{y_{m0}}$	$\frac{y_{max}}{y_{m1}}$	$\frac{y_{max}}{y_{m0}}$
13	0.88	F	0.69	1.762	1.904	0.39	0	1.08	1.830	1.973
14		SO	0.63	1.776	1.951	0.46	0	1.08	2.111	2.289
15		OT	0.57	1.235	1.422	0.55	0.461	1.04	1.460	1.523
16		F	0.55	1.835	1.976	0.39	0	1.07	1.537	1.647
17		SO	0.52	1.788	1.902	0.46	0	1.09	1.746	1.900
18		OT	0.50	1.302	1.481	0.55	0.430	1.03	1.245	1.283

Note: Flow type: F=free flow; SO=submerged orifice flow; OT=overtopping flow

For the short setback abutment (L_a/B_f = 0.88), the scour hole initially developed around the upstream corner of the abutment and then moved along the toe of the abutment in the floodplain, as shown in Figures 4.22, 4.23, and 4.24. However, as the scour hole elongated diagonally from the face of the abutment over time after approximately two to three hours, the resulting point of maximum scour hole depth

terminated at the bankline of the main channel while the maximum equilibrium scour depth was located inside the main channel on the bank side slope. Typically, the approach floodplain flow depth (y_{f1}) and the approach floodplain flow velocity (V_{f1}) can be taken as the characteristic length and velocity scales, respectively, for the long setback abutment. However, approach flow floodplain variables as well as approach flow main channel variables might be characteristic scales for the short setback abutment because the point of maximum scour depth moved from the floodplain to the bankline of the main channel after a short time (less than 2 hours), and terminated inside of the main channel in the equilibrium state.

For the bankline abutment on the right floodplain, maximum scour depth occurred in the bottom of the main channel near the toe of the right bank and at nearly the same distance downstream of the bridge as for the left abutment in the case of free flow and submerged orifice flow. In fact, there appears to be interaction between the two scour holes from the left and right abutments for these two flow cases. However, for the overtopping case, not only was the maximum depth of scour due to the right abutment considerably less, but it was located under the bridge on the bed of the main channel because the vertical flow contraction was less under the bridge in the main channel when overtopping occurred.

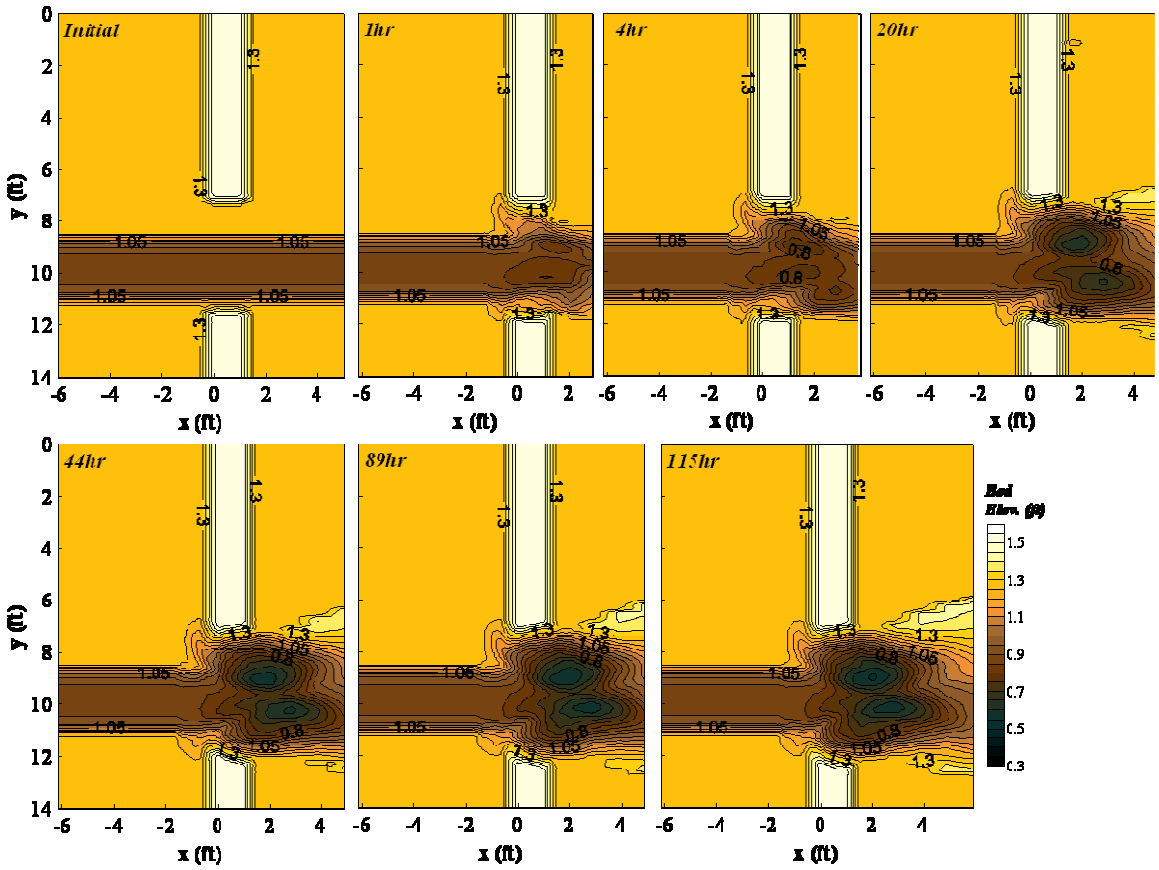

Figure 4.22 Time development of scour for Run 13 (L_a/B_f = 0.88, flow type = F)

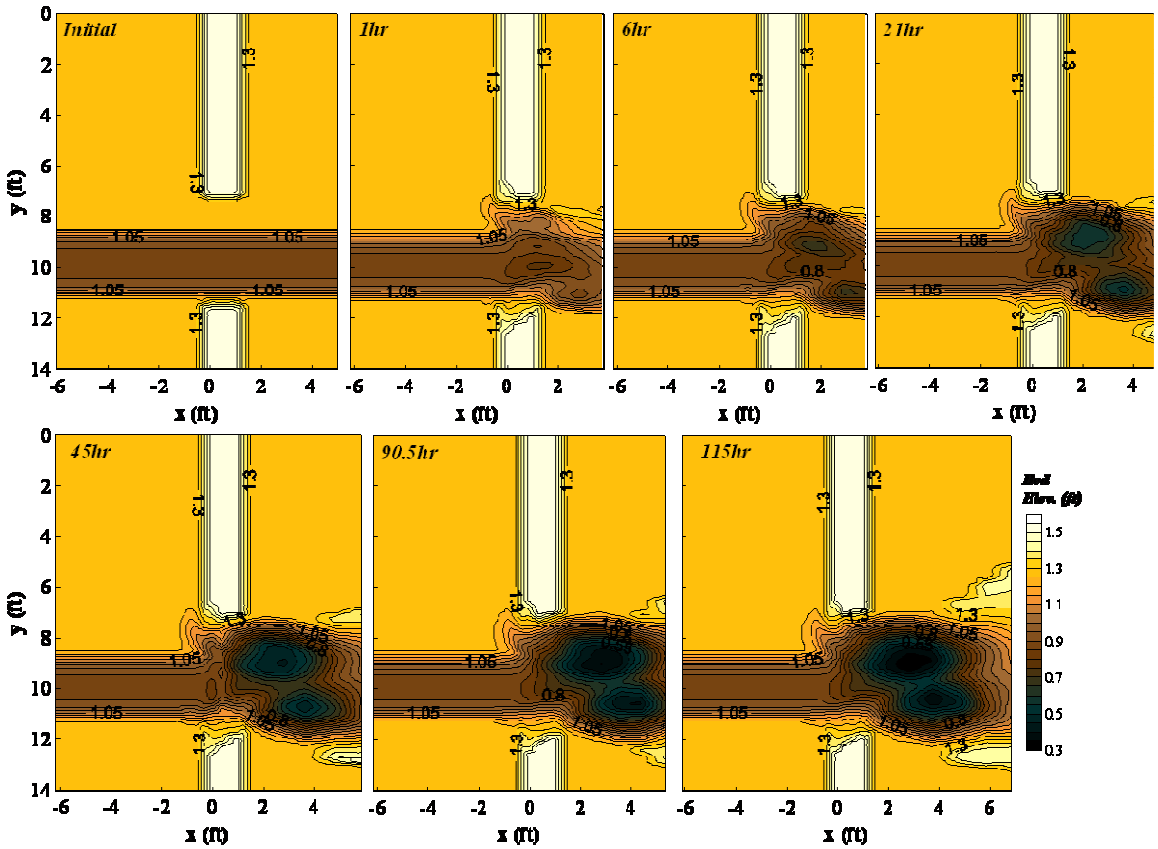

Figure 4.23 Time development of scour for Run 14 (L_a/B_f = 0.88, flow type = SO)

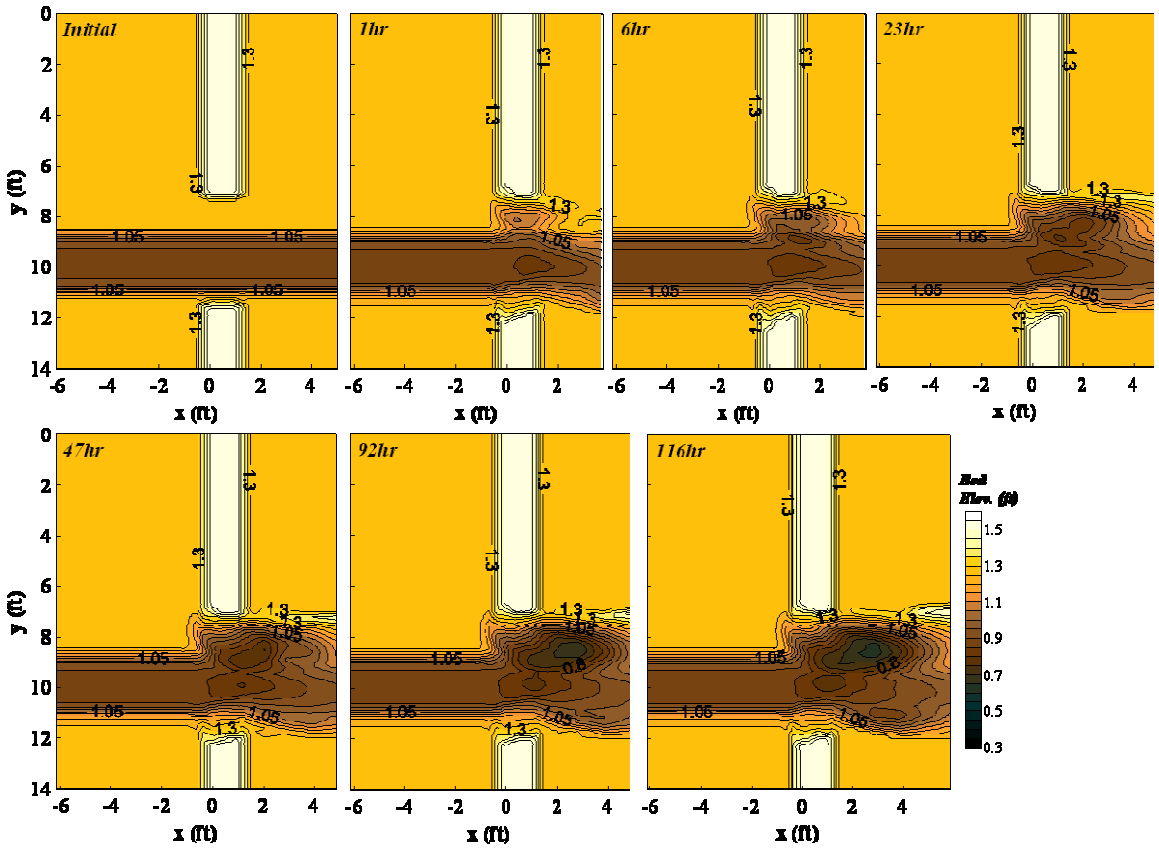

Figure 4.24 Time development of scour for Run 15 (L_a/B_f = 0.88, flow type = OT)

4.5.1 *Velocity Measurements*

The depth-averaged velocities in the approach cross section and in the bridge section for short setback abutment cases were determined by the same procedures as for the long setback abutment cases as explained previous section. Figure 4.25 shows the approach flow depth-averaged velocity distributions measured at a cross section 10 ft upstream of the bridge for Runs 12, 13, and 14. The velocities were higher in the main channel than the floodplain, as expected for an overbank flow, but the relative difference

decreased as discharge increased.

Figure 4.26 shows depth-averaged velocity distributions measured at the bridge sections (i.e. C.S. 3 and C.S. 4) for Run 14. The velocities were higher in the downstream cross section than in the upstream cross section because of the lateral and vertical contraction of the streamlines through the bridge. In the near field of the abutment at C.S. 4, the value of velocities show almost zero because of the downstream recirculation.

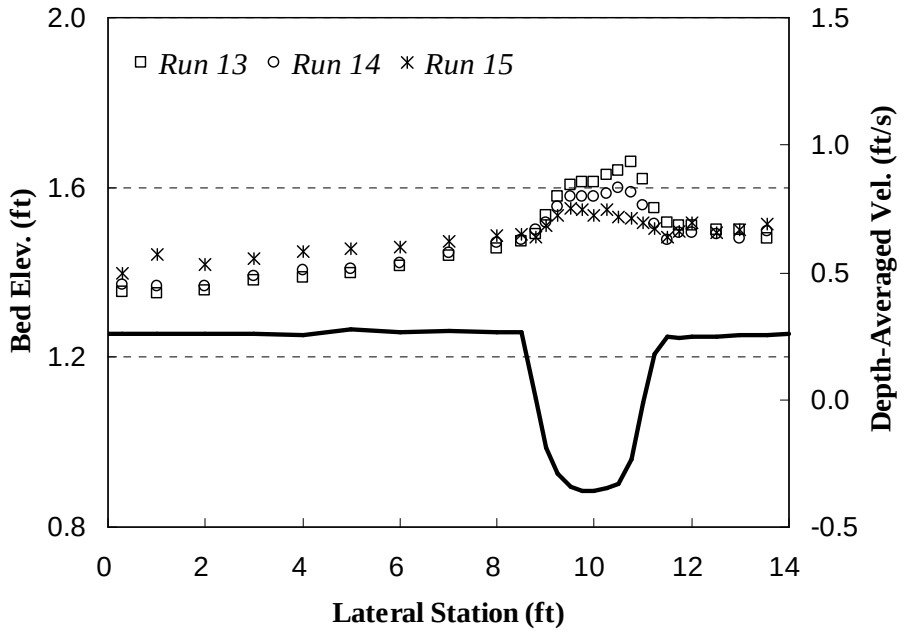

Figure 4.25 Approach flow velocity distributions for Runs 13, 14, and 15

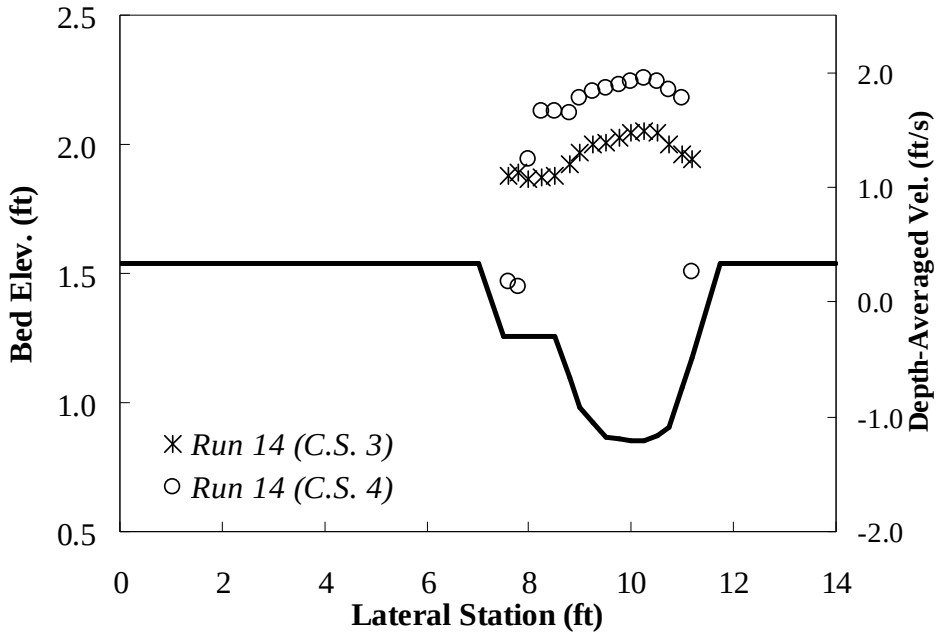

Figure 4.26 Velocity distributions at a bridge section for Run 14 (L_a/B_f = 0.88, flow type = SO)

4.5.2 *Time Development of Abutment Scour*

Figures 4.27 and 4.28 present selected temporal changes of the maximum scour depth in terms of real time on a semi-logarithmic scale for the short setback abutment and for the bankline abutment, respectively (Runs 13, 14, and 15). Similar to the experimental results shown in the previous section (i.e., time development in the long setback abutment), the scour depth rapidly changed at the initial stage, and the rate of scouring became smaller with time. However, it is interesting to note that a secondary slope change was observed in Runs 14 and 15 for the short setback abutment and Run 13 for the bankline abutment during a particular time period (5 to 50 hrs). As shown in Figures 4.22, 4.23, and 4.24, the scour holes initially developed around the downstream corners of both abutments and

in the center of the main channel due to a severe contraction. As the experiment continued, the scour holes around the abutment grew and converged to the main channel scour hole from the right abutment. After the convergence, the scour depth increased more rapidly as shown in Figures 4.22, 4.23, and 4.24. The slope of the curve is dependent on the effect of the depth and intensity of flow, the length of the embankment/abutment, and other factors. Detailed analysis of the temporal development of the short setback abutment scour hole will be discussed in Chapter 5.

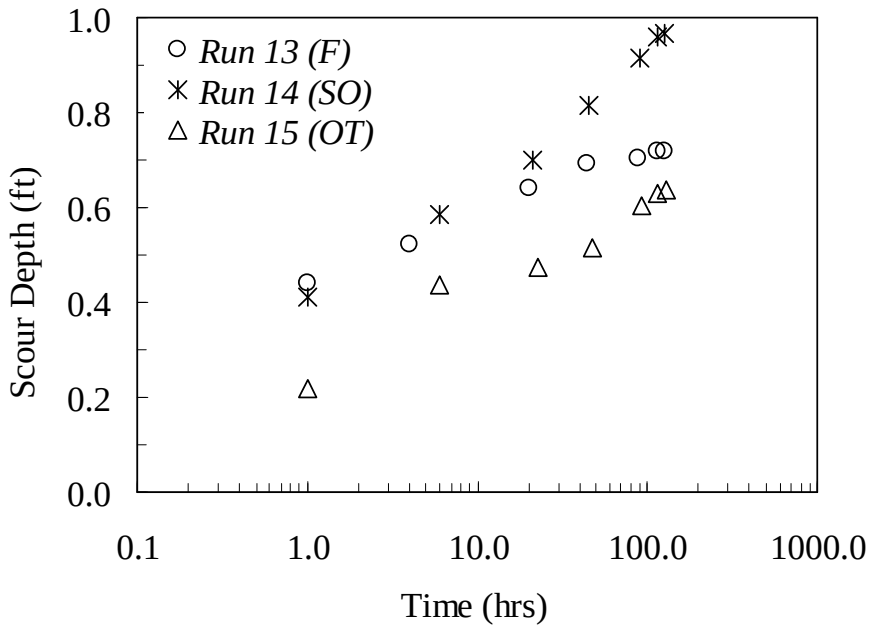

Figure 4.27 Time development of scour depth for the bankline abutment (L_a/B_f = 0.88)

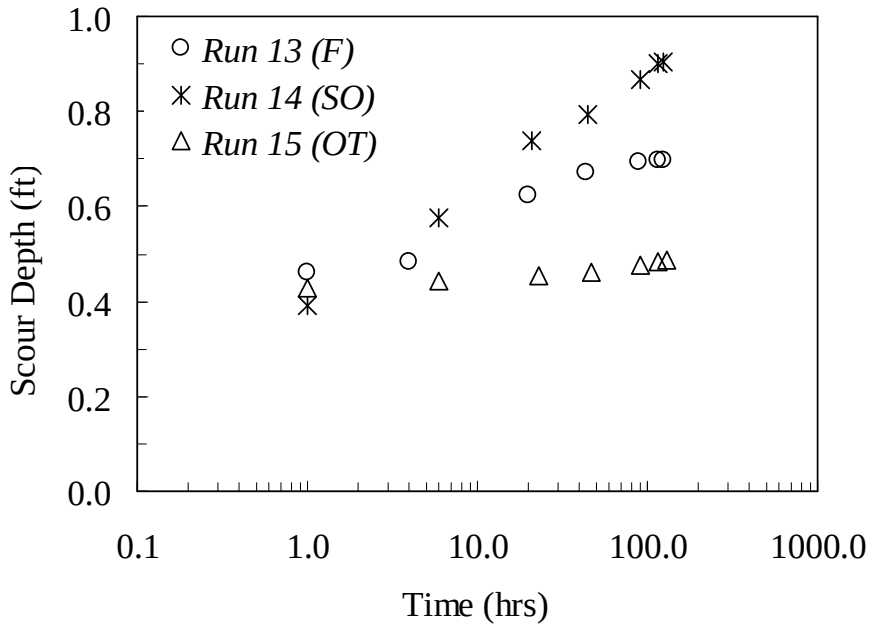

Figure 4.28 Time development of scour depth for the bankline abutment (L_a/B_f = 1.0)

4.5.3 *Measurement of Water Surface Profiles*

Figure 4.29 shows the water surface profile plot for experimental Runs 13, 14, and 15. In all three cases, the effect of back water was observed, but it was not significant (i.e., 1.02 $< y_{f1}/y_{f\ un-obst} <$1.03, in which $y_{f\ un-obst}$ is the un-obstructed floodplain water depth).

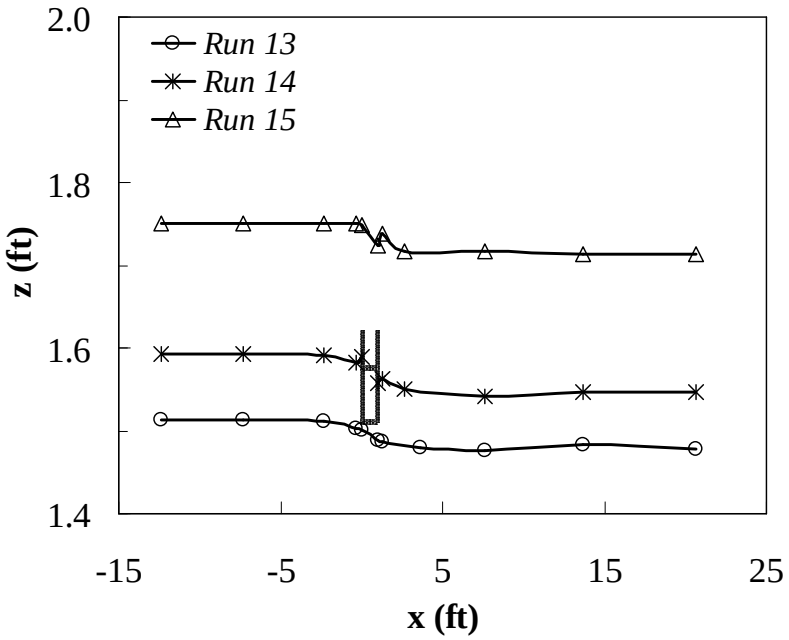

Figure 4.29 Averaged water surface profiles along the flow direction for Runs 13, 14, and 15 (L_a/B_f = 0.88)

4.5.4 *Velocity and Turbulence Flow Field Around the Short Setback Abutment*

Velocities were measured at a height of 5 mm above the fixed bed around the bridge for the short setback abutments. The measured near-field velocity vectors superimposed on initial and final bed elevation contours are shown in Figures 4.30, 4.31, and 4.32 for Runs 13, 14, and 15, respectively. For the free flow case (Run 13) and the submerged orifice case (Run 14), a larger recirculation zone occurred downstream of the separation point on the short setback abutment compared to the long setback abutment because of higher flow contraction. Higher velocities were measured just outside of the recicrulation region, where deeper scour occurred. However, for the overtopping case, the flow separation

point and the recirculation region was located farther downstream of the abutment because of the overtopping discharge, and the resulting scour hole elongated in the streamwise direction, which is a very similar flow pattern to that for the long setback abutment.

Three-dimensional turbulence intensities and turbulent kinetic energy were also measured with the ADV in the same cross-sections for the short setback abutment in the same way as they were for the fixed bed of the long setback abutment. The spatial distributions of the maximum TKE normalized by the approach main channel shear velocity (K_b/u_*^2) for each cross section were plotted for five cross sections in the streamwise direction in Figures 4.33, 4.34, and 4.35.

For the short setback abutment, the peak K_b/u_*^2 values in each lateral profile moved towards the main channel for profiles measured farther downstream (see the lower right panels of Figures 4.33 and 4.34) in free and submerged orifice flow similar to the measurements in the long setback abutment, but the amount of shifting was small compared to that of the long setback abutment. The small amount of shifting was probably due to the combination effect of the left setback abutment and the right bankline abutment because of the short setback distance. For the overtopping case, peak K_b/u_*^2 values taken in the floodplain moved away from the main channel for profiles taken farther downstream (see the lower right panel of Figure 4.35), and this phenomenon was similar to that of the overtopping case in the long setback abutment.

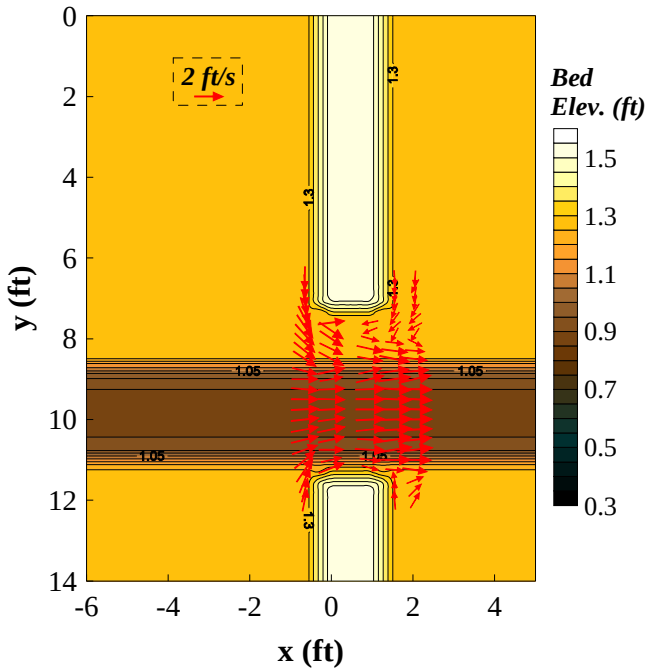

(a)

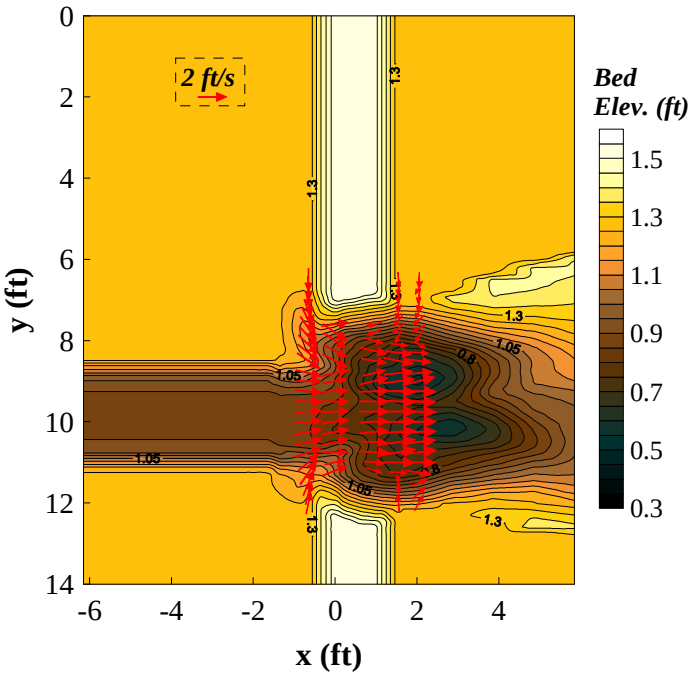

(b)

Figure 4.30 Initial velocity vectors measured at 0.5 mm above the fixed bed for Run 13 superimposed on (a) initial contours and (b) final contours (L_a/B_f = 0.88, flow type = F)

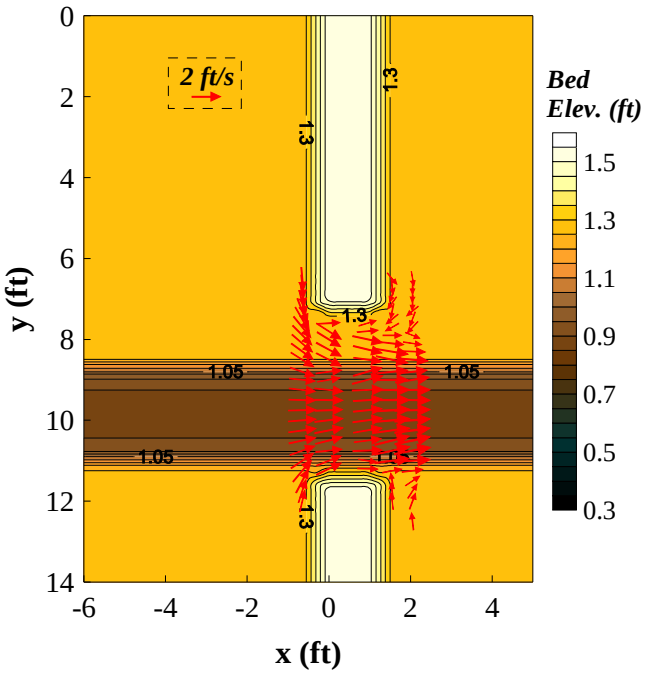

(a)

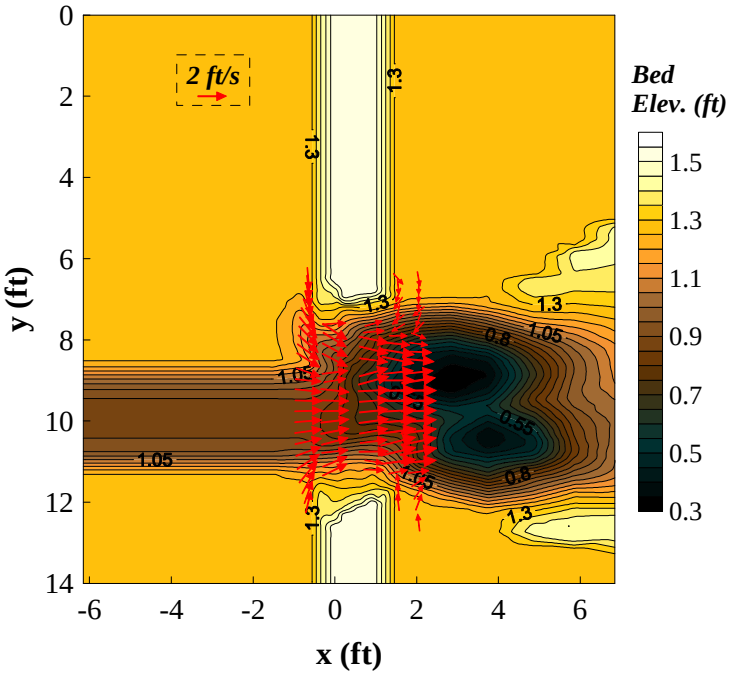

(b)

Figure 4.31 Initial velocity vectors measured at 0.5 mm above the fixed bed for Run 14 superimposed on (a) initial contours and (b) final contours (L_a/B_f = 0.88, flow type = SO)

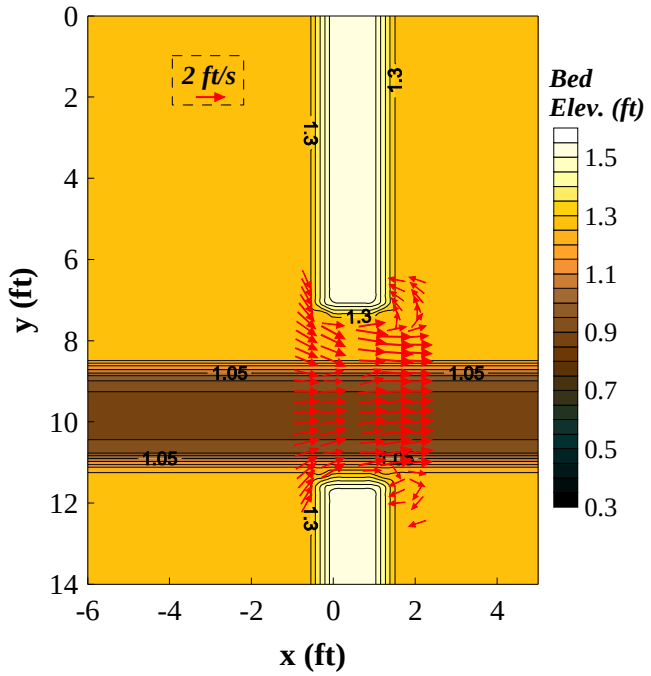

(a)

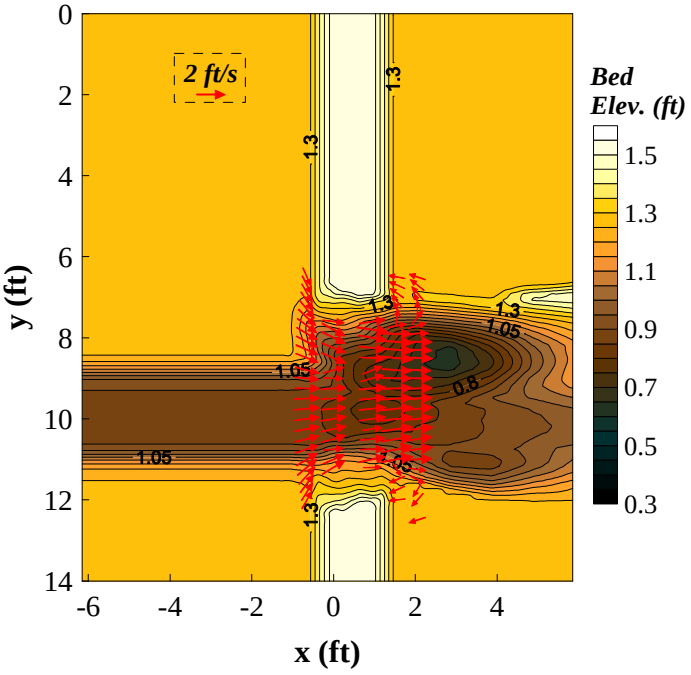

(b)

Figure 4.32 Initial velocity vectors measured at 0.5 mm above the fixed bed for Run 15 superimposed on (a) initial contours and (b) final contours (L_a/B_f = 0.88, flow type = OT)

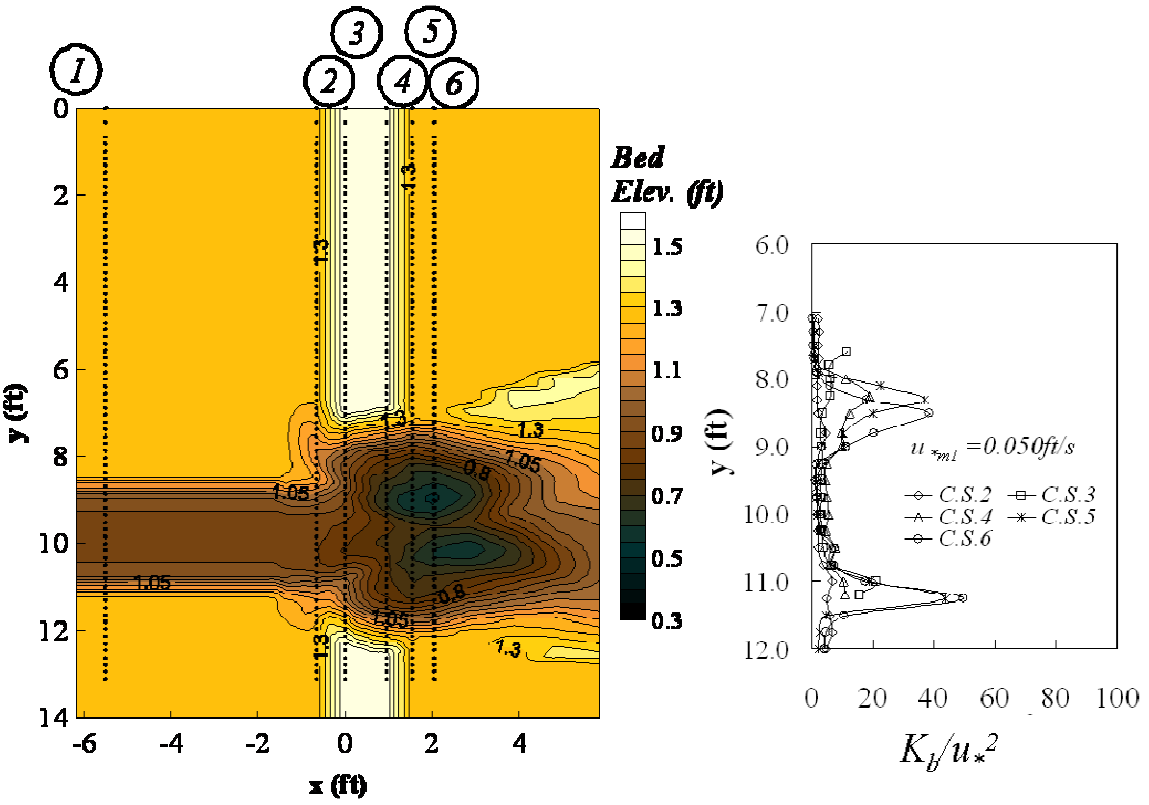

Figure 4.33 Final bed elevation picture and bed elevation contours in equilibrium condition and initial lateral turbulence kinetic energy profiles at the bed for Run 13 (L_a/B_f = 0.88, flow type = F)

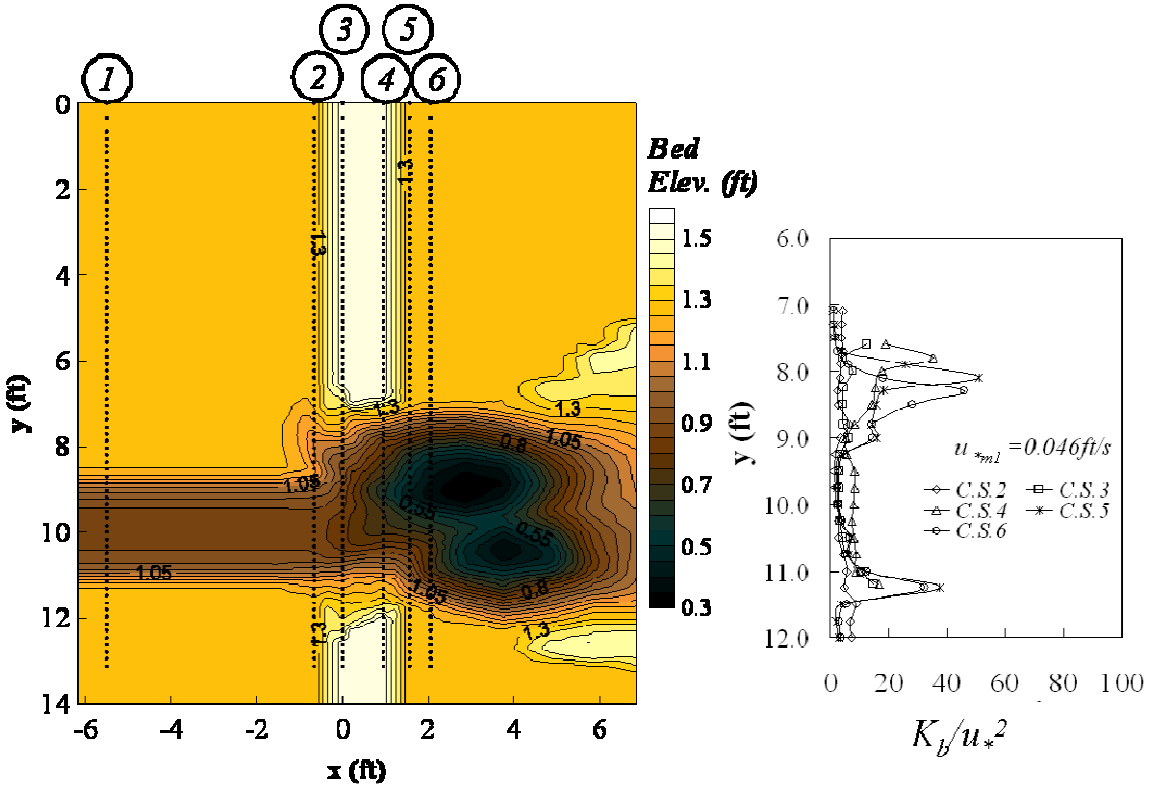

Figure 4.34 Final bed elevation picture and bed elevation contours in equilibrium condition and initial lateral turbulence kinetic energy profiles at the bed for Run 14 (L_a/B_f = 0.88, flow type = SO)

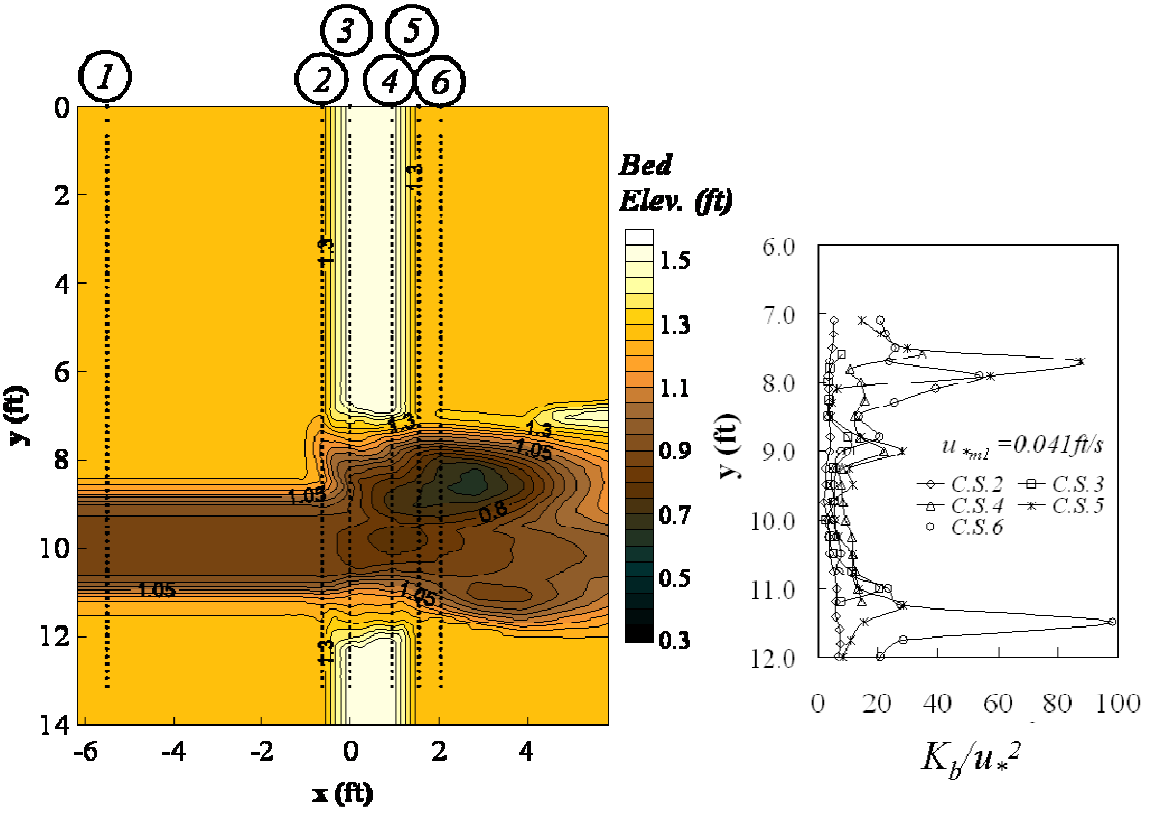

Figure 4.35 Final bed elevation picture and bed elevation contours in equilibrium condition and initial lateral turbulence kinetic energy profiles at the bed for Run 15 (L_a/B_f = 0.88, flow type= OT)

CHAPTER V

ANALYSIS OF EXPERIMENTAL RESULTS

5.1 *Introduction*

In this chapter, the laboratory results for the temporal development of abutment scour and for the maximum abutment scour depths are analyzed in terms of dimensionless variables to explain the effect of each dimensionless parameter on abutment scour. Then the effects of local turbulence structures on abutment scour are discussed in terms of turbulent kinetic energy (TKE) profiles measured for a wide range of flow contraction ratios. Based on laboratory data collected in this study, an abutment scour formula for maximum scour depth for all three flow types (F, SO, OT) is suggested for verification purposes, and then it is compared and applied to other data from several investigations conducted under different experimental conditions.

5.2 *Dimensional Analysis*

The significant parameters affecting scour at a bridge abutment found in a compound channel are obtained by dimensional analysis as shown in Chapter 2 (See Equation 2.20). With reference to Figure 2.9, which shows a setback abutment for a compound channel, the equilibrium clear-water scour is reached when the velocity in the contracted section has approached its critical value such that $V_2 = V_{cf2}$. From continuity,

$$y_{f2_c} = \frac{q_{f2}}{V_{cf2}}, \tag{5.1}$$

where y_{f2_c} is the equilibrium contraction scour depth in the contracted section after scour and q_{f2} is the discharge per unit width in the floodplain of the contracted section. Expressing the critical velocity in terms of Manning's equation with Manning's n expressed in terms of a Strickler-type expression, the result is given by

$$V_{cf2} = \frac{K_n}{c_n}\sqrt{(SG-1)\tau_{*c}}\, d_{50}^{1/3}\, y_{f2c}^{1/6}. \tag{5.2}$$

where V_{cf_2} and $y_{f_{2c}}$ are the critical velocity and the flow depth at equilibrium scour, respectively; K_n is 1.0, or 1.49 in Manning's equation, for SI, or English units; c_n is a Strickler constant of proportionality for the relationship between Manning's n and $d_{50}^{1/6}$; SG is the specific gravity of the sediment; τ_{*c} is the critical value of the Shields parameter, and d_{50} is the median grain diameter. From Equation 5.2, the ratio of critical velocity, V_{cf1}, which corresponds to the approach flow water depth y_{f1}, to V_{cf2} is proportional to the depth ratio $\left(y_{f1}/y_{f2c}\right)^{1/6}$. As a result, Equation 5.1 can be rearranged to yield

$$\frac{y_{f2c}}{y_{f1}} = \left(\frac{q_{f2}}{V_{cf1}\, y_{f1}}\right)^{6/7} = \left(\frac{V_{f1}}{V_{cf1}}\right)^{6/7}\left(\frac{q_{f2}}{q_{f1}}\right)^{6/7}. \tag{5.3}$$

If it is assumed that the local abutment scour is a local amplification of contraction scour, Equation 5.3 becomes

$$\frac{y_{2\max}}{y_1} = r_T \left(\left(\frac{V_1}{V_{c1}} \right)^{6/7} \left(\frac{q_2}{q_1} \right)^{6/7} \right), \tag{5.4}$$

where $y_{2\max}$ is the maximum water depth at the location of maximum scour around an abutment and r_T is a term that accounts for the local turbulence effects that contribute to additional scour and can be determined from experiments. If significant backwater effects are expected for the design of a bridge, the backwater effect should be taken into account. For example, when the amount of obstructed discharge in the approach flow over a length equal to the abutment length is significant compared to the total discharge, the backwater may not be negligible. The dimensionless variable, y_1/y_0, which reflects the effect of backwater (Sturm 2009), is multiplied on both sides of Equation 5.4, yielding

$$\frac{y_{2\max}}{y_0} = r_T \left(\frac{y_1}{y_0} \right) \left(\left(\frac{V_1}{V_{c1}} \right)^{6/7} \left(\frac{q_2}{q_1} \right)^{6/7} \right). \tag{5.5}$$

in which y_0 is the unobstructed flow depth at the bridge based on the tailwater elevation. If a significant backwater effect is expected for the design of a bridge, y_0 should be used for the reference depth, and if a back water effect is not significant, approach water depth y_1 can be used for the reference depth instead of y_0 in Equation 5.5 because the

value of y_1/y_0 is close to 1.

5.3 *Time Development of Abutment Scour*

The first step towards a more thorough understanding of the complex flow physics and resulting sediment transport around an abutment is to observe the scour process over time. The time development of scour around abutments was measured at six intermediate time durations. Figures 5.1, 5.2, and 5.3 show measured contours over time in the free, submerged orifice and overtopping flow cases for the long setback and the bankline abutments. For the long setback abutment, a scour hole initially developed around the upstream corner and then progressed along the toe of the abutment with scoured sand accumulating at the downstream corner of the abutment. After approximately ten hours, the region of deepest scour and the deposition area of sand moved downstream from the abutment. In the initial part of the experiment (0-10 hours), the side slope of the abutment became unstable, and riprap stones from the side slope started to slide into the scour hole. The relocated riprap then covered and partially protected the upstream and left side (when looking downstream) portions of the scour region, causing the region of deepest scour to move farther downstream. As the experiment continued (10-30 hours), the maximum scour depth increased; however, the location of deepest scour remained at the downstream corner of the abutment, where flow contraction was the greatest. After approximately 100 hours, the equilibrium scour depth was reached.

For the bankline abutment, a scour hole initially formed in the main channel just

off the toe of the abutment, and then the side slope of the abutment became unstable, causing the riprap stones to slump diagonally downstream in the main channel after a short time (less than one hour). Once settled, the slumped riprap produced a newly covered area at the side slope of the main channel with a characteristically-rounded shape. As the experiment continued, the scour hole around the slumped riprap grew and moved farther downstream. A similar phenomenon occurred for the setback abutment; however, higher velocity in the main channel added a downstream deflection of the riprap for the bankline abutment. In addition, after approximately one hour, another scour hole formed on the main channel bank downstream of the abutment. Because the newly developed slumped riprap area behaved like a submerged solid dune, the observed flow types were very similar to the flow over a dune or the flow over a backward facing step. The flow separated at the crest of the dune, causing a recirculation region downstream of the crest and reattachment, e.g., a splatting event that is expected to be responsible for the scour (Stoesser et al, 2008). As scour of the downstream side of the bankline abutment progressed (1-100 hours), the maximum scour depth increased; however, the location of deepest scour remained on the main channel bank on the downstream side of the abutment. It also required about 100 hours before reaching equilibrium scour depth.

As a result, two equilibrium scour holes were developed for the bankline abutment inside of the main channel just off the abutment and on the main channel bank downstream from the abutment, as shown in Figures 5.2 and 5.3. However, for the free flow case (shown in Figure 5.1), the two scour holes around the bankline abutment merged after approximately 20 hours because of the higher flow contraction ratio (the

higher value of q_{m2}/q_{m1} in Table 4.4). Although some experimental results showed two equilibrium scour holes around the bankline abutment and some others had only one scour hole, depending on the value of the flow contraction ratio, the maximum scour hole for the bankline abutment was located on the main channel bank at the downstream side of the abutment in all cases. Time development of abutment scour hole shows similar for the other runs and the figures can be found in the Appendix.

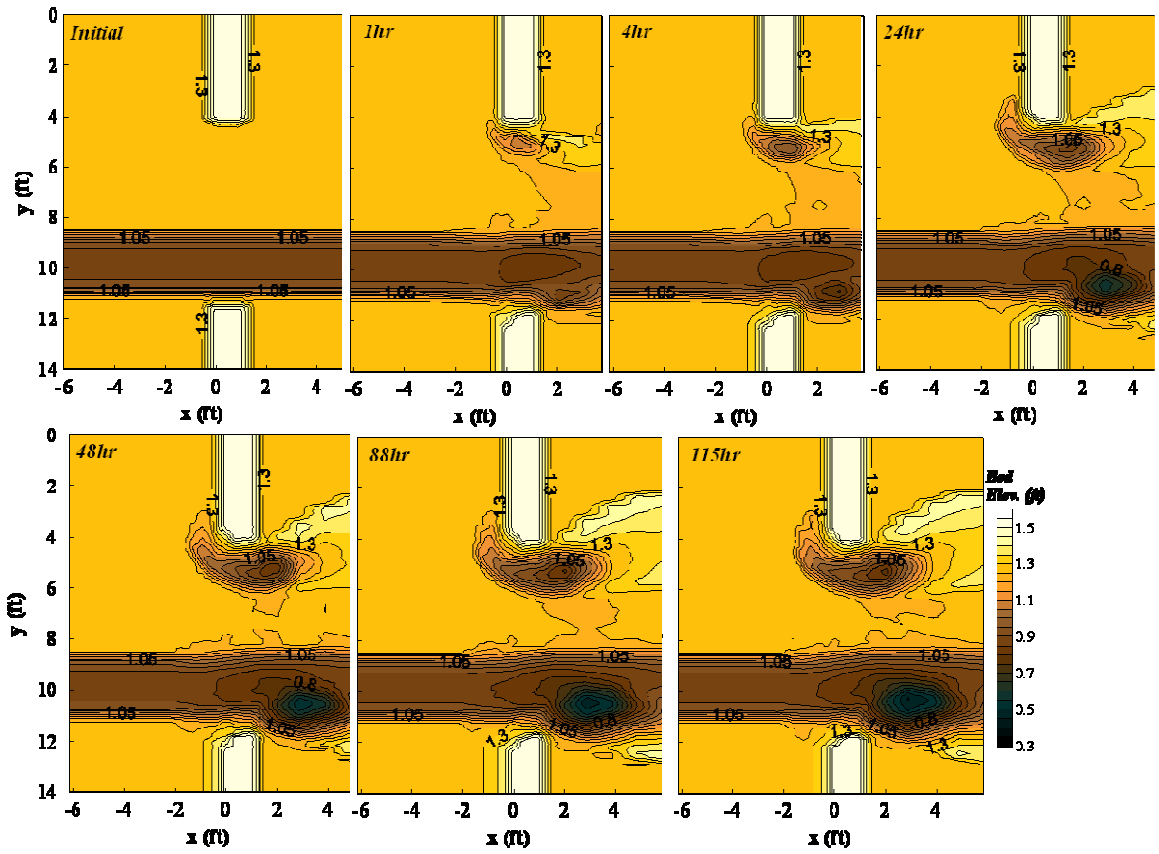

Figure 5.1 Time development of scour for Run 1 (L_a/B_f = 0.53, flow type = F)

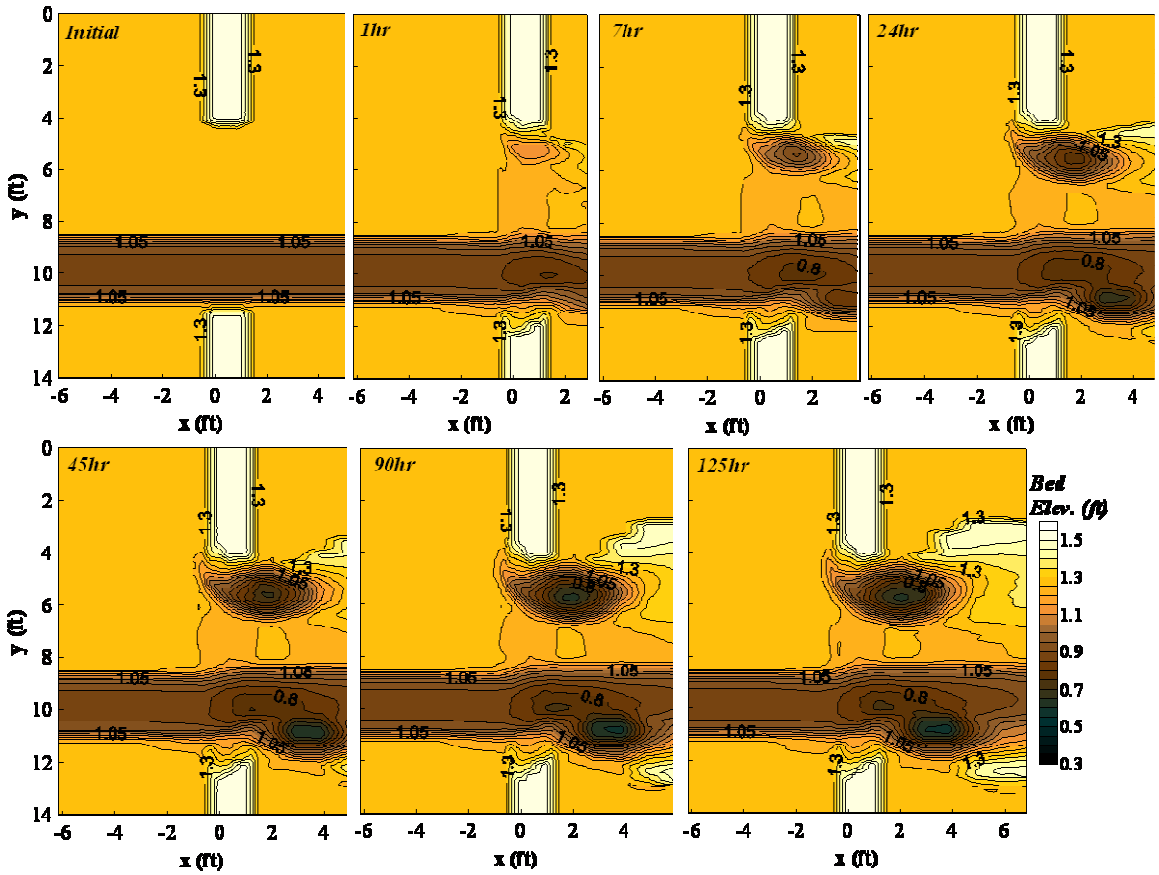

Figure 5.2 Time development of scour for Run 2 (L_a/B_f = 0.53, flow type = SO)

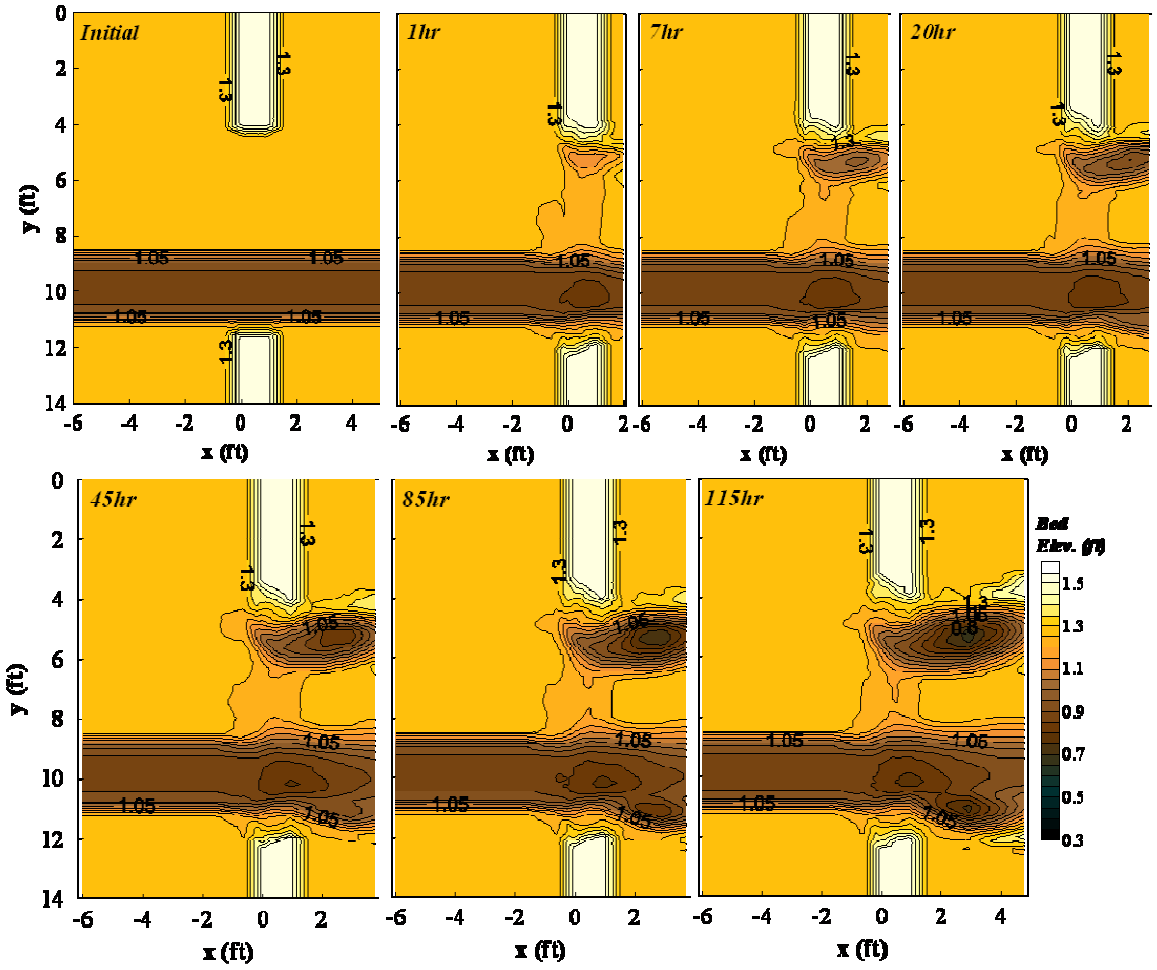

Figure 5.3 Time development of scour for Run 3 (L_a/B_f = 0.53, flow type = OT)

For the short setback abutment, the scour process (shown in Figures 4.22, 4.23, and 4.24) exhibited patterns similar to that for the long setback abutment as described in the previous paragraph. The only difference was the movement of the location of the point of maximum scour from the floodplain to the main channel over time. Scour holes initially developed around the downstream corners of a short setback abutment and a bankline abutment, and one other scour hole occurred in the center of the main channel. As the experiment continued, the scour holes around the two abutments became larger

and captured the scour hole located in the main channel. It is interesting to note that the scour hole located in the center of the main channel converged to the short setback abutment scour hole for Run 13 (flow type = F) and to the bankline abutment scour hole for Run 14 (flow type = SO). For overtopping flow in Run 15, the scour hole due to the short setback abutment was deeper and more dominant than the one caused by the bankline abutment.

5.3.1 *Time Development of Scour Around the Long Setback and Bankline Abutments*

Figures 5.4, 5.5, and 5.6 show the development of scour depth with time for free (F), submerged orifice (SO), and overtopping (OT) flow conditions, respectively, in terms of dimensionless form according to the dimensional analysis and $(q_{f2}/q_{f1})(V_{f1}/V_{cf1})$ as a third parameter based on the modified long-contraction scour theory as described in Equation 5.3. In Figure 5.7, the curves in each figure are combined to show the effect of different flow types on the time development of the abutment scour depth. The scour depth normalized by the approach water depth follows a linear trend with the logarithm of the dimensionless time variable (average R^2 is 0.98), $V_{f1}t/y_{f1}$, and then reaches equilibrium after a certain time. Observations from Figures 5.4, 5.5, and 5.6 suggest that the slopes of the time development of abutment scour in free and submerged orifice flow are independent of the value of $(q_{f2}/q_{f1})(V_{f1}/V_{cf1})$.

It is also clear that the normalized equilibrium scour depth is a function of

$(q_{f2}/q_{f1})(V_{f1}/V_{cf1})$, as suggested in the dimensional analysis. Generally, when the value of $(q_{f2}/q_{f1})(V_{f1}/V_{cf1})$ increased, the normalized equilibrium scour depth also increased. However, some cases show that the higher value of $(q_{f2}/q_{f1})(V_{f1}/V_{cf1})$ resulted in a lower value of equilibrium scour depth because of different effects of local turbulence for different lengths of the abutment. Furthermore, comparing the results from the different flow types is difficult because the local turbulence term (r_T), which directly relates to the maximum scour depth around the abutment, varies depending on the different flow types. For example, the normalized equilibrium scour depth in the free flow case (the first black line in Figure 5.7) shows a larger value than that in the pressure flow case (the first red line in Figure 5.7) even though the two cases have the same value of $(q_{f2}/q_{f1})(V_{f1}/V_{cf1})$. The effect of the turbulence term will be explained in more detail in the next section.

Time (T_{eq}) required to reach equilibrium clear water scour is summarized in Table 5.1 in dimensionless form. Figure 5.8 shows the relationship between dimensionless time and the value of $(q_2/q_1)(V_1/V_{c1})$ for different flow conditions. As shown in Figure 5.8, the dimensionless equilibrium time is slightly related to the third parameter, $(q_2/q_1)(V_1/V_{c1})$, in a clear water condition when a comparison of the same flow type is conducted. When the value of $(q_2/q_1)(V_1/V_{c1})$ increased, the dimensionless time to reach equilibrium also increased slightly. However, the data are insufficient, and the range of $(q_2/q_1)(V_1/V_{c1})$ is too small to determine a comprehensive relationship for the dimensionless equilibrium time. Additional experiments could establish a general relationship for the equilibrium time. The most that can be concluded from Table 5.1 is

that $V_1 T_{eq} / y_1 \le 1*10^6$ for all abutment length and flow types with a minimum value of about $5*10^5$.

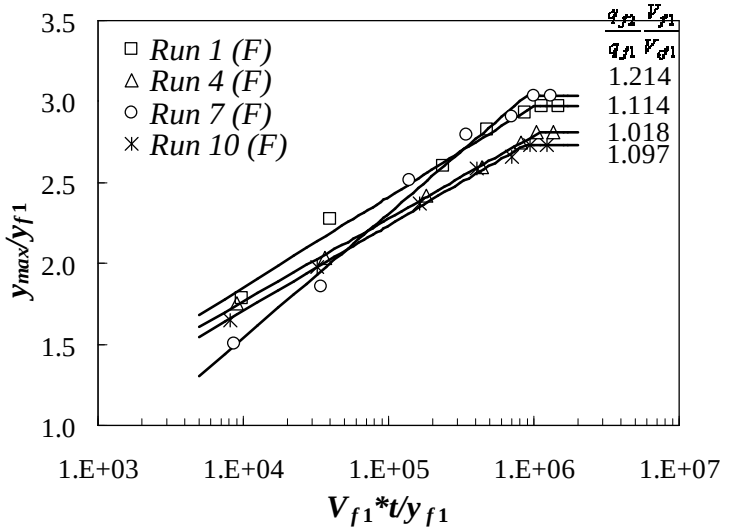

Figure 5.4 Time development of the abutment scour depth in dimensionless form with parameter $(q_{f2}/q_{f1})(V_{f1}/V_{cf1})$ for free flow cases

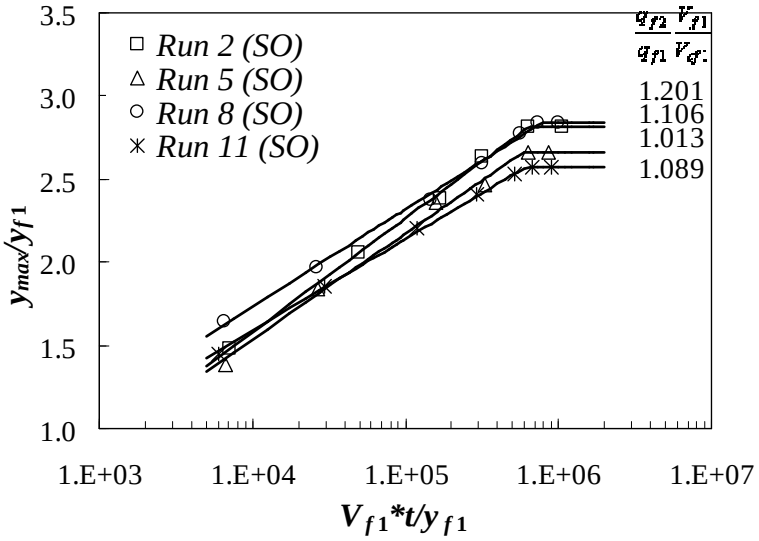

Figure 5.5 Time development of the abutment scour depth in dimensionless form with parameter $(q_{f2}/q_{f1})(V_{f1}/V_{cf1})$ for submerged orifice flow cases

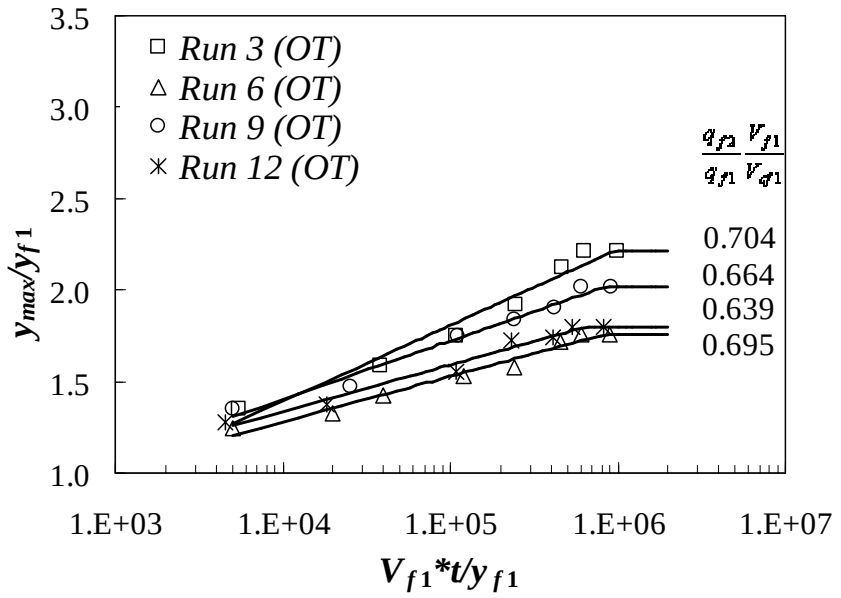

Figure 5.6 Time development of the abutment scour depth in dimensionless form with parameter $(q_{f2}/q_{f1})(V_{f1}/V_{cf1})$ for overtopping flow cases

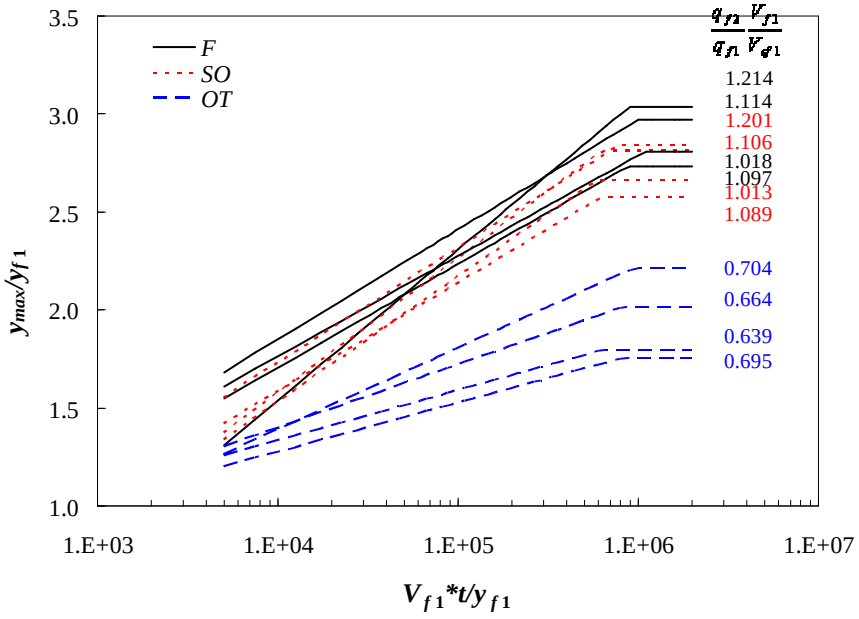

Figure 5.7 Time development of the abutment scour depth in dimensionless form with parameter $(q_{f2}/q_{f1})(V_{f1}/V_{cf1})$

Table 5.1 Summary of dimensionless equilibrium times for long setback, bankline, and short setback abutments

Long setback abutment					*Bankline abutment*				
Run	*Flow type*	L_a/B_f	$\frac{q_{f2}}{q_{f1}}\frac{V_{f1}}{V_{cf1}}$	$\frac{V_{f1}T_{eq}}{y_{f1}}$	*Run*	*Flow type*	L_a/B_f	$\frac{q_{m2}}{q_{m1}}\frac{V_{m1}}{V_{cm1}}$	$\frac{V_{m1}T_{eq}}{y_{m1}}$
7	F	0.78	1.214	$1.04*10^6$	7	F	1.0	1.296	$8.45*10^5$
1		0.53	1.114	$9.99*10^5$	1		1.0	1.282	$7.80*10^5$
10		0.78	1.097	$9.32*10^5$	4		1.0	1.114	$7.21*10^5$
4		0.53	1.018	$9.04*10^5$	10		1.0	1.111	$6.84*10^5$
8	SO	0.78	1.201	$7.13*10^5$	8	SO	1.0	1.152	$6.18*10^5$
2		0.53	1.106	$6.71*10^5$	2		1.0	1.084	$5.83*10^5$
11		0.78	1.089	$6.63*10^5$	11		1.0	1.017	$5.06*10^5$
5	OT	0.53	1.013	$6.08*10^5$	5	OT	1.0	1.007	$4.50*10^5$
3		0.53	0.704	$9.48*10^5$	3		1.0	0.822	$7.80*10^5$
6		0.53	0.695	$8.85*10^5$	9		1.0	0.822	$6.86*10^5$
9		0.78	0.664	$8.31*10^5$	12		1.0	0.726	$5.22*10^5$
12		0.78	0.639	$6.34*10^5$	6		1.0	0.705	No scour
Short setback abutment					*Bankline abutment*				
Run	*Flow type*	L_a/B_f	$\frac{q_{m2}}{q_{m1}}\frac{V_{m1}}{V_{cm1}}$	$\frac{V_{m1}T_{eq}}{y_{m1}}$	*Run*	*Flow type*	L_a/B_f	$\frac{q_{m2}}{q_{m1}}\frac{V_{m1}}{V_{cm1}}$	$\frac{V_{m1}T_{eq}}{y_{m1}}$
13	F	0.88	1.312	$5.48*10^5$	13	F	1.0	1.312	$5.59*10^5$
16		0.88	1.093	$4.27*10^5$	16		1.0	1.093	$4.05*10^5$
14	SO	0.88	1.163	$6.27*10^5$	14	SO	1.0	1.163	$5.59*10^5$
17		0.88	0.989	$4.15*10^5$	17		1.0	0.989	$4.47*10^5$
15	OT	0.88	0.811	$5.56*10^5$	15	OT	1.0	0.811	$3.03*10^4$
18		0.88	0.741	$4.45*10^5$	18		1.0	0.741	$1.69*10^4$

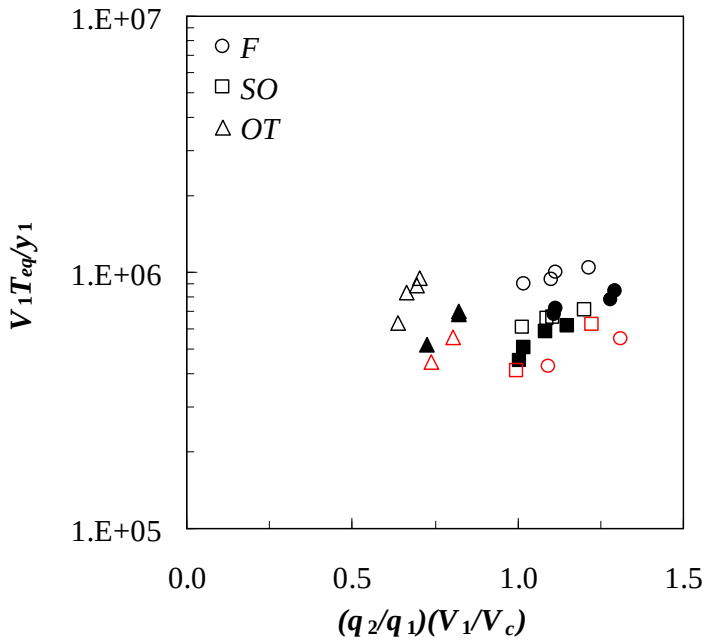

Figure 5.8 The relationship between the dimensionless equilibrium time and the value of $(q_2/q_1)(V_1/V_{c1})$; an open symbol (black) for the long setback abutment, and open symbol (red) for the short setback abutment, and the solid symbol for the bankline abutment.

The non-dimensionalization of scour development time around the abutment suggested in the above figures is similar to the results of other investigations. Hager and Oliveto (2007) and Kothyari et al. (2007) suggested a non-dimensional time scale for the abutment of $t\sqrt{g' d_{50}}/(L_a^{2/3} y_1^{1/3})$, in which $g' = g(\rho_s - \rho)/\rho$, with the third dimensionless parameter as the densimetric grain Froude number of the approach flow, $V_1/(g' d_{50})^{0.5}$. Yanmaz and Kose (2007) also suggested a time scale of $t\, d_{50}\sqrt{g' d_{50}}/L_a^{\,2}$ and a densimetric grain Froude number as the third parameter. The non-dimensional time scale of Hager and Oliveto (2007) and Kothyari et al. (2007) is

similar to $V_1 t/y_1$ in this study because the $\sqrt{g' d_{50}}$ is directly related to V_c, and then V_c can be replaced by V_1 during the dimensional analysis. Furthermore, the grain Froude number of the approach flow as a third parameter is similar to the variable V_1/V_c in this study. The main difference with respect to the results in this study is whether the length of the abutment is or is not included in the dimensionless time scale. In general, the length of the abutment was used to determine the flow contraction through the bridge section in a rectangular shaped cross section for the other studies. However, the abutment scour depth of a compound channel should not depend directly on the abutment length, but on the flow redistribution in the contracted section (Sturm, 2006). The ratio of the discharge per unit width of the approach section to that of the bridge section can be a suitable independent variable that accounts for flow redistribution and resulting flow acceleration through a bridge section. As a result, instead of abutment length, q_2/q_1 is included as the third parameter in the dimensionless plot of scour hole development with time.

For the bankline abutment, the results of the time development of the abutment scour process is similar to the experimental results from the long setback abutment, shown in Figures 5.9, 5.10, and 5.11. The normalized abutment scour depth follows a linear trend with the logarithm of the dimensionless time variable, $V_{m1} t/y_{m1}$, and the normalized equilibrium scour depth is a function of third independent variable, $(q_{m2}/q_{m1})(V_{m1}/V_{cm1})$. However, it is interesting to note that measurements for the overtopping cases are more scattered than those for the free and submerged orifice flow

cases, and the resulting values of R^2 range from 0.81 to 0.85. The value of R^2 for free and submerged orifice flow cases is about 0.98, which might be the effect of failure of the abutment caused by overtopping flow in the initial stage of the time development of scour. As explained in the previous section, when the side slope of the abutment became unstable, the riprap stones and the sand slumped downstream into the main channel and produced a newly covered area with a characteristically-rounded shape. As shown in Figure 5.3, after a short time (less than 7 hours), the side slope failure process completely finished, and local scour at the downstream side the abutment started developing at a lower scouring rate than it did for the free and the pressure flow case because of the release of 20% to 30 % of the water discharge over the bridge. This failure mode, combined with the overtopping water delayed the development of the scour hole. The resulting plot exhibits a more scattered behavior as shown in Figure 5.11.

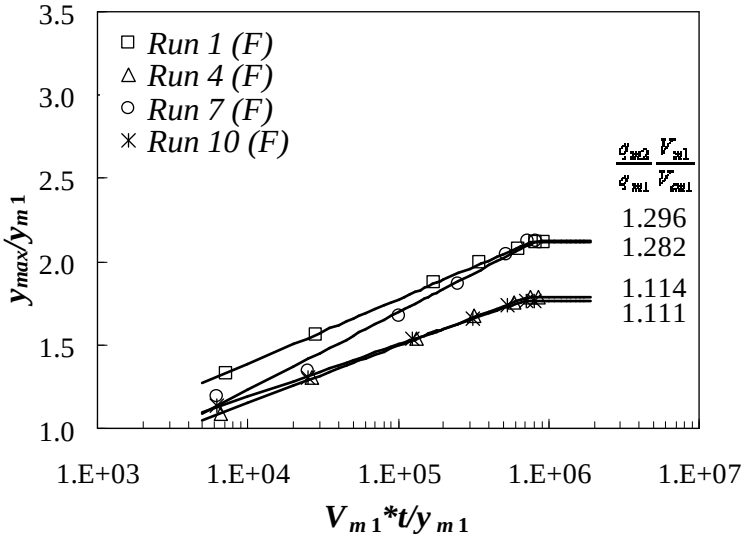

Figure 5.9 Time development of the abutment scour depth in a dimensionless form with parameter $(q_{m2}/q_{m1})(V_{m1}/V_{cm1})$ for free flow cases

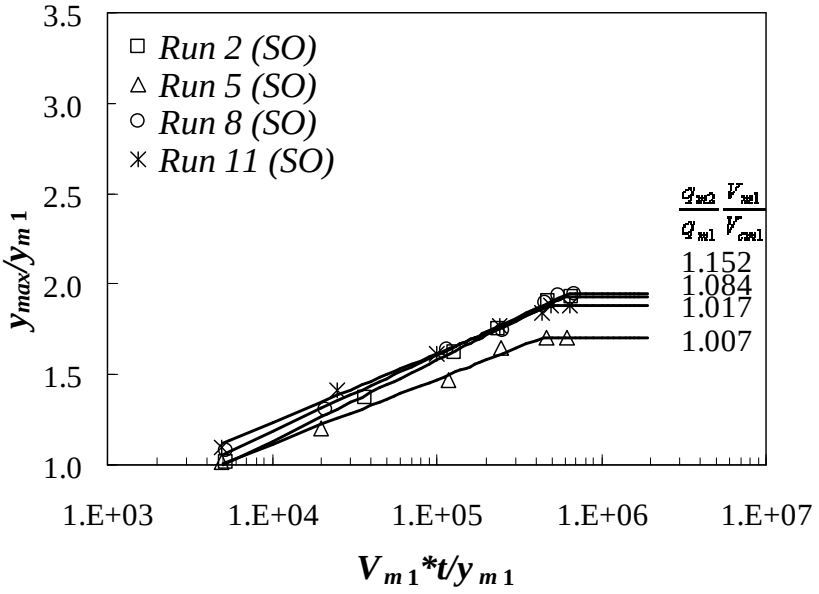

Figure 5.10 Time development of the abutment scour depth in a dimensionless form with parameter $(q_{m2}/q_{m1})(V_{m1}/V_{cm1})$ for submerged orifice flow cases

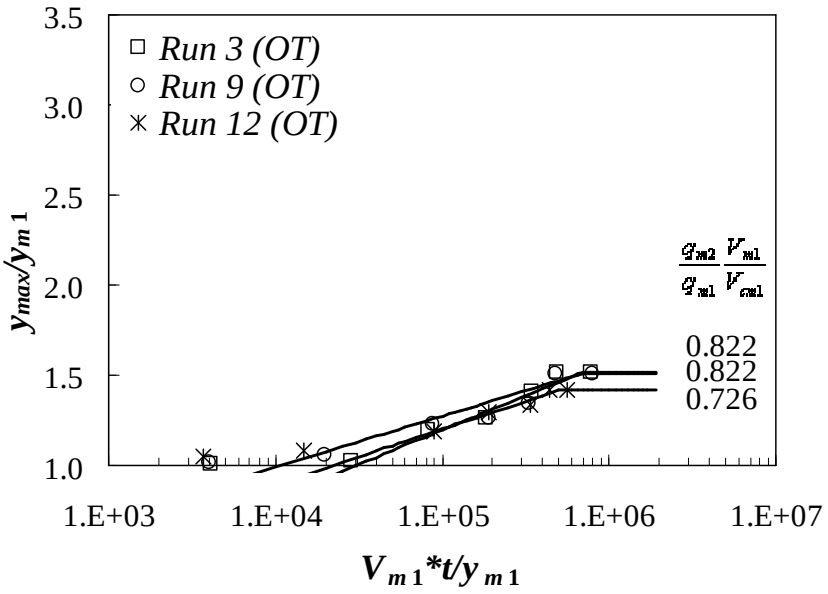

Figure 5.11 Time development of the abutment scour depth in a dimensionless form with parameter $(q_{m2}/q_{m1})(V_{m1}/V_{cm1})$ for overtopping flow cases

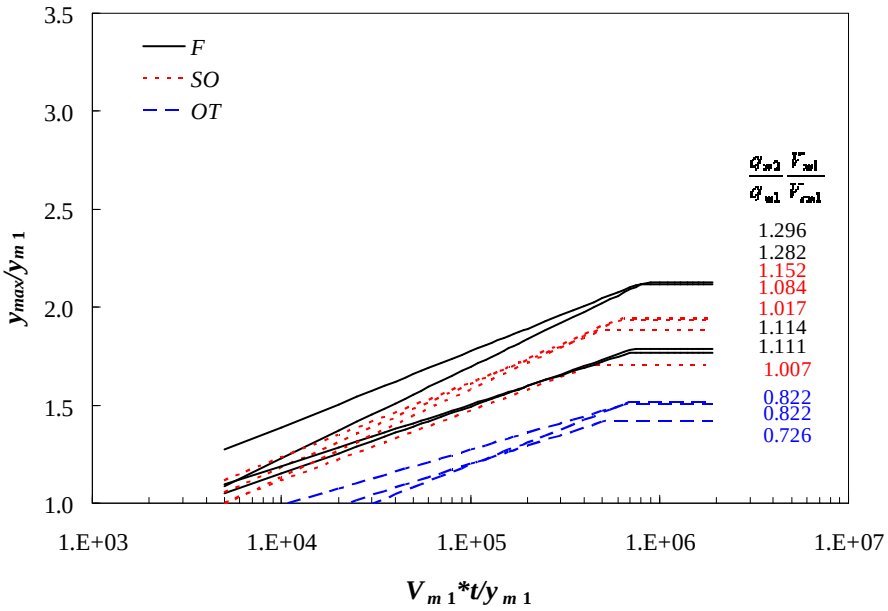

Figure 5.12 Time development of the abutment scour depth in a dimensionless form with parameter $(q_{m2}/q_{m1})(V_{m1}/V_{cm1})$

5.3.2 *Time Development of Scour Around the Short Setback Abutment*

As explained in the previous chapter, both approach floodplain and approach main channel variables could be the characteristic scale for a short setback abutment because the initial scour hole occurred in the floodplain and then extended into the main channel over time. However, because the scour hole reached its maximum depth in the main channel after only a short time (less than ten hours) and the scour depth in the equilibrium state occurred inside of the main channel, the main channel variables were used for the characteristic scale to determine the non-dimensional parameters.

Figure 5.13 (a) and (b) show the temporal development of scour contours for the free flow cases. In Figure 5.13 (a), the scour holes initially developed at three locations,

which are around the short setback abutment, around the bankline abutment, and inside of the main channel between the two abutments. As the experiment continued, the initial scour hole that developed in the floodplain around the short setback abutment became larger and the final equilibrium scour hole terminated in the main channel. For the bankline abutment, the scour hole became larger and eventually met the main channel scour hole after about ten hours. These two scour holes converged downstream of the abutment and became larger until the scour depth reached equilibrium at a higher scouring rate than was observed in the initial scour development stage (before convergence). The higher scouring rate can be observed in the time development of the scour curves shown in Figure 5.14. The measurements in Run 13 (the triangular symbol) for the bankline abutment in Figure 5.14 shows a change in the secondary slope after a certain dimensionless time ($V_{m1}\,t/y_{m1}$ is about $2*10^4$ at that point).

However, this convergence did not occur during the other free flow experiment (Run 16), shown in Figure 5.13 (b), because Run 13 has a higher value of $(q_{m2}/q_{m1})(V_{m1}/V_{cm1})$, due to a greater degree of flow contraction. As shown in Figure 5.14, the change in the secondary slope occurs only for the bankline abutment in Run 13, which is due to the convergence of the two scour holes. Except for the case mentioned above (bankline abutment for Run 13), the scour depth normalized by the approach water depth follows a linear trend with a logarithm of the dimensionless time variable similar to that of the experimental results from the long setback abutment for free flow.

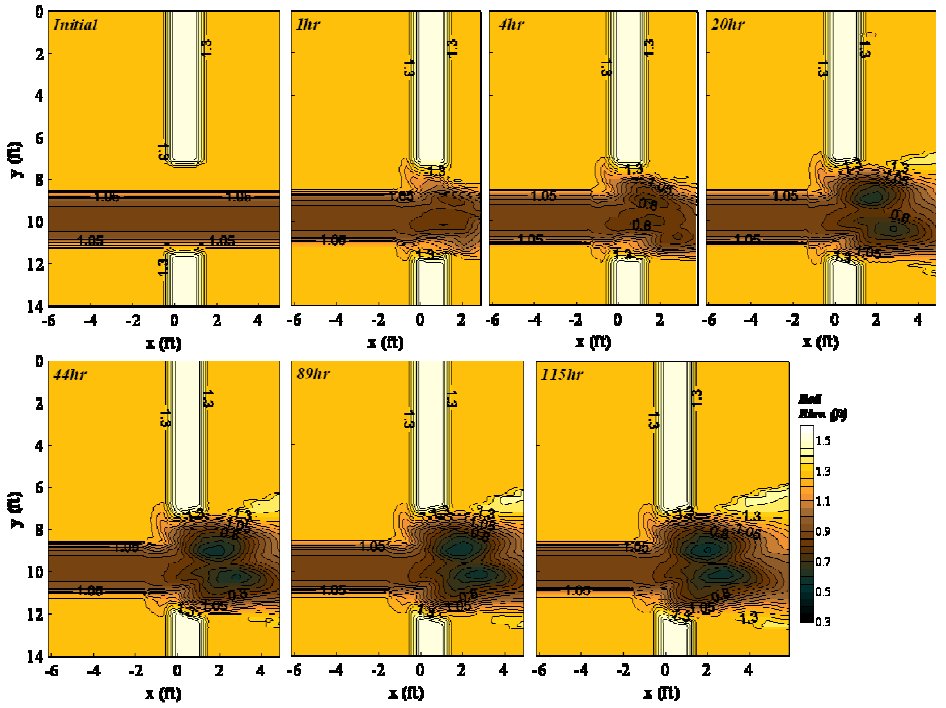

(a)

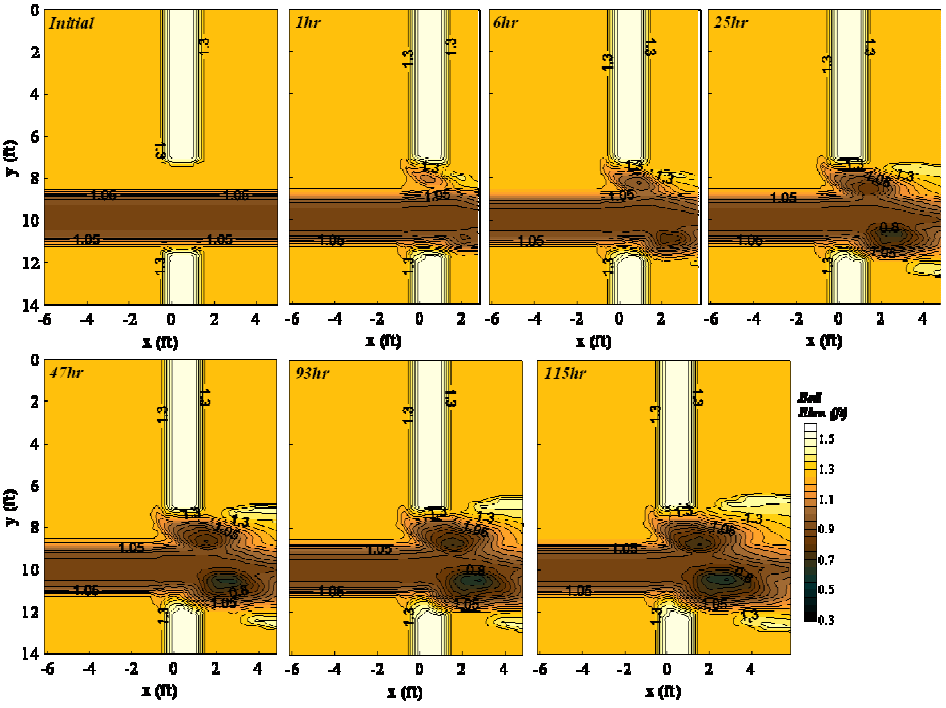

(b)

Figure 5.13 Time development of scour for free flow cases: (a) Run 13, $(q_{m2}/q_{m1})(V_{m1}/V_{cm1})$ = 1.312; (b) Run 16, $(q_{m2}/q_{m1})(V_{m1}/V_{cm1})$ = 1.093 (L_a/B_f = 0.88, flow type = F)

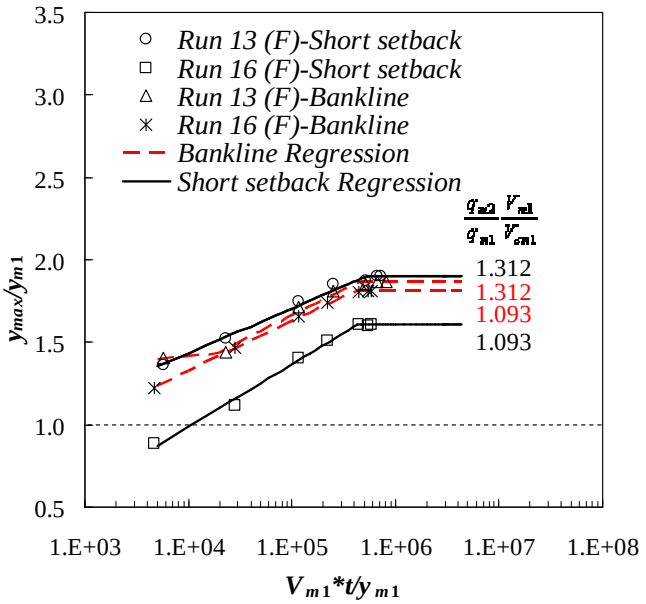

Figure 5.14 Time development of the short setback and the bankline abutment scour depth in a dimensionless form with parameter $(q_{m2}/q_{m1})(V_{m1}/V_{cm1})$ for free flow cases

The temporal development of scour contours for submerged orifice flow cases are shown in Figure 5.15 (a) and (b). The scour development around the abutment over time is similar to that of the free flow case in Run 14, shown in Figure 5.15 (a). However, the main channel scour hole converged with the scour hole around the short setback abutment after about 4 hours, not with the scour hole around the bankline abutment. After convergence of the two scour holes, scour around the short setback abutment occurred more rapidly, and this convergence resulted in a secondary slope change at a value of dimensionless time of $3*10^4$ as shown in Figure 5.16.

In Run 17, the process of scour development over time is different to that of submerged orifice flow case in Run 14 as shown in Figure 5.15 (b). In the initial part of the experiment (0-24 hours), the development of the scour depth over time exhibited

patterns similar to those of the other experimental cases, such as Run 14. However, after approximately 40 hours, the scour hole located in the center of the main channel became deeper while the other two scour holes downstream of the short setback abutment and the bankline abutment did not change over time. As the experiment continued, the scour depth in the center of the main channel increased. After approximately 100 hours, an maximum equilibrium scour depth occurred in the center of main channel, not in the downstream of the bankline and the short setback abutment.

The most probable cause for these differing scenarios in the short setback abutment is the higher flow contraction under the bridge as well as the erosional strength of the abutment. The higher flow contraction resulted in the scour hole being located near the abutment in addition to influencing the degree of abutment failure itself depending on the erosional strength of the abutment. To suggest a general scour mechanism around the short setback abutment is virtually impossible because the data in this study are insufficient. The determination of a more accurate picture of the complex flow physics and the resulting sediment transport around a short setback abutment calls for experiments under highly contracted flow conditions (e.g., flow around bankline abutments at both sides of the main channel) in extreme hydrologic conditions. From the bridge design viewpoint relative to possible scour failure, the occurrence of bankline abutments on both sides of a narrow main channel is not desirable.

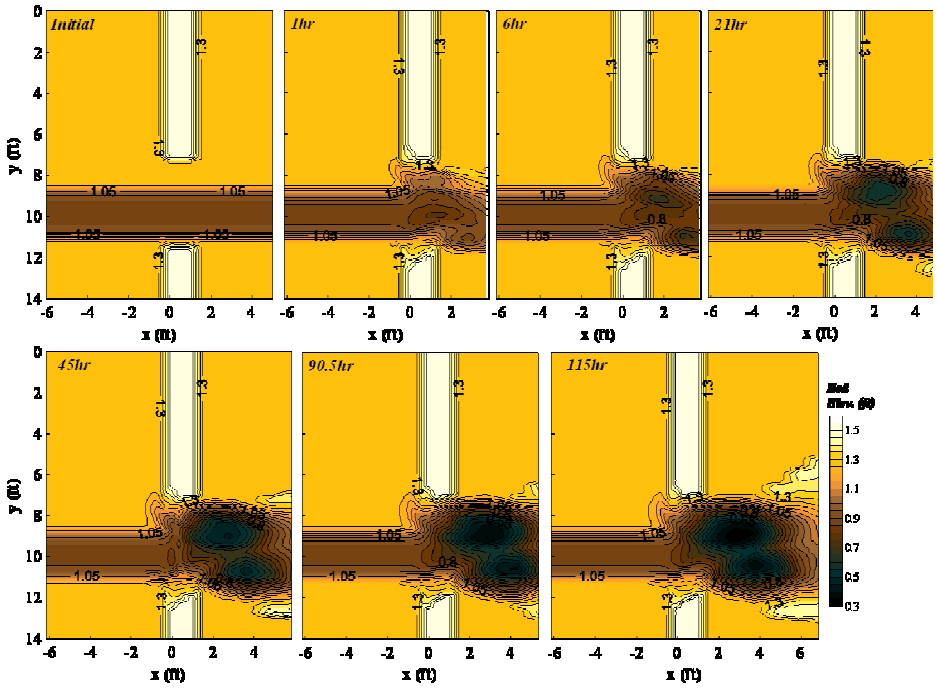

(a)

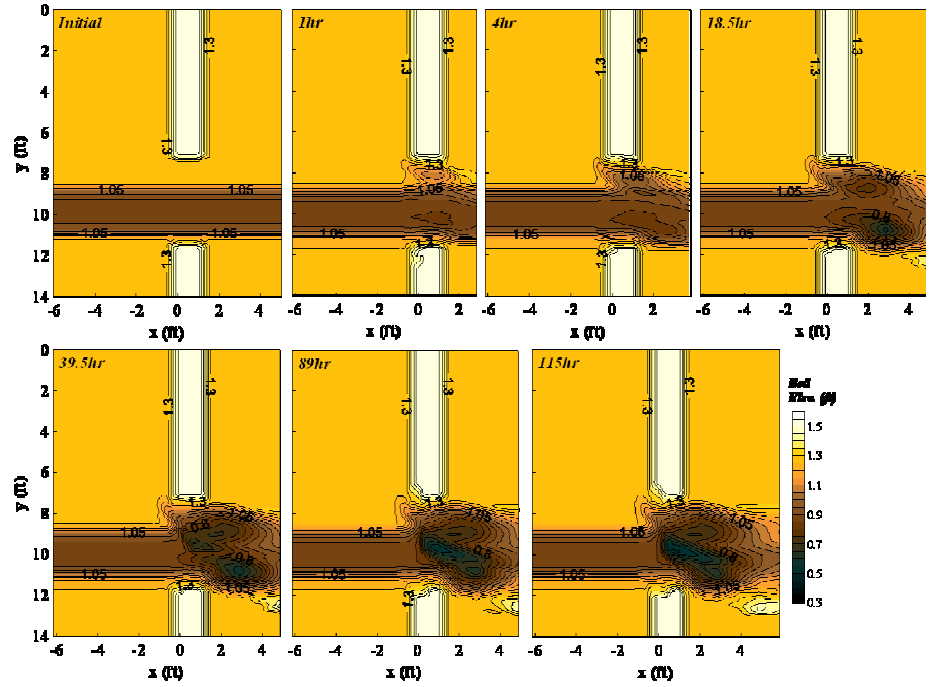

(b)

Figure 5.15 Time development of scour for submerged orifice flow cases: (a) Run 14, $(q_{m2}/q_{m1})(V_{m1}/V_{cm1})$ = 1.163; (b) Run 17, $(q_{m2}/q_{m1})(V_{m1}/V_{cm1})$ = 0.989 (L_a/B_f = 0.88, flow type = SO)

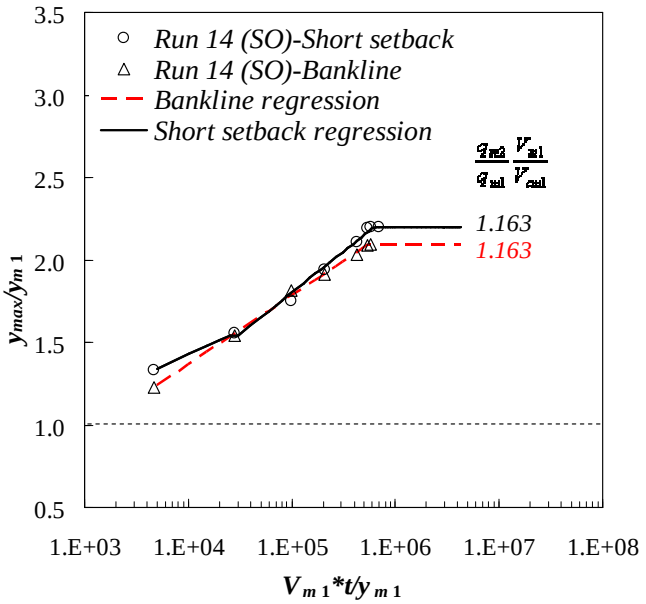

Figure 5.16 Time development of the short setback and bankline abutment scour depth in a dimensionless form with parameter $(q_{m2}/q_{m1})(V_{m1}/V_{cm1})$ for submerged orifice flow cases

Time (T_{eq}) required to reach equilibrium clear water scour is also summarized in Table 5.1 in dimensionless form for the short setback abutment. Similar to the long setback abutment cases, the dimensionless equilibrium time is related to the third parameter, $(q_2/q_1)(V_1/V_{c1})$, in a clear water condition when a comparison of the same flow types is conducted as shown in Figure 5.8. However, additional experiments should be conducted to establish a general relationship for the equilibrium time in the short setback abutment.

5.4 *Analysis of Maximum Scour Depth Around an Abutment.*

The effects of lateral and/or vertical flow contraction and local turbulence all contribute to scour around an abutment. As a result, it is hypothesized that the maximum scour depth around an abutment can be predicted by a multiple of the mean-flow contraction contribution in addition to the local turbulence term as shown in Equation 5.4. The inherent assumption of Equation 5.4 is that abutment scour is some amplification of the theoretical long-contraction scour as first suggsted by Laursen (1960). What has not been tried previously is to apply this concept to not just free flow through a bridge, but also to submerged orifice flow and overtopping flow provided that the vertical flow contraction as well as the lateral flow contraction effect can be parameterized by the ratio q_2/q_1, the ratio of discharge per unit width under the bridge to that in the approach flow. In addition, it is shown herein that the amplification ratio r_T is not a constant but rather a variable that depends on the relative contribution of the local turbulence to the overall scour depth. In the following analysis, r_T is related to a spatial average of the measured turbulence kinetic energy immediately downstream of the bridge in the vicinity of the scour hole that develops there. A new formula for calculating maximum scour depth around an erodible abutment will be developed based on these theoretical concepts and laboratory measurements.

5.4.1 *Assessment of the "Local Turbulence Effect" Term*

As summarized in the previous section, the goal of this discussion is to correlate

equilibrium scour conditions with the initial (before scour) spatial distribution of maximum TKE near the channel bed. Maximum TKE in each measured vertical profile was selected from the point ADV measurement at 5mm above the bed level as explained in Chapter 4. The range of k_s^+ and z/y_1 is from 40 to 70 and 0.04 to 0.1, respectively. Lateral distributions of maximum TKE (K_b) normalized by the approach shear velocity (u_*) were plotted for five cross sections in the streamwise direction as shown in Figures 5.17, 5.18, and 5.19 for free flow (Run 1), submerged orifice flow (Run 2), and overtopping flow (Run 3), respectively. The plots for the other experimental conditions can be found in the Appendix.

TKE near the bed can be an important variable to account for the impact of the local turbulence energy generated by the vortex structure and the separated shear zone on the scour around an abutment (Chrisohoides et al. (2003), Ge et al. (2005), and Lacey and Rennie (2012)). Thus, to quantify the local turbulence effect on the maximum scour around an abutment, the width-averaged value of near-bed TKE ($\overline{K}_b/u_*^2$) that occurred prior to scour is calculated as a measure of the potential of the turbulent flow field to create a scour hole. It was found that the peak value of near-bed TKE (K_b/u_*^2) in each profile was not as useful as the width-averaged TKE as an explanatory variable because the location of the peak value of K_b/u_*^2 did not exactly correspond to the location of the maximum scour hole depth, and because the values of K_b/u_*^2 tended to be elevated above a background value over the full width of the scour hole.

The width-averaged value of near-bed TKE ($\overline{K}_b/u_*^2$) in each lateral profile is

calculated by taking the integral of each profile across the scour hole and dividing it by the lateral width of the scour hole as shown in Figures 5.17, 5.18, and 5.19 by the dimension lines. A summary of width-averaged values of maximum TKE ($\overline{K}_b/u_*^2$) for each profile (noted as a cross-section number) are shown in Tables 5.2 and 5.3 for the setback and bankline abutments, respectively.

As shown in Figures 5.17, 5.18, and 5.19, the TKE begins increasing at Cross-Section 4 (C.S. 4), reaches a maximum at C.S. 5, and begins to decrease at C.S. 6. In analogy with an accelerating jet issuing from an orifice, the shear flow that curves away from the face of the abutment at the point of separation experiences increasing velocities, cross-stream velocity gradients, and turbulence energy over a defined area until a streamwise position corresponding to a vena contracta is reached. Thereafter, the velocity and TKE begin to decrease as the flow starts the process of deceleration due to entrainment. The maximum streamwise width-averaged values of TKE, $\overline{K}_b/u_*^2$, occur at C.S. 5 at the location of the downstream toe of the embankment. These values are highlighted in red in Tables 5.2 and 5.3 to be used as explanatory variables for the contribution of the local turbulence to the scour process.

With respect to the flow type, the values of $\overline{K}_b/u_*^2$ at C.S. 5 are largest for overtopping flow probably because of the flow cascading over the bridge deck and producing larger turbulent fluctuations. In general, $\overline{K}_b/u_*^2$ decreases in going from free flow to submerged orifice flow for the large setback abutments and vice versa for the short setback and bankline abutments.

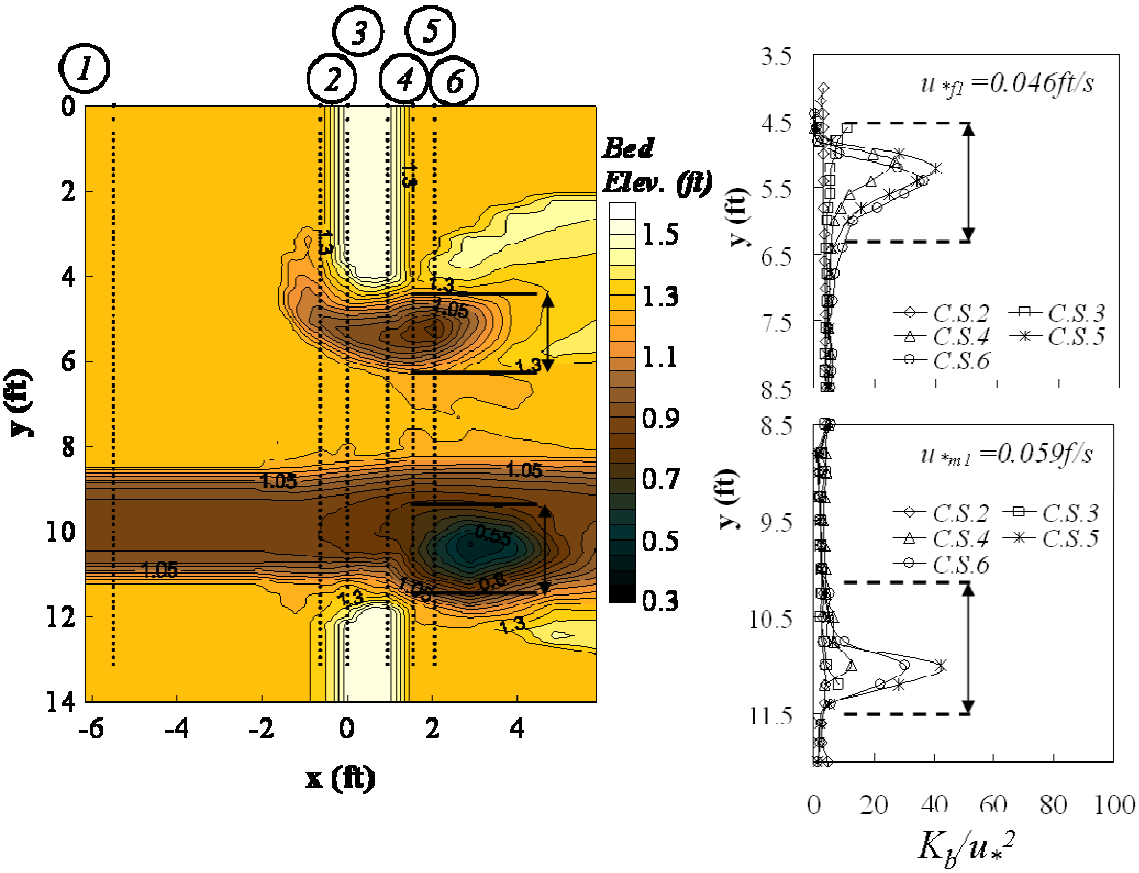

Figure 5.17 Final bed elevation contours in the equilibrium condition and the initial lateral turbulence kinetic energy profiles near the bed for the calculation of the local turbulence effect in Run 1 (L_a/B_f = 0.53, flow type = F)

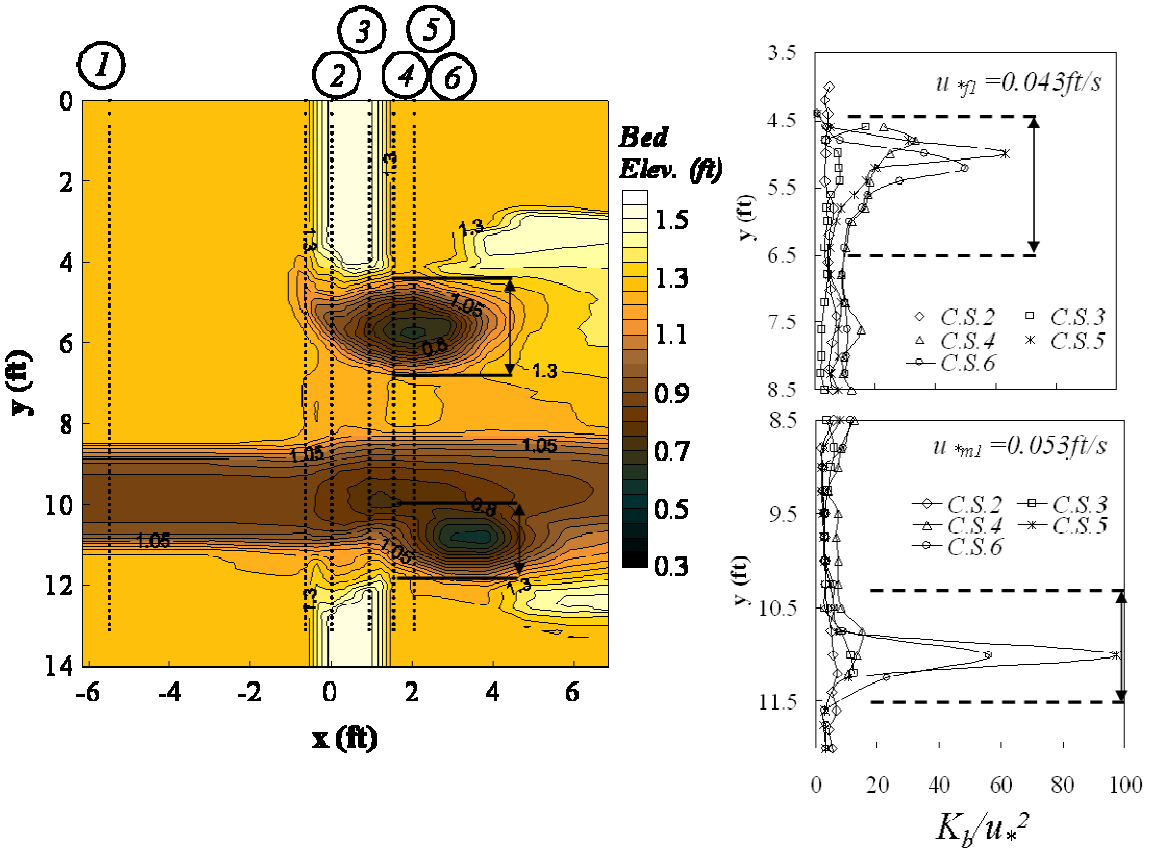

Figure 5.18 Final bed elevation contours in the equilibrium condition and the initial lateral turbulence kinetic energy profiles near the bed for the calculation of the local turbulence effect in Run 2 (L_a/B_f = 0.53, flow type = SO)

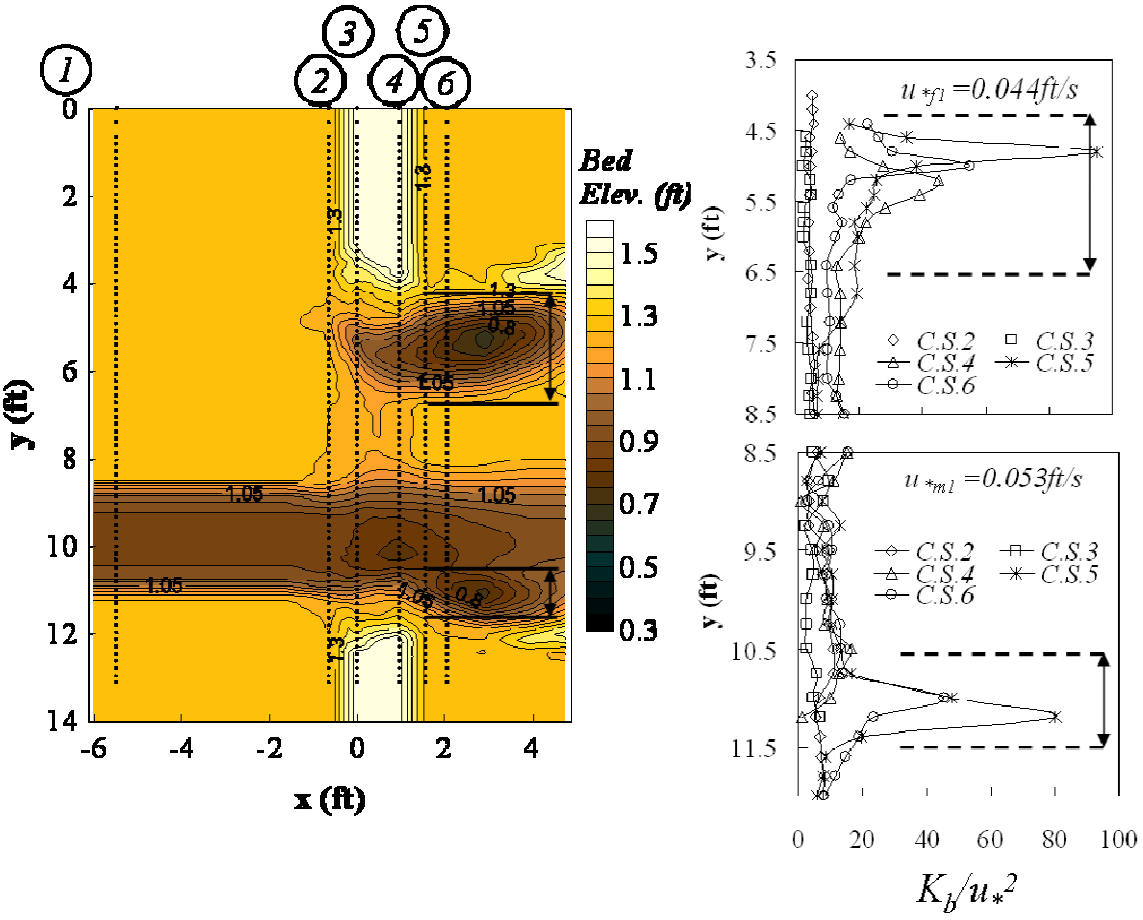

Figure 5.19 Final bed elevation contours in the equilibrium condition and the initial lateral turbulence kinetic energy profiles near the bed for the calculation of the local turbulence effect in Run 3 (L_a/B_f = 0.53, flow type = OT)

Table 5.2 Summary of width-averaged maximum TKE($\overline{K}_b/u_*^2$) for the setback abutment

Run	L_a/B_f	*Flow type*	$\overline{K}_b/u_*^2$					
			C.S.1	*C.S.2*	*C.S.3*	*C.S.4*	*C.S.5*	*C.S.6*
1	0.53	F	1.542	3.185	6.385	11.425	23.471	22.107
2		SO	2.216	4.340	6.301	18.249	22.751	17.273
3		OT	2.987	4.729	3.353	25.598	31.774	20.824
4		F	1.614	2.545	5.828	12.017	26.501	12.152
5		SO	2.132	3.843	6.080	18.958	23.152	18.603
6		OT	4.101	5.391	3.380	24.735	25.551	21.024
7	0.71	F	1.563	2.978	8.436	10.879	20.451	15.972
8		SO	2.149	3.882	7.045	15.057	18.951	18.271
9		OT	3.739	5.879	5.934	18.701	30.631	25.251
10		F	1.856	3.720	7.030	12.585	19.453	19.136
11		SO	2.026	4.101	6.286	16.734	17.530	17.321
12		OT	2.858	5.801	6.807	12.766	27.281	23.686
13	0.88	F	2.259	2.049	4.988	11.109	19.261	11.256
14		SO	2.271	3.496	5.420	18.915	26.282	18.513
15		OT	3.095	4.665	5.872	14.462	31.781	20.711
16		F	2.248	4.144	7.548	11.827	18.213	13.523
17		SO	2.761	4.582	5.984	13.851	24.944	12.115
18		OT	3.129	4.281	5.628	14.862	28.881	20.049

Note: Flow type: F=free flow; SO=submerged orifice flow; OT=overtopping flow
In the long setback abutment (L_a/B_f=0.53, 0.71) case, width-averaged TKE is normalized by the approach floodplain shear velocity.
In the short setback abutment (L_a/B_f=0.88) case, width-averaged TKE is normalized by the approach main channel shear velocity.
The values inside of the solid thick boundary show the maximum value of $\overline{K}_b/u_*^2$ for each experiment (at C.S. 5).

Table 5.3 Summary of width-averaged maximum TKE($\overline{K}_b/u_*^2$) for the bankline abutment

Run	L_a/B_f	*Flow type*	$\overline{K}_b/u_*^2$					
			C.S.1	*C.S.2*	*C.S.3*	*C.S.4*	*C.S.5*	*C.S.6*
1	1.0	F	1.625	3.968	3.888	6.649	18.371	15.829
2		SO	2.412	6.184	6.577	10.569	18.732	13.228
3		OT	3.164	7.144	4.836	10.575	22.183	19.005
4		F	1.811	3.853	3.862	7.787	15.974	12.408
5		SO	2.202	8.127	10.355	11.608	16.764	13.715
6		OT	4.782	9.869	6.420	12.206	23.463	17.803
7	1.0	F	2.092	4.699	5.097	9.064	13.331	9.332
8		SO	1.953	5.141	5.838	9.647	15.308	12.101
9		OT	2.998	6.517	10.423	15.185	23.098	18.771
10		F	2.619	4.290	4.544	7.875	15.105	9.410
11		SO	2.187	5.743	8.157	12.002	17.802	12.158
12		OT	4.731	6.739	11.548	10.400	24.195	19.021
13	1.0	F	2.099	5.894	10.028	9.313	11.812	9.198
14		SO	2.160	6.795	7.009	11.082	14.053	12.034
15		OT	3.171	6.972	12.634	12.804	16.044	13.055
16		F	2.362	5.990	7.319	7.514	12.944	10.518
17		SO	2.394	7.621	8.217	13.331	15.341	13.598
18		OT	3.181	6.121	9.621	13.655	15.244	12.118

Note: Flow type: F=free flow; SO=submerged orifice flow; OT=overtopping flow
Width-averaged TKE is normalized by the approach main channel shear velocity.
The values inside of the solid thick boundary showed the maximum value of $\overline{K}_b/u_*^2$ for each experiment (at C.S. 5).

5.4.2 *Prediction of the Maximum Scour Depth Around the Long Setback Abutment and the Bankline Abutment*

The measured maximum abutment scour depths are plotted in Figures 5.20 and 5.21 for the long setback abutment and the bankline abutment, respectively, according to the dimensionless variables suggested by the theoretical contraction scour analysis shown in Equation 5.7. In the initial regression analysis, the exponent of $[(V_1/V_{c1})(q_2/q_1)]$ was allowed to vary as an unknown because the exponent of 6/7 in Equation 5.5 was decided from the long contraction assumption, which might not be true through the bridge contraction. However, the exponents from the initial regression analysis were 0.75 and 0.78 for the long setback abutment and for the bankline abutment, respectively, and the values were similar to the theoretical exponent, which is 6/7 (=0.857). Therefore, the exponent of 6/7 was used in all succeeding regression analyses as shown in Equation 5.5.

As shown in Figures 5.20 and 5.21, as the dimensionless variable, $[(V_1/V_{c1})(q_2/q_1)]^{6/7}$, in the x-axis increases, normalized scour depth gradually increases. As an initial fit, a straight line was used in the regression analysis, which would imply that the effect of turbulence on abutment scour is a constant. The results clearly reveal that maximum abutment scour can be considered a multiple of contraction scour effects instead of an addition of local and contraction scour components that are incorrectly assumed to be independent, which is a basic hypothesis of this thesis.

The measured scour depths seem to follow the same trend in Figures 5.20 and 5.21, even if they have different flow types. Even though the observed data for

overtopping flow are in a slightly lower range than the other two flow types, regression analysis shows a continuous relationship in both figures. As Q increases, less flow goes under the bridge and the value of q_2/q_1 is less on the x-axis for the overtopping flow cases.

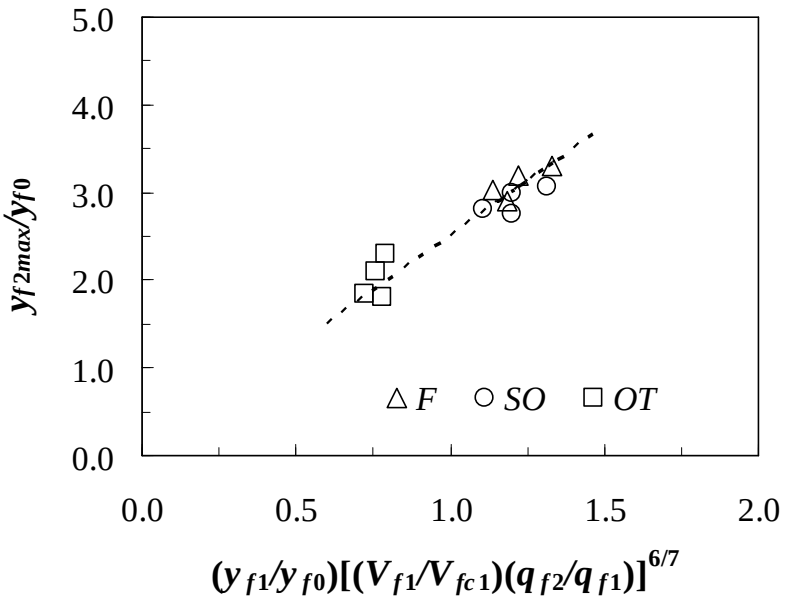

Figure 5.20 Normalized scour depth, $y_{\max}/y_0$, as a function of $[(V_1/V_{c1})(q_2/q_1)]^{6/7}$ for the long setback abutment

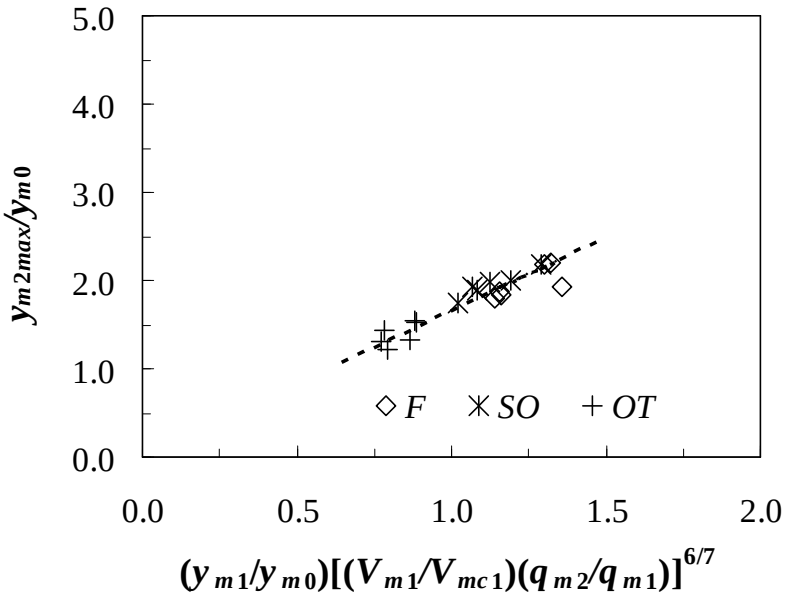

Figure 5.21 Normalized scour depth, $y_{\max}/y_0$, as a function of $[(V_1/V_{c1})(q_2/q_1)]^{6/7}$ for the bankline abutment

A least-squares regression analysis was conducted on the data given in Figures 5.20 and 5.21, and the best-fit equation is given by

$$\frac{y_{f2\max}}{y_{f0}} = 2.51\frac{y_{f1}}{y_{f0}}\left(\left(\frac{V_{f1}}{V_{fc1}}\right)\left(\frac{q_{f2}}{q_{f1}}\right)\right)^{6/7} \quad for \quad LSA \tag{5.6a}$$

$$\frac{y_{m2\max}}{y_{m0}} = 1.66\frac{y_{m1}}{y_{m0}}\left(\left(\frac{V_{m1}}{V_{mc1}}\right)\left(\frac{q_{m2}}{q_{m1}}\right)\right)^{6/7} \quad for \quad BLA \tag{5.6b}$$

with coefficient of determination of 0.86 and 0.84, and standard errors of $y_{\max}/y_0$ of 0.173 and 0.117 for the long setback abutment (LSA) and for the bankline abutment

(BLA), respectively (see Figure 5.22).

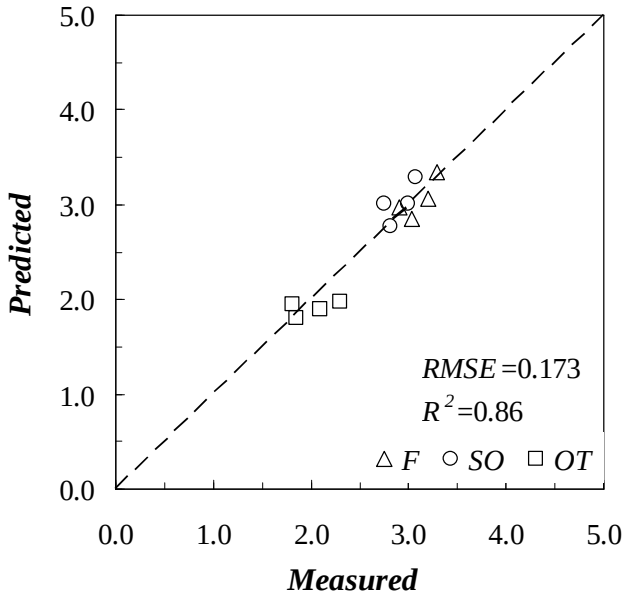

(a)

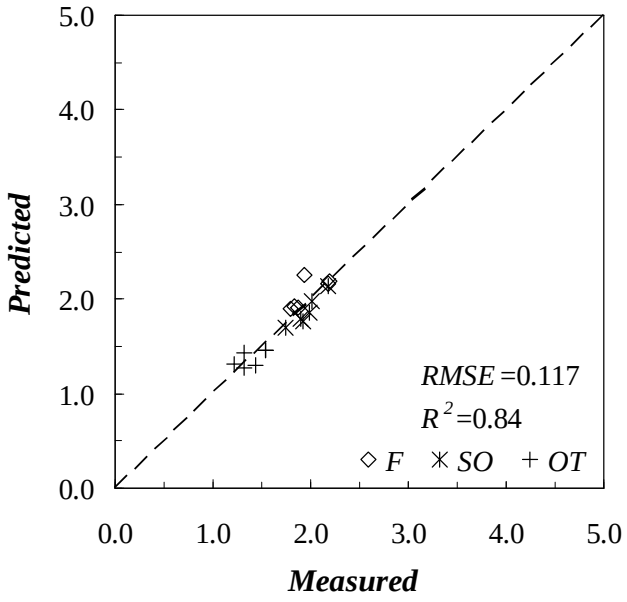

(b)

Figure 5.22 Correlation of scour depth data for (a) the long setback abutment and (b) the bankline abutment as in Equations 5.6

Equations 5.6 state that maximum dimensionless abutment scour ratio relative to theoretical contraction scour, r_T, is approximately a constant of 2.51 and 1.66 for LSA and BLA, respectively. The constant value of r_T in Equations 5.6 implicitly suggests that the contribution of local turbulence effects to the total abutment scour is unchanging as the discharge contraction ratio increases. For a number of reasons, this preliminary result is oversimplified. First, in terms of limiting cases, the very short abutment, which in reality is a half-pier on a sidewall, experiences scour that is driven by the dynamics of the horseshoe vortex (Koken and Constantinescu, 2006) alone. The very long abutment, on the other hand, experiences scour dominated by flow contraction (Sturm et al. 2011). Second, for an erodible abutment, the degree of scour protection afforded by failure of the riprap as it slides into the scour hole suggests that abutment scour relative to the theoretical contraction scour should decrease as q_2/q_1 increases assuming that total riprap and embankment failure do not occur. Finally, the data in Figures 5.20 and 5.21 hint at a decreasing slope with increasing q_2/q_1. In summary, the values of 2.51 and 1.66 in Equations 5.6a and 5.6b are not necessarily expected to be constants over a larger range of the independent variables as limiting cases are approached because the relative effect of turbulence will be different depending on the abutment length, the approach flow velocity distribution, the flow types, and other factors.

Under these circumstances, parameterizing the role of turbulence through its structure (oscillating horse shoe vortex (HSV), increased Reynolds stresses in the vicinity of the abutment, and increased vorticity due to the HSV and separated shear flow) seems to be a formidable task. However, at the most basic level, it is hypothesized that the

contribution of the turbulence is an increase in TKE at the bed that provides the energy for initiating motion and sustaining sediment transport to create a scour hole. This contribution of the turbulence could be expected to dominate the scour process for a short abutment, as for a pier, and be overpowered by the flow contraction in the case of a long abutment.

As shown in Tables 5.2 and 5.3, the maximum value of width-averaged TKE is observed in C.S. 5, where flow contraction is the greatest and a higher-velocity shear layer occurred. Accordingly, the value of width-averaged TKE ($\overline{K}_b/u_*^2$) at C.S. 5 is tentatively selected as a representative parameter to account for the turbulence effect on the maximum abutment scour depth. Other investigators who measured the turbulent flow field around spur dikes have also explored TKE as a possible parameter in the scour process, but they did not make a definitive connection (Lacey and Rennie (2012)). The data given in Figures 5.20 and 5.21, and the measured values of $\overline{K}_b/u_*^2$ in C.S. 5. were used to conduct a regression analysis for the long setback abutment and bankline abutments. The results showed a linear relationship as shown in Equations 5.7 and Figures 5.23.

$$\frac{y_{f2\max}}{y_{f0}} = 0.96\frac{y_{f1}}{y_{f0}}\left(\frac{\overline{K_b}}{u_*^2}\right)^{0.31}\left(\left(\frac{q_{f2}}{q_{f1}}\right)\left(\frac{V_{f1}}{V_{fc1}}\right)\right)^{6/7} \quad for \quad LSA \qquad (5.7a)$$

$$\frac{y_{m2\max}}{y_{m0}} = 0.92\frac{y_{m1}}{y_{m0}}\left(\frac{\overline{K_b}}{u_*^2}\right)^{0.21}\left(\left(\frac{q_{m2}}{q_{m1}}\right)\left(\frac{V_{m1}}{V_{mc1}}\right)\right)^{6/7} \quad for \quad BLA \qquad (5.7b)$$

which, for this relationship, yields the coefficient of determination of 0.98 and 0.92, and standard errors in y_{max}/y_0 of 0.088 and 0.086, for the long setback abutment (LSA) and the bankline abutment (BLA), respectively (see Figure 5.23). The relationships from the best-fit regression analysis given by Equations 5.7 result in an increase in the value of the coefficient of determination from 0.86 to 0.98 and from 0.84 to 0.92 for the long setback abutment and the bankline abutment, respectively. Furthermore, the standard error of estimate for the relative scour depth from Equations 5.7 shows almost half of that from Equations 5.6, which confirms that the width-averaged TKE term can be a representative parameter for the turbulence effect on maximum scour depth.

Maximum dimensionless abutment scour ratio relative to theoretical contraction scour, r_T, varies with the width-averaged TKE in Equations 5.7. The ranges of r_T are 2.3 to 2.8 and 1.5 to 1.8 as the flow contraction ratio (q_2/q_1) varies from 2.3 to 1.1 and 2.0 to 1.1 for the long setback and bankline abutments, respectively. As the flow under the bridge was highly contracted because of the obstruction offered by the roadway abutment/embankments, the dominance of scour was caused primarily by flow contraction with some influence of turbulence (lower value of r_T). This is observed in Figures 5.20 and 5.21 as a decreasing slope with increasing $[(V_1/V_{c1})(q_2/q_1)]$ because the relative effect of turbulence on the maximum scour depth became smaller in the higher flow contraction. However, for the smaller value of q_2/q_1 ($q_2/q_1 \approx 1$) for the limiting condition of the short length of the abutment compared to a very wide channel, the dominance of scour was caused by the turbulence structure such as pier scour (higher value of r_T). Thus, the Equations 5.7 supplemented the Equations 5.6 by taking the width-

averaged TKE into account in the regression analysis.

However, for practical purposes, quantifying TKE in the field or even in the lab is challenging because the local turbulence varies depending on the abutment shape, the bed material, the flow types, and other factors. Therefore, based on the findings of this study, another method will be suggested in the following section as a compromise.

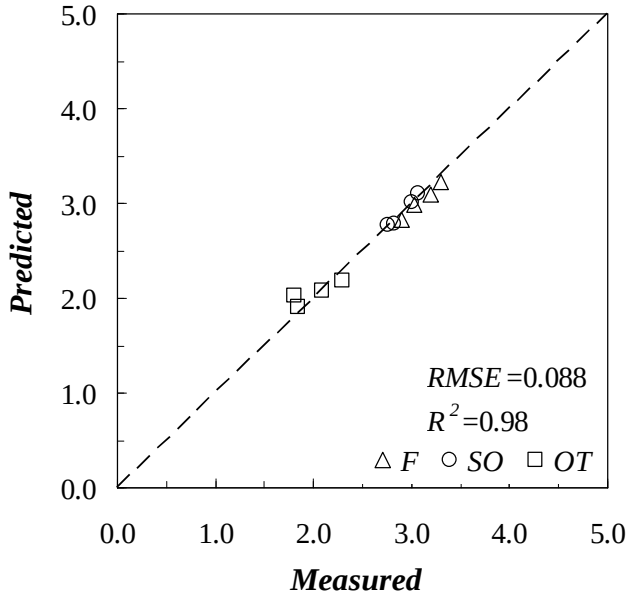

(a)

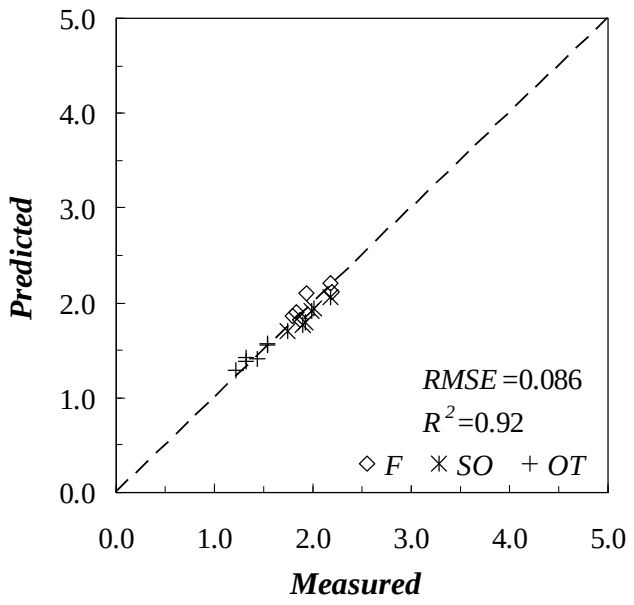

(b)

Figure 5.23 Correlation of scour depth data for (a) the long setback abutment and (b) the bankline abutment as in Equations 5.7

As an alternative to parameterizing r_T in terms of the width-averaged TKE, it is suggested that an alternative hypothesis is to assume that the relative magnitude of TKE may itself vary with (q_2/q_1). Therefore, the flow contraction ratio (q_2/q_1) and the approach intensity factor (V_1/V_{c1}) were taken into account in the regression analysis separately, without considering TKE, in this section. Instead of using a fixed exponent, which is 6/7 suggested from the theoretical contraction scour for $[(V_1/V_{c1})(q_2/q_1)]$, the exponents of each term, (V_1/V_{c1}) and (q_2/q_1), were decided by the regression analysis. The result shows that the exponent for (V_1/V_{c1}) is still close to the 6/7(=0.857), which is 0.82 for the bankline abutment and slightly higher (1.07) for the long setback abutment;

however, the exponents for (q_2/q_1) are less than 6/7. Thus, to keep the same format as in the previous results suggested in Equations 5.6 and 5.7 for the direct comparison of r_T, the regression analysis was conducted again to decide the exponent of (q_2/q_1) while the exponent of the (V_1/V_{c1}) kept the value of 6/7. The results produced a best-fit relationship as shown in Equations 5.8 and Figures 5.24.

$$\frac{y_{f2\max}}{y_{f0}} = 2.75\frac{y_{f1}}{y_{f0}}\left(\frac{q_{f2}}{q_{f1}}\right)^{-0.16}\left(\left(\frac{q_{f2}}{q_{f1}}\right)\left(\frac{V_{f1}}{V_{fc1}}\right)\right)^{6/7} \quad for \quad LSA \qquad (5.8a)$$

$$\frac{y_{m2\max}}{y_{m0}} = 1.75\frac{y_{m1}}{y_{m0}}\left(\frac{q_{m2}}{q_{m1}}\right)^{-0.12}\left(\left(\frac{q_{m2}}{q_{m1}}\right)\left(\frac{V_{m1}}{V_{mc1}}\right)\right)^{6/7} \quad for \quad BLA \qquad (5.8b)$$

For this relationship, the coefficients of determination are R^2 = 0.94 and 0.87, and standard errors in $y_{\max}/y_0$ are 0.132 and 0.111 for the LSA and for the BLA, respectively, as shown in Figure 5.24. The predictions from Equations 5.8 increase the standard error of estimate for the relative scour depth from 0.088 to 0.132 and 0.086 to 0.111 for the LSA and for the BLA, respectively in comparison to Equation 5.7.

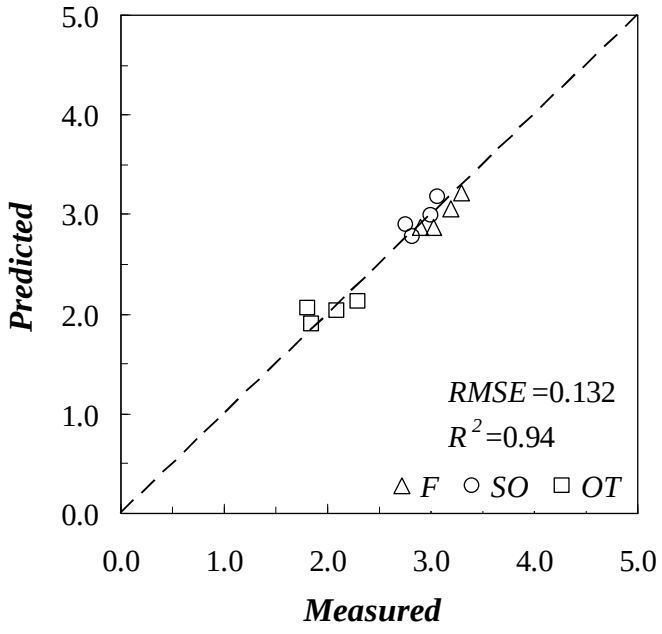

(a)

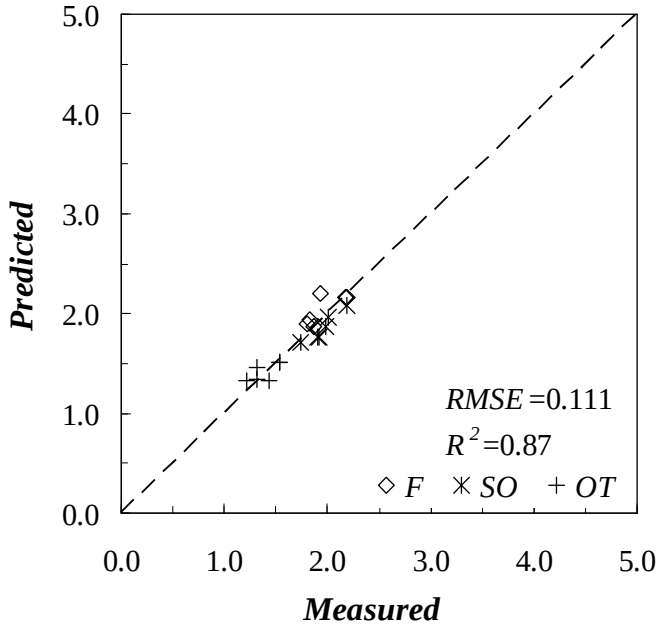

(b)

Figure 5.24 Correlation of scour depth data for (a) the long setback abutment and (b) the bankline abutment as in Equations 5.8

Equations 5.8 state that the maximum dimensionless abutment scour ratio relative to theoretical contraction scour, r_T, is a product of a constant of 2.75 and 1.75 times the theoretical flow contraction ratio for LSA and BLA, respectively. The contribution of local turbulence effects to the total abutment scour is inversely related to the flow contraction ratio. The values of $\overline{K_b}/u_*^2$ are shown in terms of a flow contraction ratio in Figure 5.25. The measurements in Figure 5.25 are consistent with the scenarios described in the previous paragraph. As the flow contraction ratio increases, the value of $\overline{K}_b/u_*^2$, which represents the effect of turbulence around the abutment, decreases and the corresponding value of r_T becomes smaller.

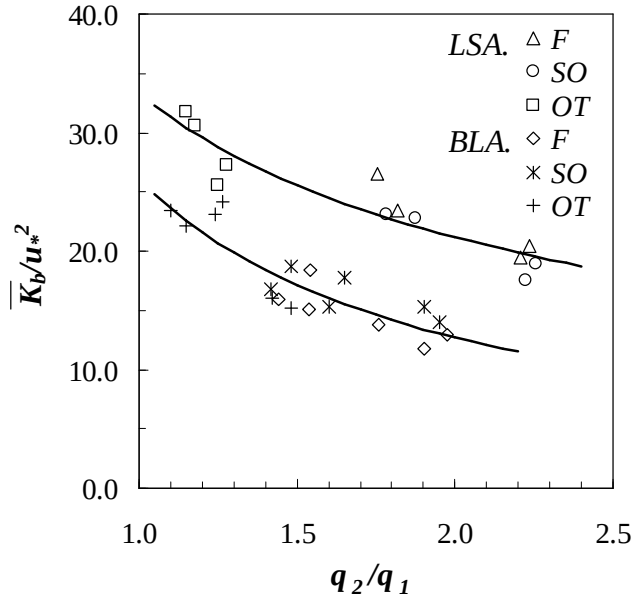

Figure 5.25 Variation of maximum value of width-averaged maximum TKE ($\overline{K}_b/u_*^2$) with discharge contraction ratio (q_2/q_1) for setback and bankline abutment including free, submerged orifice, and overtopping flow cases.

5.4.3 *Maximum Scour Depth Around the Short Setback Abutment*

It is clear how to define scour parameters for the long setback abutment (LSA) and for the bankline abutment (BLA). If the initial scour occurs in the floodplain, and the maximum scour remains in the floodplain, this scour condition can be categorized as long setback abutment scour. And if the initial scour and the maximum equilibrium scour occurred in the main channel, this condition can be called bankline abutment scour. Floodplain approach flow variables and main channel approach flow variables are used for the characteristic scale to calculate the non-dimensional independent parameters for the LSA scour and BLA scour, respectively, as explained in the previous sub-section.

However, it is unclear how to decide the characteristic scales when the initial scour occurs in the floodplain, but the maximum equilibrium scour depth is observed in the main channel because both floodplain and main channel approach flow variables (and their interaction) are contributing to the scour process. For the purpose of this study, which is to predict the maximum abutment scour depth, main channel approach flow variables are selected for the calculation of the normalized independent scour parameters for the short setback abutment (SSA) because maximum scour occurred in the main channel for this case. Furthermore, the experimental data from the SSA seem to follow the same trend as those from the BLA.

The results for the SSA are shown in Figure 5.26. The measured maximum water depth at the point of maximum scour is normalized by the approach main channel water depth on the y-axis. Equation 5.7b for the BLA is used to predict the scour depth shown on the x-axis. The suggested equation results in approximately 6 to 13% overestimate of

scour depth compared to the measured scour depth. The data are insufficient to conclude that the suggested equation can be applied to the SSA case; however, this could represent the first step in the development of a framework for further research and analysis to more accurately predict the scour depth around the SSA.

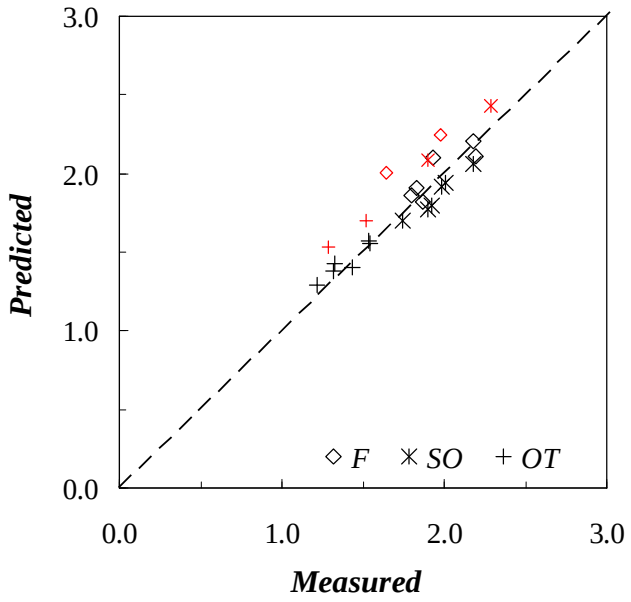

Figure 5.26 The prediction of maximum scour depth around the short setback abutment (red color) using the suggested bankline abutment prediction method (Equation 5.7b)

5.5 *Proposed Procedure for the Abutment Scour Prediction*

This section introduces a procedure for predicting the equilibrium abutment scour depth. Based on extensive experimental results reported in this thesis, a method for estimating the equilibrium clear-water scour depth around a spill-through abutment with and without

overtopping is suggested and shown in Equations 5.7. The right-hand side of the equation shows three dimensionless ratios of interest:

1) Unit discharge contraction ratio (q_2/q_1)
2) Approach flow intensity (V_1/V_c)
3) Ratio of maximum abutment scour to theoretical contraction scour (r_T)

In this section, methods for evaluating the independent dimensionless variables in Equations 5.7 are explored based on experimental findings in this thesis. The results are compared with the findings of other investigators.

5.5.1 *Calculation of the Unit Discharge Contraction Ratio*

One of the most popular software packages to calculate water surface profiles through bridge is the HEC-RAS (Hydrologic Engineering Center's River Analysis System). HEC-RAS was created to calculate one-dimensional steady and unsteady flow. When the main channel and floodplain geometry, information about bridge foundations including embankments, and data on stage and discharge are given, HEC-RAS can estimate flow characteristics such as mean velocities in the channel and floodplain, velocity distribution at each cross-section, flow depth, and hydraulic radius. While the predicted velocity distribution in the contracted bridge section is known to be deficient, reasonably good predictions of the approach velocity distribution can be made (Sturm and Chrisohoides, 2003)

After creating the HEC-RAS files with the geometry and flow data measured in

the laboratory, hydraulic variables for each experiment were determined from HEC-RAS. Then, the unit discharge contraction ratios were computed from the HEC-RAS results. Discharge per unit width through the bridge in the floodplain and the main channel was calculated by taking the integral of the depth-averaged velocities within the floodplain and the main channel under the bridge and dividing by the width of the floodplain and the main channel, respectively. Figure 5.27 shows a correlation between the measured and the calculated q_2/q_1 used by HEC-RAS in the bridge section, confirming that the 1D model is not good enough to predict velocity distribution in the contracted bridge section because the flow field in the bridge section has complex three-dimensional behavior.

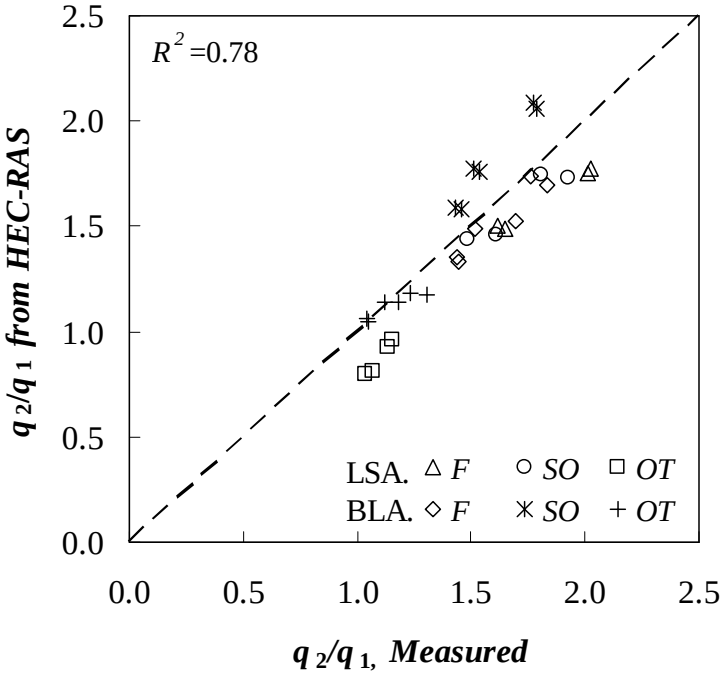

Figure 5.27 Correlation between measured and predicted q_2/q_1 by HEC-RAS

One other method was suggested by Sturm and Janjua (1994). They suggested the use of the discharge contraction ratio, M, defined as the ratio of unobstructed discharge due to the bridge embankments in the approach flow channel to total discharge at the beginning of scour as an estimate of q_1/q_2 .

$$M = \frac{Q - Q_{obst}}{Q}, \tag{5.9}$$

where $Q(= Q_{m1} + Q_{f1a} + Q_{f1b})$ is the total discharge through the bridge opening and $Q_{obst}(= Q_{f1b})$ is the obstructed floodplain discharge over a length equal to the abutment length projected onto the approach flow section as shown in Figure 5.28. The authors showed that M is approximately equal to the ratio of the discharge per unit width in the approach and the contracted floodplain areas, q_{f1}/q_{f2} , for an abutment that terminates on the floodplain in their experiments. The compound channel geometry was different in their experiments and only free flow was considered

Sturm (2004) suggested using an imaginary interface as the centerline of the main channel when abutments are situated on both sides of the main channel because their experiments were conducted in a half section of the compound channel as shown in Figure 5.28. However, if abutments are situated on both sides of the floodplain, using the imaginary interface at the centerline of the main channel might not be appropriate. For example, in the experiments reported herein, the right abutment is set on the bank of the main channel for all cases, and the width of the main channel is small compared to the width of the right floodplain as shown in Figure 5.29. The flow in the right floodplain

interacted with the main channel flow in the bridge section, and the interaction was propagated to the left bank of the main channel bank as shown previously by the velocity measurements in Figures 4.13, 4.14, and 4.15. Thus, this experiment used a modified version of M.

$$M = \frac{Q_{un-obstructed}}{Q_{total}} = \frac{Q_{m1} + Q_{f0}}{Q_{m2} + Q_{f2}} \approx \frac{q_{m1}}{q_{m2}} \approx \frac{q_{f1}}{q_{f2}} \qquad (5.10)$$

where Q_{total} is the total discharge through the bridge opening, which is the same as the total approach flow discharge for free and submerged orifice flow cases but is only discharge under the bridge section for the overtopping flow cases. Figure 5.30 shows a correlation between the measured discharge per unit width values and the calculated discharge per unit width values based on M in the bridge section, confirming that the M can be a good estimate of q_2/q_1 (R^2=0.89). However, 2D or 3D numerical modeling should be developed for better measurements.

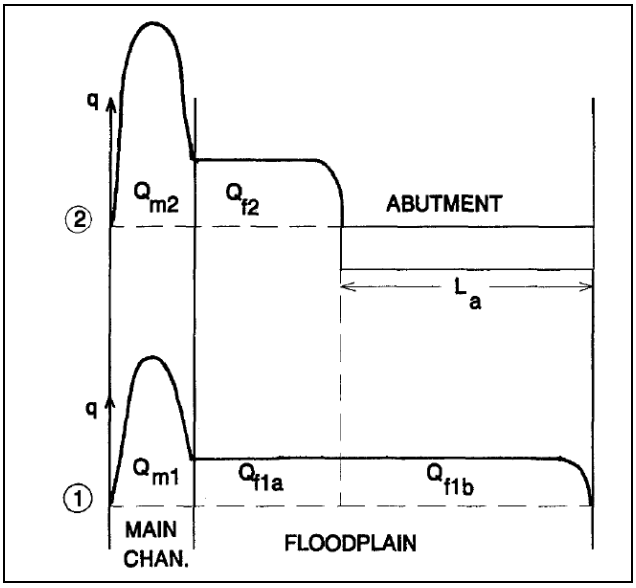

Figure 5.28 Definition sketch of the discharge distribution in the compound channel (reproduced from Sturm and Janjua, 1994)

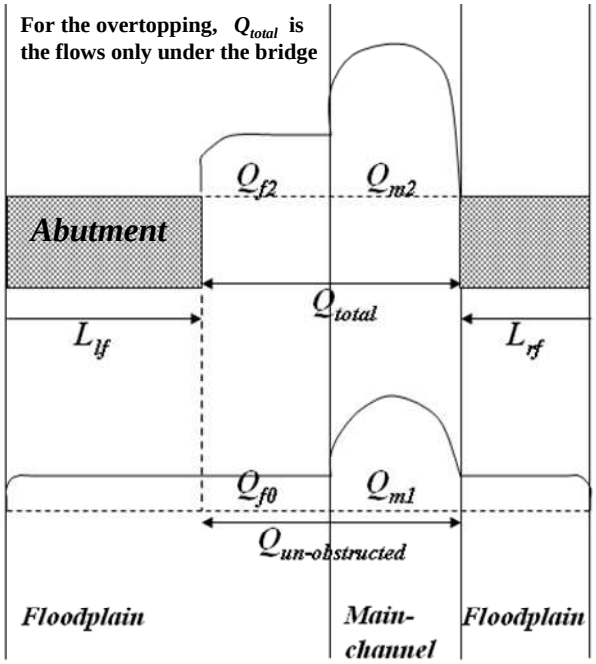

Figure 5.29 Definition sketch of the discharge distribution for this experimental setup

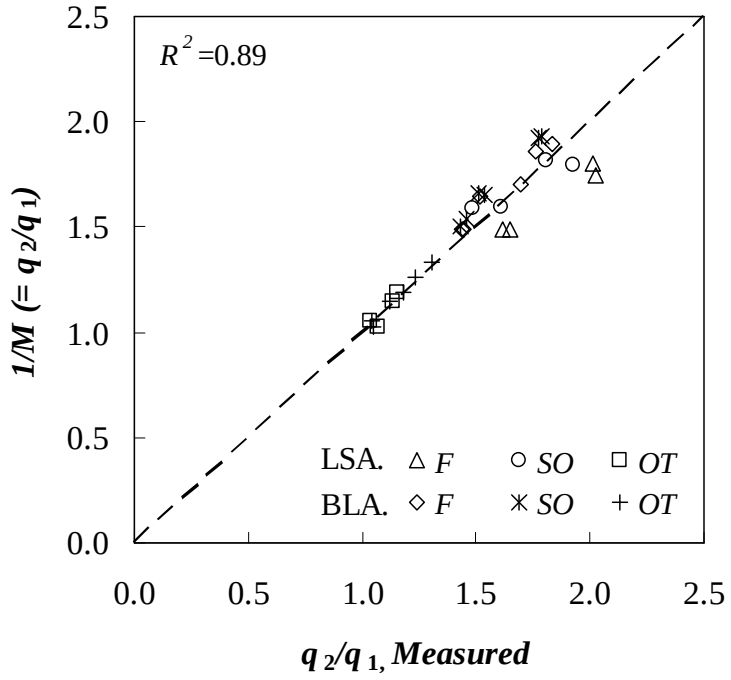

Figure 5.30 Correlation between measured and predicted q_2/q_1 by using M

The hydraulic variables in the approach section, V_1, V_c, y_1, and others, can be determined from a one- or two-dimensional numerical simulation of the water surface profiles such as HEC-RAS and WSPRO, and the q_2 can be predicted by the method explained above. However, one question arises for the calculation of M in the overtopping case because the denominator of M in Equation 5.10 is the total discharge under the bridge. Generally, the total discharge under the bridge can be assumed to be the same as the approach flow discharge for the free and submerged orifice flow cases because of continuity. However, for the overtopping case, the amount of overtopping discharge has to be calculated to predict the discharge under the bridge.

As shown in Figure 3.9, the bridge deck behaves like a broad-crested weir when the water overtops the bridge. Thus, the broad-crested weir equation was applied to predict the amount of overtopping discharge.

$$Q = C_w L (HW_r)^{3/2} \tag{5.11}$$

where Q is the amount of overtopping discharge, C_w is the weir discharge coefficient, L is the length of the roadway perpendicular to the flow, and HW_r is the head measured above the crest. The value of C_w can be determined by the discharge coefficient and submergence factor (Federal Highway Administration, 2001). The overtopping discharges on top of the left floodplain, the main channel, and the right floodplain were calculated separately, and summed to determine the total amount of overtopping discharge. Table 5.4 shows the summary of the experimental results, and Figure 5.31 shows the correlation between the measured overtopping discharge and the calculated overtopping discharge using Equation 5.11. The value of stand error was 0.035 and the value of R^2 = 0.85.

Table 5.4 Summary of the experimental results for the calculation of overtopping discharge

Run	L_a/B_f	*Measured Q (cfs)*			*Calculated Q (cfs)*			
		Q_{total}	Q_{br}	Q_{ot}	LF Q_{ot}	MC Q_{ot}	RF Q_{ot}	Total Q_{ot}
3	0.53	5.89	3.80	2.097	1.218	0.503	0.340	2.062
6		5.33	3.39	1.941	1.069	0.471	0.314	1.854
9	0.71	5.55	3.29	2.265	1.367	0.559	0.381	2.306
12		4.82	2.93	1.890	1.161	0.471	0.317	1.949
15	0.88	4.71	2.54	2.174	1.263	0.526	0.333	2.123
18		4.06	2.32	1.743	1.104	0.463	0.297	1.864

Note: Measured Q_{br} = Discharge under the bridge; $Q_{ot} = Q_{total} - Q_{br}$

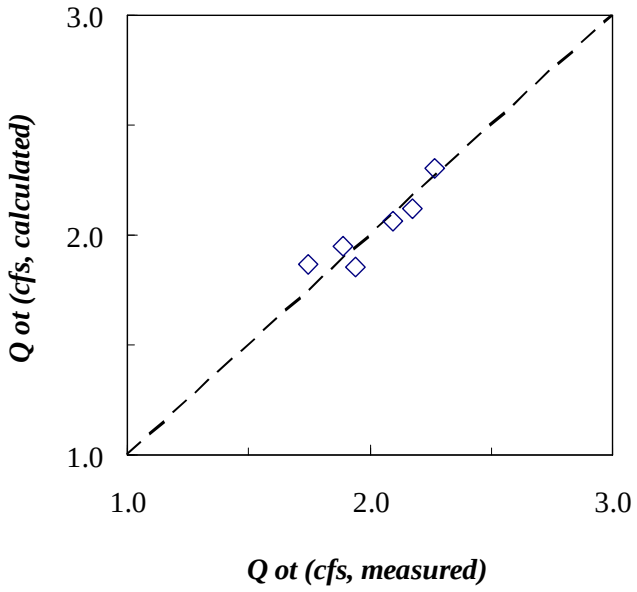

Figure 5.31 Correlation between measured and calculated overtopping discharge

5.6 *Comparison With Other Investigators' Results*

The maximum scour depths measured around the abutment were compared with the experimental data of two other investigators (Sturm (2004, 2006)) and Ettema et al. (2008)) whose experiments were conducted in a compound channel with several different lengths of fixed abutments (Sturm (2004) and erodible abutments (Ettema et al. (2008)) in the free flow condition. Their suggested methods were derived based on dimensional analysis and the experimental data with the same assumption as in this thesis, which is that abutment scour can be a local amplification of contraction scour associated with flow through a long contraction. Results of the comparison show that the degree of erodibility of an abutment is an important variable that should be more thoroughly investigated for a more accurate prediction of the abutment scour depth.

Sturm (2004) conducted clear water abutment scour experiments in a half-section of a compound channel with a floodplain width of 12 ft and a main channel width of 1.8 ft. The abutment was a solid spill-through (ST) abutment; that is, it was a solid block that extended to the floor of the flume as a model of a sheet-pile protected abutment. The ratio of the abutment length to the floodplain width, L_a / B_f, varied from 0.32 to 1.0, and the ratio of the approach velocity to the approach critical velocity, V_1 / V_{c1}, varied from 0.25 to 0.6 in the floodplain and from 0.3 to 0.7 in the main channel. The ratio of the floodplain flow depth to the flow depth in the main channel in the approach section, y_{f1} / y_{m1}, varied between 0.13 and 0.43. Based on the location of the maximum scour depth, experimental results for $L_a / B_f \geq 0.88$ were categorized as bankline abutment

(BLA) scour while results from the case of $L_a / B_f < 0.88$ were categorized long setback abutment (LSA) scour. The time to reach equilibrium scour varied between 1 and 3 days, depending on the degree of flow contraction and flow velocity distribution. Detailed experimental results can be found in Sturm (2004, 2006).

Ettema et al. (2008) also conducted abutment scour experiments in a half section of a compound channel. Instead of using a solid, non-erodible embankment, the authors used compacted sand to model a spill-through abutment protected by rock riprap for their experiments. Their experimental results involved two scour conditions, which were called Scour Conditions A and B. Scour Condition A occurred as scour of the main channel portion of a compound channel for abutments close to the main channel bed. Scour Condition B was scour of the floodplain. It occurred in the abutments set well back from the main channel, which was the same scour condition as that in the LSA.

Ettema et al (2008) varied the length of an abutment to create a wide range in the discharge contraction ratio through the bridge section. The ratio of the abutment length to the floodplain width, L_a / B_f, varied from 0.0 to 0.69 for Scour Condition B and 0.0 to 1.0 for Scour Condition A. However, they maintained a constant value of V_1 / V_{c1}, which was 1.2 for Scour Condition A in the approach main channel (i.e., live bed scour) and 0.9 for Scour Condition B in the approach floodplain (i.e., clear water scour). They also maintained a constant approach flow depth during the entire set of experiments.

The experimental data from the LSA experiments in this study were plotted along with Sturm (2004) and Ettema et al (2008) in terms of the non-dimensional approach floodplain variables as shown in Figure 5.32. In the erodible abutment experiments (i.e.,

this study and Ettema et al (2008)), the non-dimensional maximum scour depth gradually increases and reaches a constant value for large values of the independent variable shown on the x-axis. However, results from the solid abutments followed almost a linear trend with the independent non-dimensional variable and showed a much larger value of the normalized maximum scour depth than that those from the erodible abutments. This confirms that the solid and erodible abutments behave differently during the scour process. The solid abutment remains intact during the experiments, and the resulting maximum scour hole occurs around the upstream toe of the abutment; for the erodible abutment, however, the side slope of the abutment became unstable during the experiments, and the resulting region of the deepest scour was observed around the downstream side of the abutment because of the relocated riprap, as explained in the previous section.

Furthermore, this comparison explains why engineering judgment is important in the design of an abutment because if the abutment is designed to remain completely intact during flooding, the resulting scour depth is larger. Therefore, deeper footing piles that prevent damage to both the abutment and the pier are imperative. If an abutment allows only slight failure, the resulting scour depth is less, but superstructures such as girders or pavement might be vulnerable to even slight abutment failure, which could lead to disaster. Thus another question arises: “How much failure should an abutment design allow?”. Determining an acceptable degree of failure will require more extensive research on embankment erosional strength. The comparison also explains why current methods overpredict scour depth: because current research on abutment scour has focused only on

scour around a solid abutment.

The importance of embankment erosional strength can be understood if one reviews the comparison between this study and Ettema et al (2008) in Figure 5.32. Results from this study showed a slightly larger scour depth than those from Ettema et al., even though the experimental data appeared to follow a similar trend. This finding might be explained by the erosional strength of the erodible embankment. In this study, the erodible embankment was compacted by hand, and the resulting erosional strength was sufficient to withstand hydraulic failure (see the time development of abutment scour in Appendix C). However, a greater portion of the embankments in Ettema et al. failed completely during their experiments, and several photographs showed that entire abutments were washed out because they were weak. As a result, the discrepancy between the results of this study and those of Ettema et al. (2008) probably stemmed from differences in embankment erosional strength. This finding indicates that embankment erosional strength should be more thoroughly examined for a more accurate prediction of abutment scour depth.

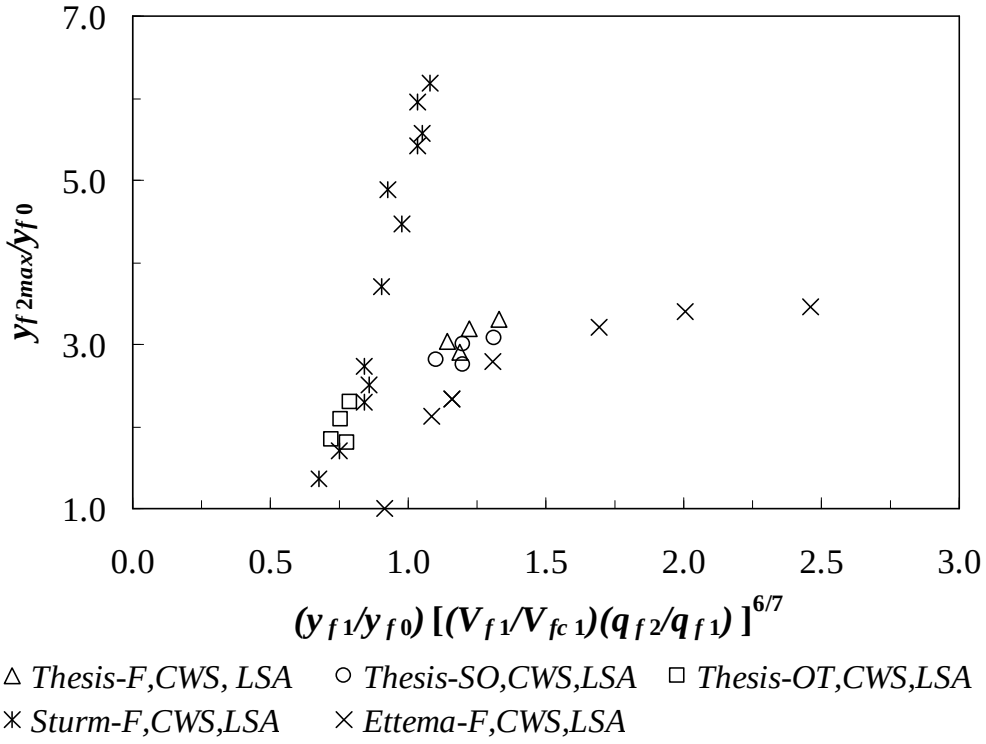

Figure 5.32 Comparison with other investigators' results for the long setback abutment (Note: Flow type: F=free flow; SO=submerged orificeflow; OT=overtopping flow: CWS=clear-water scour; LSA=long setback abutment)

The results of the comparison of BLAs can be seen in Figure 5.33. The results from BLA experiments in Ettema et al were only used for comparison in this section to keep the consistency between the results from Sturm (2004) and Ettema et al (2008). In contrast to the LSA results, the data relating to solid abutments are quite similar to those for erodible abutments in the case of the BLA. For the LSA, maximum scour occurred around the downstream side of the abutment for an erodible embankment and at the upstream corner of the abutment for a solid abutment, respectively. Maximum scour for the erodible BLA still occurred around the downstream side of the abutment, but for the

solid BLA, the maximum point was located in the main channel and laterally displaced from the abutment face rather than at the upstream corner of the abutment. For the BLA, severe flow contraction plays a greater role in the development of maximum scour depth than the local flow structure around the abutment. As a result, it is clear that the erosional strength of the embankment becomes less important for BLA scour because it is farther away from the abutment rather than at the upstream corner of the abutment. The scour depth results of Ettema et al. (2008) for BLA showed slightly lower values than in this study because the scour condition of the former was live-bed.

This study has established upper and lower limits on abutment scour based on whether the embankment is solid or erodible and protected by rock riprap. In the short term, while further studies of the effect of embankment erosional strength are made, it is recommended that abutments be set back from the bank of the main channel and protected by a rock riprap blanket and apron designed as indicated in HEC-23. The amount of the setback should be at least $6y_{f1}$.

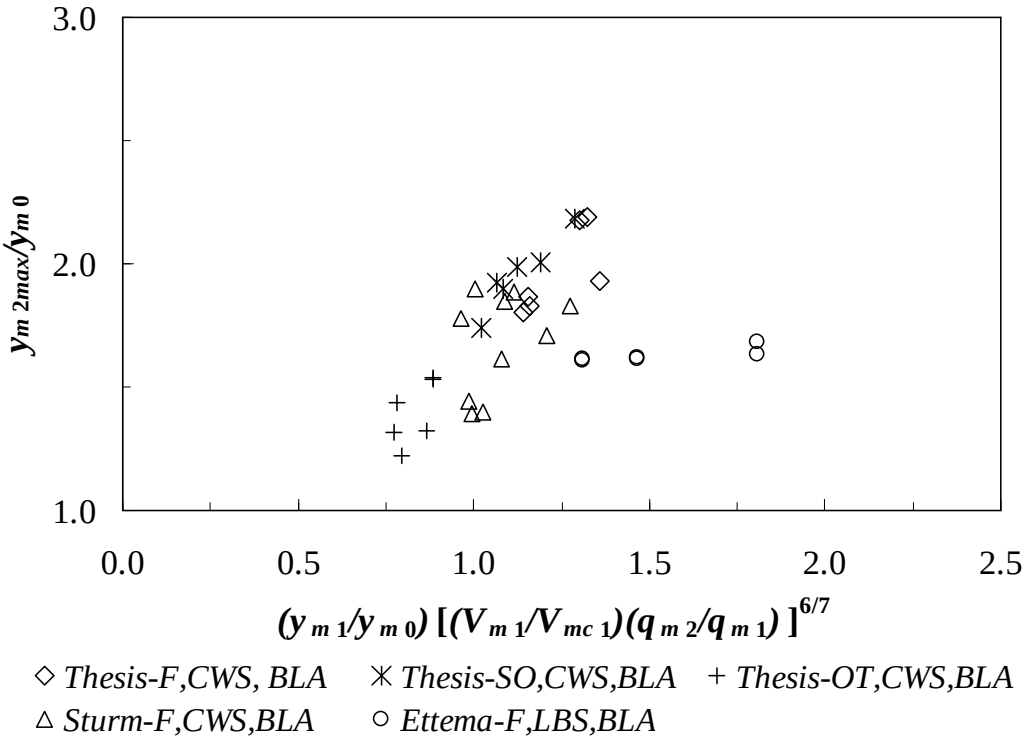

Figure 5.33 Comparison with other investigators' results for the bankline abutment (Note: Flow type: F=free flow; SO=submerged orifice flow; OT=overtopping flow: CWS=clear-water scour; LBS=live-bed scour; BLA=bankline abutment)

CHAPTER VI

SUMMARY AND CONCLUSIONS

6.1 *Summary*

One of the most common causes of bridge failure is scouring around a bridge abutment. Despite the numerous studies of scour around abutments, the physical mechanisms of abutment scour still remain unclear because they are very complex. In general, the main causes of abutment scour are the effects of higher velocity and local turbulence created by the bridge constriction. When the flow area is reduced by a bridge abutment and a highway earth-fill embankment, flow accelerates because of channel flow constriction, and the higher velocity and associated shear stress remove bed material from the contracted section. In addition to the higher velocity due to the flow acceleration, local flow structures, such as the horseshoe and tornado-like vortices resulting from flow separation associated with higher turbulence kinetic energy, result in additional scour around the abutment.

Furthermore, recent extreme rainfall events associated with global warming can often result in submerged orifice flow or embankment and bridge overtopping flow, in which the flow field around the abutment is more complex because of vertical flow contraction in addition to existing lateral flow contraction. As a result, problems pertaining to abutment scour pose overwhelming challenges resulting from a lack of a thorough understanding of complex flow structures and scour mechanisms around the

bridge abutment.

Most current laboratory studies focus only on cases of free-surface flow conditions and therefore, do not take bridge submergence into account. Furthermore, considerable research on abutment scour has focused on the simpler and idealized situations of scour around solid abutments placed in straight rectangular channels even though many abutments are erodible and located in compound channels whose geometry and hydraulic characteristics are site-specific in the real world.

Therefore, in this study, to suggest clear-water abutment scour prediction methods under extreme hydrologic conditions, abutment scour experiments were carried out in a compound channel with various lengths of erodible abutments. Three different flow types (free, submerged orifice, and overtopping flow) were simulated in the experiments. The scaled model cross sections, including river bathymetry, were based on field surveys for a previous physical model study but were slightly modified and simplified for this study. The erodible abutments and embankments were carefully compacted by hand and protected by rock riprap using an existing design standard in order to withstand hydraulic failure. This approach was successful in maintaining the general integrity of an embankment during overtopping, as observed in the prototype of the hydraulic model study. We used three different lengths of embankment on the left floodplain while setting the abutment on the bankline of the right floodplain. This arrangement allowed the simultaneous study of both bankline and setback abutments. For the investigation of the characteristics of abutment scour in free-surface flow, submerged orifice flow, and overtopping flow cases, a scaled prototype bridge deck typically specified in Georgia was

modeled in the laboratory. An acoustic Doppler velocimeter was utilized to measure the velocity and the turbulence intensity as well as the bed elevations before and after scour.

The time development of scour around abutments was measured at six intermediate time durations for each experiment to understand the complex flow physics and resulting sediment transport around an abutment. It was observed that the scouring process and the resulting scour hole around a long setback abutment was different depending on the flow type. For free and submerged orifice flow, the shape of the scour hole periphery was curved around the abutment. The resulting location of the maximum scour depth in the floodplain moved over time from the upstream corner of the abutment face to a point that was diagonally displaced in the downstream direction from the downstream toe of the abutment over time. However, for overtopping flow, the scour hole was further elongated in the streamwise direction, and the resulting location of the maximum scour depth moved over time in the streamwise direction to a point farther downstream of the setback abutment.

The different shapes of the scour hole and the location of maximum scour depth can be explained by the measured velocity distributions around the abutment. The velocity measurements near the bed showed that the accelerated flow around the abutment was deflected around the upstream face of the abutment and separated on the face of the abutment. The recirculation zone occured behind the separation point for the setback abutment in free flow and submerged orifice flow, and the higher velocities occurred just outside of the recirculation region where the deepest scour was located. However, for the overtopping case, the flow separation and recirculation region were

located farther downstream of the abutment because the overtopping discharge acted like a surface jet, resulting in an elongated scour hole in the streamwise direction.

For the bankline abutment, the maximum scour depth occurred on the main channel bank on the downstreamside of the abutment in all three different flow types. However, the scouring process over time displayed different characteristics than for the setback abutment. Scour holes initially developed at two locations in the main channel just off the toe of the abutment and on the downstream side of the abutment which then converged after some time had passed because of the higher degree of flow contraction.

The scouring process for the short setback abutment showed more complicated scenarios. Because of a greater degree of flow contraction through the bridge opening (short setback on the left floodplain and bankline on the right floodplain), three different scour holes initially developed and converged over time, and then finally some cases showed two remaining scour holes while the others showed only one remaining scour hole through the bridge section. The more severe flow contraction resulted in the scour hole being located near the abutment and in the main channel in addition to influencing the degree of abutment failure itself depending on the erosional strength of the abutment.

In this study, it was observed that the maximum scour hole occurred near the downstream side of the erodible abutment, in contrast to the solid abutment in which case it has been observed to concentrate near the upstream corner of the abutment in previous studies. The unstable nature of an erodible abutment and the resulting riprap sliding into the scour hole during the experiments played an important role in moving the location of the maximum point of scour over time and limiting its maximum depth.

The scour depth normalized by the approach water depth followed a linear trend with the logarithm of the dimensionless time variable, $V_1 t / y_1$, and then reached equilibrium after a measured equilibrium time (T_{eq}). It was observed that the normalized equilibrium time is a weak function of $(q_2/q_1)(V_1/V_{c1})$ but depends more on the flow type and the degree of abutment setback. Nevertheless, for all experiments, $V_1 T_{eq}/y_1 \leq 1 \times 10^6$; this criterion is important for the conduct of future experiments as well as for designing abutment foundations for a specified flood duration.

The effects of lateral and/or vertical flow contraction and local turbulence all contribute to scour around an abutment. As a result, the basic hypothesis in this study is that the maximum scour depth around an abutment can be predicted by a multiple of the mean-flow contraction contribution in addition to the local turbulence term. Dimensionless maximum scour depths were shown to collapse to a single relationship for all flow types when plotted in terms of an amplification factor r_T times the theoretical contraction scour given by $[(q_2/q_1)(V_1/V_{c1})]^{6/7}$; however, the constant value of r_T was 2.51 for the long setback abutments with the scour hole in the floodplain and 1.66 for bankline abutments with scour holes in the main channel (Equations 5.6). Short setback abutments were found to be a combination of these two cases but the scour hole was conservatively estimated using the main channel variables and the bankline abutment equation.

The maximum streamwise width-averaged values of TKE, $\overline{K}_b / u_*^2$, occurred at the location of the downstream toe of the embankment. These values were elevated over the width of the scour hole and were used as explanatory variables for the contribution of

the local turbulence to the scour process in order to further refine the scour depth relationship. In this formulation, decreasing values of r_T were explained by increasing degrees of flow contraction and decreasing values of TKE as flow contraction effects increased and dominated local turbulence influences. The result is a suggested scour depth predictor developed in this research that depends on flow contraction ratio (q_2/q_1), sediment transport capacity $V_1/V_{c,}$ and TKE as shown in Equations 5.7; it encompasses free flow, submerged orifice flow, and overtopping flow cases for large setback, bankline, and short setback abutments. The flow contraction ratio reflects not only the effects of lateral contraction but vertical contraction as well due to submerged orifice flow and overtopping flow. A simplification of the proposed formula (Equations 5.8) was also developed by showing that r_T can be related inversely to (q_2/q_1) as a surrogate for TKE decreases with increasing flow contraction ratios.

Based on theoretical concepts and laboratory measurements, a new formula for calculating maximum scour depth around an erodible abutment has been developed in this research. It has also been shown how either HEC-RAS or a discharge contraction ratio M can be used to predict the parameters in the proposed scour depth formula until more sophisticated numerical models with variable free surface and refined turbulence modeling have been developed.

Based on the suggested formulas, a procedure for predicting the equilibrium abutment scour depth was introduced:

1. Determine approach independent hydraulic variables using WSPRO or HEC-RAS to compute water surface profiles through the bridge

2. Calculate approach flow intensity (V_1/V_c) from the results in the first step and the sediment properties related to initiation of motion
3. Determine unit discharge contraction ratio (q_2/q_1) directly from HEC-RAS or M (Equation 5.10)
4. If the bridge is to be designed for overtopping, the broad-crested weir equation as shown in Equation 5.11 can be used to calculate overtopping discharge. The result can be used in step 3.
5. Ratio of maximum abutment scour to theoretical contraction scour (r_T) can be estimated as a constant or as a function of computed TKE from a 3D numerical model or from (q_2/q_1) obtained from Step 3.

Finally, this research has contributed for the first time an analysis of the present sour depth results for different flow conditions (free, submerged orifice, and overtopping flow) as well as the results of others which include the influence of the degree of erodibility of the embankment. The comparisons between erodible and solid long setback abutment show that the solid and erodible abutments behave differently during the scour process and explain why engineering judgment is important in the design of an abutment. When the abutment is designed to remain completely intact during flooding such as a solid abutment, the resulting scour depth is larger. However, if an abutment allows only slight failure such as with an erodible abutment protected by rock riprap, the resulting scour depth is less, but the bridge superstructure might be vulnerable depending on the "degree of failure". In effect, this research shows the minimum and maximum bounds of abutment scour depending on the type of abutment material between the extremes of a

solid sheet pile abutment and a rock riprap protected abutment designed according to current standards.

6.2 *Conclusions*

One of the important contributions of this research to the problem of bridge abutment failure due to scour is development of a new scour prediction formula for erodible embankments that includes submerged orifice flow and overtopping flow in addition to free flow. This study reproduced possible flow and geometry conditions that are very similar to those encountered in the field such as a bridge with rock-riprap protected erodible abutments subject to overtopping flow conditions, and suggested a newly developed abutment scour formula for extreme hydrologic conditions. Numerous studies have been conducted since the 1980s on scour around an abutment, but almost of the studies have focused on the case of free-surface flow in simpler idealized situations with a solid abutment. Some researchers studied scour depth for vertical flow contractions, but they only considered the vertical contraction without lateral contraction. It is concluded that the suggested scour depth prediction formula in this thesis based on amplification of the theoretical contraction scour can form the basis for future work that broadens the range of dimensionless variables covered by the formula between the two limits for solid vs. erodible abutments. In the near term, it offers an improved and more informed estimate of abutment scour depths and suggests how the effects of flow turbulence and flow constriction can be combined in a single formula for abutment scour depth prediction.

In the development of a new scour formula, this study presented a connection between measured TKE and the scour process. It is concluded that these results can be used as a guide for future development and validation of CFD models that accurately predict the properties of turbulence resulting from flow interaction with obstructions in order to generate numerical results for a wider range of channel and bridge geometries. The goal will be to increase the applicability of the proposed scour formula for more conditions than can be reasonably explored with physical models alone.

Finally, it is concluded that the reasons why a large disparity has existed previously between laboratory formulas for abutment scour and field data is due to a lack of laboratory data collected from more realistic compound channel models; an overconservative addition of abutment and contraction scour; and a previous lack of accounting for the differences between solid and erodible abutments. The embankment erosional strength has been shown to be a key explanatory variable in estimating abutment scour. As a result, the necessity for more research on the measurement of embankment erosional strength is now better understood.

6.3 *Recommended Future Study*

This study showed that abutment scour can be considered a local amplication of contraction scour and suggested three prediction equations for the calculation of maximum abutment scour. However, further research should be conducted on abutment scour in order to evaluate and protect scour-critical bridges that are subject to possible

failure. The following are suggested areas for research:

- More laboratory study of abutment scour could confirm the relationship suggested in this study for three different flow types. More laboratory studies over a wider range of (q_2/q_1) and (V_1/V_{c1}) in each flow type should be conducted, especially for very long setback abutments and very short setback abutments.
- Because velocities and turbulence properties were measured at three vertical points along the cross-section of the downstream toe of the abutment, the detailed vertical velocity and turbulence profiles should be measured along the cross-sections of the downstream and upstream toe as well as along the cross-sections of the immediate bridge upstream and downstream to explain flow structures more thoroughly.
- A three-dimensional CFD numerical model with advanced turbulence closure schemes should be applied to the laboratory model used in this research for several selected cases of abutment scour. If this comparison suggests that numerical calculations are in good agreement with laboratory experimental results, the results from numerical modeling can be used to understand the scour mechanism and complex flow structures around a bridge abutment for a wider range of flow conditions than can be studied in the laboratory alone. This effort should include three-dimensional velocity and turbulence measurements around bridge sections at different stages of scour hole development with respect to time to expand our understanding of time development of scour.

- Abutment strength should be more thoroughly examined for a more accurate prediction of abutment scour depth. Therefore, a technique that measures abutment strength should be developed.
- A well-planned, detailed field study of a bridge including real-time scour monitoring is needed for the verification of the method developed in this study.
- Further experimental investigation of the live-bed scour case should be conducted.

APPENDIX A

Final Bed Elevation Contours and Pictures

(a)

(b)

(c)

(d)

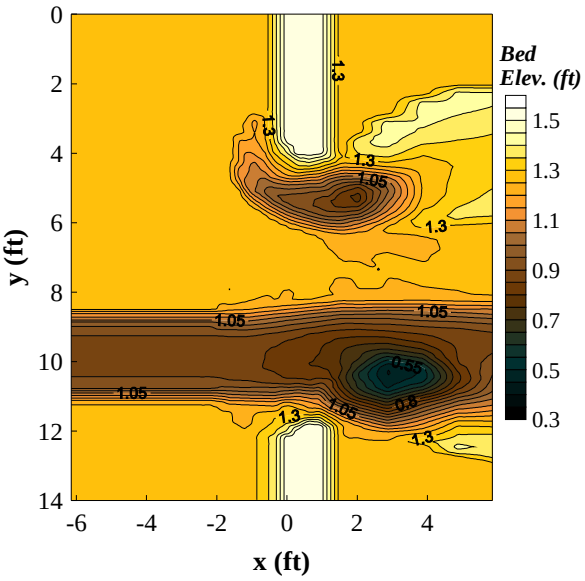

(e)

Run 1 (F), $L_a/B_f = 0.53$, Q = 3.3 cfs

(a) Looking from left-floodplain

(b) Looking from right-floodplain

(c) Looking at left abutment

(d) Looking at right abutment

(e) Contours in equilibrium

(a)

(b)

(c)

(d)

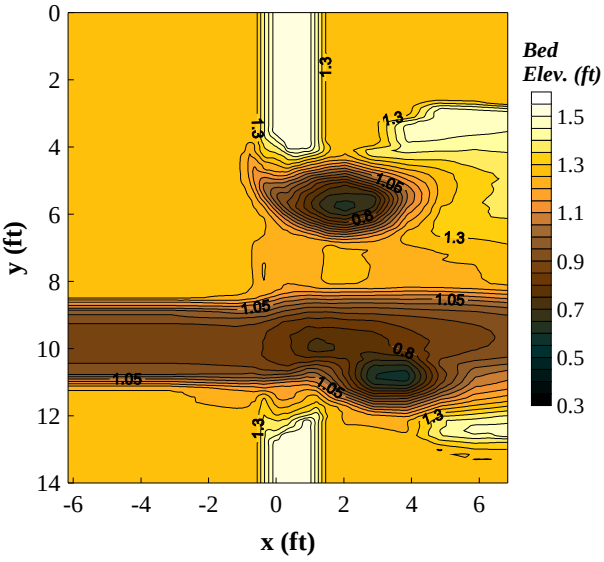

(e)

Run 2 (SO), $L_a/B_f = 0.53$, Q = 4.1 cfs

(a) Looking from left-floodplain

(b) Looking from right-floodplain

(c) Looking at left abutment

(d) Looking at right abutment

(e) Contours in equilibrium

(a)

(b)

(c)

(d)

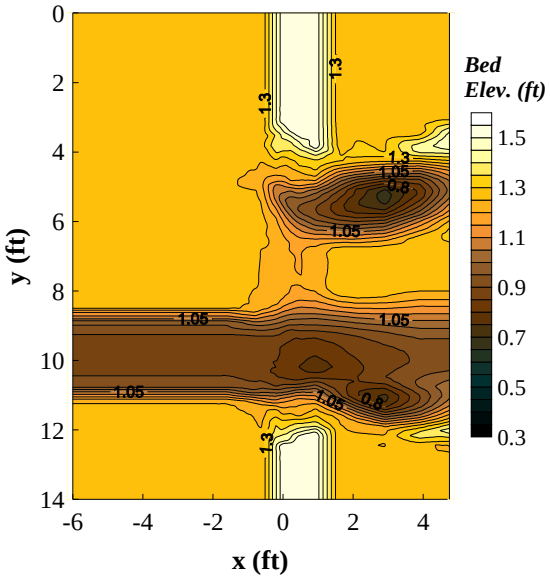

(e)

Run 3 (OT), $L_a/B_f = 0.53$, Q = 5.8 cfs

(a) Looking from left-floodplain

(b) Looking from right-floodplain

(c) Looking at left abutment

(d) Looking at right abutment

(e) Contours in equilibrium

(a)

(b)

(c)

(d)

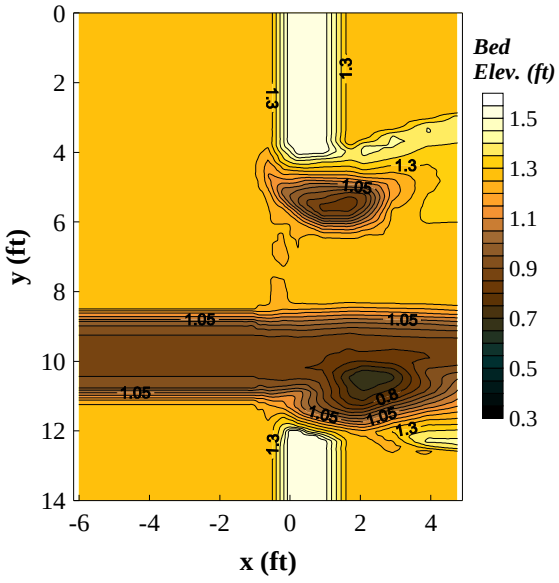

(e)

Run 4 (F), $L_a/B_f = 0.53$, Q = 3.0 cfs

(a) Looking from left-floodplain

(b) Looking from right-floodplain

(c) Looking at left abutment

(d) Looking at right abutment

(e) Contours in equilibrium

(a)

(b)

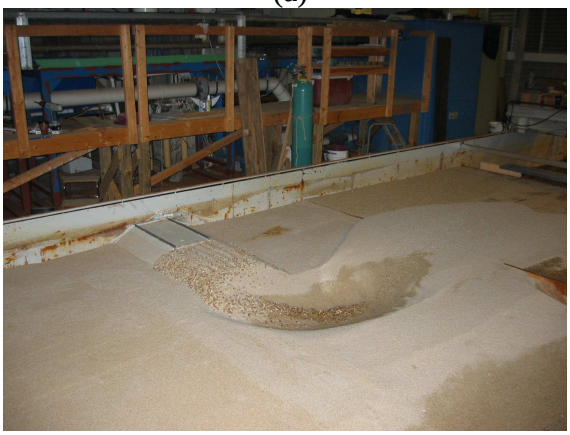

(c)

(d)

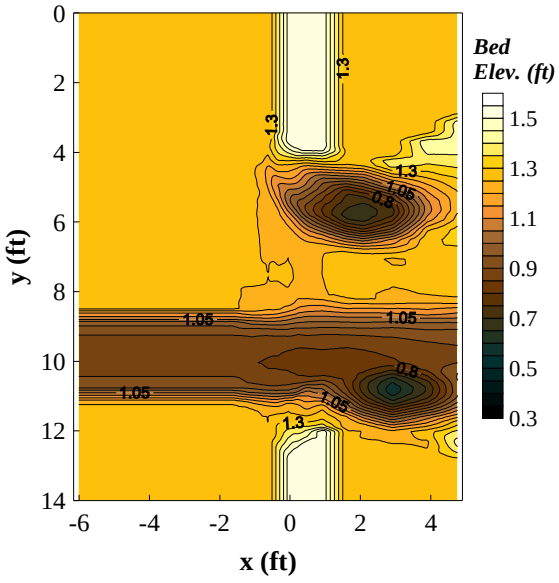

(e)

Run 5 (SO), $L_a/B_f = 0.53$, Q = 3.9 cfs

(a) Looking from left-floodplain

(b) Looking from right-floodplain

(c) Looking at left abutment

(d) Looking at right abutment

(e) Contours in equilibrium

(a)

(b)

(c)

(d)

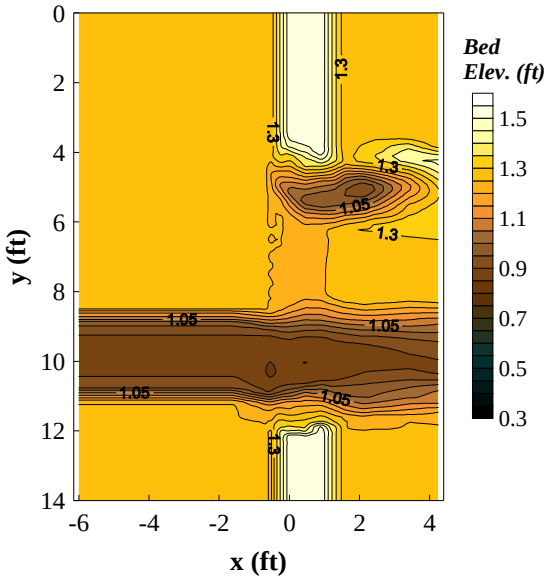

(e)

Run 6 (OT), $L_a/B_f = 0.53$, Q = 5.3 cfs

(a) Looking from left-floodplain

(b) Looking from right-floodplain

(c) Looking at left abutment

(d) Looking at right abutment

(e) Contours in equilibrium

(a)

(b)

(c)

(d)

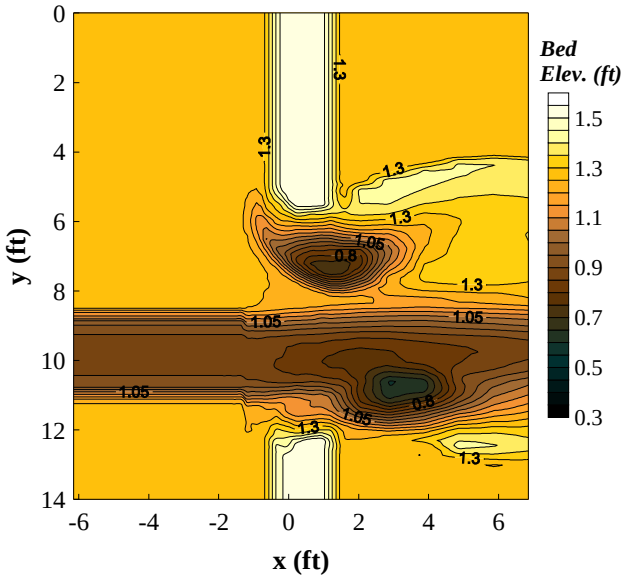

(e)

Run 7 (F), $L_a/B_f = 0.71$, Q = 3.0 cfs

(a) Looking from left-floodplain

(b) Looking from right-floodplain

(c) Looking at left abutment

(d) Looking at right abutment

(e) Contours in equilibrium

(a)

(b)

(c)

(d)

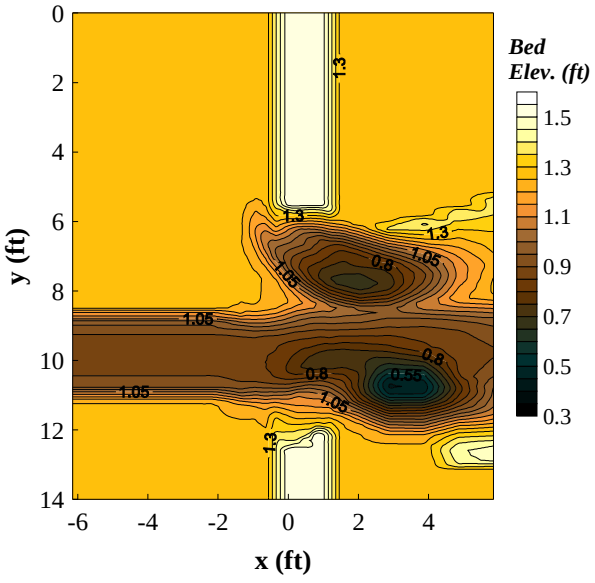

(e)

Run 8 (SO), $L_a/B_f = 0.71$, Q = 3.65 cfs

(a) Looking from left-floodplain

(b) Looking from right-floodplain

(c) Looking at left abutment

(d) Looking at right abutment

(e) Contours in equilibrium

(a)

(b)

(c)

(d)

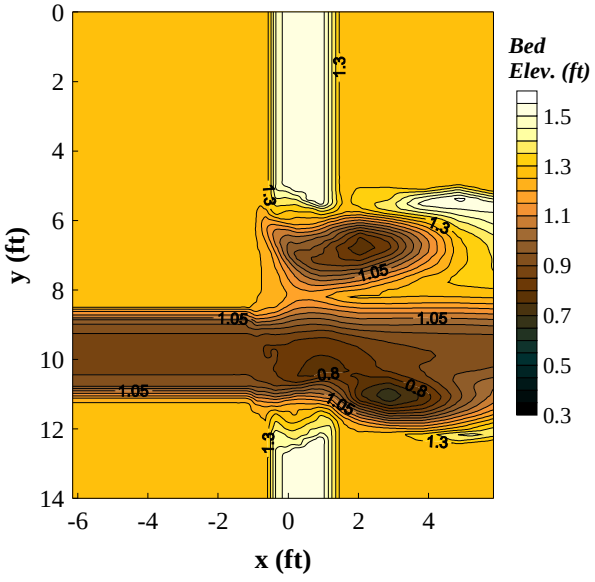

(e)

Run 9 (OT), $L_a/B_f = 0.71$, Q = 5.3 cfs

(a) Looking from left-floodplain

(b) Looking from right-floodplain

(c) Looking at left abutment

(d) Looking at right abutment

(e) Contours in equilibrium

(a)

(b)

(c)

(d)

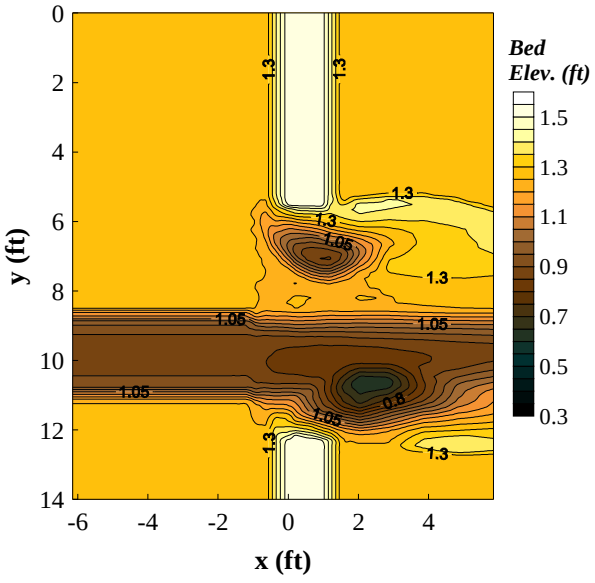

(e)

Run 10 (F), L_a/B_f = 0.71, Q = 2.6 cfs

(a) Looking from left-floodplain

(b) Looking from right-floodplain

(c) Looking at left abutment

(d) Looking at right abutment

(e) Contours in equilibrium

(a)

(b)

(c)

(d)

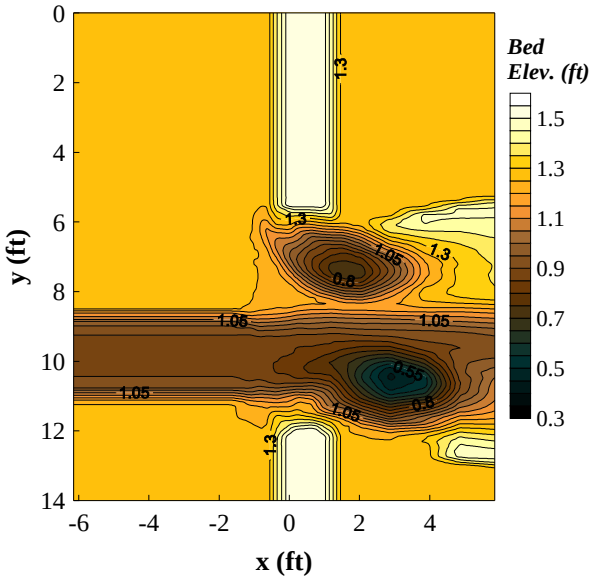

(e)

Run 11 (SO), L_a/B_f = 0.71, Q = 3.2 cfs

(a) Looking from left-floodplain

(b) Looking from right-floodplain

(c) Looking at left abutment

(d) Looking at right abutment

(e) Contours in equilibrium

(a)

(b)

(c)

(d)

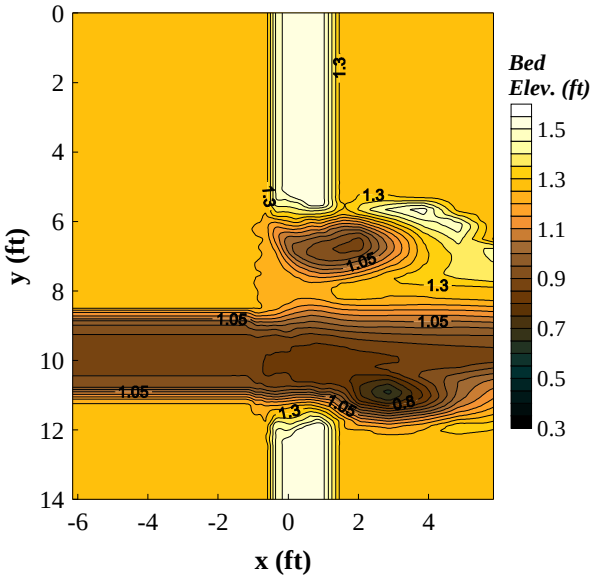

(e)

Run 12 (OT), L_a/B_f = 0.71, Q = 4.6 cfs

(a) Looking from left-floodplain

(b) Looking from right-floodplain

(c) Looking at left abutment

(d) Looking at right abutment

(e) Contours in equilibrium

(a)

(b)

(c)

(d)

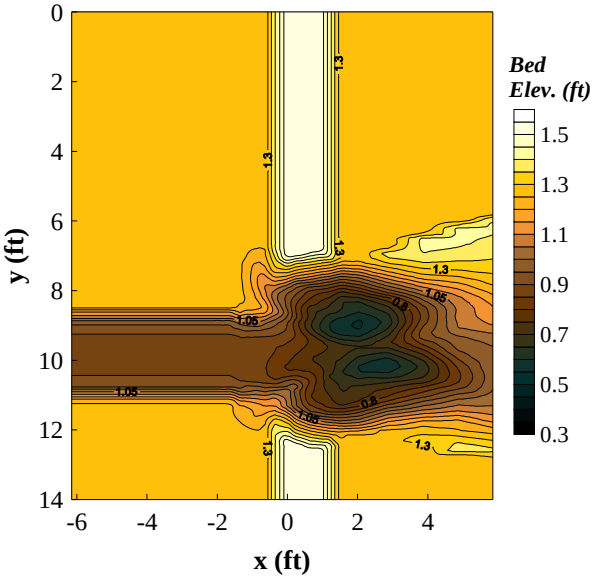

(e)

Run 13 (F), L_a/B_f = 0.88, Q = 2.6 cfs

(a) Looking from left-floodplain

(b) Looking from right-floodplain

(c) Looking at left abutment

(d) Looking at right abutment

(e) Contours in equilibrium

(a)

(b)

(c)

(d)

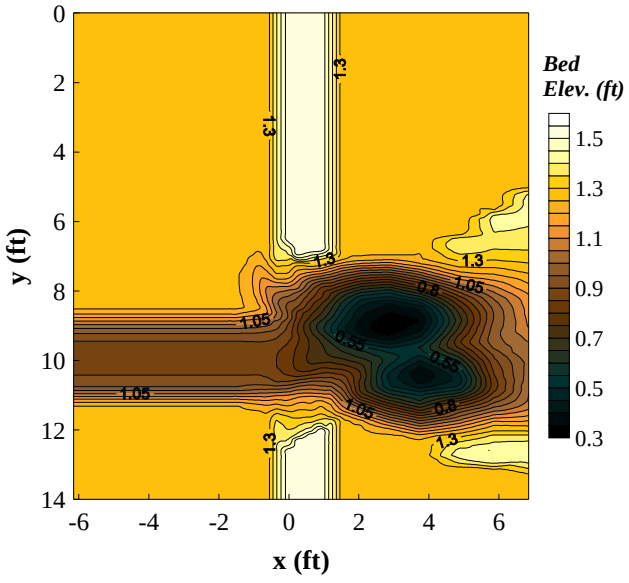

(e)

Run 14 (SO), L_a/B_f = 0.88, Q = 3.1 cfs

(a) Looking from left-floodplain

(b) Looking from right-floodplain

(c) Looking at left abutment

(d) Looking at right abutment

(e) Contours in equilibrium

(a)

(b)

(c)

(d)

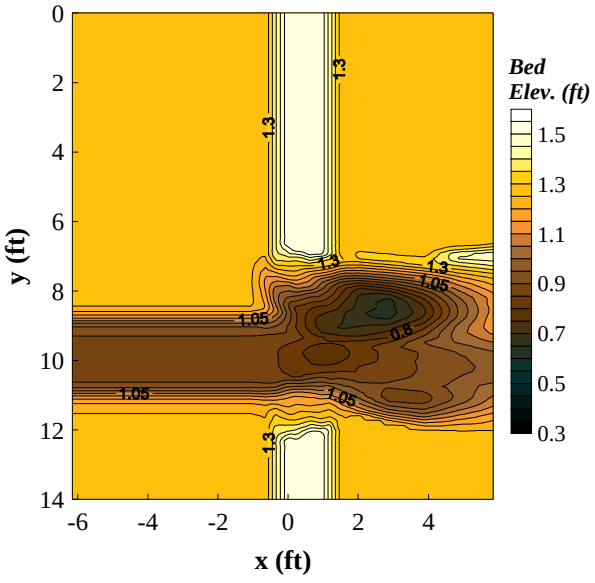

(e)

Run 15 (OT), L_a/B_f = 0.88, Q = 4.6 cfs

(a) Looking from left-floodplain

(b) Looking from right-floodplain

(c) Looking at left abutment

(d) Looking at right abutment

(e) Contours in equilibrium

(a)

(b)

(c)

(d)

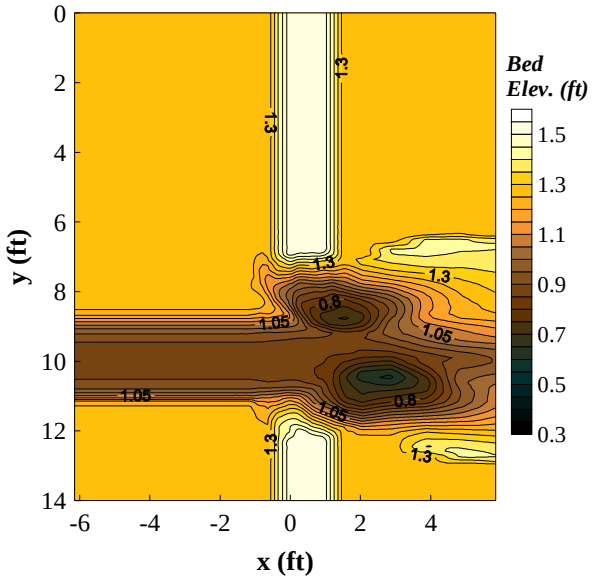

(e)

Run 16 (F), L_a/B_f = 0.88, Q = 2.2 cfs

(a) Looking from left-floodplain

(b) Looking from right-floodplain

(c) Looking at left abutment

(d) Looking at right abutment

(e) Contours in equilibrium

(a)

(b)

(c)

(d)

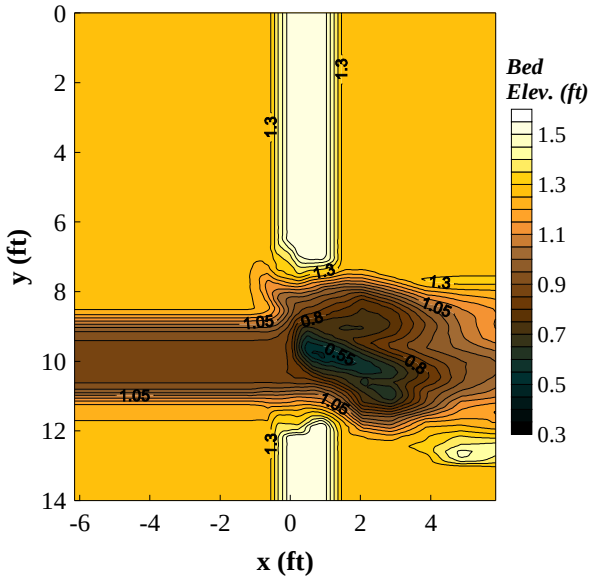

(e)

Run 17 (SO), L_a/B_f = 0.88, Q = 2.6 cfs

(a) Looking from left-floodplain

(b) Looking from right-floodplain

(c) Looking at left abutment

(d) Looking at right abutment

(e) Contours in equilibrium

(a)

(b)

(c)

(d)

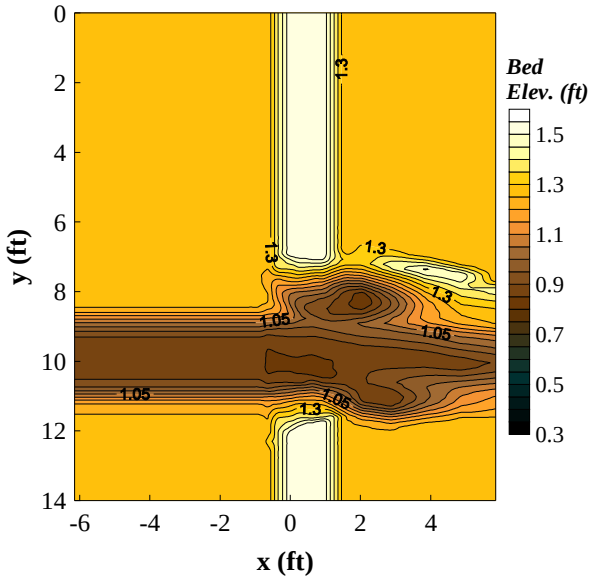

(e)

Run 18 (OT), L_a/B_f = 0.88, Q = 3.9 cfs

(a) Looking from left-floodplain

(b) Looking from right-floodplain

(c) Looking at left abutment

(d) Looking at right abutment

(e) Contours in equilibrium

APPENDIX B

Water Surface Profiles

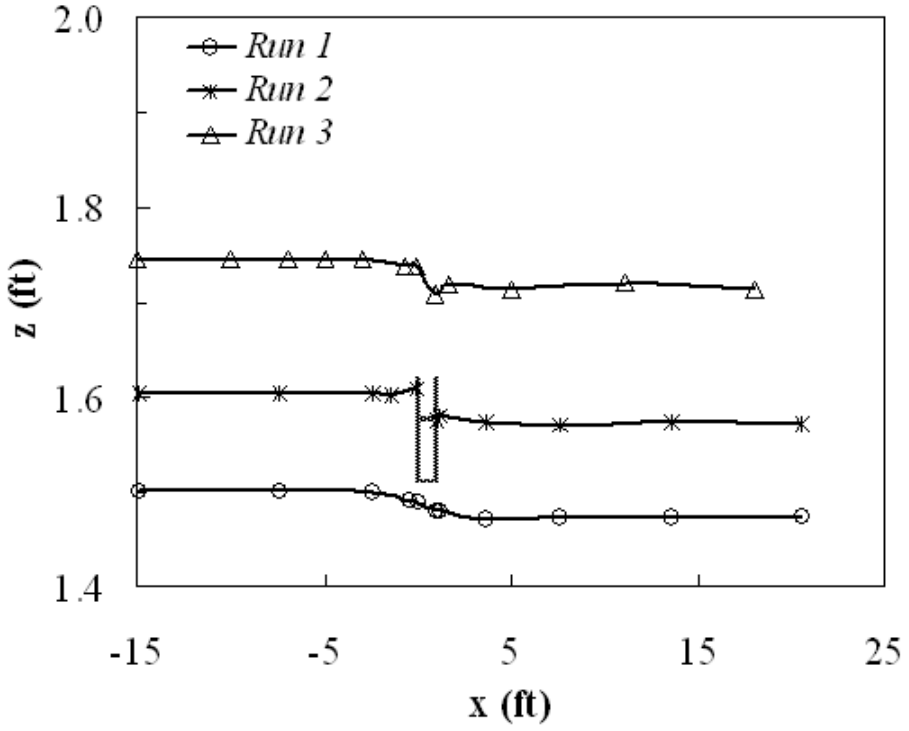

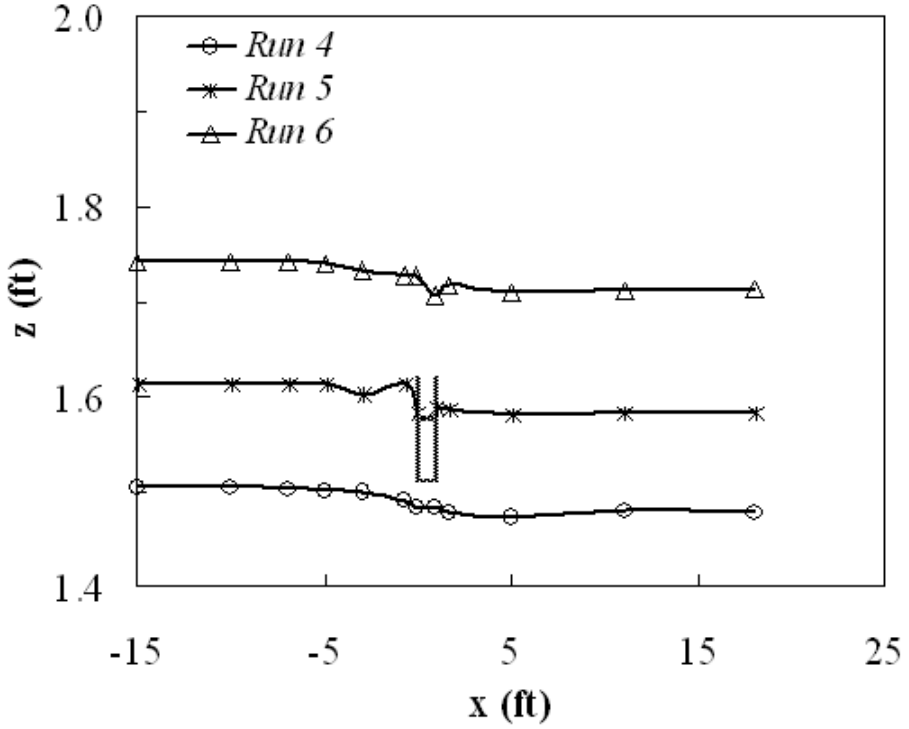

Water surface profile measurements for $L_a/B_f = 0.53$

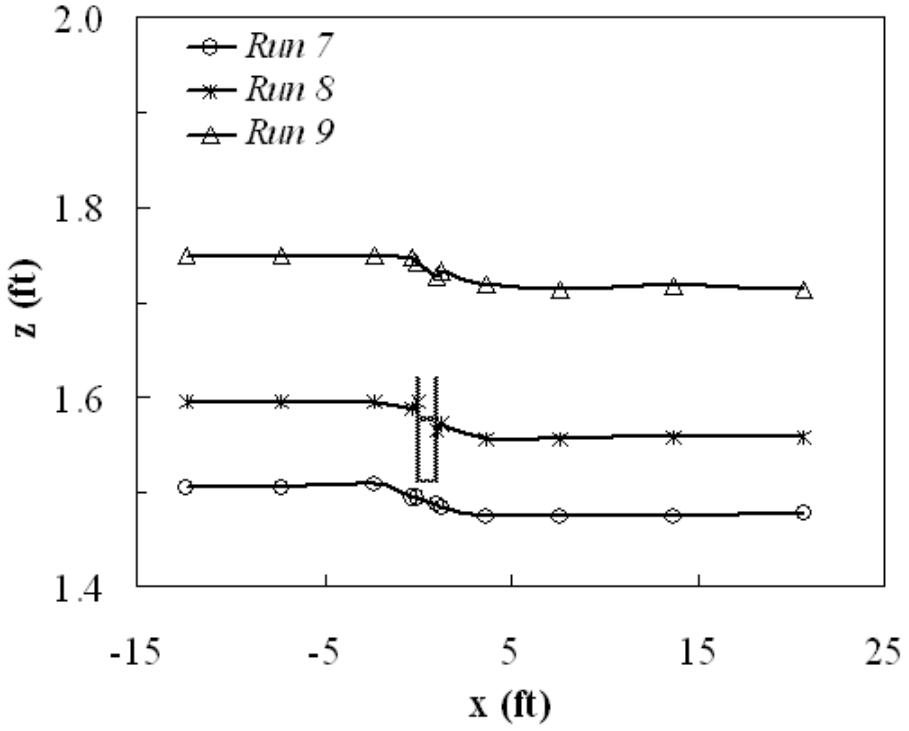

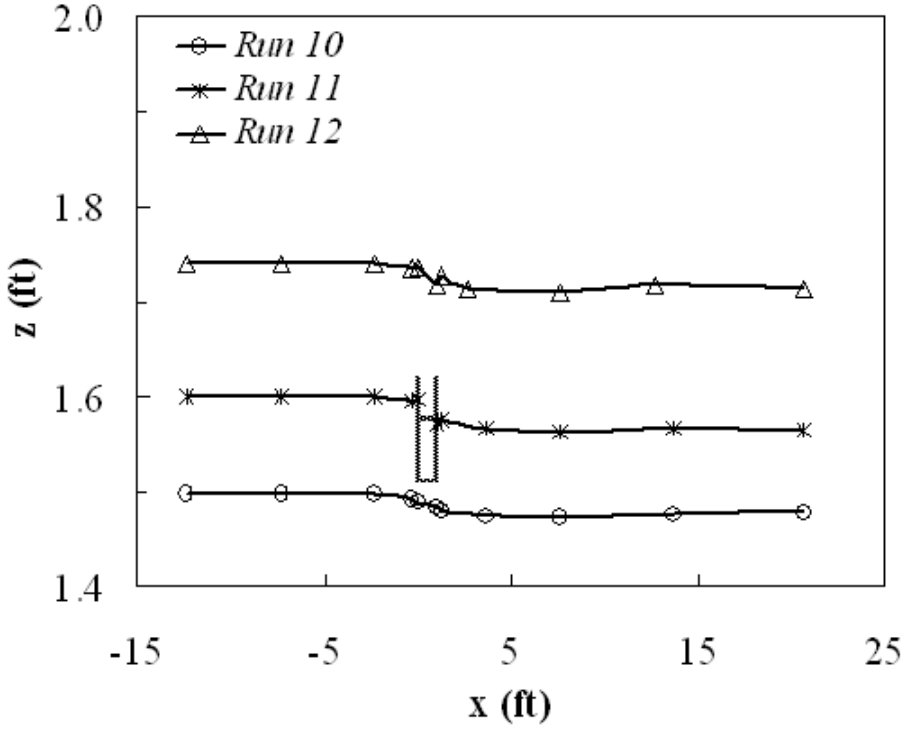

Water surface profile measurements for $L_a/B_f = 0.71$

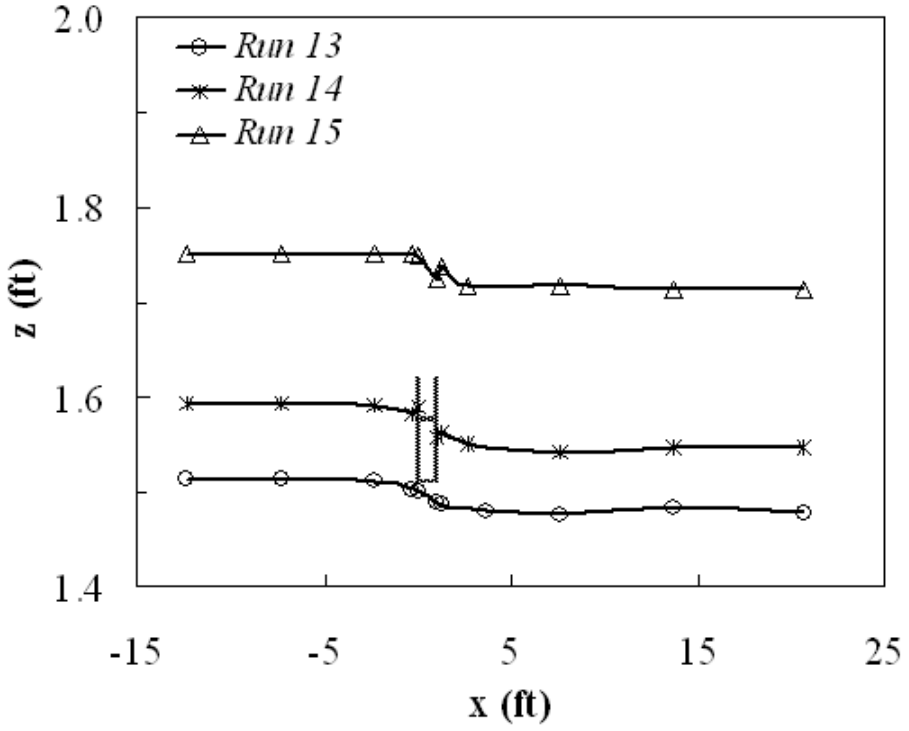

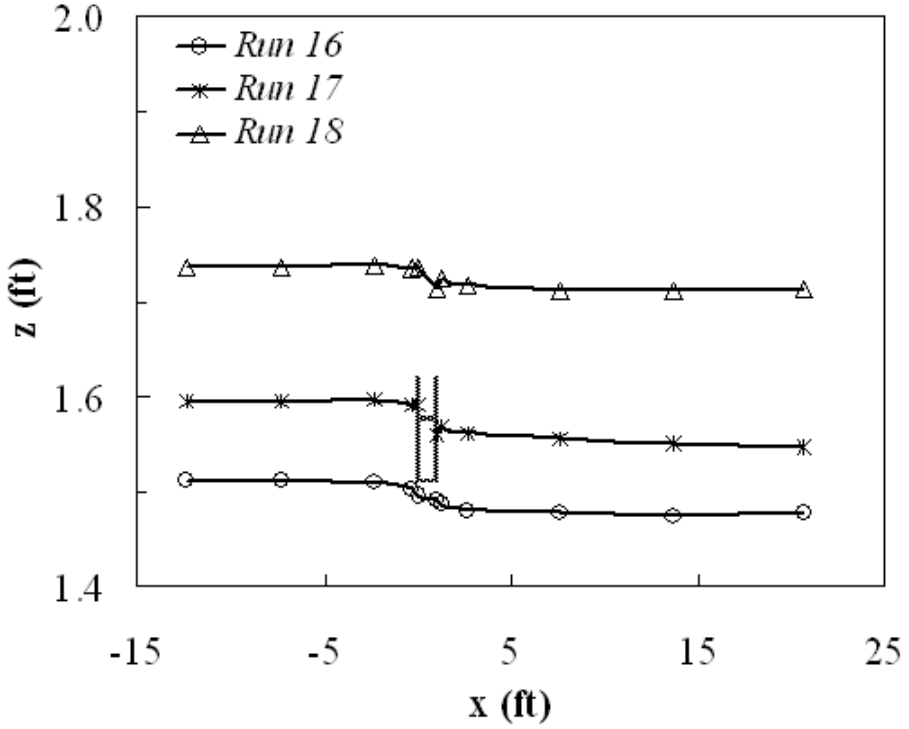

Water surface profile measurements for $L_a/B_f = 0.88$

APPENDIX C

Time Development of Abutment Scour

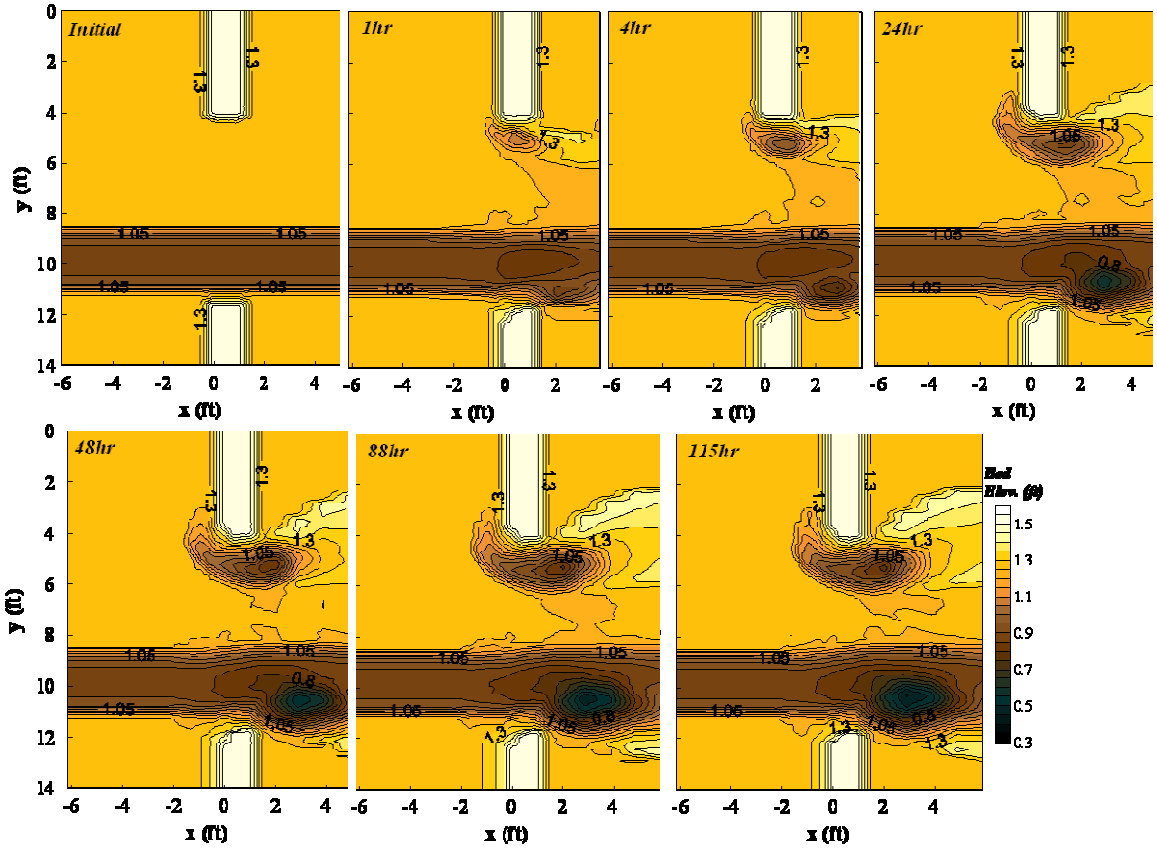

Run 1 (F), $L_a/B_f = 0.53$, Q = 3.3 cfs

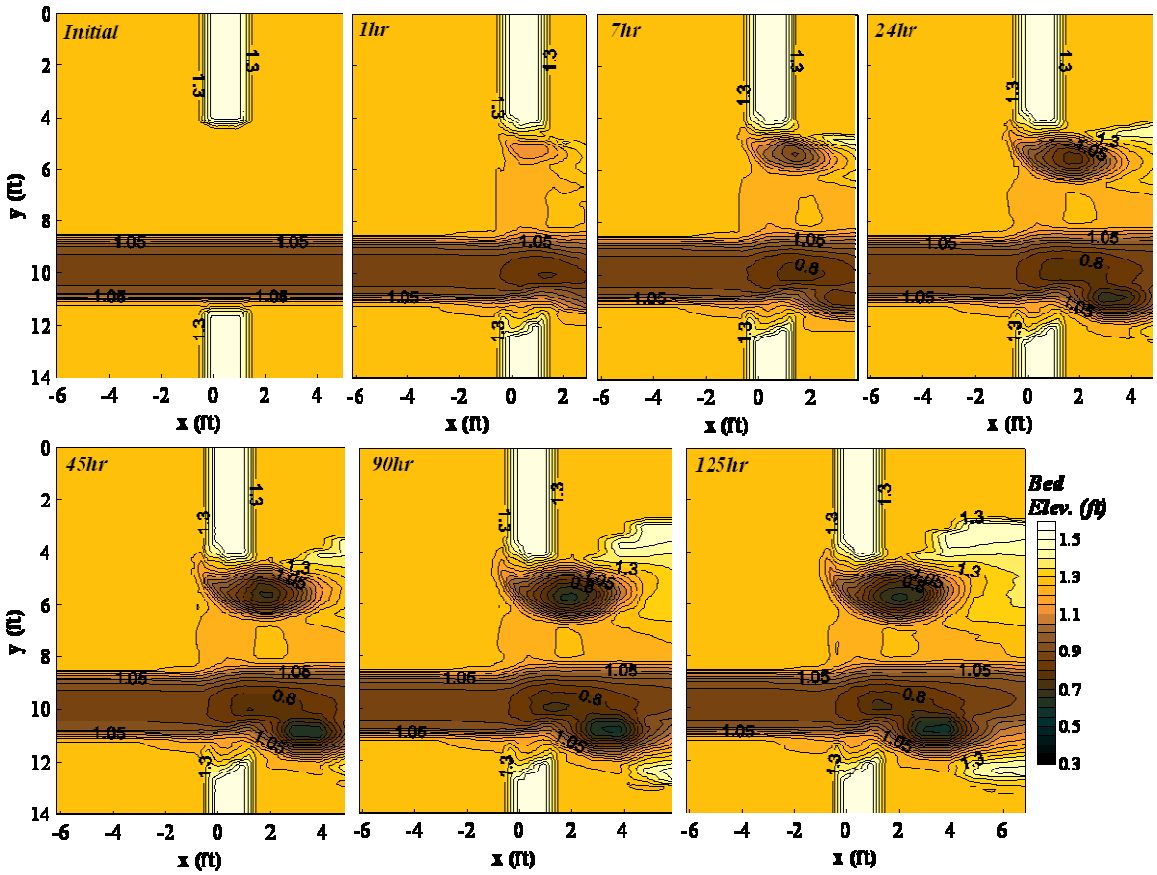

Run 2 (SO), $L_a/B_f = 0.53$, Q = 4.1 cfs

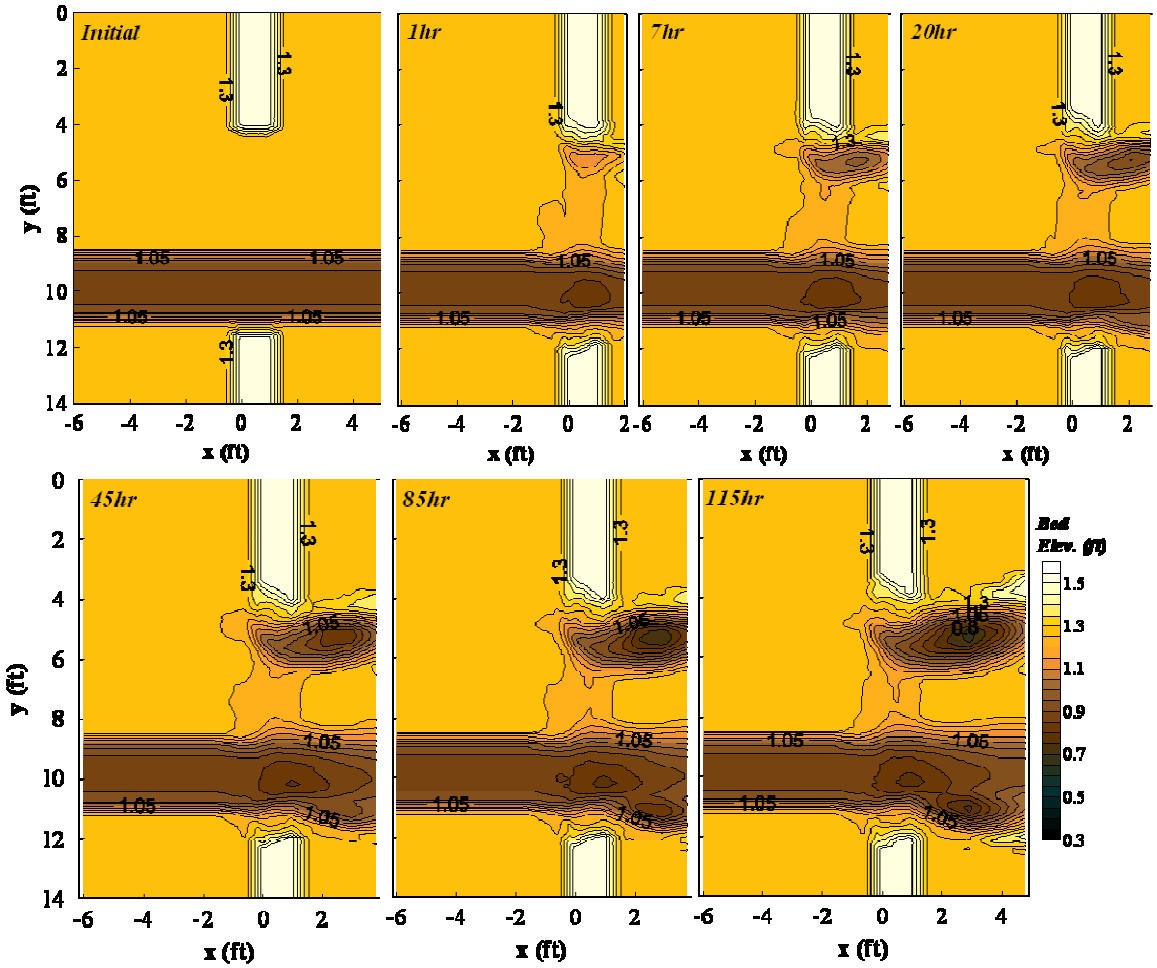

Run 3 (OT), $L_a/B_f = 0.53$, Q = 5.8 cfs

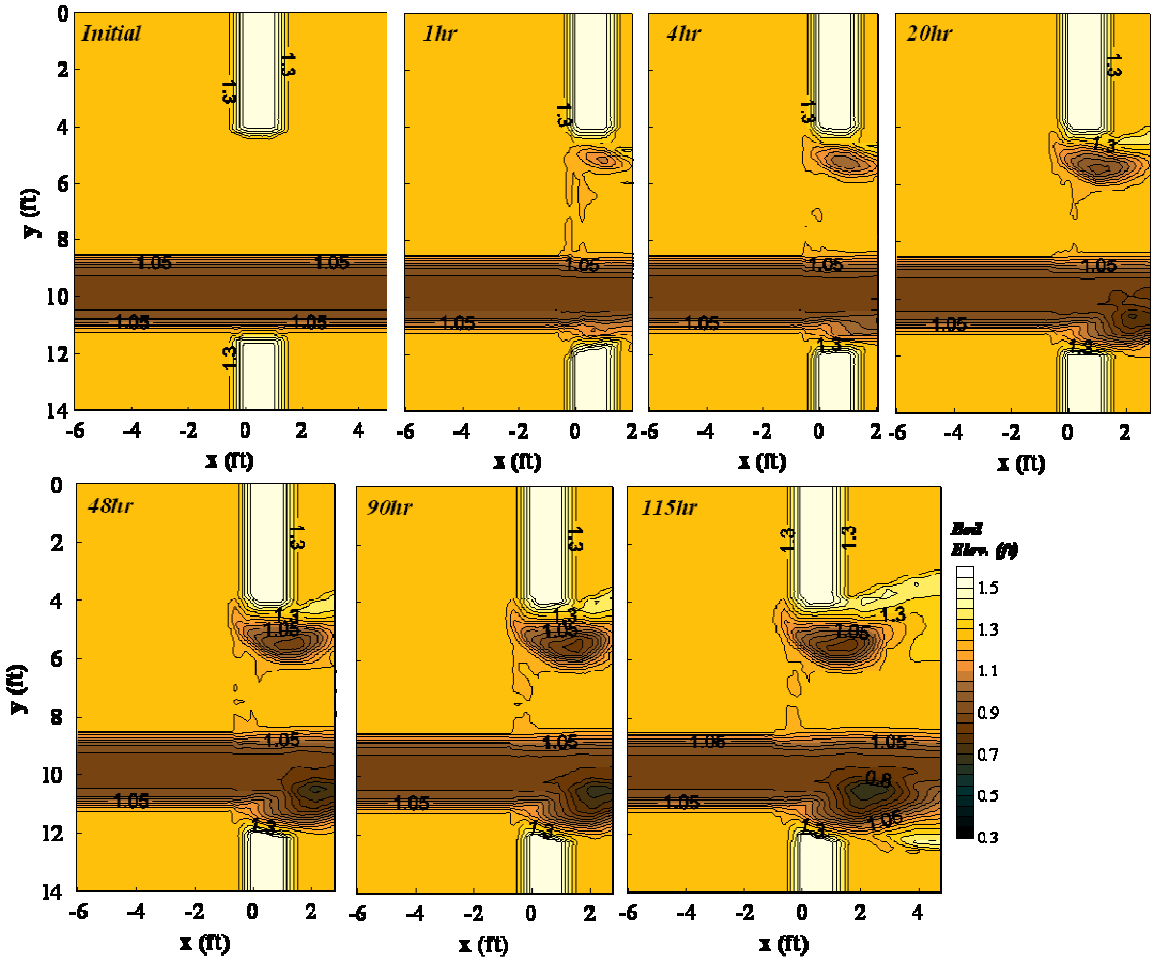

Run 4 (F), L_a/B_f = 0.53, Q = 3.0 cfs

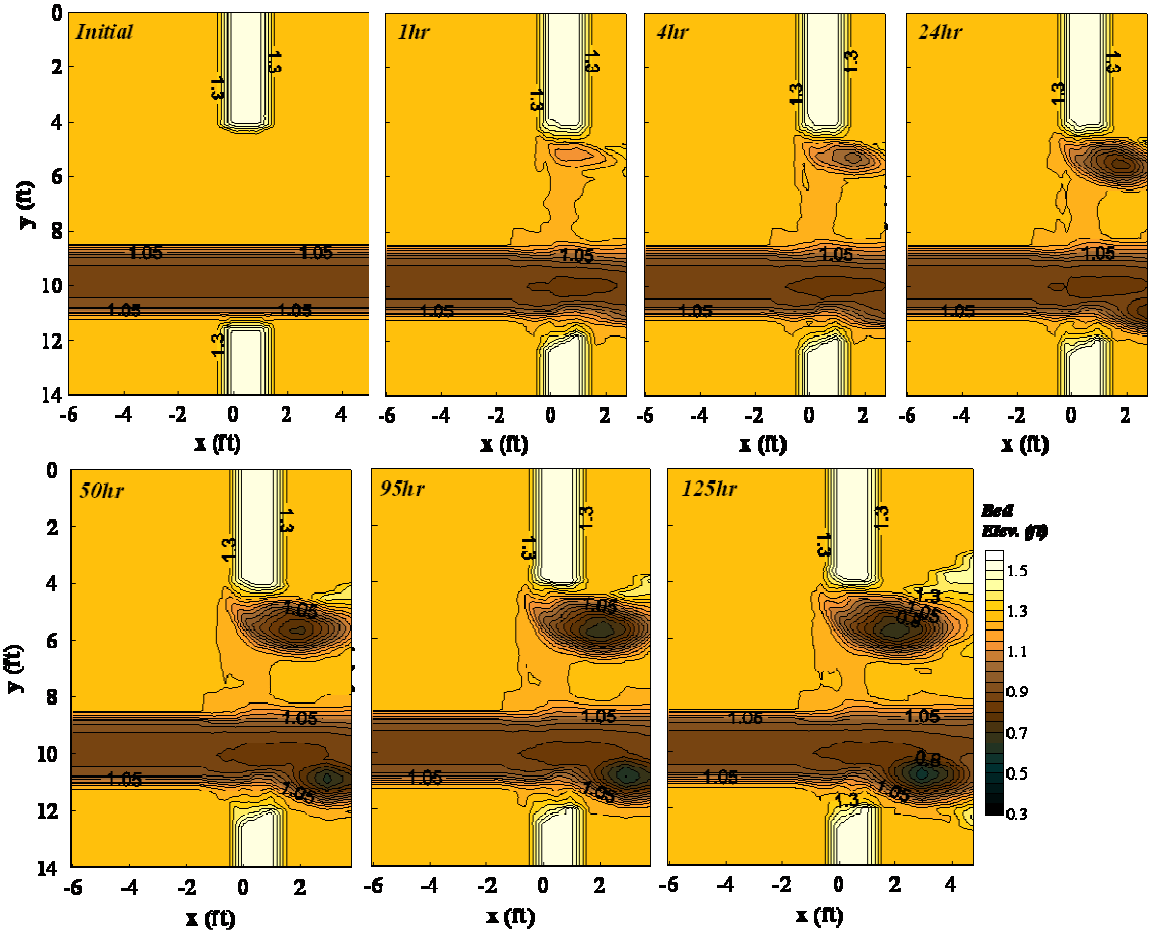

Run 5 (SO), $L_a/B_f = 0.53$, Q = 3.9 cfs

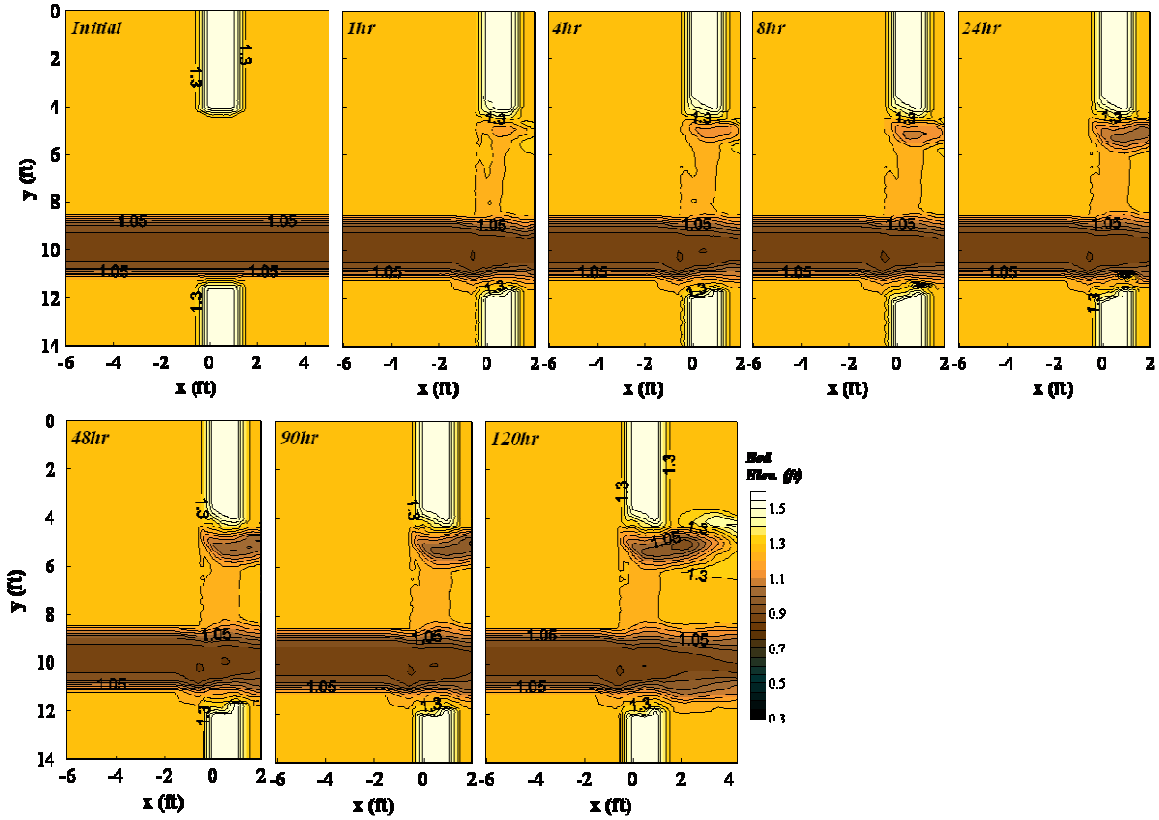

Run 6 (OT), $L_a/B_f = 0.53$, Q = 5.3 cfs

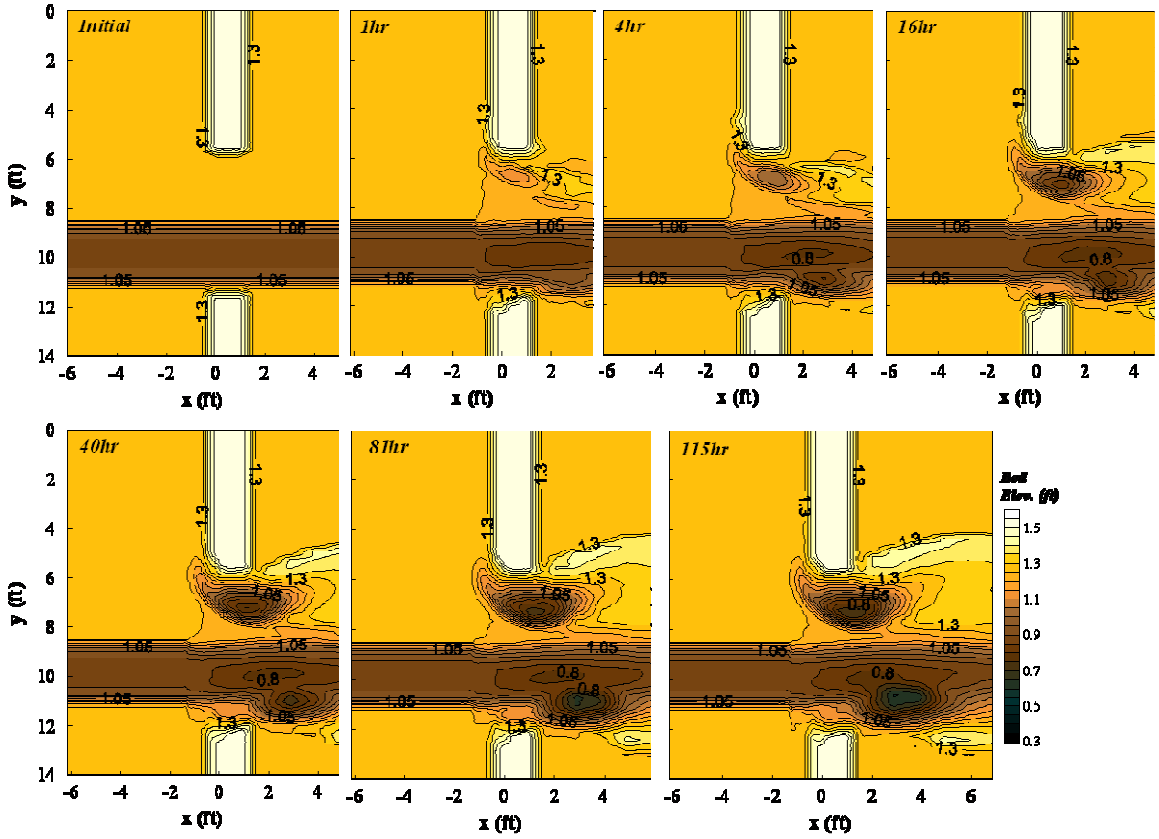

Run 7 (F), $L_a/B_f = 0.71$, Q = 3.0 cfs

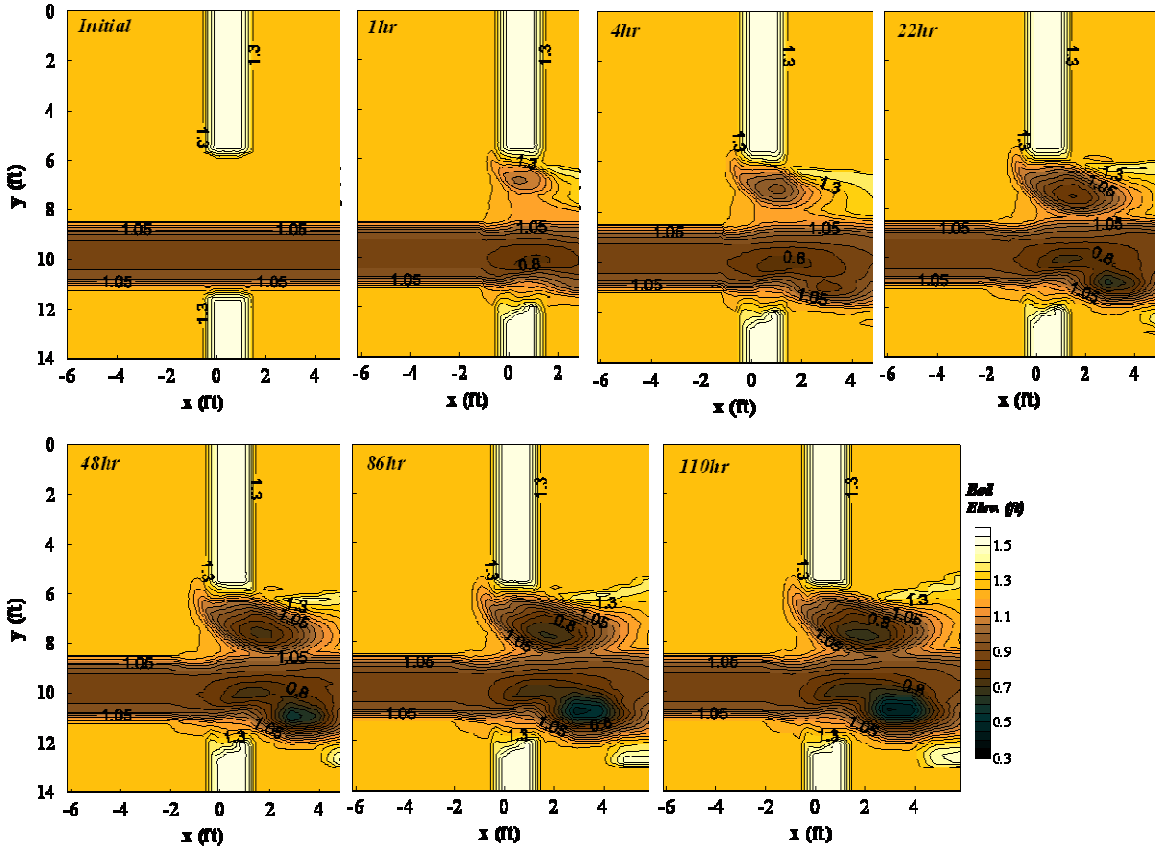

Run 8 (SO), $L_a/B_f = 0.71$, Q = 3.65 cfs

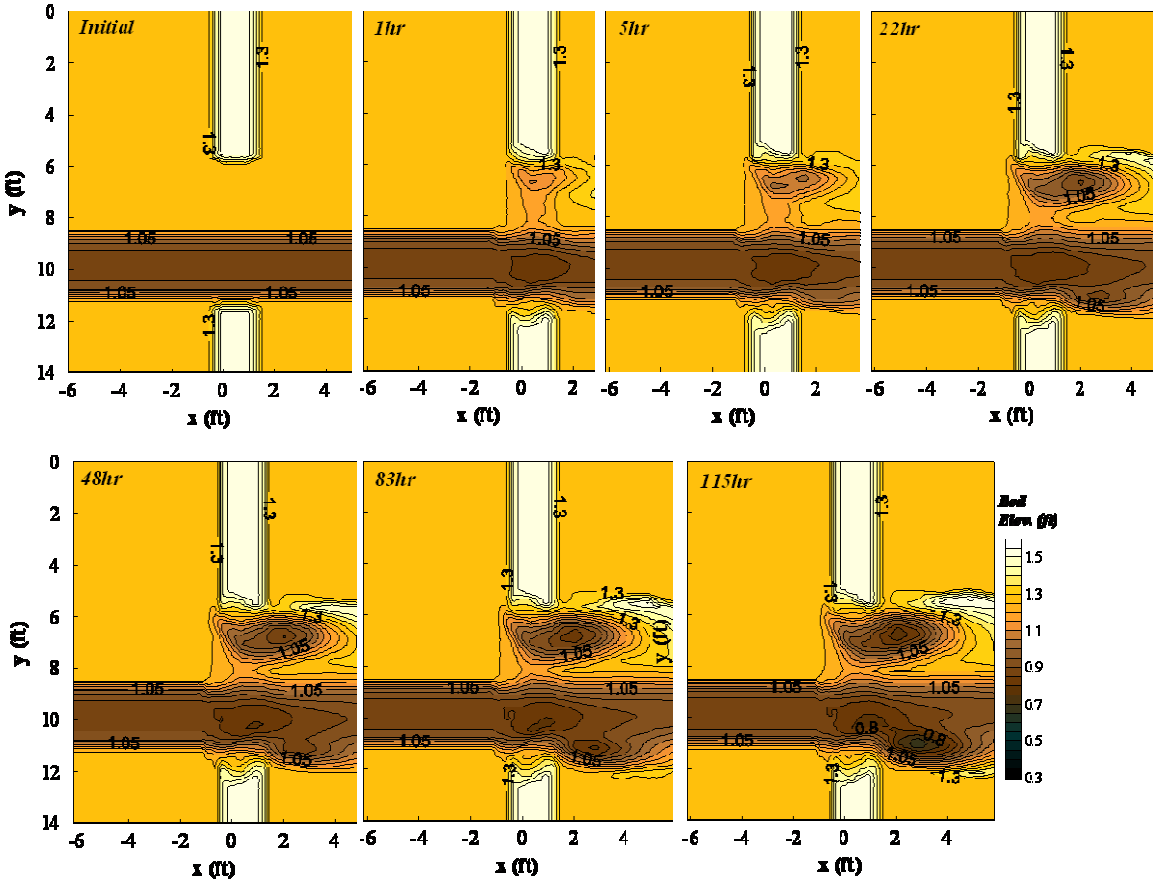

Run 9 (OT), $L_a/B_f = 0.71$, Q = 5.3 cfs

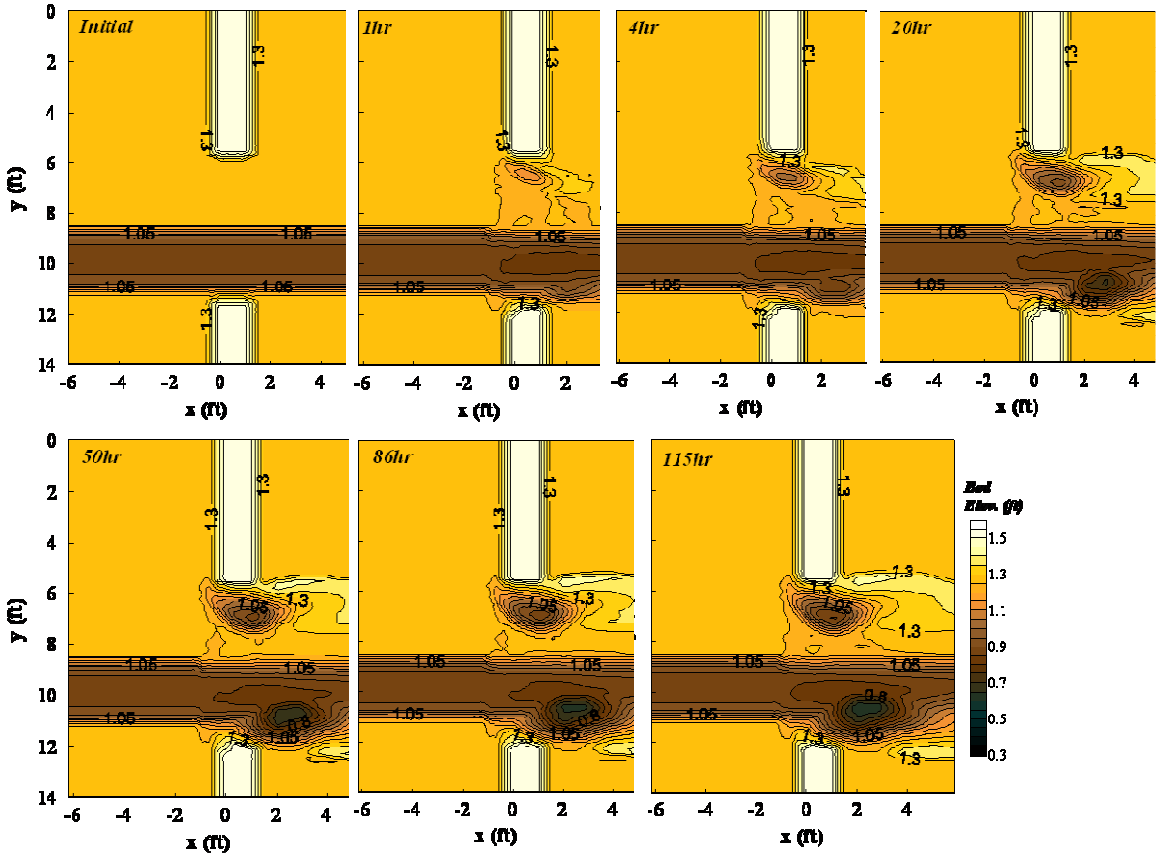

Run 10 (F), $L_a/B_f = 0.71$, Q = 2.6 cfs

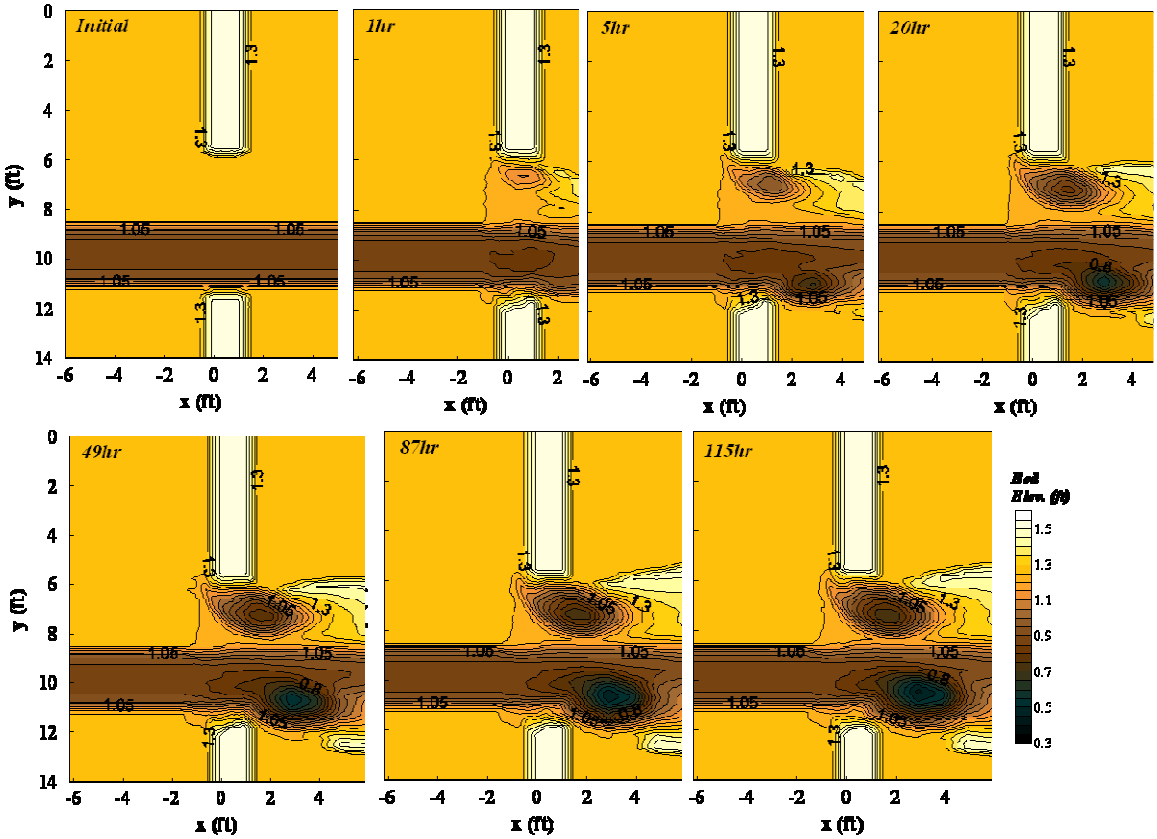

Run 11 (SO), $L_a/B_f = 0.71$, Q = 3.2 cfs

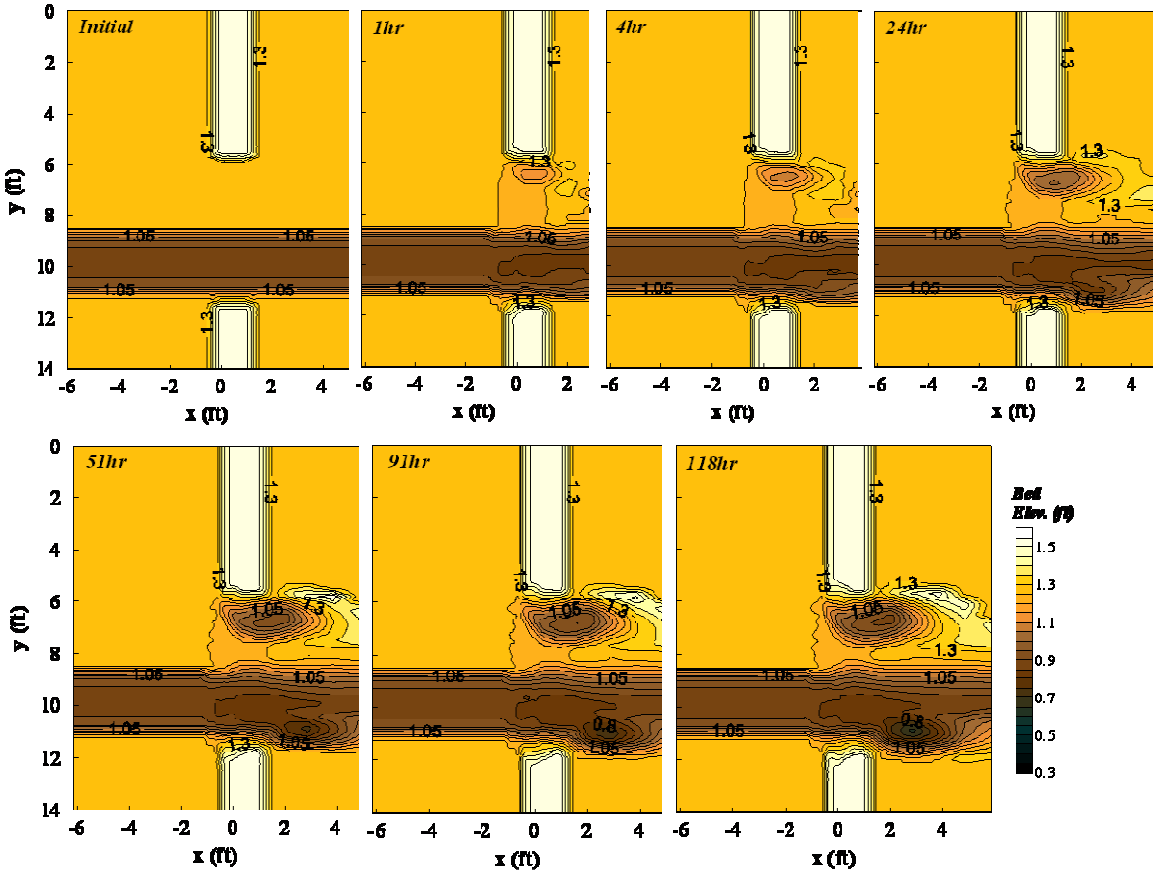

Run 12 (OT), $L_a/B_f = 0.71$, Q = 4.6 cfs

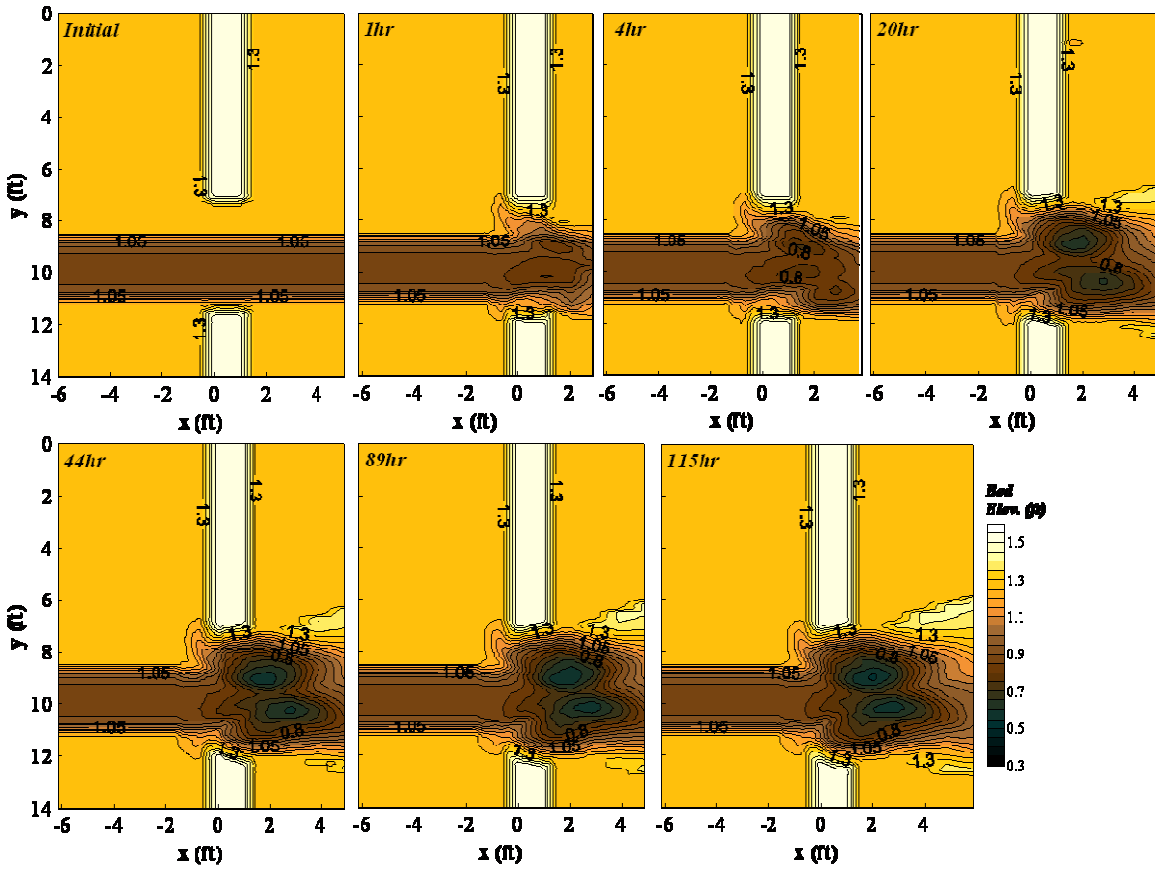

Run 13 (F), $L_a/B_f = 0.88$, Q = 2.6 cfs

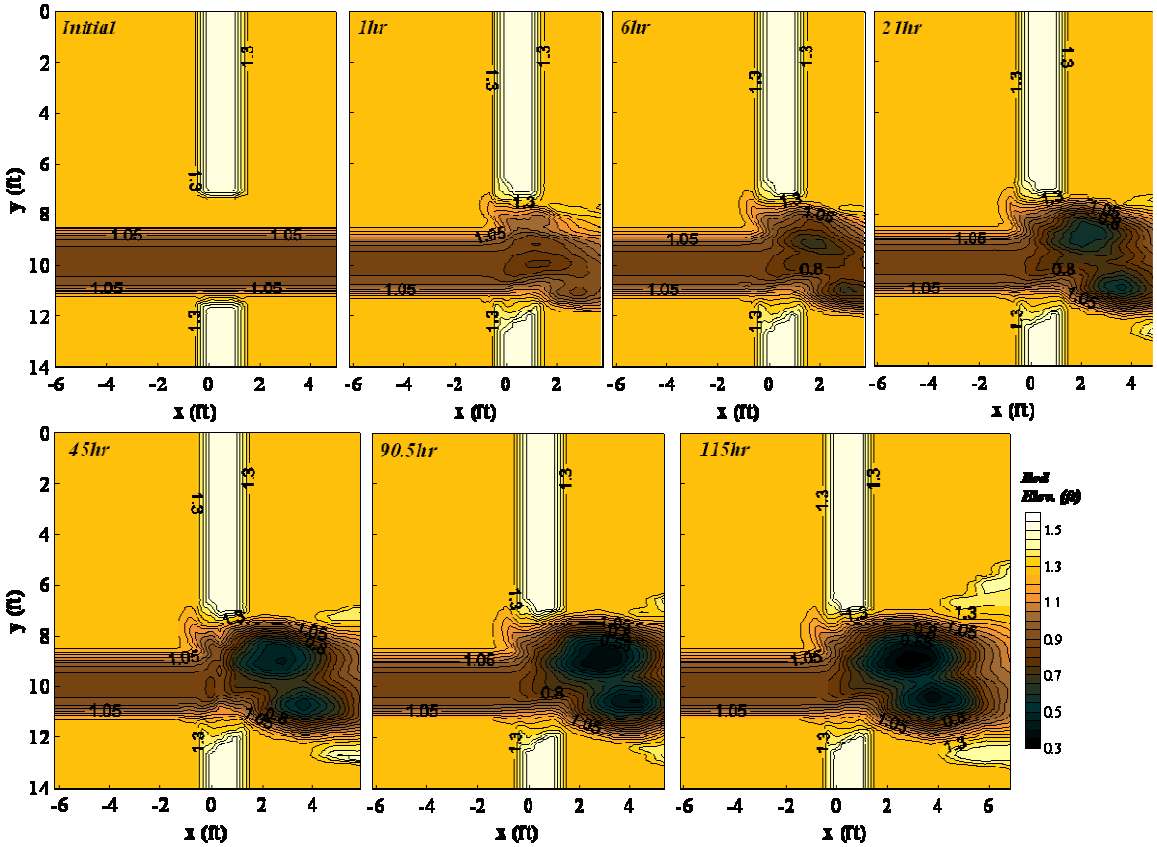

Run 14 (SO), $L_a/B_f = 0.88$, Q = 3.1 cfs

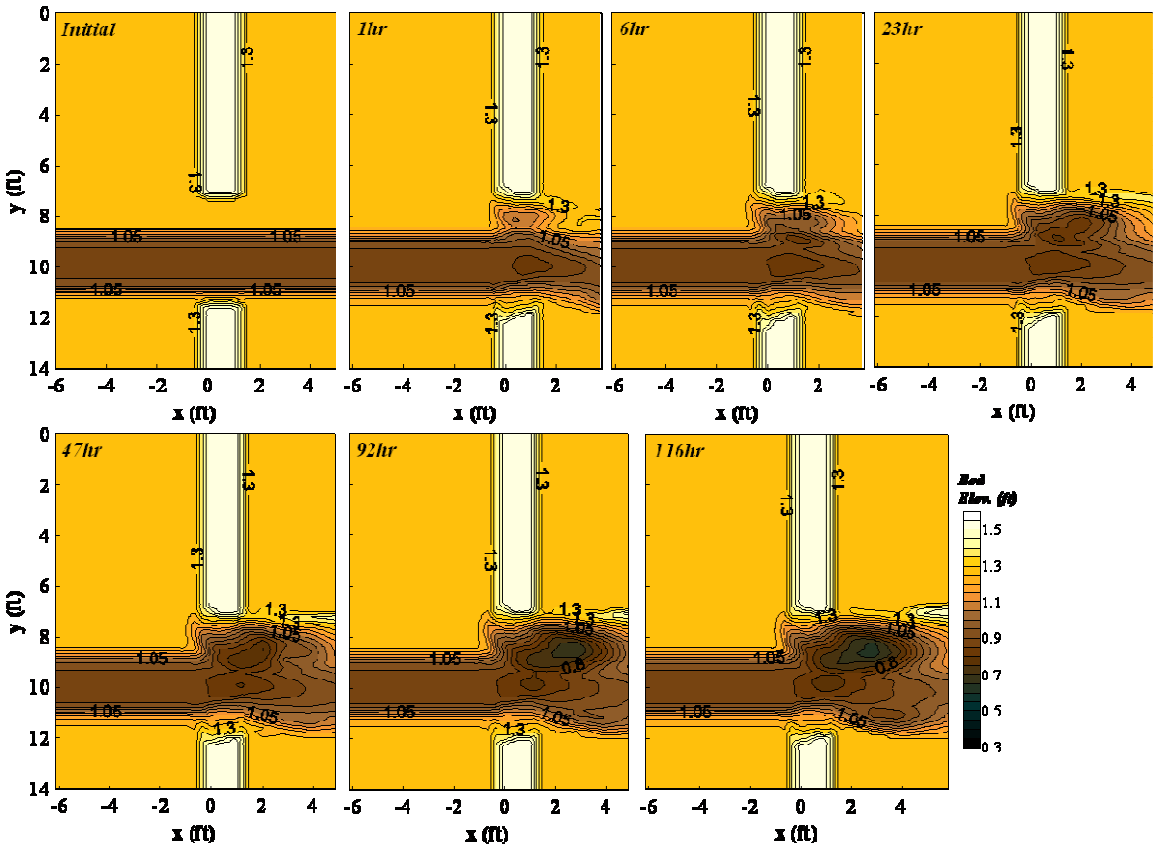

Run 15 (OT), $L_a/B_f = 0.88$, Q = 4.6 cfs

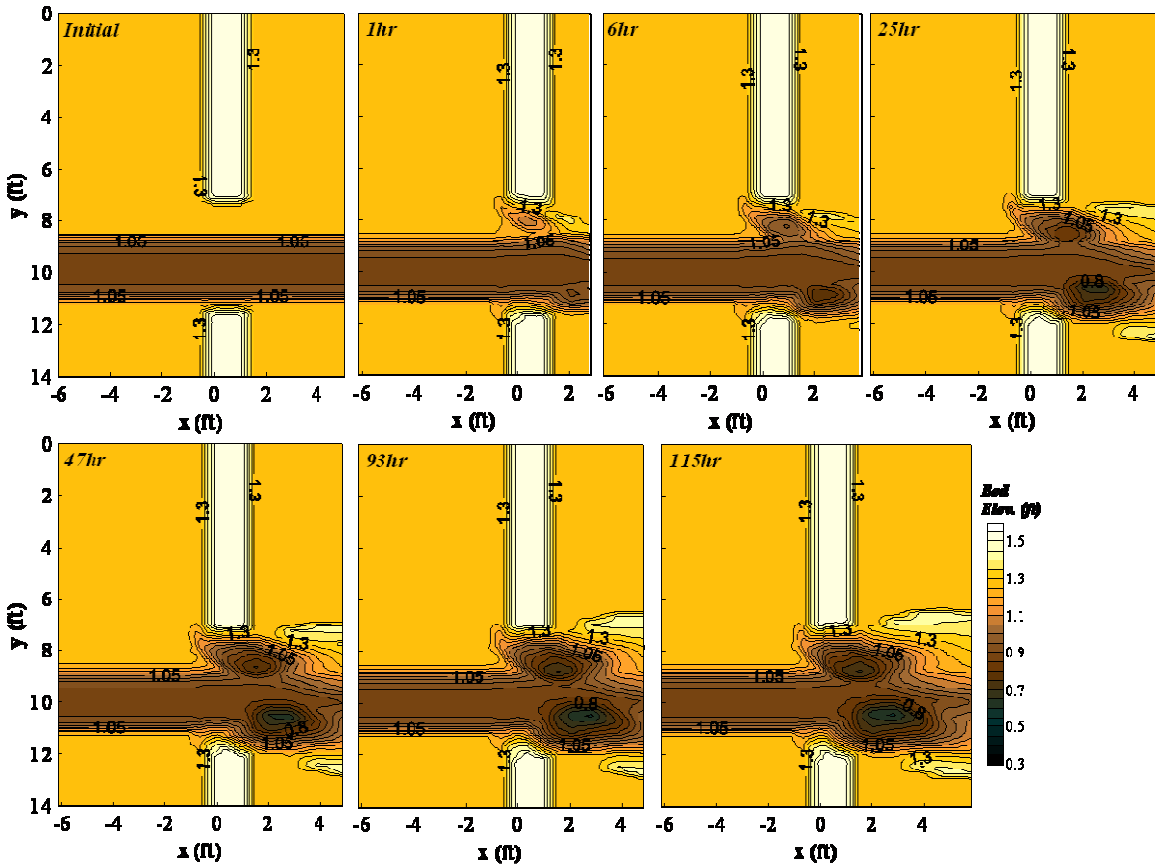

Run 16 (F), $L_a/B_f = 0.88$, Q = 2.2 cfs

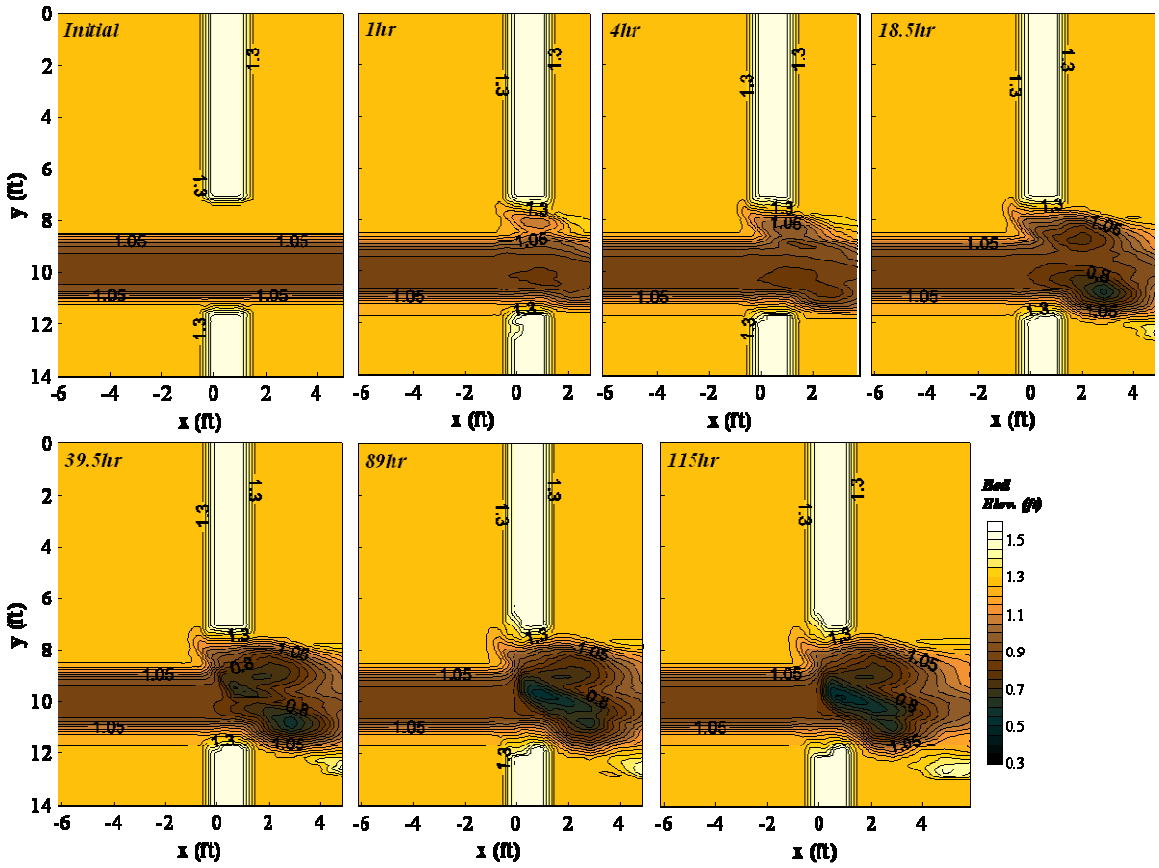

Run 17 (SO), L_a/B_f = 0.88, Q = 2.6 cfs

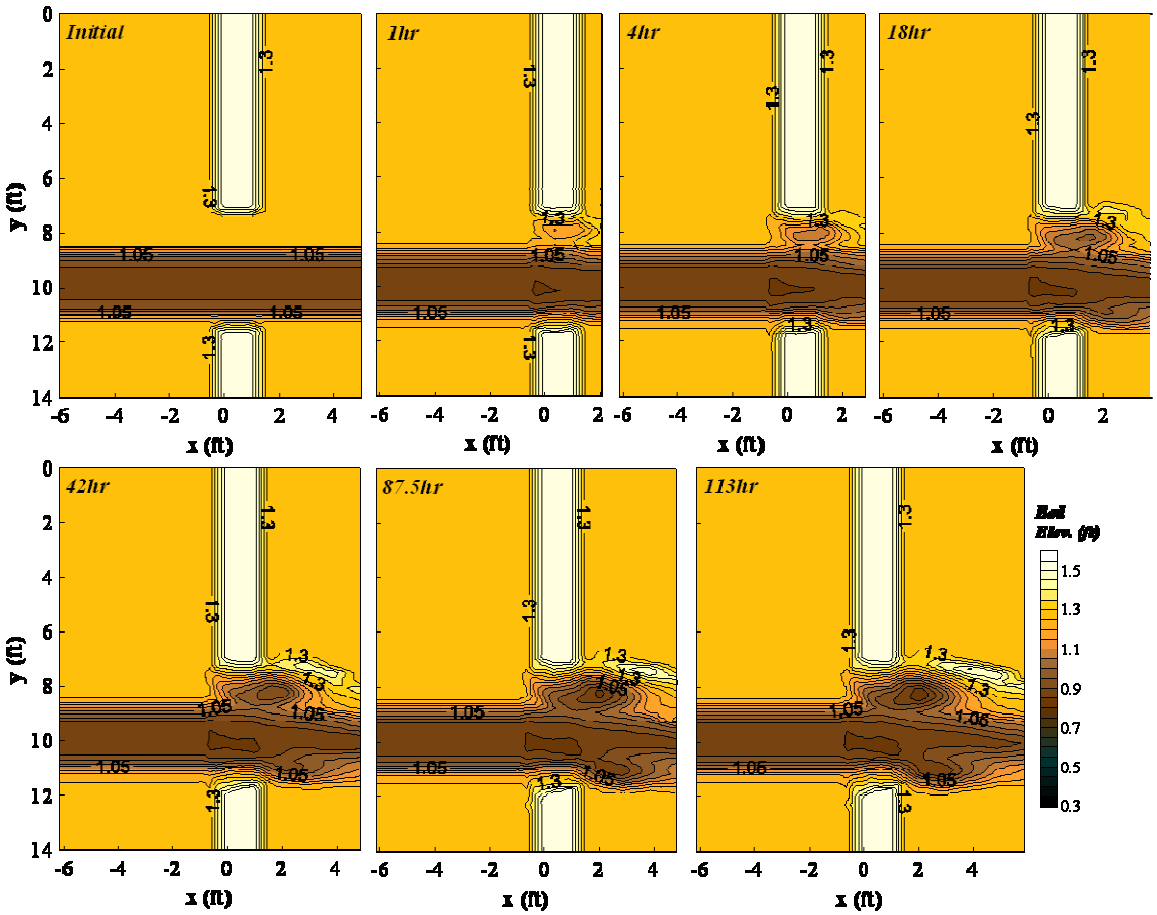

Run 18 (OT), $L_a/B_f = 0.88$, Q = 3.9 cfs

APPENDIX D

Velocity Distributions Measured 5 mm Above the Bed

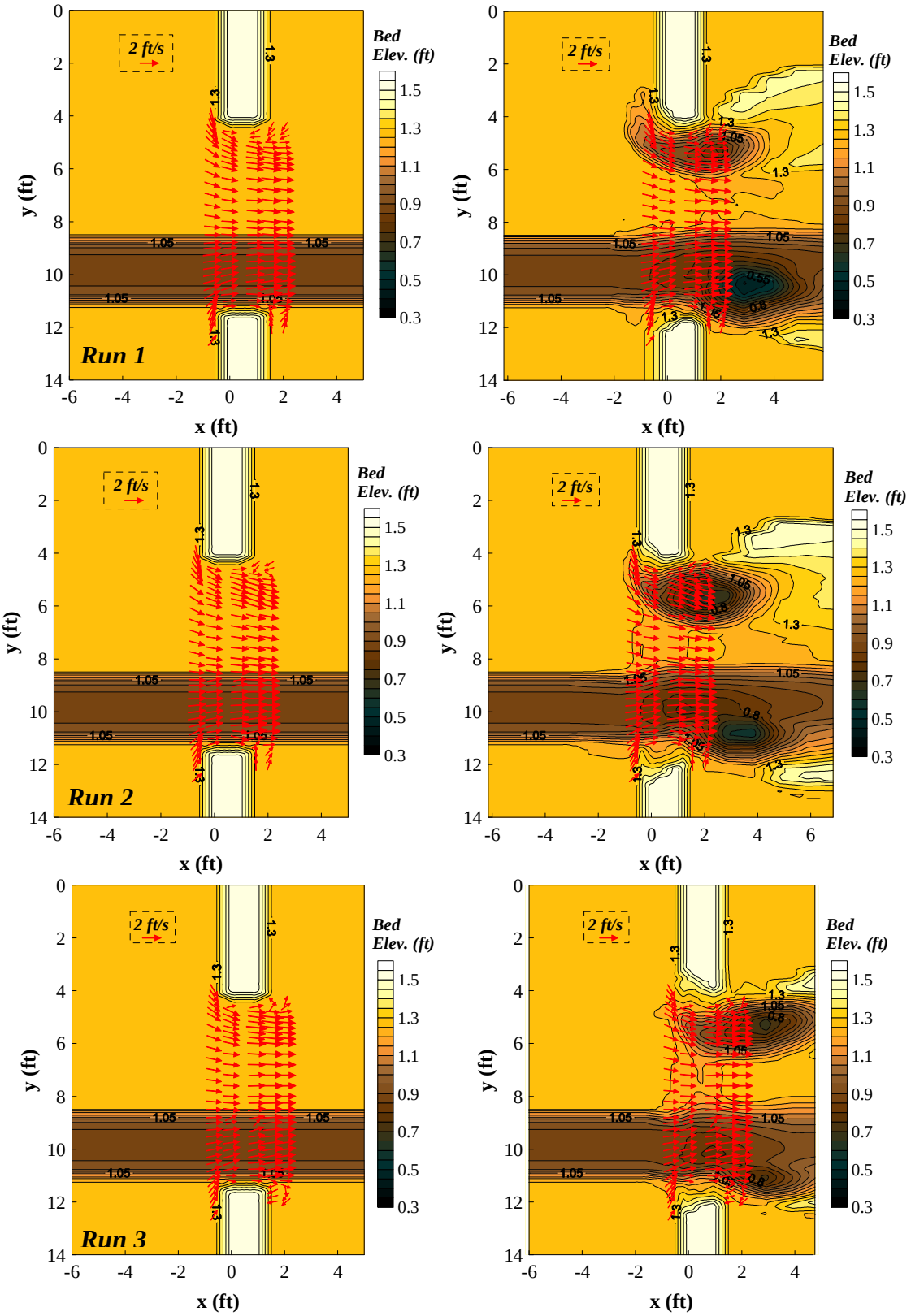

Velocity Distribution at the bed on the initial and final contours

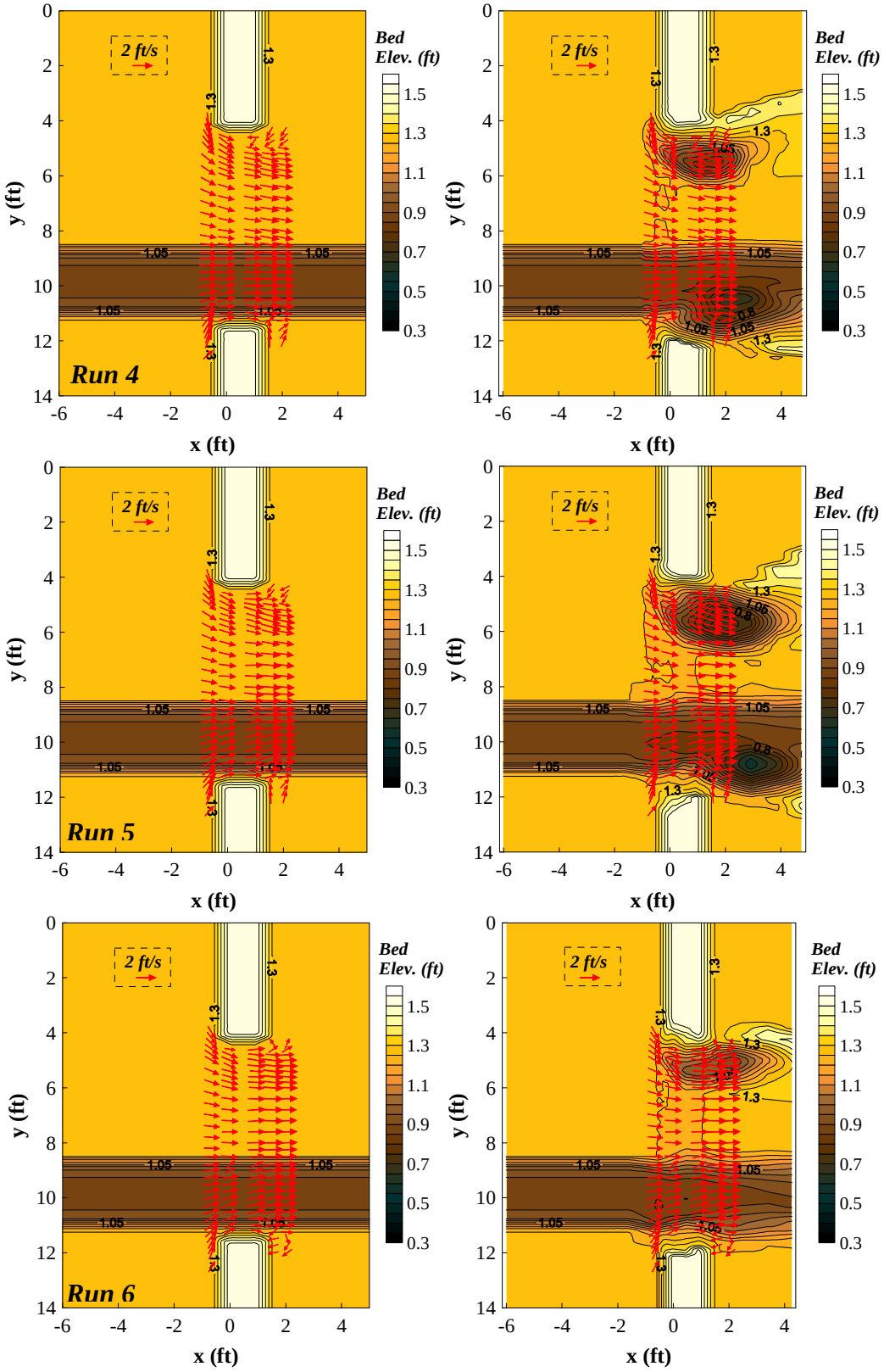

Velocity Distribution at the bed on the initial and final contours

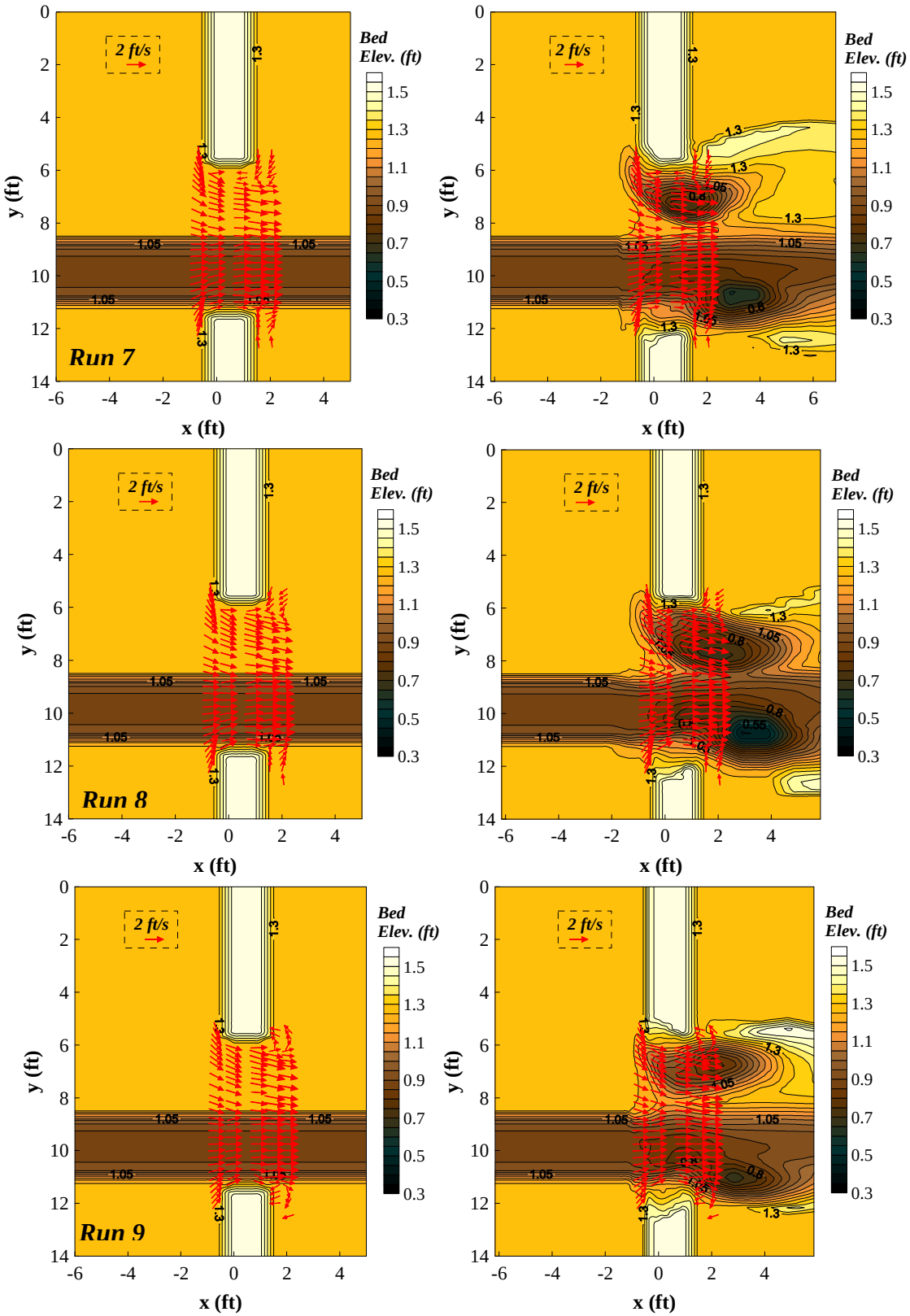

Velocity Distribution at the bed on the initial and final contours

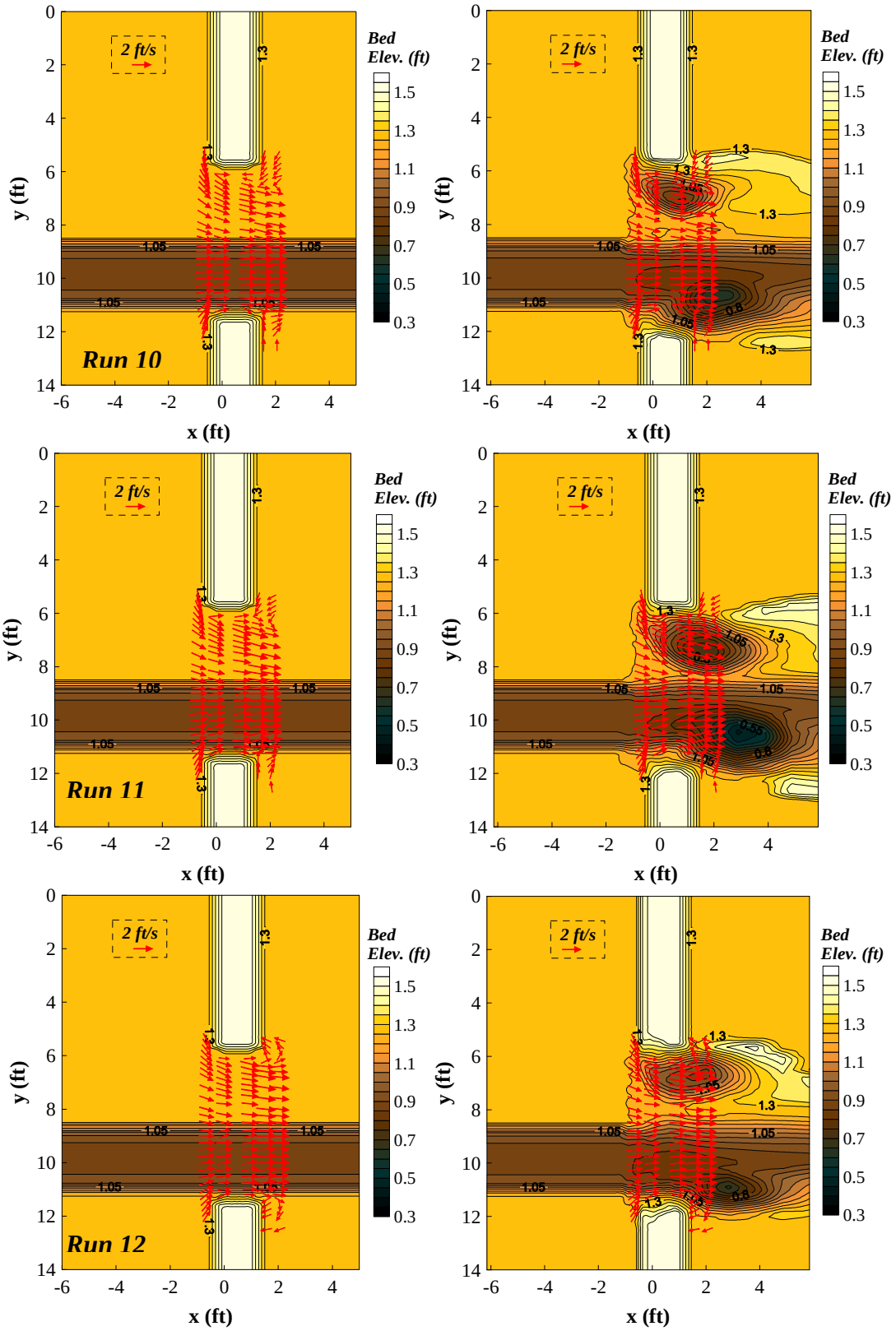

Velocity Distribution at the bed on the initial and final contours

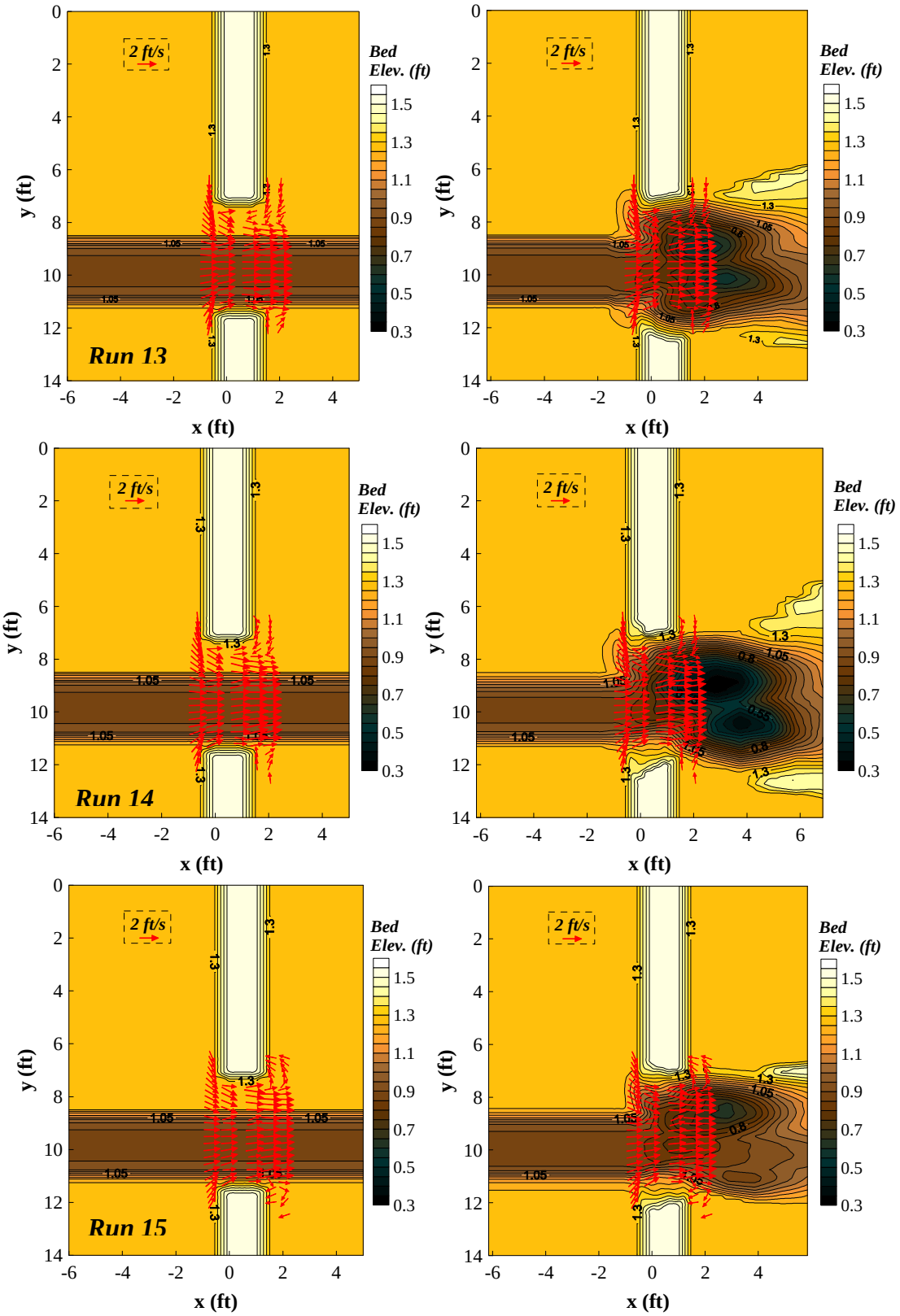

Velocity Distribution at the bed on the initial and final contours

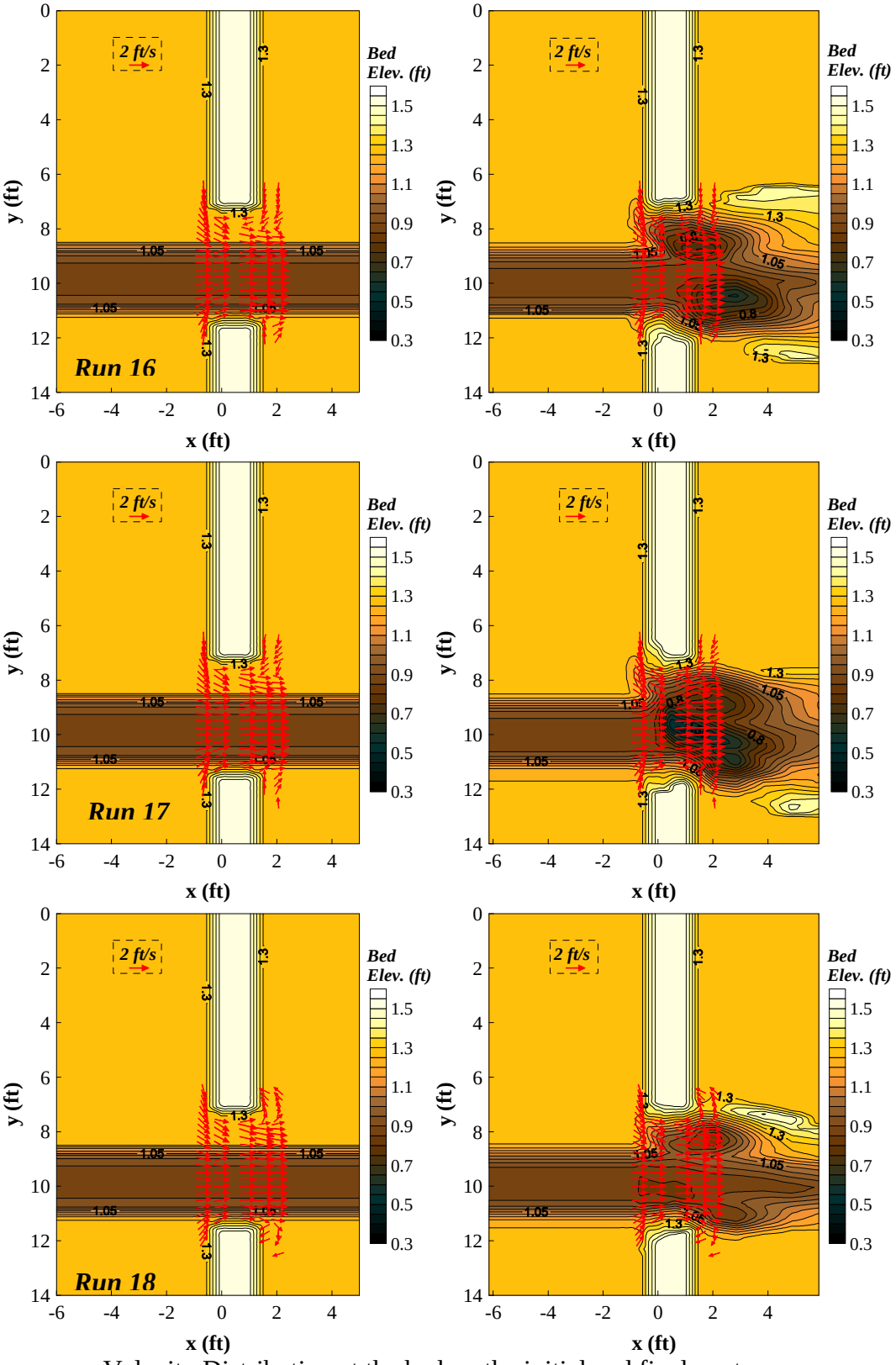

Velocity Distribution at the bed on the initial and final contours

APPENDIX E

Turbulent Kinetic Energy (TKE) Distributions Measured 5 mm Above the Bed

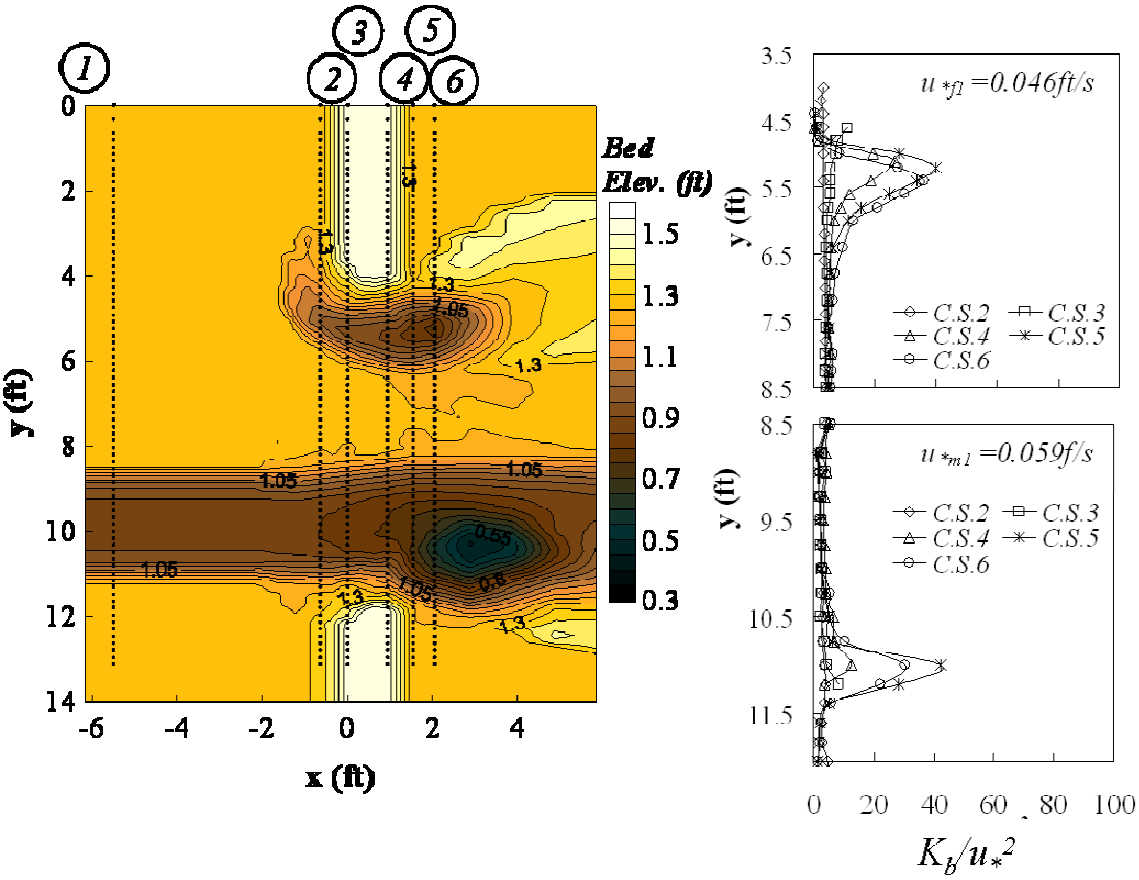

Run 1 (F), L_a/B_f = 0.53, Q = 3.3 cfs

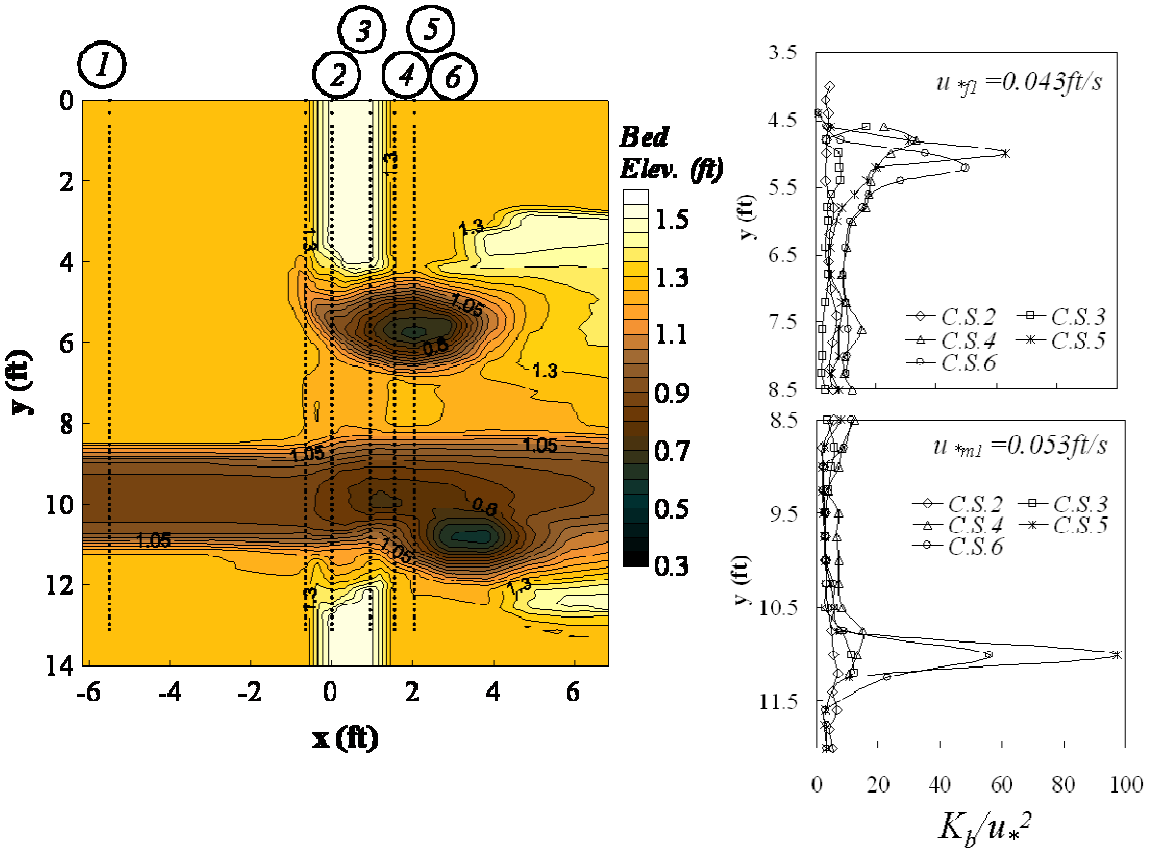

Run 2 (SO), L_a/B_f = 0.53, Q = 4.1 cfs

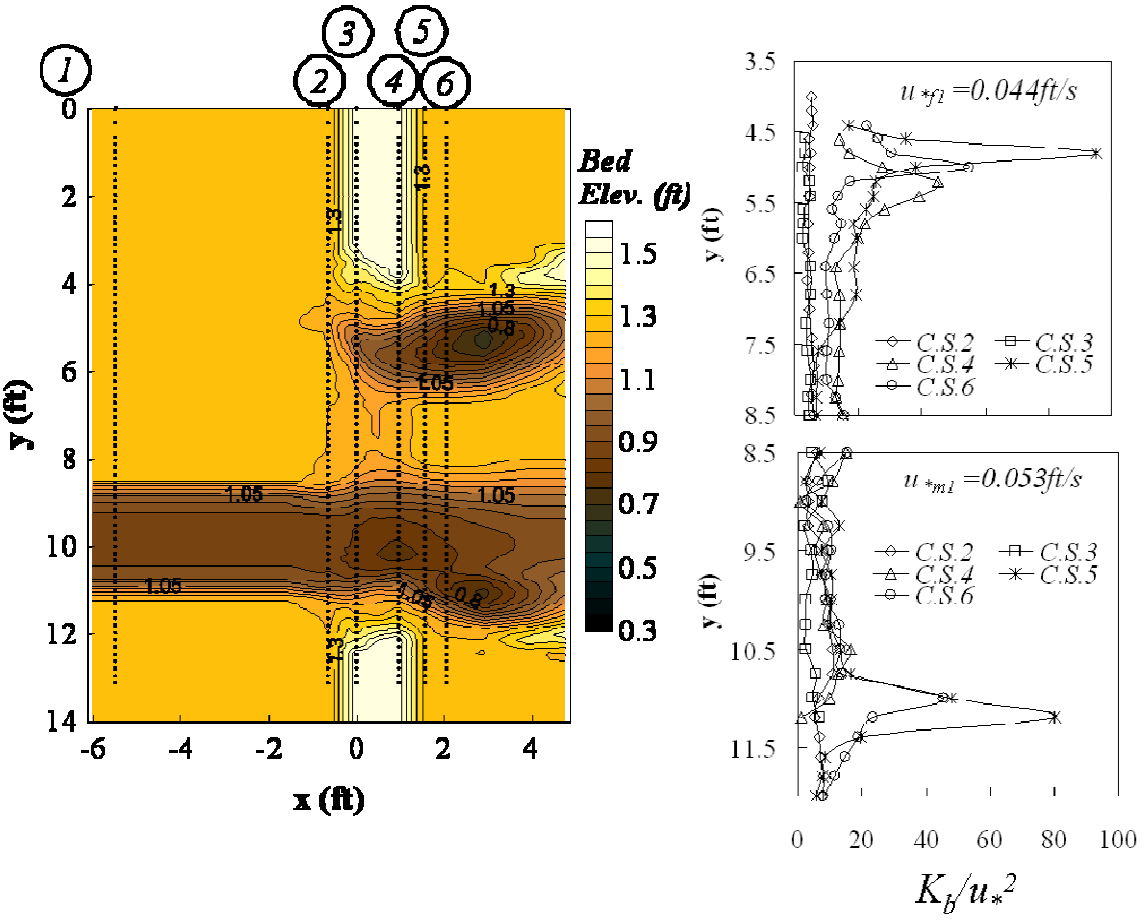

Run 3 (OT), L_a/B_f = 0.53, Q = 5.8 cfs

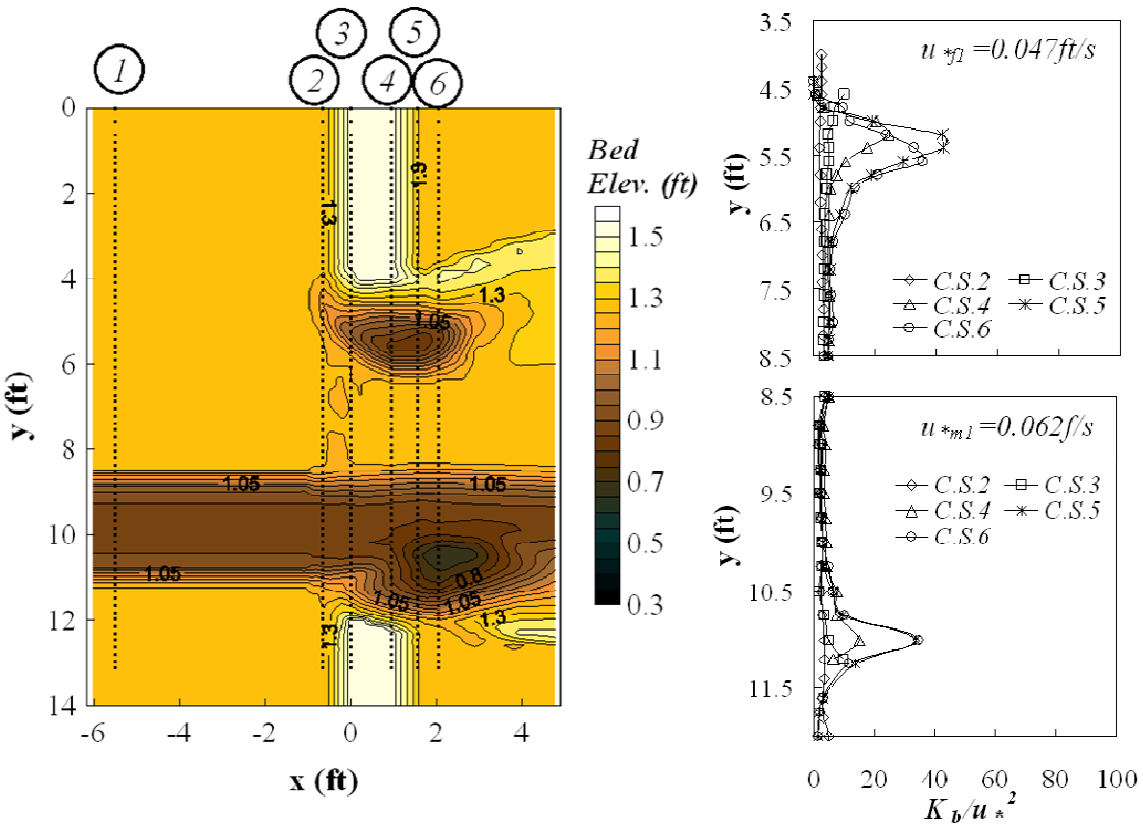

Run 4 (F), L_a/B_f = 0.53, Q = 3.0 cfs

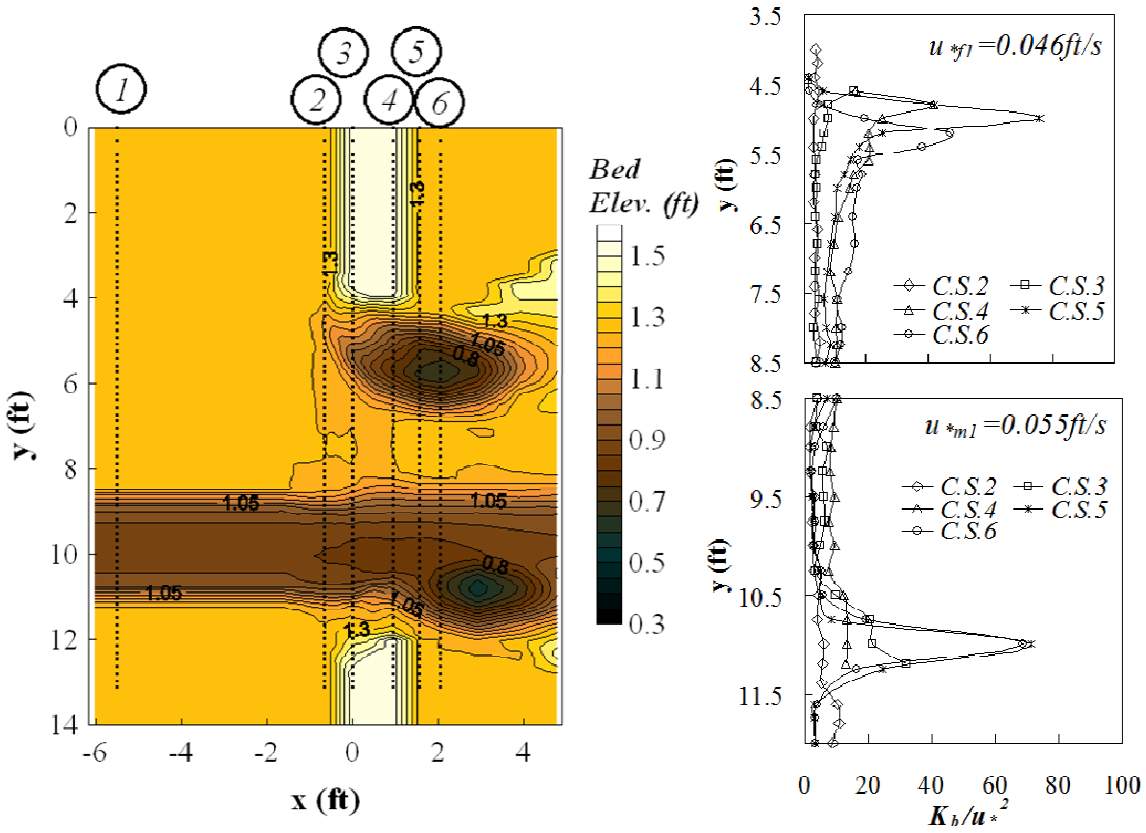

Run 5 (SO), L_a/B_f = 0.53, Q = 3.9 cfs

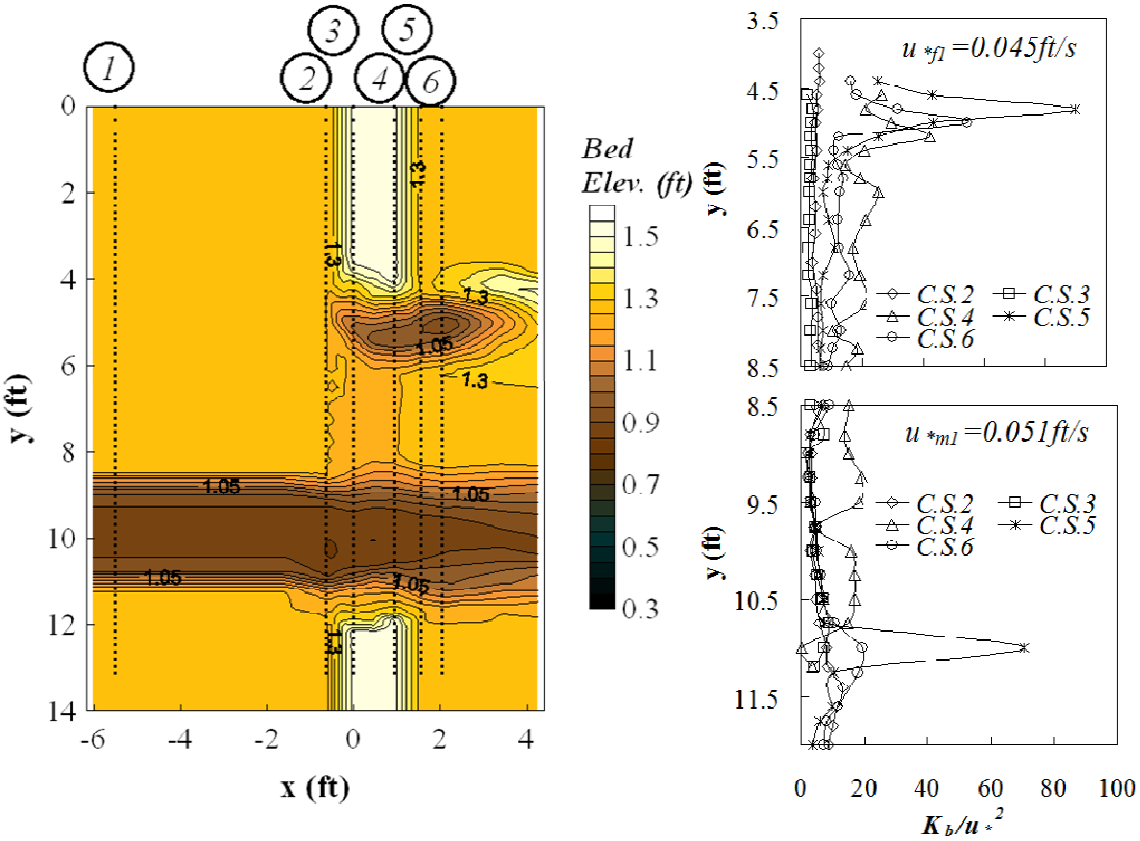

Run 6 (OT), L_a/B_f = 0.53, Q = 5.3 cfs

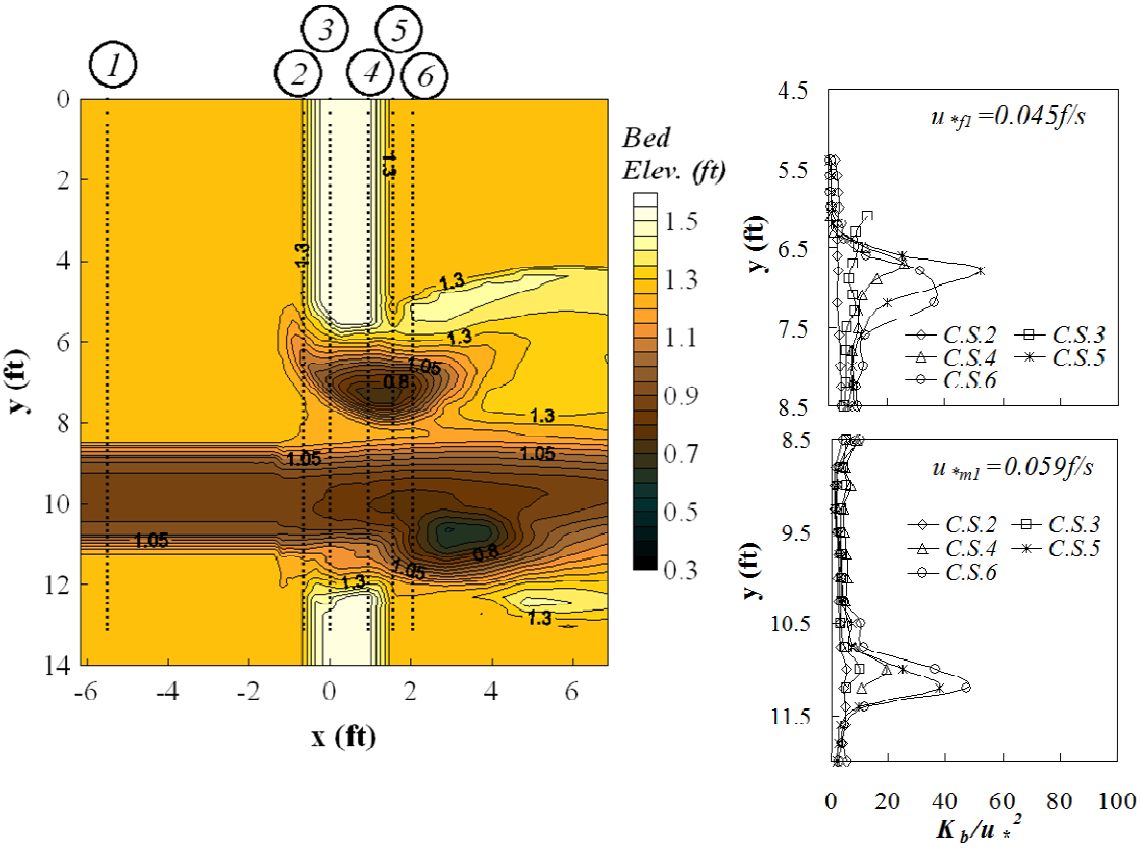

Run 7 (F), L_a/B_f = 0.71, Q = 3.0 cfs

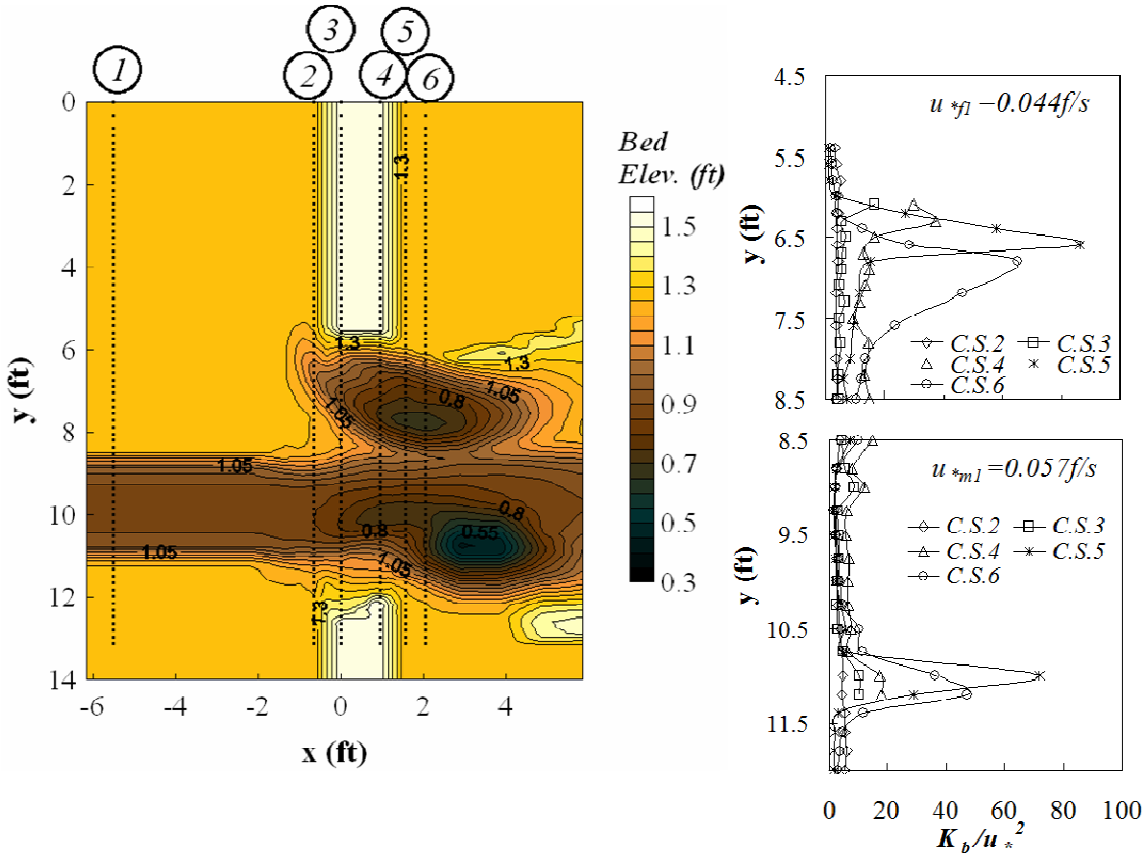

Run 8 (SO), L_a/B_f = 0.71, Q = 3.65 cfs

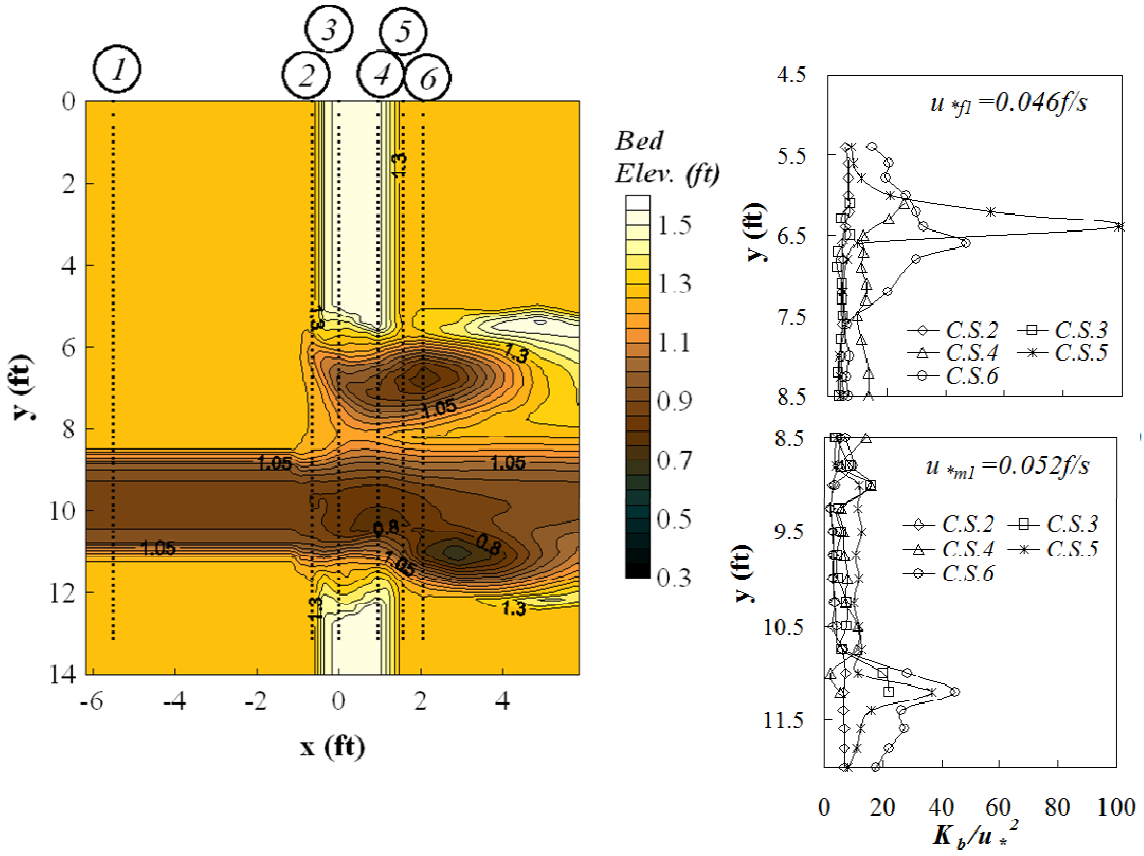

Run 9 (OT), L_a/B_f = 0.71, Q = 5.3 cfs

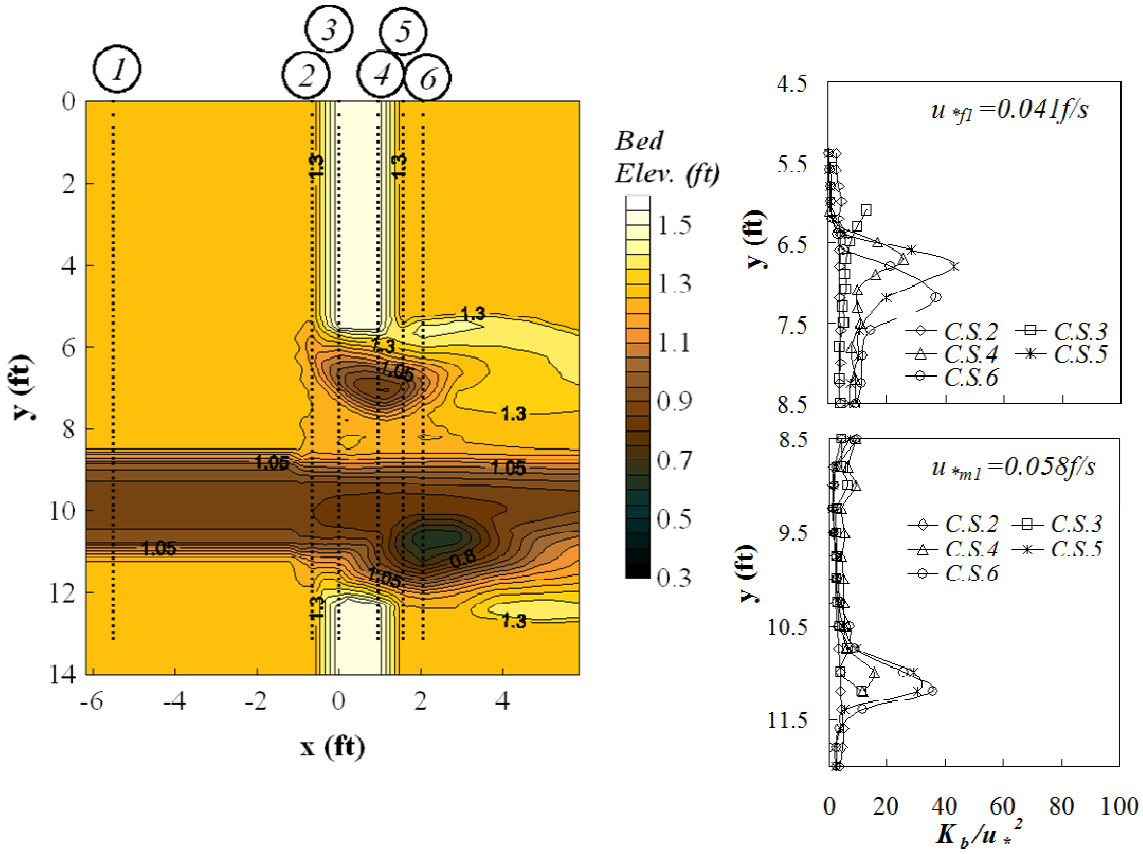

Run 10 (F), $L_a/B_f = 0.71$, Q = 2.6 cfs

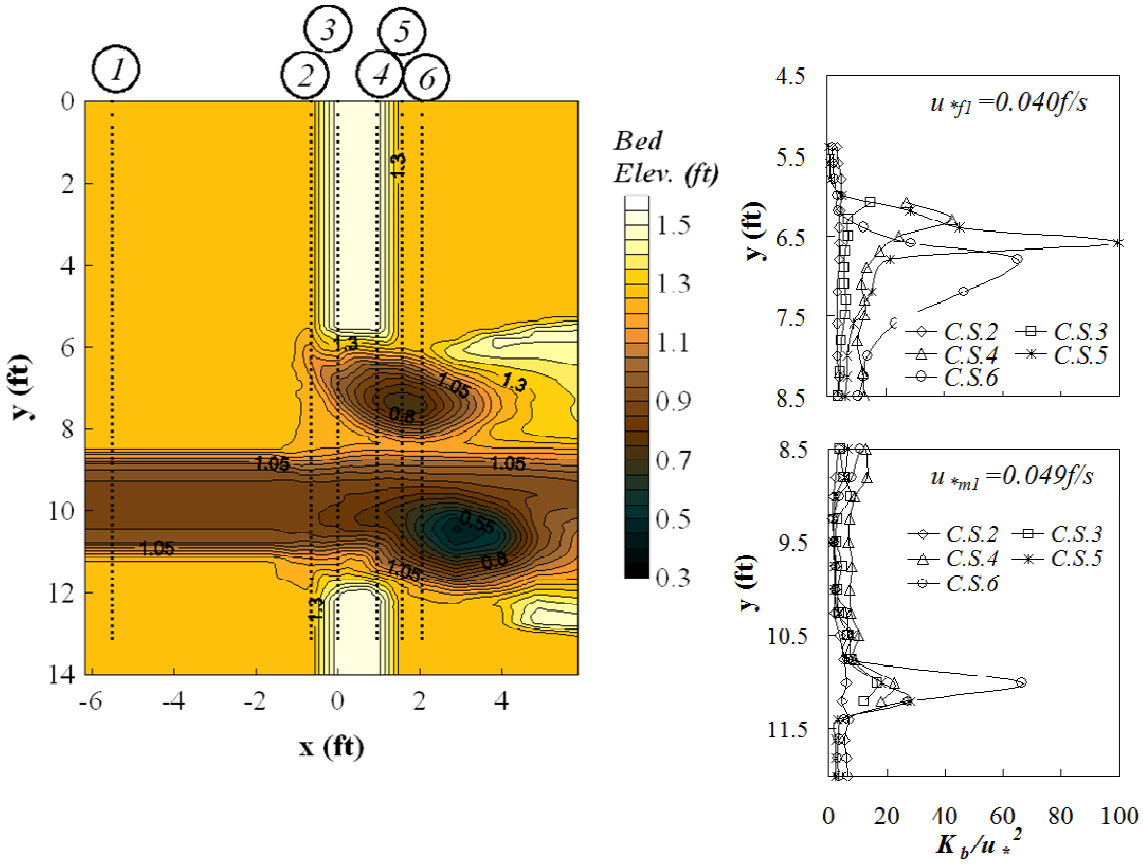

Run 11 (SO), L_a/B_f = 0.71, Q = 3.2 cfs

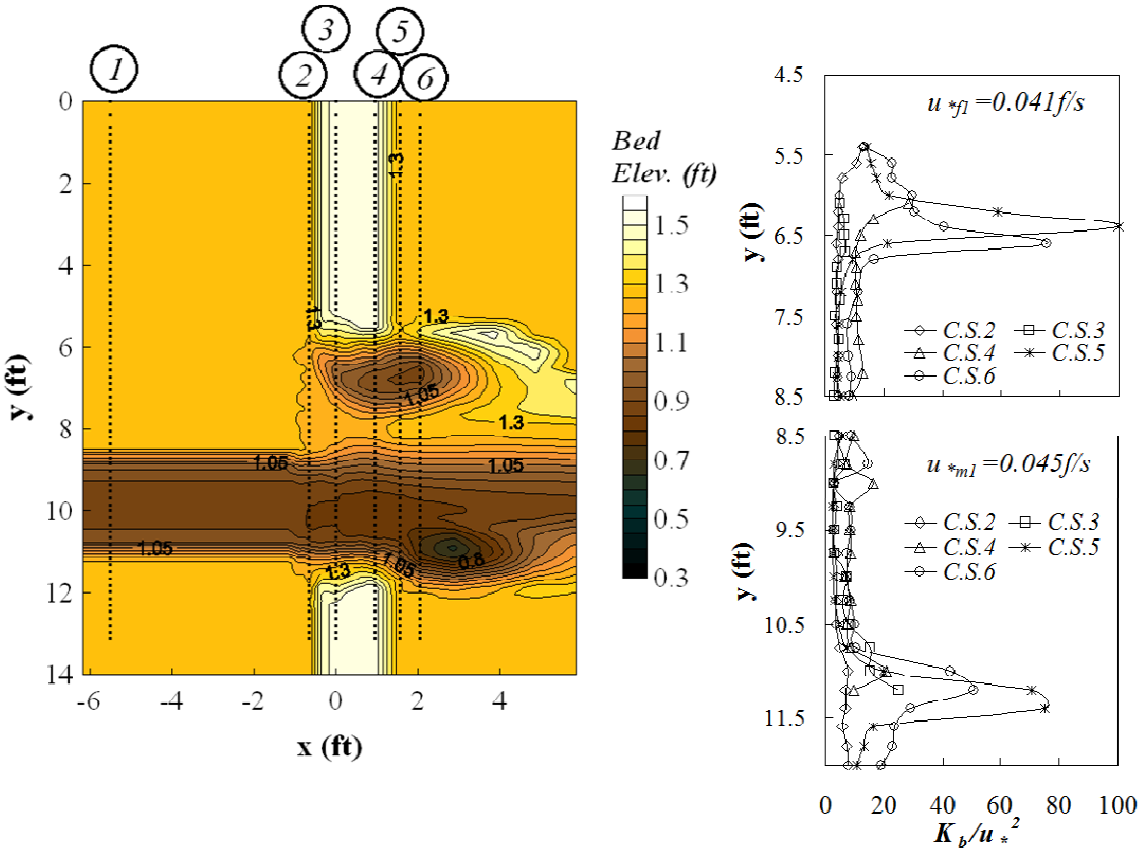

Run 12 (OT), L_a/B_f = 0.71, Q = 4.6 cfs

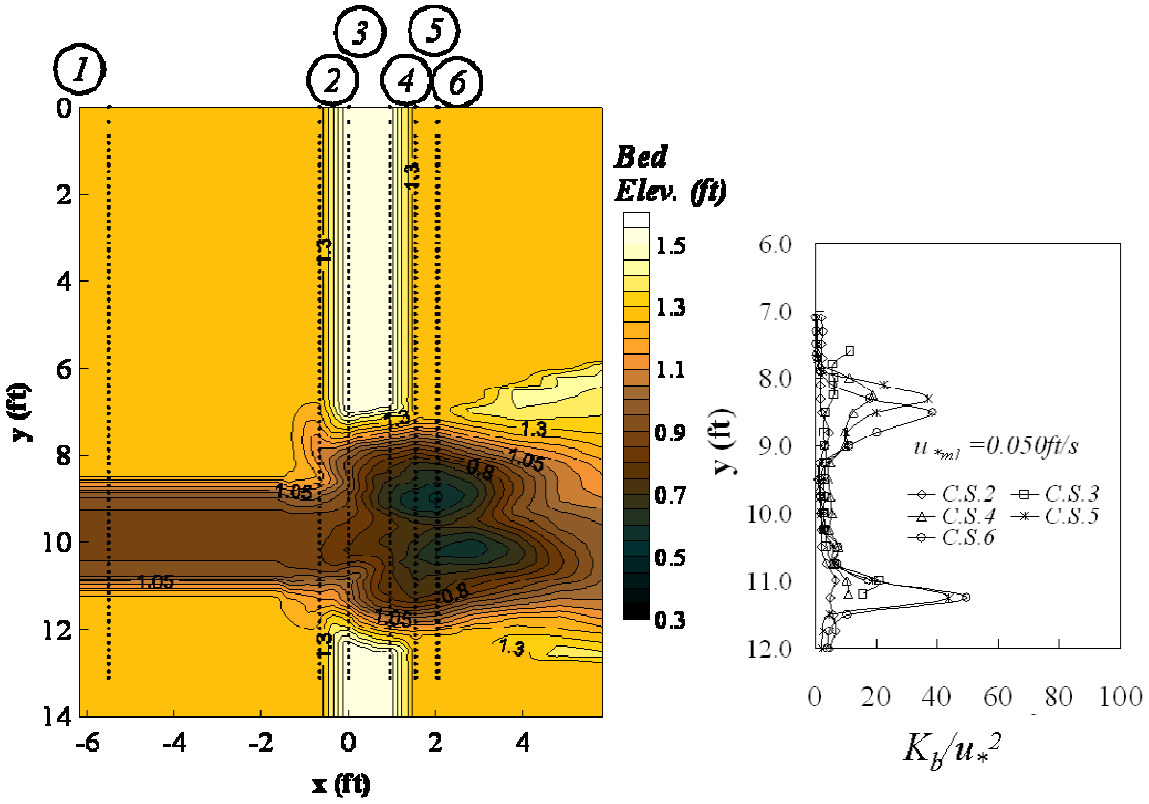

Run 13 (F), $L_a/B_f = 0.88$, Q = 2.6 cfs

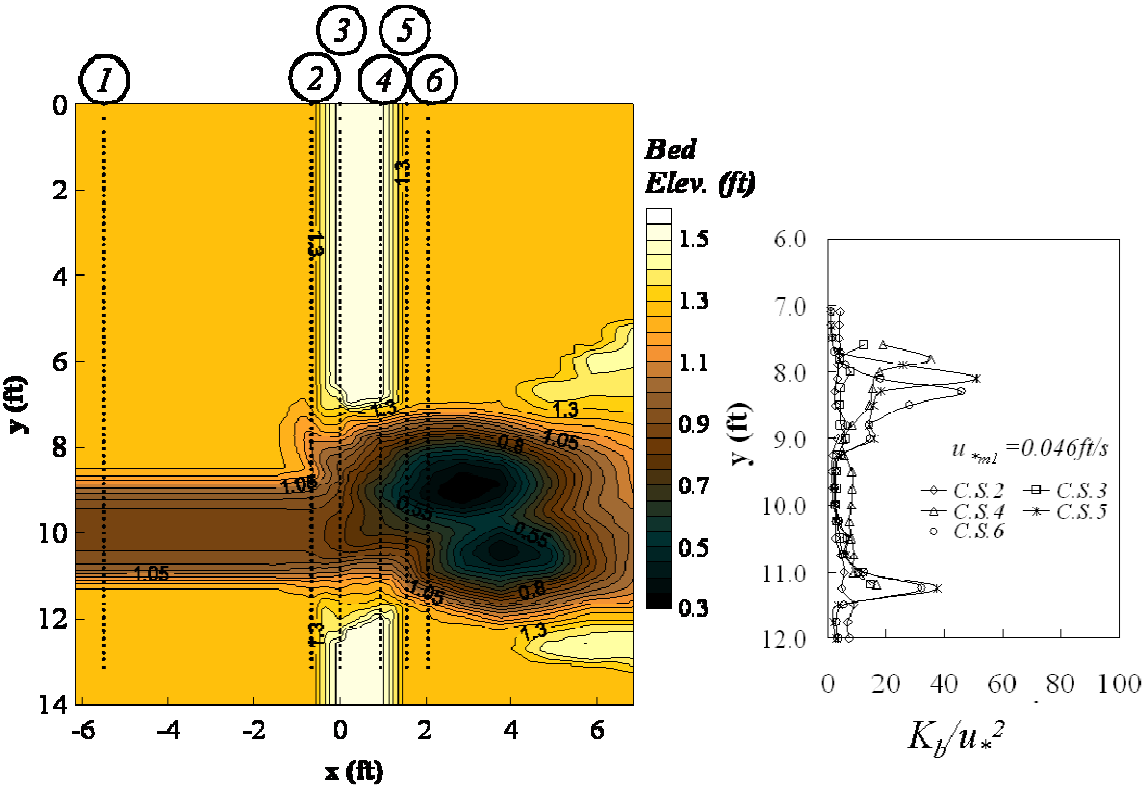

Run 14 (SO), L_a/B_f = 0.88, Q = 3.1 cfs

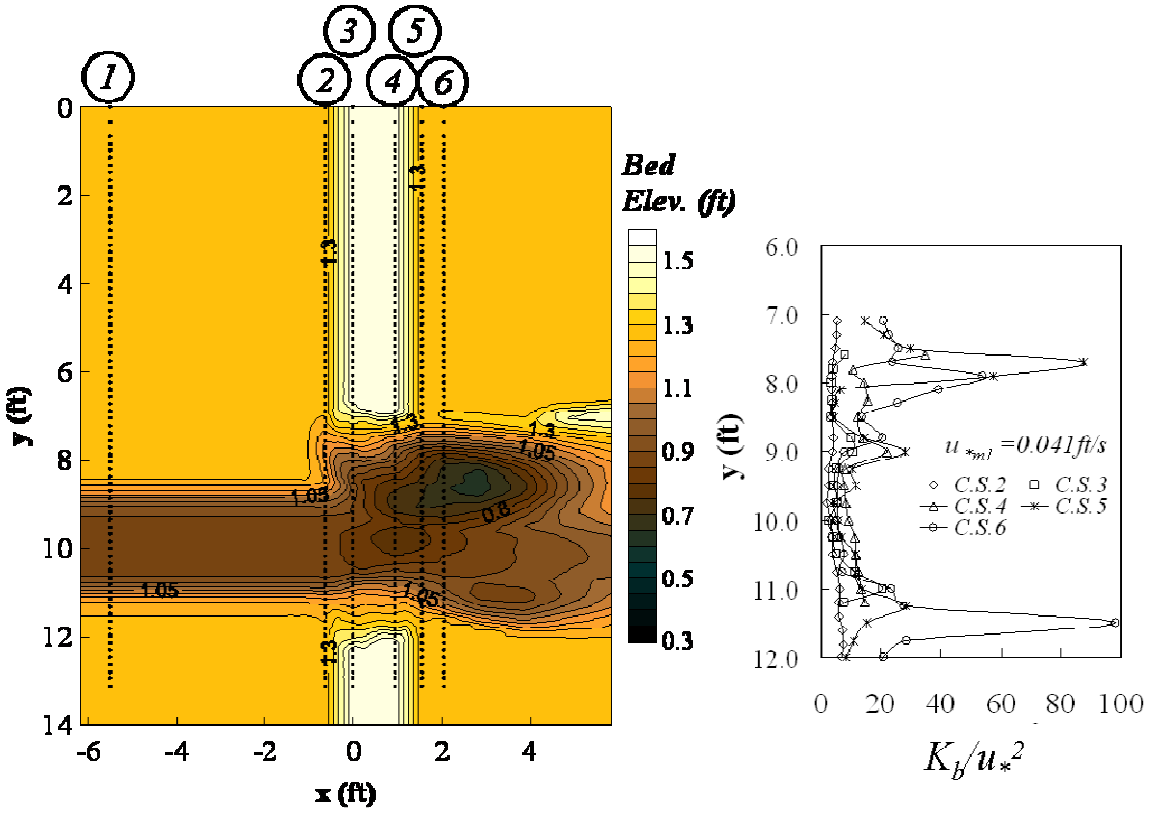

Run 15 (OT), L_a/B_f = 0.88, Q = 4.6 cfs

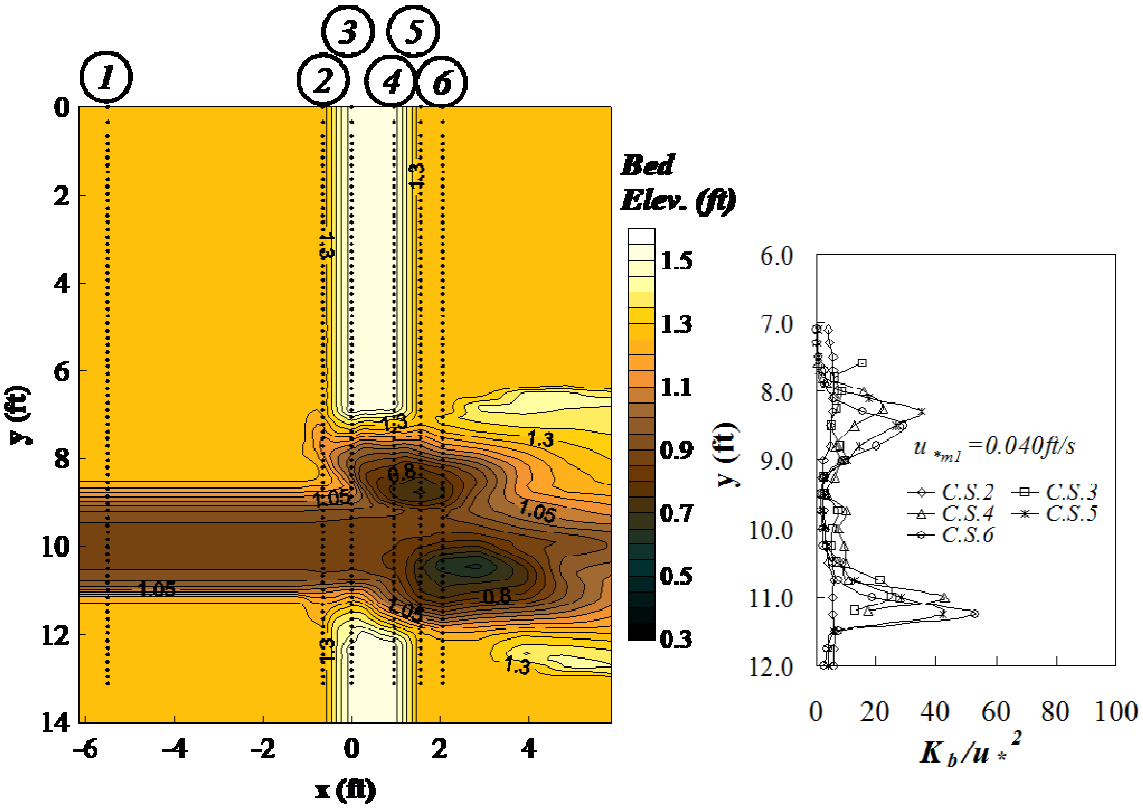

Run 16 (F), L_a/B_f = 0.88, Q = 2.2 cfs

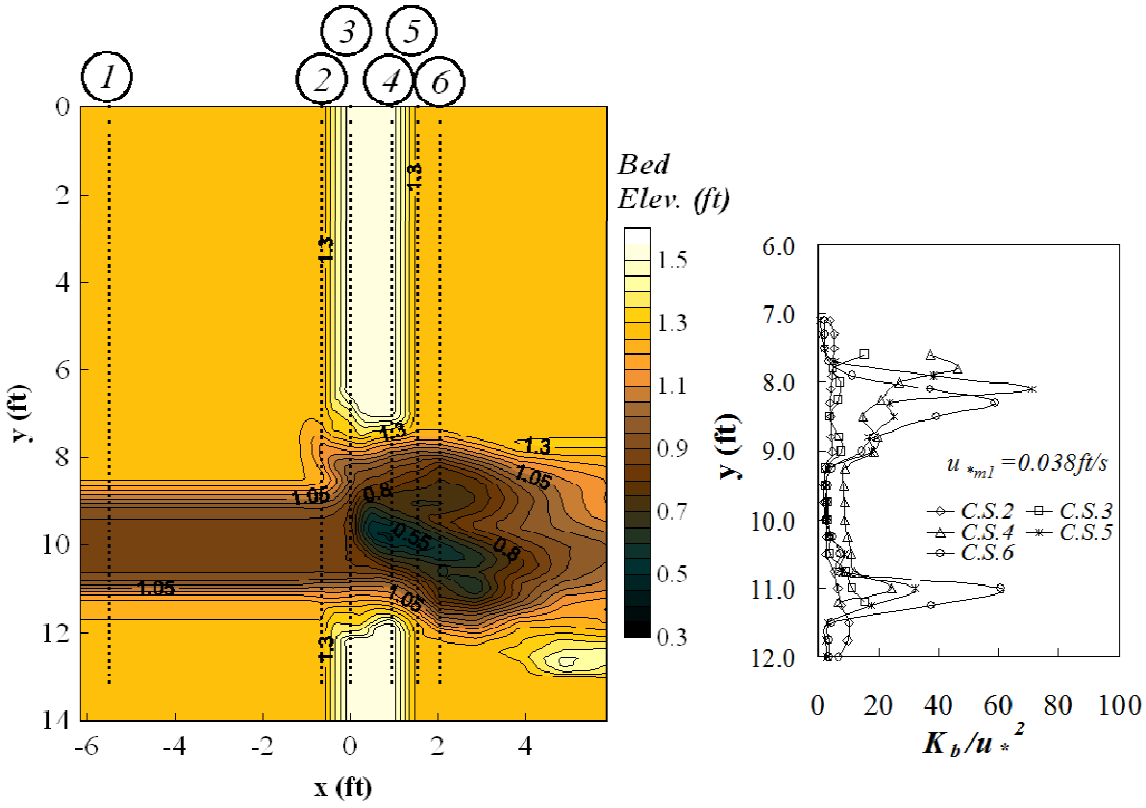

Run 17 (SO), L_a/B_f = 0.88, Q = 2.6 cfs

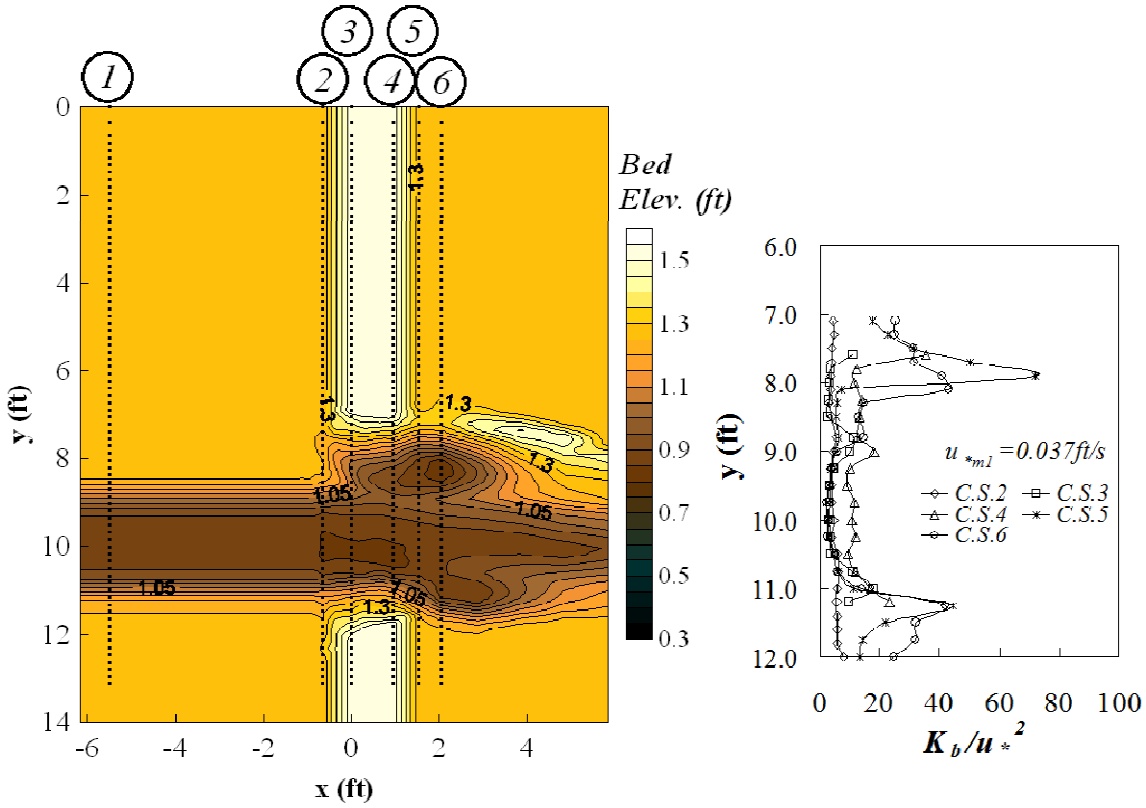

Run 18 (OT), L_a/B_f = 0.88, Q = 3.9 cfs

REFERENCES

Abt, Steven R. et al. (1998). “Riprap sizing at toe of embankment slopes”, Journal of Hydraulic Engineering, ASCE 124, no 7, pp. 672-677

Ahmed, Ferdous and Rajaratnam, N. (2000). “Observations on flow around bridge abutment”, Journal of Hydraulic Engineering, ASCE 126, no 1, pp. 51-59

Arneson, Larry A., and Abt, Steven R. (1998). “Vertical contraction scour at bridges with water flowing under pressure conditions”, Journal of Transportation Research Record, no 1647, pp. 10-17

Ballio, Francesco, Teruzzi, Anna and Radice, Alessio. (2009). “Constriction effects in clear-water scour at abutments”, Journal of Hydraulic Engineering, Technical Notes, ASCE 135, no. 2, pp. 140-145

Ballio, Francesco, Dey, Subhasish and Radice, Alessio. (2010). “Temporal scales for live-bed scour at abutments”, Journal of Hydraulic Engineering, Technical Notes, ASCE 136, no. 7, pp. 395-402

Benedict, S.T. and Caldwell, A.W. (1998). “The collection of clear-water contraction and abutment scour data at selected bridges sites in the coastal plain and piedmont of South Carolina”, Water Resources Engineering, ASCE, Menphis, TN, pp. 216-222

Benedict, S.T., Deshpande, N. and Nadim M. Aziz (2007). “Evaluation of abutment scour prediction equations with field data”, Journal of Transportation Research Board no. 2025, pp. 118-026

Biglari, B. and Sturm. T.W. (1998). “Numerical modeling of flow around bridge abutments in compound channel”, Journal of Hydraulic Engineering, ASCE 124, no. 2, pp. 156-164

Blodgett, J.C. and Harris Carroll D. (1993). “Measurement of bridge scour at the SR-32 crossing of the Sacramento river at Hamilton City, California, 1987-92”, Proc.,Hydraulic Engineering, ASCE, San Francisco, CA, pp. 1860-1865

Brabets, T.P. (1994). “Scour assessment at bridges from flag point to Million Dollar Bridge, Copper River Highway, Alaska.”, Anchorage, AK, U.S. Geological Survey Water-Resources Investigations Report 94-4073

Brabets, T.P. (1995). “Application of surface geophysical techniques in a study of the geomorphology of the lower Copper River, Alaska”, Anchorage, AK, U.S. Geological Survey Water-Resources Investigations Report 94-4165

Buffington, J.M. (1999). “The legend of A.F. Shields”, Journal of Hydraulic Engineering, ASCE 125, no. 4, pp. 376-387

Cardoso, A.H. and Bettess, R. (1999). “Effects of time and channel geometry on scour at bridge abutments”, Journal of Hydraulic Engineerig, ASCE 125, no 4, pp. 388-399

Chrisohoides, A., Sotiropoulos, F. and Sturm, T.W. (2003). “Coherent structures in flat-bed abutment flow: Computational fluid dynamics simulations and experiments”, Journal of Hydraulic Engineering, ASCE 129, no 3, pp. 177-186

Coleman, S.E. and Melville, B.W. (2001). “Case study: New Zealand bridge scour experiences”, Journal of Hydraulic Engineering, ASCE 127, no 7, pp. 535-546

Cristina Maria Sena Fael, et al. (2006). “Local scour at vertical wall abutments under clear-water flow conditions”, Water Resources Research, ASCE 42, pp. 1-12

Dey, Subhasish and Barbhuiya A.K. (2005). “Time variation of scour at abutments”, Journal of Hydraulic Engineering, ASCE 131, no 1, pp. 11-23

Dey, Subhasish and Barbhuiya A.K. (2006). “Velocity and turbulence in a scour hole at a vertical-wall abutment”, Flow Measurement and Instrumentation, ASCE 17, pp. 13-21

Dey, Subhasish, Chiew, Y.M. and Kadam, M.S. (2008). “Local scour and riprap stability at an abutment in a degrading bed”, Journal of Hydraulic Engineering, ASCE 134, no. 10, pp. 1496-1502

Diplas, P., Dancey, C., Celik, A., Valyrakis, M., Greer, K., and Akar, T. (2008). “The role of impulse on the initiation of particle movement under turbulent flow conditions”, Science, Vol. 322, pp. 717-720

Duc, Bui minh and Rodi, Wolfgang (2008). “Numerical simulation of contraction scour in an open laboratory channel”, Journal of Hydraulic Engineering, ASCE 134, no. 4, pp. 367-377

Ettema, R., Nakato, T., Yorozuya, A., and Muste, M. (2008). “Three abutment scour conditions investigated with laboratory flume” Proc. Fourth International Conference on Scour and Erosion, Chou University, Tokyo, Japan.

Ettema, R., Nakato, T., and Muste, M. (2010). “Estimation of scour depth at bridge abutments” NCHRp pp. 24-20, National Co-operative Highway Research Program, Washington D.C., U.S.A.

Ettema, R., Constantinescu, G., and Melville, B.M. (2011) “Evaluation of bridge-scour research: Pier scour processes and prediction” NCHRP pp. 24-27(01), National Co-operative Highway Research Program, Washington D.C., U.S.A.

Fischer, Edward E. (1993). “Scour at bridge over the Weldon river, Iowa”, Proc., Hydraulic Engineering, ASCE, San Francisco, CA, pp. 1854-1859

Fischer, Edward E. (1994). “Contractions scour at a bridge over the Iowa river”, Proc., Hydraulic Engineering, ASCE, Buffalo, NY, pp. 31-35

Fischer, Edward E. (1995). “Contractions scour at a bridge over Wolf creek, Iowa”, Proc., Water Resources Engineering, ASCE, San Antonio, TX, pp. 430-434

French, Richard H. (1986). Open Channel Hydraulic. Text book series in Water resources and Environmental Engineering, McGraw-Hill, NY.

Froehlich, David C. (1989). “Local scour at bridge abutments”, Proc. National Conference of Hydraulic Engineering, ed. M.A. Ports, ASCE, New Orleans, LU pp. 13-18

Froehlich, David C. (1995). “Armor-limited clear water contraction scour at bridge”, Journal of Hydraulic Engineering. ASCE 121, no 6, pp. 490-493

Franzeit, S., Larcan, E., and Mignosa, P. (1982). “Influence of tests durations on the evaluation of ultimate scour around circular piers” Proc. International Conference on Hydraulic Modeling of Civil Engineering Structure., Cranfield, Bedford MK43 OAJ, England, pp. 381-396.

Garcia, C.M., Cantero, M. I., Nino, Y., and Garcia, M. H. (2005). “Turbulence measurements with acoustic Doppler velocimeters”, Journal of Hydraulic Engineering, ASCE 131, no12, pp. 1062-1073.

Garcia, C.M., Cantero, M. I., Nino, Y., and Garcia, M. H. (2007). *Closure to* “Turbulence measurements with acoustic Doppler velocimeters”, Journal of Hydraulic Engineering, ASCE 131, no12, pp. 1062-1073.

Ge, L., Lee, S., Sotiropoulos, F., and Sturm, T. W. (2005). “3D unsteady RANS modeling of complex hydraulic engineering flows. Part II: Model validation and flow physics”, Journal of Hydraulic Engineering, ASCE 131, no 9, pp. 809-820.

Goring, D. and Nikora, V. (2002). “Despiking acoustic Doppler velocimeter data”, Journal of Hydraulic Engineering, ASCE 128, no1, pp. 117-126.

Hayes, D.C. (1996). “Scour at bridge sites in Delaware, Maryland, and Virginia”, Richmond, VA, U.S. Geological Survey Water-Resources Investigations Report pp. 96-4089

Hunt, B.E. et al (1998). “Scour monitoring of the Woodrow Wilson bridge”, Water Resources Engineering, ASCE, Memphis, TN, pp. 57-62

Holnbeck, Stephen R., Parrett, Charles., and Tillinger, Todd N. (1993). “Bridge scour and change in contracted section, Razor Creek”, Proc., Hydraulic Engineering, ASCE, San Francisco, CA, pp. 2249-2255

Hong, S. (2005). “Interaction of Bridge Contraction Scour and Pier Scour in a Laboratory River Model.” Master’s thesis, Georgia Institute of Technology.

Hong, S., Gotvald, A. Sturm, T.W. and Landers, M. (2006). “Laboratory and field measurement of bridge contraction scour”, Proc. Third International Conference on Scour and Erosion, CURNET, Gouda, Netherlands.

Hong, S. and Sturm, T.W. (2009). “Physical model study of bridge abutment and contraction scour under submerged orifice flow conditions”, 33rd IAHR Congress: Water Engineering for a Sustainable Environment, VANCOUVER, British Columbia, Canada.

Hong, S. and Sturm, T.W. (2010). “Physical modeling of abutment scour for overtopping, submerged orifice and free surface flows”, Proc. Fifth International Conference on Scour and Erosion, Sanfrancisco, U.S.A.

Johnson, Peggy A. and Niezgoda, Sue L. (2004). “Risk-based method for selection bridge scour countermeasures”, Journal of Hydraulic Engineering, ASCE 130, no 2, pp. 121-128

Kirkil, G., Constantinescu, S.G. and Ettema, R. (2008). “Coherent structures in the flw field around a circular cylinder with scour hole”, Journal of Hydraulic Engineering, ASCE 134, no. 5, pp. 572-587

Knight, Donald W. and Demetriou, John D. (1983). “Flood plain and main channel flow interaction”, Journal of Hydraulic Engineering, ASCE 108, no. 8, pp. 1073-1092

Korkut R. et al. (2007). “Geobag performance as scour countermeasure for bridge abutments”, Journal of Hydraulic Engineering, ASCE 133, no. 4, pp. 431-439

Krogstad, P.A. and Antonia, R.A. (1999). “Surface roughness effects in turbulent boundary layers”, Experiments in Fluids, 27, no. 5, pp. 450-460

Kuhnle, R.A., Alonso, C.V. and Shields, F.D. (2002). “Local scour associated with angled spur dikes”, Journal of Hydraulic Engineering. Technical Notes, ASCE 128, no 12, pp. 1087-1093

Lacey, R.W. Jay and Rennie, C.D. (2012). “Laboratory investigation of Turbulent flow structure around a bed-mounted cube at multiple flow stages”, Journal of Hydraulic Engineering, ASCE 138, no. 1, pp. 71-84

Laursen, E.M. (1958a) “Scour at bridge crossings.”, Iowa Highway Research Board Bulletin No. 8. Iowa City: Iowa Institute of Hydraulic Research, University of Iowa

Laursen, E.M. (1958b) “The total sediment load of streams”, Journal of Hydraulic Div., ASCE 54, no. HY1, pp. 1-36

Laursen, E.M. (1960) “Scour at bridge crossings”, Journal of Hydraulic Div., ASCE 86, no. HY2, pp. 39-54

Laursen, E.M. (1963) “An analysis of relief bridge scour”, Journal of Hydraulic Div., ASCE 89, no. HY3, pp. 93-117

Landers, M.N., and Mueller, D.S. (1993). “Reference surfaces for bridge scour depth”, Proc., National Conference on Hydraulic Engineering, ASCE, San Francisco, CA, pp. 2075-2080

Lane, S.N., Biron, P.M., Bradbrook, K.F., Butler, J.B., Chander, J.H., Crowell, M.D., Mclelland, S.J., Richards, K.S., and Roy, A.G. (1998). “Three-dimensional measurment of river channel flow processes using Acoustic Doppler Velocimetry”, Earth Surface Processes and Landforms, Vol. 23, pp. 1247-1267

Lee, Seung oh, Sturm, T.W., Gotvald, A., and Landers, M. (2004). “Comparison of laboratory and field measurements of bridge pier scour.” Proc. Second International Conference on Scour and Erosion, ed. By Y.M. Chiew, S.Y. Lim, and N.S. Cheng, Singapore, pp. 231-239

Lee, Seung Oh (2006). “Physical modeling of local scour around complex bridge piers”, Ph.D. Thesis, School of Civil and Environmental Engineering, Georgia Institute of Technology, Atlanta, GA.

Lee, Seung oh and Sturm, T.W. (2009). “Effect of sediment size scaling on physical modeling of bridge pier scour”, Journal of Hydraulic Engineering, ASCE 135, no 10, pp. 793-802

Ligrani, P.M. and Moffat, R.J. (1986). “Structure of transitionally rough and fully rough turbulent boundary layers”, Journal of Fluid Mechanics, Vol. 162, pp. 69-98

Lim, Siow-yong (1997). “Equilibrium clear-water scour around an abutment”, Journal of Hydraulic Engineering, ASCE 123, no. 3, pp. 237-243

Lim, Siow-yong., and Cheng, Nian-Sheng. (1998). “Scouring in long contraction”, Journal of Irrigation and Drainage Engineering, ASCE 124, no 5, pp. 258-261

Lim, Siow-yong., and Cheng, Nian-Sheng. (1998). “Prediction of live-bed scour at bridge abutments”, Journal of Hydraulic Engineering, ASCE 124, no 6, pp. 635-638

Martin, V., Fisher, T.S.R., Millar, R.G., and Quick, M.C. (2002). “ADV data analysis for turbulent flows: low correlation problem”, Hydraulic Measurement and Experiment Methods 2002, Proc. Of the Specialty Conf., ed. By T.L. Wahl, C.A. Pugh, K.A. Oberg, and T.B. Vermeyen, ASCE, Reston, VA

Melville, B.W. (1992) “Local scour at bridge abutments”, Journal of Hydraulic Engineering, ASCE 118, no. 4, pp. 615-631

Melville, B.W. (1995) “Bridge abutment scour in compound channels”, Journal of Hydraulic Engineering, ASCE 121, no. 12, pp. 863-868

Melville, B.W. (1997) “Pier and abutment scour: integrated approach”, Journal of Hydraulic Engineering, ASCE 123, no. 2, pp. 125-136

Melville, B.W. and Coleman, S.E. (2000). Bridge Scour. Water Resources Publications, Highlands Ranch, Colorado.

Melville, B.W. et al. (2006). “Countermeasure toe protection at spill-through abutments”, Journal of Hydraulic Engineering, ASCE 132, no. 3, pp. 235-245

Melville, B.W. et al. (2006). “Scour countermeasure for wing-wall abutments”, Journal of Hydraulic Engineering, ASCE 132, no. 6, pp. 563-574

Melville, B.W. et al. (2007). “Riprap size selection at wing-wall abutments”, Journal of Hydraulic Engineering, ASCE 133, no. 11, pp. 1265-1269

Morales, R., Ettema, R. and Barkdoll, B. (2008). “Large-scale flume tests of riprap-apron performance at bridge abutment on a floodplain”, Journal of Hydraulic Engineering, ASCE 134, no. 6, pp. 800-809

Morris, J.L. and Pagan-Ortiz, J.E. (1999). “Bridge scour evaluation program in the United States.”, Stream Stability and Scour at Highway Bridges, E.V. Richardson and P.F. Lagasse, eds., ASCE, pp. 61-70

Mueller, D.S. and Hitchcock, H.A. (1998). “Scour measurements at contracted highway crossing in Minnesota, 1997”, Water Resources Engineering, ASCE, Menphis, TN, pp. 210-215

Mueller, D.S. and Wagner, C.R. (2005). “Field observation and evaluations of streambed scour at bridges”, Lousiville, KY, U.S. Department of Transportation FHWA-RD-03-052

Myers, R.C. and Lyness, J.F. (1997). “Discharge rations in smooth and rough compound channels”, Journal of Hydraulic Engineering, ASCE 123, no. 3, pp. 182-188

Naot, D. et al (1993) “Hydrodynamic behavior of compound rectangular open channels”, Journal of Hydraulic Engineering, ASCE 119, no. 3, pp. 390-408

Niezgoda, Sue L., and Johnson, Peggy A. (1999). “Abutment scour at small severly contracted bridges”, Proc., Cold Regions Engineering ‘Putting Into Practice’., ASCE, Lincoln, NH, pp. 600-611

Nikora, V.I. and Smart, G.M. (1997). “Turbulence characteristics of new zealand gravel-bed rivers”, Journal of Hydraulic Engineering, ASCE 123, no. 9, pp. 764-773.

Nikora, Vladimir I. and Goring, Derek G. (1998). “ADV measurements of turbulence: Can we improve their interpretation?”, Journal of Hydraulic Engineering, ASCE 124, no. 6, pp. 630-634.

Nikora, Vladimir I. and Goring, Derek G. (2000). “Flow turbulence over fixed and weakly mobile gravel beds”, Journal of Hydraulic Engineering, ASCE 126, no. 9, pp. 679-690.

Norman, V.W. (1975). “Scour at selected bridge sites in Alaska”, Anchorage, AK, U.S. Gelolgacal Survey Water-Resources Investigations Report 32-75.

Oliveto, G. and Hager, W.H. (2002). “Shields’ Entrainment Criterion in Bridge Hydraulics”, Journal of Hydraulic Engineering, ASCE 128, no. 5, pp. 538-542

Oliveto, G. and Hager, W.H. (2002). “Temporal Evolution of Clear-Water and Abutment Scour”, Journal of Hydraulic Engineering, ASCE 128, no. 9, pp. 811-820

Oliveto, G. and Hager, W.H. (2005). “Further Results to Time-dependent Local Scour at Bridge Elements”, Journal of Hydraulic Engineering, ASCE 131, no. 2, pp. 97-105

Oliveto, G. and Hager, W.H. (2007). “Generalized Approach for Clear-water Scour at Bridge Foundation Elements”, Journal of Hydraulic Engineering, ASCE 133, no.11, pp. 1229-1240

Paik, Joongcheol. and Sotiropoulos, Fotis.(2007). “Coherent structure dynamics upstream of a long rectangular block at the side of a large aspect ratio channel”, Physics of Fluids, no. 17, 115104

Paik, Joongcheol., Escauriaza, Cristian. and Sotiropoulos, Fotis.(2007). “On the bimodal dynamics of the turbulent horseshoe vortex system in a wing-body junction”, Physics of Fluids, no. 19, 045107

Paik, Joongcheol., Escauriaza, Cristian. and Sotiropoulos, Fotis.(2010). “Coherent structure dynamics in turbulent flows past in-stream structures: some insights gained via numerical simulation”, Journal of Hydraulic Engineering, ASCE 136, no. 12, pp. 981-993

Parola, A.C., Hagerty, D.J., Mueller, D.S., Melville, B.W., Parker, G., and Usher, J.S.(1997b). “The need for research in scour at bridge crossings”, Proc., Of XXVII IAHR Congress, Managing Water: Coping with Scarcity and Abundance, San Francisco, CA, pp. 124-129

Pagan-ortiz,J.E. (1998). “Status of the scour evaluation of bridges over waterways in the United States”, Water Resources Engineering, ASCE, Memphis, TN, pp.2-4

Pezzinga, Giuseppe (1994). “Velocity distribution in compound channel flows by numerical modeling”, Journal of Hydraulic Engineering, ASCE 120, no. 10, pp. 1176-1198

Rahman, S. and Webster, D.R. (2005). “The effect of bed roughness on scalar fluctuations in turbulent boundary layers”, Experiments in Fluids, 38, no. 3, pp. 372-384

Radice, Alessio., Porta, Giovanni and Franzetti, Silvio. (2009). “Analysis of the time-averaged properties of sediment motion in a local scour process”, Water Resources Research, Vol. 45, pp 1-12

Radice, Alessio., Malavasi, Stefano. and Ballio, Francesco. (2008). “Sediment kinematics in abutment scour”, Journal of Hydraulic Engineering, ASCE 134, no. 2, pp. 146-156

Rajaratnam, N and Ahmadi, R.M. (1979). “Interaction between main channel and flood-plain flows”, Journal of Hydraulic Div., ASCE 105, no. 5, 573-588

Rajaratnam, Nallamuthu and Nwachukwu, Benjamin. (1983). “Flow near groin-like structures”, Journal of Hydraulic Engineering, ASCE 109, no. 3, pp. 463-480

Richardson, E.V. and Richardson, J.R. (1999). “Determining contraction scour”, In Stream Stability and Scour at Highway Bridges, ed. E. V. Richardson and P.F. Lagasse, ASCE, pp. 483-491

Richardson, E.V. and Davis, S.R. (2001). “Evaluating scour at bridges, Fourth edition”, Hydraulic engineering circular No.18, Federal Highway Administration, U.S. Department of Transportation Report No. FHWA NHI 01-001 HEC-18.

Schlichting, H (1979). Boundary-Layer theory. New York: McGraw-Hill.

Schreider, Mario., Scacchi, Graciela., Franco, Felipe., and Romano, Carlos. (2001). “Contraction and abutment scour in relief bridge in a flood plain”, Proc., Wetlands Engineering and River Restoration, ASCE, Reno, NV, pp. 1375-1386

Shatanawi, K.M., Aziz, N.M. and Khan, A.A. (2008). “Frequency of discharge causing abutment scour in south carolina”, Journal of Hydraulic Engineering, ASCE 134, no. 10, pp. 1507-1512

Shields, A. (1936). “Application of similarity principles and turbulence research to bed-load movement. trans.”, W.P. ott and J.C. van Uchelen. Hydrodynamics Laboratory Publ. No. 167. Pasadena: USDA, Soil Conservation Service Cooperative Laboratory, California Institute of Technology.

Shirole, A.M. (1991). “Planning for a comprehensive bridge safety assurance program”, Transportation Research Board, 1290: pp. 137-142.

SonTek (2001). “Acoustic Doppler Velocimeter (ADV) principles of operation”, SonTek Technical Notes, SonTek, San Diego, CA.

Sturm, T.W. and Janjua, N.S. (1994) “Clear-water scour around abutments in floodplains”, Journal of Hydraulic Engineering, ASCE 120, no. 8, pp. 956-972

Sturm, T.W. (1999). “Abutment scour in compound channels.”, In Stream Stability and Scour at Highway Bridges, ed. E. V. Richardson and P.F. Lagasse, ASCE, pp. 443-456

Sturm T.W. (1999). “Abutment scour studies for compound channels”, Washington, DC, Federal Highway Administration, U.S. Department of Transportation Report No. FHWA-RD-99-156

Sturm, T.W. (2001). Open Channel Hydraulics. Text book series in Water resources and Environmental Engineering, McGraw-Hill, NY.

Sturm, T. W. et al (2004). "Laboratory and 3D numerical modeling with field monitoring of regional bridge scour in Georgia", Atlanta, GA, Georgia Department of Transportation Final Project, Project No. 2002

Sturm, T.W. (2006) "Scour around bankline and setback abutments in compound channels", Journal of Hydraulic Engineering, ASCE 132, no. 1, pp. 21-32

Sturm, T.W., Ettema, R., and Melville, B.M. (2011) "Evaluation of bridge-scour research: Abutment and contraction scour processes and prediction" NCHRP p 24-27(02), National Co-operative Highway Research Program, Washington D.C., U.S.A.

Teruzzi, A., Ballio, F. and Armenio, V. (2009). "Turbulent stresses at the bottom surface near an abutment: Laboratory-scale numerical experiment", Journal of Hydraulic Engineering, ASCE 135, no. 2, pp. 106-117

Tominaga, Akihiro and Nezu, Iehisa (1991) "Turbulent structure in compound open-channel flows", Journal of Hydraulic Engineering, ASCE 117, no. 1, pp. 21-41

Umbrell, Edward R. et al. (1998). "Clear-water contraction scour under bridges in pressure flow", Journal of Hydraulic Engineering, ASCE 124, no. 2, pp. 236-240

U.S. Army Corp of Engineers. (1998). HEC-RAS Hydraulic Reference Manual, Version 2.2. Davis, CA: U.S. Army Corps of Engineers, Hydrologic Engineering Center.

Van Rijn, L.C. (1984a) "Sediment transport, Part I: Bed load transport.", Journal of Hydraulic Engineering, ASCE 110, no. 10, pp. 1431-56

Van Rijn, L.C. (1984b) "Sediment transport, Part II: Suspended load transport.", Journal of Hydraulic Engineering, ASCE 110, no. 11, pp. 1613-41

Van Rijn, L.C. (1984c) "Sediment transport, Part III: Bed form and alluvial roughness.", Journal of Hydraulic Engineering, ASCE 110, no. 12, pp. 1733-54

Wahl, T. (2002). "Analyzing ADV data using WinADV.", Hydraulic Measurements and Experiemts Methods 2002, Proc. Of the Specialty Conf., ed. By T.S. Wahl, C.A. Pugh, K.A. Oberg, and T.B. Vermey

White, F.M. (1991). Viscous Fluid Flow second edition. Text book series in Mechanical Engineering, McGraw-Hill, NY.

Whitehouse, R. J. S. (1997). “Scour at marine structures: A manual for engineers and scientists” Research Rep. SR417, HR Wallingford Ltd., Wallingford, U.K.

Wormleaton, P.R. and Hadipanos, P. (1985). “Flow distribution in compound channels”, Journal of Hydraulic Engineering, ASCE 111, no. 2, pp. 357-361

Yalin, M.S., and Karahan, E. (1979). “Inception of sediment transport”, Journal of Hydraulic Div., ASCE 105, no. HY11, pp. 1433-1443

Yanmaz, A.M., and Kose, O. (2007). “Time-wise variation of scouring at bridge abutments”, Sadaha-Academic Proc. in Engineering Sciences, Vol. 32, no. 3, pp. 199-213